Optimal array design for low tidal resource regions

MSc Offshore and Dredging Engineering

T.J.A. Bekkers

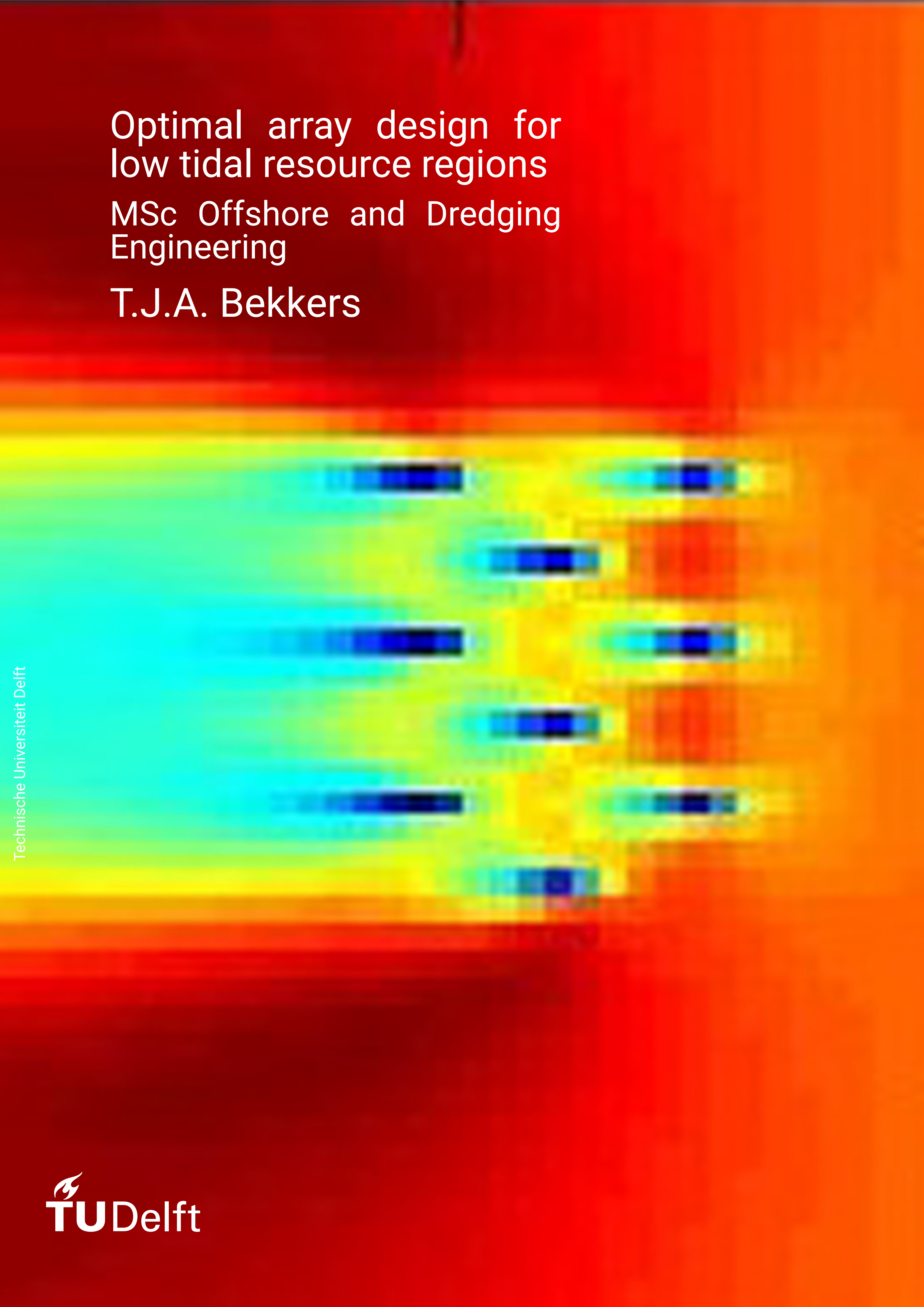

Technische Universiteit Delft

Optimal array design for low tidal resource regions

by

T.J.A. Bekkers

To obtain the degree of Master of Science in Offshore and Dredging Engineering
at the Delft University of Technology,
Ter verkrijging van de graad van Master of Science in Offshore and Dredging Engineering
aan de Technische Universiteit Delft.

Student number:	4474910
Project duration:	December 2021 (November 20, 2021) – September 27, 2022
Thesis committee:	Dr. George Lavidas
Chair of the committee:	Dr. George Lavidas
Daily and Main Supervisor:	Dr. George Lavidas
Committee Member:	Dr. Matias Alday Gonzalez
Committee Member:	Dr. Ing. Karel Van Dalen

Preface

The thesis focuses on optimal array design for low tidal resource areas and the question of whether such designs could be economically profitable. The thesis builds on previous research done in the field of high tidal resource areas, and tests whether such designs could also be successfully introduced in low tidal areas such as the Netherlands. Using the Dutch coast configuration, tidal data and applying an array configuration with the turbines positioned closely together significantly increases the production of the farm. This is an important finding because it increases the number of locations where tidal farms may be considered significantly. Furthermore, the economic viability of the tidal farm is increased.

As for the process of writing the thesis, I want to thank George Lavidas for supervising, guiding and challenging me throughout these past nine months. His help really gave me the confidence to keep going, even in these challenging covid-times. I also want to express my sincere gratitude to Alberto Perez, who helped me check my model and who gave me viable feedback.

Finally, I would like to express my gratitude to my family and my fellow students at the TU Delft for motivating and supporting me.

I hope you will enjoy reading this thesis.

T.J.A. Bekkers
September 14, 2022

Abstract

Tidal energy has the potential to be an important and necessary addition to the available sources of energy in the coming energy transition. While there is an extensive body of research on the topic of high tidal resource locations, little research exists on low tidal resource locations such as The Netherlands. The thesis aims to reduce this gap by designing the optimal Dutch tidal farm and determining its economic viability. Using Delft 3D and Telemac, 2D models are created to simulate the tidal resources based on shallow water equations. The models are used to determine the best location for the Dutch tidal stream farm through a multi-criteria decision making analysis using the analytic hierarchy process model. For the optimal location, a tidal cycle is extracted from delft dashboard data and the optimal configuration is designed. In the design stage of a tidal farm in low current velocities, the simulation shows the wake effect positively influences the production. The power production of such a tidal farm over a tidal cycle is calculated using various economic metrics. The results show that currently a tidal farm cannot be economically viable without substantial governmental support. However, this paper argues that tidal energy comes with a number of important benefits that cannot be neglected, such as sustainability, output consistency/predictability and potential future energy independency. Therefore, tidal farms in low resource areas show potential, but further technological-, economical-, and (geo) political developments are needed in the coming years for them to become sufficiently beneficial in the Dutch energy transition to a sustainable energy mix.

Contents

List of Figures

List of Tables

List of Abbreviations and Nomenclature

The next list describes several symbols and abbreviations that will be used in the literature study

List of Abbreviations

$alpha$	Reflection coefficient
..D	Distance of x time the diameter
1 D	One-dimensional
2 D	Two-dimensional
3 D	Three-dimensional
ADCP	Acoustic doppler current profilers
AD	Actuator disk
AHP	Analytic hierarchy process
BK	Blue Kenue
CAPEX	Capital expenditures
CFD	Computational fluid dynamics
CFL	Courant-Friedrichs-Lewy
CI	Consistency index
CR	Consistency ratio
DDB	Delft dashboard
DECEX	Decommissioning expenses
ES	European shelf
Fudaa	Fudaa prePro
GIS	Geographical information systems
IRR	Internal rate of return
LCOE	Levelized cost of energy
LMAD	Linear momentum actuator disc theory
MCDM	Multi-criteria decision making
NPV	Net present value
O&M	Operation and maintenance
OPEX	Operating expenses
OSU	Oregon State University
PP	Payback period

RANS	Reynolds averaged Navier-Stokes
RI	Random index
RMSE	Root mean square error
r	Pearson coefficient
SI	Scatter index
SST	Shear-stress-transport
TADA	Tuned actuator disk approach
TPXO	TOPEX, Poseidon global inverse solution
UTM	Universal transverse mercator zone

Nomenclature

ΔP	Pressure difference
Δt	Time step
Δx	Grid size
ϵ	Dissipation of the eddies
γ	Momentum passing through
λ	Eigenvalue
μ	Viscosity
μ_t	Eddy viscosity
ρ_w	Density of water
σ	Multiple depth layers
ζ	Water level
a	Axial induction factor
A_R	Area of the rotor area
A_S	Total area of the turbine
C	Roughness coefficient
c_0	Initial investment
C_D	Drag coefficient
C_d	Bottom friction
C_P	Power coefficient
C_t	Thrust coefficient
c_t	Cash flow
C_{loss}	Porosity
D	Turbine diameter
DP_i	Dimensionless production coefficient

e	Thickness of the disk
E_T	Annual energetic production
E_{xi}	Expenditure for a year
f	Coriolis effect
F_t	Thrust force
$F_{x,y}$	Reynolds stress component
g	Gravitational constant
h	Water depth
H_s	Significant wave height
i_{cr}	Critical year
K	Turbulence kinetic energy
k	Resistance coefficient
L	Lifetime
l	Length of the eddies
LC_{total}	Total lifetime cost
LP_{total}	Total lifetime output
$M_{x,y}$	Source terms
n	Amount of turbines
n	Manning coefficient
n_{node}	Amount of nodes at the AD
P	Power production
P_i	Power production for a single turbine
$P_{average}$	Average power potential
P_{BE}	Break even power
$P_{x,y}$	Pressure terms
PP	Preference percentage
r	Discount rate
R_H	Hydraulic radius
S	Discharge
S_0	Hydraulic gradient
S_i	Source term
$S_{h,x,y}$	Source terms
t	Time
T_e	Electrical tariff

t_i	Number of hours
T_p	Wave period
T_{actual}	Actual production over a time period
$T_{equivalent}$	Equivalent production over a time period
U	Depth average velocity
u	Velocity
u and v	U velocity component lateral direction, V velocity component longitudinal direction
U_*	Friction velocity
U_∞	Upstream velocity
U_d	Velocity at disk
Z	Free surface

1

Introduction

Climate change is a big challenge that not only The Netherlands is facing, but also the rest of the world. In order to reduce the speed at which climate change occurs, it is important to reduce our carbon footprint. A way of reducing this footprint is by reducing our reliance on fossil fuels. However, given that energy consumption remains unchanged, a reduction in the use of fossil fuels will lead to a rise in the demand for electricity. To offset the increased demand for electricity, new methods of energy generation should be developed and implemented. In search for new sustainable energy sources, tidal energy is a source that should not be overlooked [89]. The advantage of using tidal energy is that the amount of energy that can be generated and the time this occurs can be forecasted accurately. Because tidal energy is mostly dependent on the position of the moon [111]. Other sustainable energy resources, such as wind energy, are less predictable as they are more dependent on the weather. Therefore, tidal stream energy can be a valuable addition to the energy transition which the world will be facing in the coming years.

Tidal energy can be generated in two ways. The first method is tidal barrage, which uses which uses dams to keep the water during high tide and release the water during low tide generating electricity. This method is the more widely used one, as it has proven to be successful in the past. However, the environmental impact of tidal barrage is quite high, since the tidal range is modified. Upstream of the barrage changes in the salinity flow and flow of the estuary will have a big impact on Marine life. The second method uses tidal stream, which focuses on the current velocity and the power that is produced by a turbine, see Figure 1.1.

The environmental impact of the tidal stream method is believed to be much lower than the method using tidal barrage, because the tidal flow is less influenced and the size of the turbine is much smaller. The tidal stream method is not as often used as the tidal barrage method, and research on the tidal stream method is more scarce. Up to now, the true capabilities and adaptability of the tidal stream energy for the Dutch coastal line have not been assessed. The thesis will therefore be focusing on using tidal stream for energy production, testing whether this method could be suitable in low tidal areas such as The Netherlands. This is important research because all indigenous renewable resources should be utilized in the Energy Transition.

1.1. Problem statement

The challenge with tidal stream energy, is that at the moment it seems difficult to generate sufficient power to make it viable for low tidal locations such as The Netherlands. Due to the fact that the tidal resource in The Netherlands is considered to be low [46, 45, 22] and most tidal turbines are constructed for high velocities only. Like The Netherlands, most places in the world have low tidal currents which make it harder to generate enough energy. In order to make it possible to generate tidal stream energy in The Netherlands, research must be done to find the most optimal setup and adequate locations.

1.2. Value of the research

Because tidal stream energy is still in the beginning phase of its development, such an optimal setup has not yet been developed. Previously conducted research in tidal stream energy focusses only on areas where there is a high potential due to stronger currents. Therefore, research will need to be conducted to create a new model that is able to determine the best configuration for tidal stream energy generation under low tidal circumstances. This brings us to the following research question:

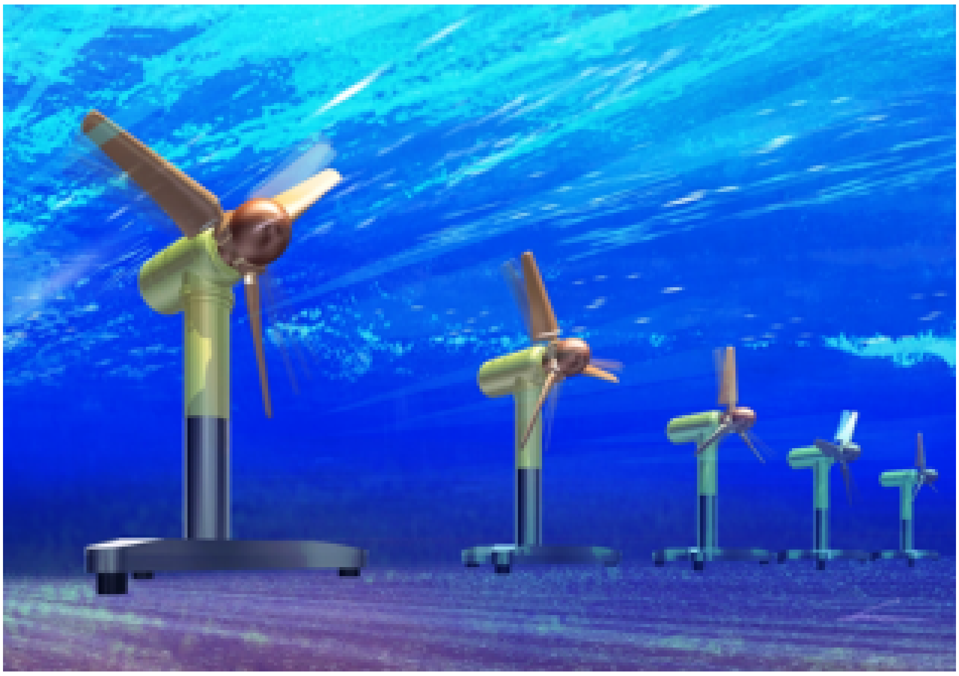

Figure 1.1: Tidal stream turbines artist's impression, [98]

"What is the best location and design for a tidal stream energy farm in The Netherlands?"

To answer the research question the following sub-questions must also be discussed:

1. What is the best location in The Netherlands to generate tidal energy?
2. Which design for tidal stream energy generation is most suitable for The Netherlands?
3. What is the best configuration of tidal stream generators to generate the highest amount of energy?
4. What will be the loads on the tidal stream generators, and how does that influence the design of the generators?
5. What are the economics of the project, is it possible to make the project economically viable?

A literature study to address the above stated research questions is carried out between January and March 2021. The thesis research is from March till the end of August. The structure of the report is that in chapter 2 a literature overview of previously conducted researches is given. Furthermore, the research gap is defined. In chapter 3 the methodology for answering the research question is presented. In chapter 4 different models used to simulate the tidal stream are shown. In chapter 5 the resource assessment is presented. In chapter 6 the turbines that are used and the implementation of these turbines for the power extracting is explained. In chapter 7 the best location for the tidal turbine is determined. In chapter 8 the most ideal array configuration for low tidal resource areas are described. In chapter 9 the economics of a tidal farm are described. Finally, the conclusion and discussion are described in chapter 10.

2

Literature review

The main objective of the literature review is to find relevant articles and books to better understand the workings of tidal energy and to summarise what other researchers have already published in this field of research. The focus on how past research on the subject of tidal energy has been conducted and provide the level of relevancy of the past research is shown in section 2.1 and section 2.2. A literature study on the subject of the sub-questions is conducted in section 2.3, section 2.5, section 2.6 and section 2.7. Finally, the identified research gaps are discussed in section 2.8.

2.1. Literature search

Particularly relevant literature regarding tidal power has been published by my supervisor George Lavidas. This assisted me to get started with state-of-the-art literature. Additional literature was found through Google scholar and Scopus database, by using the following search keywords: "Tidal energy", "Tidal resource", "Tidal resource assessments", "Actuator disk theory", "Tidal site assessment", "MCDM", "AHP", "Offshore wind site assessment", "Ocean tide", "Wake field study", "Delft 3D tidal", "Telemac tidal", "THETIS tidal" and "Tidal turbines". Furthermore, additional literature was found by using the reference lists of the obtained literature, through a so-called snowball effect.

2.2. Previous research

Tidal energy is a widely-researched subject, with research dating back to the last 50 years [68].Due to climate change and the increasing demand for sustainable energy, the interest in innovative tidal energy has gained momentum. Currently, most of the studies assess the viability of tidal energy at different locations with the use of varying methods. At small scale it was found that tidal energy is viable and can be a good addition to the energy transition [22]. However, the effect of large scale tidal farms still has to be fully investigated. Therefore, the effects of large scale tidal farms and their impact on the environment, marine life and tidal estuaries are so far not fully understood [78].

Another problem is that the costs of energy produced through tidal turbines are currently much higher than the costs of other forms of renewable energy. Due to the installation-, maintenance- and service-costs associated with tidal energy. Fortunately, investment in sustainable energy production has increased in general, resulting in an incentive for increasing innovation and research budgets with regards to tidal energy as well. Because of this, multiple countries have plans for large scale tidal projects, which could increase the total energy produced by tidal energy to 200 MW world wide [16, 87].

2.3. Location

As mentioned before, choosing the right location of a tidal farm is crucial. The location determines the tidal resource available due to the surrounding environment (orography), the topographical height of the sea bottom and subsequent water depth (bathymetry) and tidal range. Most tidal energy studies available have chosen the sea between Ireland and Great Britain, more specifically the Rathlin Sound location. The characteristics of this location make a very large tidal energy potential accessible. The high tidal energy potential results from the strait between the island (Rathlin Island) and the landmass of Ireland, see Figure 2.1. A high tidal energy potential will generally occur at locations with a channel or a river delta with flowing tides. This is indeed the case for the channel between Ireland and Great Britain [79].

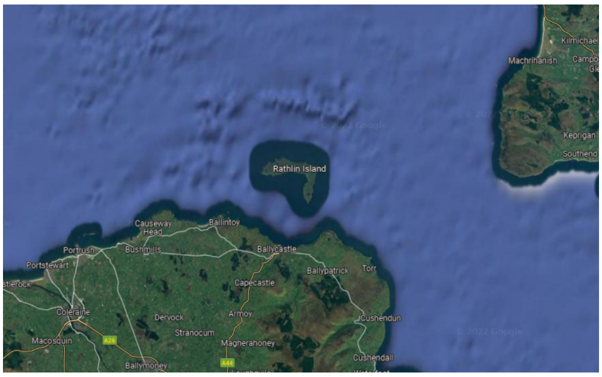

Figure 2.1: The Rahtlin Sound location

However, the amount of power extraction calculated was significantly lower than originally anticipated, which was due to higher bottom friction. Moreover, the influence of local geometry was not investigated sufficiently in depth [77, 58, 39, 47, 49, 78, 81, 4]. Although the tidal energy production came out lower than expected, the studies showed that it is possible to produce significant amounts of tidal energy at these locations. Following the Rathlin Sound location, multiple investigations have been done assessing the potential for tidal energy at different locations.

These locations are for example Norway and the English Channel [43, 80, 41, 19, 102]. The Netherlands has been regarded as a location with low tidal potential [46, 29]. The main reason why no research could be found regarding tidal resource potential for The Netherlands. Therefore, choosing the most optimal location in The Netherlands cannot simply be based on locations chosen in the past. To determine the optimal location in The Netherlands for tidal energy, I propose to use a Multi criteria decision making process. Amongst others, this decision making process accounts for power-, environmental- and socio-economic aspects. Based on the literature research these criteria are listed and explained further in chapter 7 and will be used in the thesis to identify potential site locations. From a first look, the geometry of the Dutch coastline presents two more promising regions. These locations are the channel between Den Helder and Texel in the north and the Oosterschelde and Westerschelde in the south. These regions are also presented in the red boxes in Figure 2.2 below.

Figure 2.2: The estimated locations for tidal energy in The Netherlands

2.4. Tidal forcing

Tidal flows are created by the gravitational force from the Moon and Sun. These forces move the water on Earth. The forces change due to the position of the Moon and Sun with respect to the Earth. The low and high tide each day is caused by the position of the Moon and the changes of tide over the different seasons due to the location of the Sun. These changes repeat over time and the changes can be measured and predicted. In Figure 2.3 the tidal forcing due to the Moon is illustrated. It shows that due to the gravitational pull of the Moon on the water on Earth two bulges on the opposite sides of the Earth are created, resulting in a high tide two times a day. These two bulges occur due to the fact that the water always moves from high pressure locations to low pressure locations. Due to the gravitational pull there is a high pressure and low pressure and so the water will flow. The Sun has a similar effect on the tidal force on Earth.

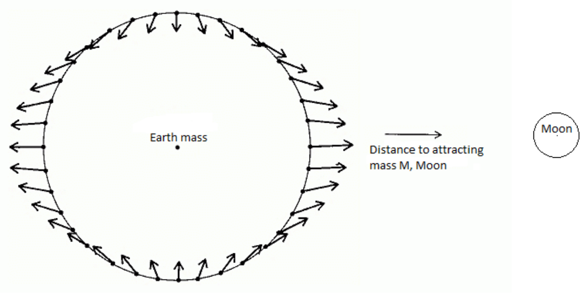

Figure 2.3: The tidal force due to the location of the Moon.

The motion between the Moon, Sun and Earth can be described by hundreds of periodic motions. These different motions are described as tidal constituents. These constituents are the mathematical value describing the motion of the Moon, Sun and Earth with respect to each other. From this the most important tidal constituents can be determined and the tides can be predicted for different locations. There are 37 constituents in total representing the location of the Moon, Sun and Earth. In Delft 3D and in Telemac, the tidal constituents that can be used are M2, S2, N2, K2, K1, O1, P1, and Q1 [21, 30].

Here, the constituents M2, S2, N2 and K2 express the semi-diurnal modes. The semi-diurnal cycle expresses the two high and two low tides that occur every day. M2 is the largest Lunar semi-diurnal constituent, and represents the direct gravitational effect of the Moon on the tides. M2 shows two peaks every day plus 50 minutes,[1] which is the result of the Moon orbiting in the same direction as the Earth. S2 is the largest semi-Solar diurnal constituent and is related to the gravitational effect of the Sun. Because the Earth rotates on its axis every 24 hours, this results in two peaks every 24 hours as a result of the Earth facing the Sun. N2 is the larger Lunar elliptic semi-diurnal constituent. K2 is the Luni Solar semi-diurnal constituent. The constituents K1, O1, P1, and Q1 express the diurnal modes. The diurnal mode expresses the location of the Sun and has a single high tide a day. K1 is the Lunar diurnal constituent, O1 is the Lunar diurnal constituent, P1 is the Solar diurnal constituent and Q1 is the larger Lunar elliptic diurnal constituent.

The constituents are represented by a cosine curve, of which the values provide the amplitudes and phases of the constituent motions. Unsurprisingly, summing all 37 tidal constituents results in a complex curve for the tides. Because Delft 3D and Telemac cannot accommodate the usage of all constituents, only the M2, S2, N2, K2, K1, O1, P1, and Q1 are used in the analysis of the tidal resource. While using all constituents might give a more accurate outcome, it is expected that using all constituents will only result in small changes in the outcome compared to the use of the above mentioned constituents, so the benefits are relatively small. The amplitude of constituents used is much higher than the other constituents, adding these will therefore have a small impact. Figure 2.4 shows the difference between the semi-diurnal and diurnal constituents. To visualise all possible locations of the Moon, Sun and Earth for a tidal resource, a single year analysis need to be constructed so that all cycles and positions are included. For the comparison between tidal gauge data and simulated data a minimum of 30 days needs to be used to represent the majority of the Lunar and Solar cycles.

2.5. Requirements of resource characterisation

When reviewing the resource potential of a location, the objective is to evaluate the different characteristics that determine the feasibility of constructing a project at this location. EquiMar (Commission of the European Communities) has published a protocol for conducting a resource assessment [74].The protocol sets out the required variables and the process of how to conduct the assessment. The protocol will be followed during this research.

Based on the protocol, three different methods for conducting the resources assessment at locations investigated can be used. The first method is the one-dimensional (1D) model. The model uses sea bed friction and channel dimensions to determine the energy extraction potential. A limitation with the use of the model

---

[1] The effect has a catch up time of 50 minutes.

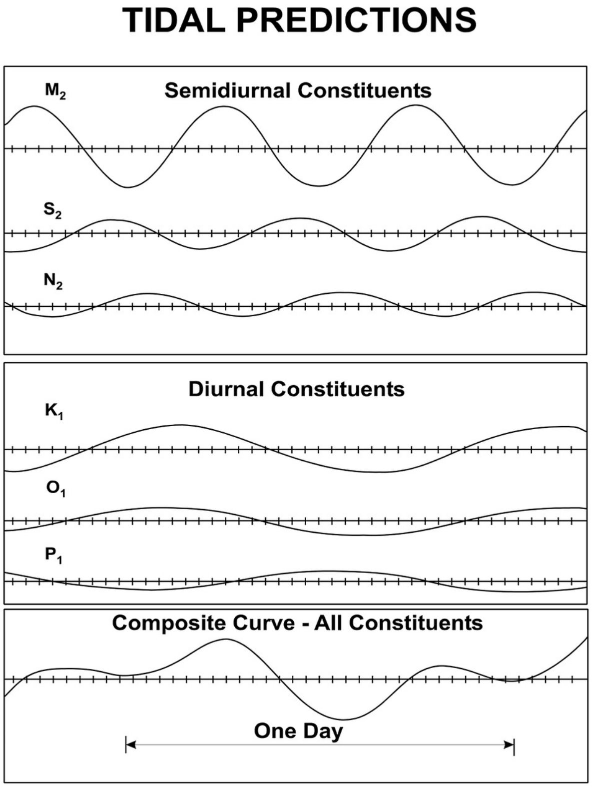

Figure 2.4: The difference between semi-diurnal and diurnal constituents, [10].

is that changes in bathymetry and/or changes in the design of the tidal farm are not possible.

The second method is the two-dimensional (2D) model. This method is able to take bathymetry and geometric changes into account. 2D models are applied in medium/large resource assessment areas and can assess the far field effect (wake) of a tidal farm. However, the 2D model cannot accurately predict the near wake effect. Furthermore, it is possible to create depth averaged velocity when using a 2D model.

The third method is the three-dimensional (3D) model. This model is able to identify the velocity of a water column and flow diversions caused by the tidal turbine. However, the issue with this method is that the computational time is significantly higher compared to the other methods. The 3D model will in practice only be used for small scale applications, like determining the exact location of a single tidal turbine or to determine the sediment transport caused by a turbine. Meaning that for resource assessments of medium to large area tidal farms the 3D method is not ideal and so 2D models are most commonly used for tidal assessments [77].

Because the required accuracy can be reached with the use of 2D models and the computational time is acceptable, the research constructs a 2D model to assess the resource of a given location. The research body that uses such 2D models used the following software programs [7]:

- Telemac, `https://opentelemac.org` [30]
- THETIS, `https://thetisproject.org/` [44]
- Delft 3D, `https://oss.deltares.nl/web/delft3d` [21]
- POM, `http://www.ccpo.odu.edu/POMWEB/` [83]
- Mike 21, `https://www.mikepoweredbydhi.com/products/mike-21-3` [24]

Table 2.1 presents different papers using Telemac, Delft 3D or THETIS. Because Delft 3D and Telemac are the most frequently used programs, the thesis will make use of these programs as well. These different methods will be further elaborated in subsection 2.5.1 and subsection 2.5.2.

The data that are used for the thesis are consistent with the data used in literature regarding tidal energy. The following data types are used:

- Tidal gauges and satellite altimetry are used to determine the sea level heights.
- The flow velocity can be determined with acoustic doppler current profilers (ADCP), these are installed on the seabed.
- Bathymetry data, seabed roughness and climate conditions are also used to determine the energy extraction of the tidal turbines. The bathymetry data that is used are provided by GEBCO [52]. The resolution used by GEBCO is 15 arc second or around the 463 meter. The model created is a 2D model, where the mean sea level is required for the resource assessment and for the energy extraction. Hence the GEBCO bathymetry that is based on the mean sea level satisfies the requirements. The impact of having a smaller resolution means that within the mesh the depths used are better corresponding to a real life scenario.

2.5.1. Telemac 2D

Telemac is an open source program that is created to solve the free-surface equations. This is done by using the finite-element approach for numerical simulations. A tidal turbine extracts energy from a tidal flow. Placing the tidal turbine will lead to a drag force on the flow, caused by the turbine structure and by the energy extraction of the rotor. The total drag on the structure can be calculated as follows:

$$F_D = \frac{1}{2}\rho C_t A_R U^2 + \frac{1}{2}\rho C_D A_S U^2 \tag{2.1}$$

U is the velocity of the flow, ρ is the density of the water, C_t is the thrust coefficient, C_D is the drag coefficient, A_R is the area of the rotor and A_S is the total area of the structure [49].

The formula is used within Telemac to determine the wake effect of the turbine. This is achieved by implementing the actuator disk (AD) theory. The program Blue Kenue [67] is used to create the mesh. Literature confirms that the Telemac method in combination with the AD theory is able to generate a correct wake field and resource assessment for a certain area [77, 84]. Furthermore, the method is relatively easy to use and the computational time required is acceptable. [2]

2.5.2. Delft3D

The program is created by Deltares, a Dutch research organisation. Delft 3D also uses the finite element modelling to solve the Reynolds averaged Navier-Stokes (RANS), making it possible to determine the tidal dynamics. Delft 3D is an open source method, but an account must be created and validated by Deltares before the license for the software will be provided. With Delft 3D it is possible to include the AD theory to determine the wake effect of a turbine and to determine the hydrodynamic loads on the turbine [86]. These findings have been validated with the use of a Computational Fluid Dynamics (CFD) program [2]. There are papers using Delft 3D to determine the energy extraction of a tidal turbine which take into account the effect of bottom friction [108]. The literature showed that Delft 3D is a viable tool to determine the energy extraction [108]. One paper investigated and validated the flow impact of a tidal farm with the use of Delft 3D [114]. No papers were found which combined the AD, the resource assessment and the flow impact into a single assessment of a tidal farm with the use of Delft 3D.

Delft 3D and Telemac can be validated by comparing the results with data from Rijkswaterstaat, and the outcomes can be cross-compared with each other. This validation makes it possible to use Delft 3D to determine the loads and combine the Delft 3D and Telemac findings to create the best design for the tidal farm.

2.6. Actuator disk

The actuator disk (AD)theory is a method to assess the interaction between a flow with a tidal turbine. This theory will be further elaborated and the reasons explained for using the AD.

---

[2] An alternative for Telemac is THETIS. THETIS is based on the same principles as Telemac. It uses a finite element approach to solve numerical models. THETIS works with the Firedrake framework [44] to generate the mesh. It is an open source software program that is used in multiple papers [58, 39, 47]. THETIS used the bottom friction to validate its results with gauge data available [39]. The papers show that THETIS is able to provide good agreement results. Furthermore, with THETIS it is possible to determine the energy extraction of a tidal turbine [41, 4]. THETIS will not be used for this thesis, because Telemac and THETIS are very similar and have both been validated to work for the design required and because the workability of THETIS is considered lower compared to Telemac.

Table 2.1: Aim of the papers found using the different methods.

Method	Aim	Papers
Telemac	Resource assessment	[77, 81, 80, 19]
	Wake Study	[49, 102]
	Bottom drag	[54]
THETIS	Resource assessment	[58, 39, 4]
	Economics	[58, 47, 41]
Delft 3D	Tidal dynamics	[86, 2, 108, 114, 1]
Numerical modelling	Resource assessment	[78, 43, 79, 55]

2.6.1. Literature

The AD theory was first used for wind turbines but can also be used for tidal turbines. This is possible because the significant difference is in the density of the fluid (water instead of air) that moves through the turbines. The theory rests on the assumption that the pressure and velocity are constant over the entire area of the turbine, as can be seen in Figure 2.5[12].
The AD theory also has the following limitations. The turbulence behind the turbine cannot be modelled correctly. The motion of the blades cannot be modelled and their effect on the flow and the AD theory does not take transient flows into account. These limitations are, however, not an issue for the thesis because the main use for the AD is to determine the wake effect, and subsequently create the design of the tidal farm [48]. There are multiple approaches for applying the AD theory:

- The tuned actuator disk approach (TADA).
- The linear momentum actuator disk theory (LMADT).
- The AD approach.

For the thesis the AD theory is used, because the literature indicates that this theory is the most commonly used method to determine the energy extraction.

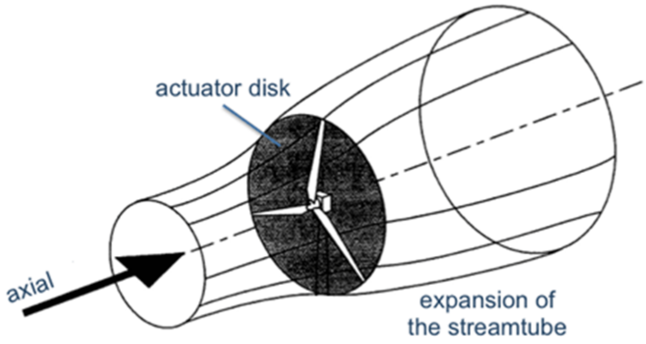

Figure 2.5: AD overview, [93]

2.6.2. Actuator disk theory

In the AD theory the rotor of the tidal turbine is depicted as a thrust force (Ft) that is homogeneously distributed over the disk. The disk is considered to be porous. An issue with this is that the AD is not capable to represent the flow right behind the tidal turbine, meaning that it is not possible to show how the fluid will react to the motion of the blades (swirl). However, in the thesis the design of the tidal farm is investigated. The swirl will be dissipated between the 2D and 5D from the turbine, the 2D stands for 2 times the diameter of the turbine away and 5D for 5 times the diameter away.

Consequently, a good and accurate estimation of the wake effect caused by the turbine can be modelled because only in the near wake the swirl will have an effect but in the far wake this effect will dissipate. In the thesis the definition of the wake effect is the velocity reduction due to the turbine over a distance behind the turbine. With the AD theory it is possible to get a good estimation of the far wake effect of the turbines and investigate the design of the tidal farm with regards to staggered-, non-staggered- spacing and dimensions [71].

The thrust force can be determined with the use of Equation 2.2 below. The thrust force is calculated from the reduction in kinetic energy before and after the AD. A change in flow velocity and pressure can be measured and calculated.

$$F_t = S\Delta P = \frac{1}{2}C_t\rho A_S U_\infty^2 \tag{2.2}$$

A_S is the total area of the turbine, ΔP is the pressure difference, ρ is the water density, C_t is the thrust coefficient and U_∞ is the upstream flow velocity. The thrust coefficient is dependent on the geometrics of the tidal turbine. These variables can be calculated with the use of the following formulas:

$$U_\infty = U_d(1+\frac{1}{4}K) \tag{2.3}$$

$$\Delta P = P_1 - P_2 = \frac{1}{2}\rho K U_d^2 \tag{2.4}$$

$$C_t = \frac{K}{(1+\frac{1}{4}K)^2} = \frac{T}{\frac{1}{2}\rho|U|^2 A_S^2} \tag{2.5}$$

$$S_i = -\frac{F_t}{Se} = -\frac{1}{2}\rho\frac{K}{e}U_d^2 \tag{2.6}$$

e is the thickness of the disk, K is the resistance coefficient and U_d is the velocity at the disk. The turbine power coefficient can be calculated with the use of the following Equation 2.7:

$$C_p = \frac{P}{\frac{1}{2}\rho|U|^3\pi R^2} \tag{2.7}$$

The thrust force of the disk on the fluid can be found using the Reynolds averaged Navier-Stokes equations (RANS). The source term is shown in the equations as S_i Equation 2.6. The RANS equations are able to solve the equation of the momentum conservation Equation 2.8 and of mass conservation Equation 2.9.

$$\frac{\partial(\rho U_i U_j)}{\partial x_j} = -\frac{\partial p}{\partial x_i} + \frac{\partial}{\partial x_j}[\mu(\frac{\partial U_i}{\partial x_j} + \frac{\partial U_j}{\partial x_i} + R_{ij}] + \rho g_i + S_i \tag{2.8}$$

$$\frac{\partial U_i}{\partial x_j} = 0 \tag{2.9}$$

For the RANS equation it is important to define the turbulence model. The most common model that is used for the wake effect is the k-ω shear-stress-transport (SST) turbulence model [48, 95, 84, 60]. This model is used because the over prediction of the initial wake effect recovery is mitigated. Furthermore, the SST model has been validated by multiple papers. The RANS formula with the turbulence model looks as follows:

$$-\rho u_i^{'} u_j^{'} = \mu_t(\frac{\partial U_i}{\partial x_j} + \frac{\partial U_j}{\partial x_i}) - \frac{2}{3}\rho k\delta_{ij} \tag{2.10}$$

In the formula μ_t is the eddy viscosity and it can be calculated by: $\mu_t = \rho\frac{k}{\omega}$. The following formula is used for a more exact wake effect prediction.

$$\mu_t = \frac{\rho k}{max(\omega, \sqrt{3}\sqrt{2S_{ij}S_{ij}})} \tag{2.11}$$

Next to the determination of the wake effect it is also possible to determine the power production of the turbines with the use of the AD theory [102]. The power of a turbine can be determined with the use of Equation 2.12:

$$P_i(t) = \frac{1}{n_{node}} sum_{j=1}^{n_{node}} \frac{1}{2} C_P \rho\pi(\frac{D}{2})^2 u_{i,j,\infty}(t)^3 \tag{2.12}$$

In the formula n_{node} is the amount of nodes in the AD, D is the turbine diameter and C_P is the power coefficient. This formula determines the power production of a single turbine. To determine the production of a tidal farm, the power production is found by:

$$P(t) = \sum_{i=1}^{n} P_i(t)/n(amount of turbines) \tag{2.13}$$

Furthermore this method is able to show the power production at a certain time, flood or ebb. The dimensionless production coefficient is used to standardise the production of the different turbines. The calculation can be seen in the Equation 2.14:

$$DP_i(t) = \frac{\frac{1}{n_{node}}\sum_{j=1}^{n_{node}}\frac{1}{2}\rho\pi(\frac{D}{2})^2 u_{i,j,\infty}(t)^3}{\frac{1}{n_{node}}\sum_{j=1}^{n_{node}}\frac{1}{2}\rho\pi(\frac{D}{2})^2 u_{i,j,0}(t)^3} = \frac{\sum_{j=1}^{n_{node}} u_{i,j}(t)^3}{\sum_{j=1}^{n_{node}} u_{i,j,0}(t)^3} \tag{2.14}$$

The power production of the entire farm can be determined following these equations, after which a cost analysis can be constructed to determine the economic viability of this project.

2.6.3. Boundary

Multiple boundary conditions need to be set for the AD theory. Firstly, the inlet of the boundary condition can be set as open so the flow can move through the AD. Secondly, the model bottom friction must be taken into account [102]. This is done by using the following formulas:

$$C_d = \frac{g}{St^2 H^{1/3}} \tag{2.15}$$

$$\tau = \frac{1}{2}\rho C_d U^2 = -\rho u_*^2 \tag{2.16}$$

Where U is the depth average velocity and u_* is the friction velocity.
The velocity Equation 2.17 and turbulence Equation 2.18 at the inlet can be found using the following formulas:

$$U_I = 2.5 * u_* ln(\frac{\gamma_w u_*}{\nu}) + A \tag{2.17}$$

$$I = \frac{\sqrt{(1/3)u_i^2}}{U} \tag{2.18}$$

$$k = \frac{3}{2} I^2 U^2 \tag{2.19}$$

$$\epsilon = C_\mu^{3/4}\frac{k^{3/2}}{l} \tag{2.20}$$

In these formulas μ is the viscosity, k is the turbulence kinetic energy, l is the length of the eddies, ϵ is the dissipation of the eddies. The free surface is modelled as a constant volume of fluid, making it easier to model velocity change. Unfortunately, the mesh and cell size are limited due to computational time constraints. Instead, the best cell size will be determined with regards to accuracy and computational time. The outlet boundary conditions are the same as for the inlet, but the free surface at the outlet must be smaller compared to the inlet due to energy extraction of the turbine [96, 103].

The last boundary condition is the mesh of the AD and of the surrounding area. The same mesh of the area is created in Delft 3D and in Telemac. Hereafter, the AD and its hub and support structure need to be included in the mesh. It is important that the mesh resolution is correct and sufficiently accurate, because the mesh resolution can influence the model and can therefore increase or decrease the energy loss in the model. This can happen because there are for example different sized meshes and so the force on the different meshes can influence the outcome of the model [66].

2.7. Design

Using a suitable design can lower the number of turbines needed in order to achieve the required amount of energy. This is related to the effect the turbine wake has on the energy production [77].Therefore, more turbines do not necessarily mean more power generated. A good design can more specifically reduce the construction-, installation- and maintenance costs. There have already been multiple studies published regarding the influence of the design on the produced amount of electricity [107]. A tidal farm can be designed on two levels, macro-design and micro-design. Macro-design focuses on the size, general arrangement of the array, location and total amount of turbines. On the other hand, micro-design focuses on the individual design and position of each turbine. Because this is the first assessment of a tidal resource and farm design for The Netherlands, the macro-design will be used to give a good first overview of the design of the farm [102, 107]. Furthermore, a 2D model is ideal for macro-design due to the fact that in a 2D model the depth is represented as a single layer and depth average velocity can be determined.

To implement the AD theory into the programs, the turbine is assumed to be a porous disk meaning that it can let the flow partially through. The AD represented by a porous plate gives a good estimation of the wake effect of the turbines and helps to design the layout of the turbines. This estimation is required to understand the effect of the wake on the other turbines within the farm [84, 54]. The AD theory has been validated for tidal energy extraction in both closed- and open settings [26, 54, 84], meaning that this theory can be used for the design of the tidal farm in The Netherlands for open settings.

The wake effect does not only influence the turbine energy generation but also the far field effect on the seabed characteristics and environmental effect on tidal areas [49].The far wake effect should also be used in the site assessment for the Dutch case to determine the effects on the environmental area that are caused by a change in the tidal flows. The layout of the farm involves the:

- Spacing between the turbines
- The way the turbines will be placed: staggered or non-staggered (aligned)
- The number of turbines
- The number of turbines and the shape of the support structure

The spacing determines how far apart the turbines will be placed. The spacing will be shown as distance between turbines (D). Here D represents the diameter of the turbine, so a 2D spacing is a spacing of 2 time the diameter of the turbine. This is applicable to both the staggered and non-staggered layout [35]. Figure 2.6 shows the different layout options. An aligned layout, as shown by the green dots, places all turbines right behind each other. For the staggered layout the turbines lines are shifted so the turbines are not straight behind each other. Multiple manuscripts show that the staggered layout reduces the influence of the wake effect on the turbines and increases the amount of energy generated [102, 57, 56, 33, 72]. This is because the distance between the turbines is increased and so the influence of the wake effect is reduced. For aligned turbines a bigger lateral spacing will limit the wake effect, which increases energy production, but will increase the tidal farm area significantly [102].In the thesis both situations are simulated to determine the optimal design with regards to energy extractions and the minimization of environmental impact [58]. A good array design can result in the optimum between the energy extracted and the number of turbines used.

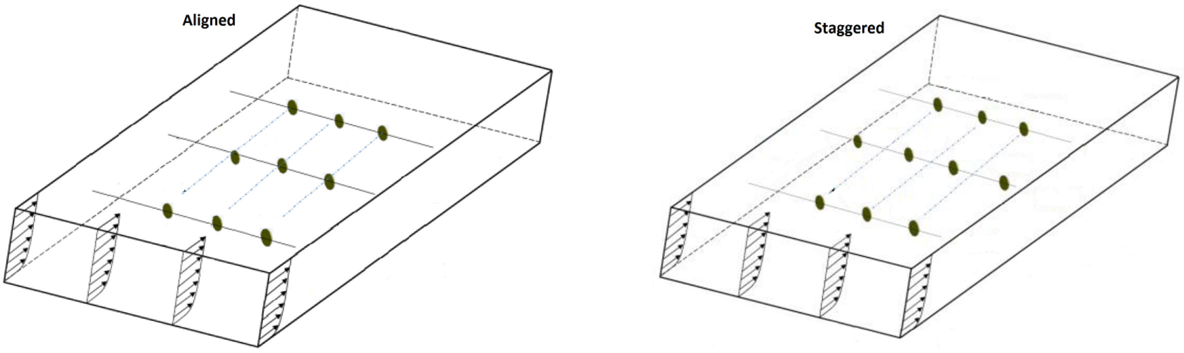

Figure 2.6: Aligned and staggered layout of tidal turbines.

The last parameter is the design of the support structure of the turbine. The support structure and the foundation of the turbine have a big impact on the wake effect and on the costs of the farm. With the AD it is possible to determine the loads on the turbine [86, 107]. No study has been found using the combination of AD theory and array configuration for determining the loads on the support structure of the turbine. There is a research gap with regards to design changes of the turbine support structure. Therefore, the foundation of the turbine chosen could potentially be modified in order to minimize construction costs. When the design of the tidal farm has been determined it is very useful to do a cost benefit analysis, in order to show the economic viability of the farm. For this cost benefit analysis, a levelized cost of energy (LCOE) of the project has to be constructed [58]. Within this analysis, it is also important to take into account that tidal energy will provide a more constant and predictable amount of energy compared to other sustainable energy sources [47]. The cost benefit analysis will ultimately lead to an answer to the question of whether tidal energy is a viable addition to energy generation in The Netherlands.

Another issue that can be investigated is about the sediment depositions in the areas further behind the tidal farm. This can potentially have a big influence on the surrounding area. The thesis does not take these sediment depositions into account because in order to simulate a good sediment transport the accuracy of the models need to be increased significantly. This would require a 3D model with an unacceptable increase in computational time as a consequence. However, this analysis is suggested for future research.

2.8. Conclusions

There have been studies in the field of Offshore Renewable Energy that have investigated the use of tidal turbines and the resource assessment of different locations for tidal energy. In the literature multiple methods have been used for resource assessment of certain locations. To the author's knowledge none of these methods have been applied or validated for locations in The Netherlands.

Manuscripts about site selection for offshore wind farms and offshore tidal farms are used to determine the best location for a tidal energy farm in The Netherlands. Furthermore, with regards to the modelling of the turbines the AD theory will be used. This theory has been validated in multiple researches. With the AD theory and the use of Telemac and Delft 3D software the design of the farm will be determined.

The AD theory is also capable of determining the loads on the turbines. However, during the literature review no papers were found that have investigated the influence of the support structure on the loads and electricity produced by the tidal turbine. This is also the case for the Delft 3D application. The application has been used for assessing a single tidal turbine but has not been used for assessing the energy extraction with regards to the flow impact of an entire tidal farm or the resource assessment of a tidal location. From the literature review these research gaps were identified. In the thesis new knowledge will be created for these research gaps. In short, the research gaps identified are as follows.

- No recent manuscripts where found about the resource assessment of tidal stream energy in The Netherlands. The first part of the thesis will be used to determine the best location for a tidal farm in The Netherlands. While some preliminary findings were presented, more in dept analysis needs to be performed in order to determine the optimal locations with more precision.
- With the use of Telemac and Delft 3D it is possible to do a resource assessment for tidal energy. These tools have both been validated before in other research. However, no papers have been found that use Delft 3D for the resource assessment at a specific location while combining the use of an AD for the design of a tidal farm with multiple turbines.
- No literature has been found regarding the design of the support structure of the turbine, impacting the wake effect and the loads. The loads on support structures have not been assessed with the use of the AD. An analysis will be part of the thesis which includes the optimal design of the support structure and its foundation.

No literature has been found which investigated the viability of placing a tidal stream farm in low tidal resource areas, such as The Netherlands. If it is economically viable to place the turbines it would be a great addition to the energy mix of The Netherlands.

3

Methodology

With the literature review completed and the research gaps found it is important that a method to answer the research questions is developed. To make sure the thesis is structured correctly the methodology and scope are defined in this chapter. The models used in the thesis need to be accurate, practical, reliable, and replicable. To make sure this is possible it is important to have a structured and well defined project methodology.

Moreover, a data log will be kept of the steps and procedures that have been taken for the creation of the different models. The data log makes it possible to replicate and extend the models in the future.

Furthermore, because two different models are used, it is possible to check and compare the margin of error between the models. The methodology of the project can be seen in Figure 3.1, and the sub steps are further explained in the following sections.

3.1. Data source

Both Delft 3D and Telemac require input data consisting of bathymetry data, boundary data and tidal gauge data. The bathymetry data is used to determine the water depth and geography for the area of interest. The boundary conditions are required to drive the simulation. From these data sets the tidal resource and loads on the turbines can be determined. The bathymetry data can be retrieved from different providers [31, 37, 88, 52, 18, 13].

The GEBCO bathymetry data set [52] is used for the thesis, because the data provided by this data set is given in the form of the mean sea level and has a relatively high spatial resolution (400 meters). The other bathymetry data sets use either the maximum sea level or minimum sea level instead, which would result in extra need for computation in order to get the mean sea level for these data sets.

For both the models the TOPEX/POSEIDON [28] mission is used to simulate the tidal force in the model. In multiple papers the accuracy of using the TPXO as driving force in the models have been analysed [77, 108, 27].

Before the models are created, one should also determine the time frame that is required for the analysis. The time frame is determined by two parts, namely the step size as well as the period over which data is analysed. The step size determines the intervals over which the simulations are taking place, see also subsection 4.3.1 The periods over which the simulation takes place are used to determine the numbers of units of time the data needs to cover. Both the step size component, as well as the total time period component need to be taken into account in relation to the computational costs. Here, it is important that the step size is not too small and the total time period not too big so that the computational costs are not too high. Moreover, the total time period of data used should not be too short, so that validation of the model is still possible.

3.2. Modelling

The models are created with Delft 3D and Telemac. For both programs it is possible to create a mesh for the area of interest and determine the resource assessment at this location.

The loads and energy production of the tidal turbines are implemented as an AD into the nested model of the area of interest. After the model, both with and without the AD has been created, the next step is to combine these models. From this point it is possible to perform a resource assessment and to check the best array configuration for the tidal turbines. Both models are validated with the use of tidal gauge data. There will also be an intermodel evaluation to determine the most important parameters for the different models.

From Rijkswaterstaat it is possible to obtain this tidal gauge data. The data gathered from Rijkswaterstaat are found on EMODnet [37] and the data are provided for a step size of 10 minutes and cover different tidal stations. The thesis uses average monthly data. The data produced by the Telemac model and Delft 3D model are checked by using these data from Rijkswaterstaat [88]. The data from Rijkswaterstaat is gathered with the use of buoys, and from this buoys the tidal range can be determined. A short time period of a month plus a few days is sufficient for the validation of the model. This is due to the fact that when looking at tide driven water elevation, it is very consistent over the tidal cycle. Because the complete tidal cycle is consistent over a single year, the period for the resource assessment is set at a single year.

3.3. Locations

After the resource assessment, the following step is to determine the ideal location for generating tidal energy. Based on the literature study it is possible to determine which criteria are required to determine which area has the highest potential. The location is determined with the use of a Multi-criteria decision making (MCDM). Some of these criteria can be evaluated with information on the location gathered from literature review and GIS data. Either Delft 3D or Telemac is used to finalize the MCDM and give exact values with respect to the resource assessment and determine the most preferable location for tidal stream energy converters. Which program will be selected, depends on the results found in chapter 5.

3.4. Design of the array configuration

From the analysis of the different models, only the most optimal model is used to calculate the energy extraction. The best design of the array configuration is found by creating multiple design configurations for the potential arrays. The designs differ in size of the tidal turbine, in whether the configuration of the turbines is staggered or not and in the spacing between the turbines.

The model with the highest power production is ultimately chosen. The best array is selected by using the mean velocity at the location of the energy extraction. Furthermore, it is also important to make sure the hydrodynamic response and loads on the tidal converter are determined and are as small as possible, to minimise capital expenditure. After this the capacity factor and exact energy extraction of a tidal cycle is determined for the best array configuration.

3.5. Economic calculation

For the viability analysis multiple economical parameters need to be determined. These include the net present value, levelized cost of energy, break even power, payback period and internal rate of return. With the metrics determined, it is possible to give a good estimation if the project can be economic feasible. Furthermore, the metrics provide a good indication as to whether the benefits could outweigh the costs of such a project.

3.6. Scope of the project

Due to the available time for the project it is very important to define the scope. The boundaries are related to the research question. The main goal of the research is to determine the new configuration that will generate the highest amount of energy. This leads to the research question: *"What is the best location and design for a tidal farm in The Netherlands?"*. The main focus is on resource assessment, tidal turbine configuration, hydrodynamic response and the best location for tidal energy farm.

Majority of current tidal research has been to determine the tidal resources at locations in the United Kingdom where the potential for tidal energy is very high. Another interesting investigation in this research is to determine the economics of the project, it can be determined if the project is economically feasible.

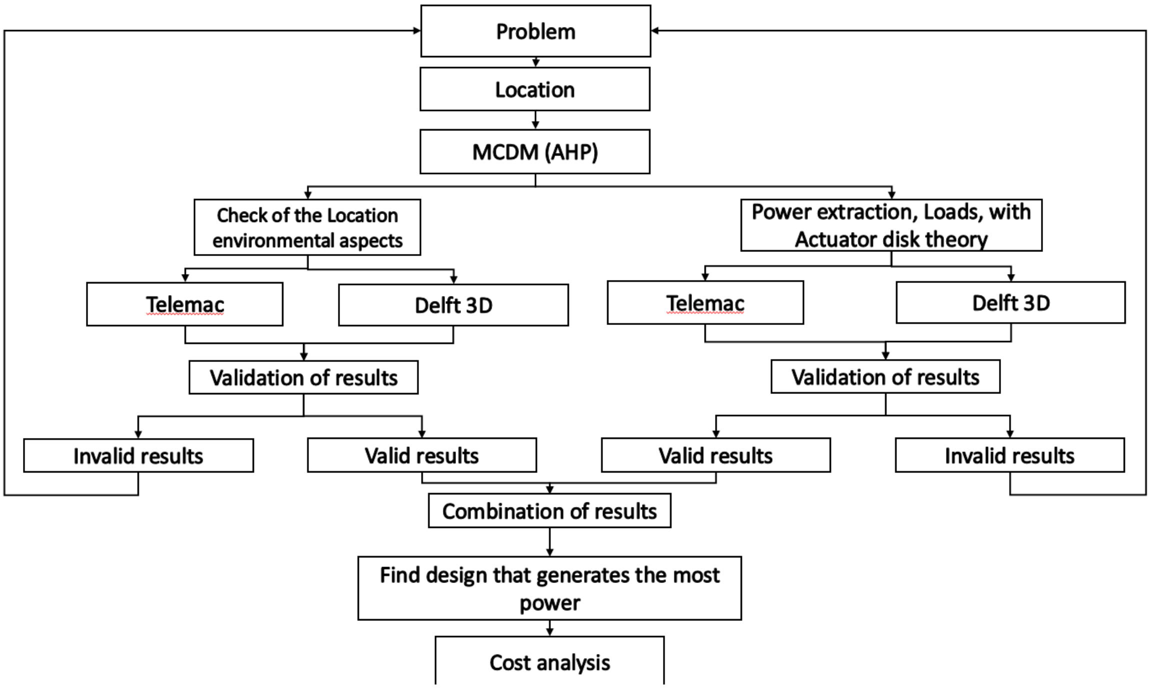

Figure 3.1: Schematic overview of the methodology of the project

4

Tidal stream models set-up & calibration

This chapter discusses the models used for the resource assessment of low tidal resource areas, for which Telemac 2D and Delft 3D are used. In this chapter the process of resource assessment of both these 2D models are explained. Six steps can be distinguished.

1. Geometric layout
2. Computational mesh
3. Boundary conditions
4. Determine the parameters of the model
5. Running the model
6. Post-processing and analysing the output of the model

With a 2D model it is still possible to assess the resource with a high enough accuracy in the Dutch case, because the Dutch coastal line has shallow water conditions. This is however only the case for the months were tidal forcing is the dominant forcing condition. Furthermore, as mentioned before, the computational time for a 2D resource assessment of the entire Dutch coast is much smaller than that of a 3D model.[1]

4.1. Data acquisition

Both models make use of the same data. This is to ensure the best cross reference between the models. As stated before the bathymetry data will be provided by the GEBCO 19 data set. The tidal harmonic database used to force the model is based on TPXO. In Delft dashboard (DDB) there is an incorporation of these harmonic tidal databases. In Telemac 2D the user is able to use different tidal harmonic databases, which includes the TPXO data set. The tidal harmonic database is derived from the Oregon State University (OSU) TOPEX, Poseidon global inverse solution (TPXO). The spatial resolution of the entire database is 0.25 by 0.25 degrees.

The database uses the sea surface elevation to determine the tidal constituents. From the database the following constituents can be used: eight primary (M2, S2, N2, K2, K1, O1, P1, Q1) and 3 non-linear (M4, MS4, MN4) [28]. The TPXO also includes the European shelf (ES). The ES database covers the north-east of the Atlantic Ocean with spatial resolution 1/30 of a degree.[2] The ES database can be used because The Netherlands resides within the European shelf.

In addition, because the TPXO is used for the model, the time period that is required for resource assessment is just one year. This is because the TPXO is based on the tidal constituents, and these constituents are dependent on the location of the Sun and Moon with respect to Earth. When looking at a year all the different locations of the Sun and Moon have passed. Due to the predictability of the tides, it is therefore sufficient to

---

[1] It is important to note that in Delft 3D a 2D model will be run, but because the program name is Delft 3D in the thesis it will be referred to as Delft 3D.

[2] This is a relatively high resolution compared to the TPXO database, which has a resolution of 1/12 of a degree.

do a one-year simulation. The analysis will make use of the year 2016, because for this year it was possible to get the sea level change of multiple tidal stations and therefore the year 2016 has the greatest comparison sample. The location of tidal stations used for both analysis can be seen in Figure 4.1. Furthermore, these locations were used to show the effect of locations near the shore and further in sea.

Figure 4.1: The tidal stations that will be used in the analysis of both Delft 3D and Telemac

4.2. Bottom friction

4.2.1. Bottom friction general

Due to the shallow water depth in the area of interest, shallow water equations are well suited. Shallow water equations can be used when the horizontal length is much greater than the vertical length, so that the vertical water column is behaving hydrostatically over its length or in other word the amplitudes of the motion of the water is consistent over the water depth. Shallow water is defined by water depth and domain width, meaning that $h/l \leq 0.04$. Therefore, when doing a 2D analysis of the area, it can be assumed that the depth averaged velocity occurs at each vertical location of the columns. Because of the shallow water equations the bottom friction needs to be taken into account as well.

Bottom friction is the resistance the bottom has on the water column and it depends on the slope, hydraulic radius and the roughness coefficient. Both Telemac 2D and Delft 3D can describe bottom friction in multiple ways. In order to decrease the computational time of the simulation, the same roughness coefficient is used for the entire area.

The first method for bottom friction is the Chezy coefficient. With Chezy it is possible to determine the mean velocity of a certain area, see Equation 4.1. In this formula V is average velocity, R_h is hydraulic radius, S_0 is hydraulic gradient and C is roughness coefficient. For Chezy the roughness coefficient ranges between the 30 and 90 $m^{1/2}/s$.

$$V = C\sqrt{R_h S_0} \tag{4.1}$$

With the Chezy roughness known it is possible to determine the drag coefficient. The drag coefficient can be found by the Equation 4.2:

$$C_d = \frac{g}{C^2} \tag{4.2}$$

The second method is Manning's roughness coefficient. The Manning roughness uses a different method to determine the roughness coefficient C in Equation 4.3:

$$C = \frac{R^{(1/6)}}{n} \tag{4.3}$$

In this formula R is the hydraulic radius, C is the roughness coefficient and n is Manning roughness. From this equation it is also possible to determine the drag coefficient using Equation 4.2.

The values used for the analysis of the bottom friction are found from the literature. In both models there is the possibility to use different bottom friction formulas, other than Chezy and Manning. However, in the literature the Chezy and Manning formulas proved to be the most commonly used models and they give a good comparison with regards to the tidal gauge data.

4.2.2. Sensitivity analysis on bottom friction

The sensitivity analysis is performed on the bottom friction parameter. This analysis determines the effect of using the different bottom friction parameters on the outcome of the models. The sensitivity analysis consists of 3 parameters that determine the accuracy of the model.

The first analysis uses the Pearson's relationship coefficient (r). Coefficient (r) measures the linear correlation between the two data sets, the model and the tidal gauge data. The correlation depends on the ratio between the covariance of the two variables and the product of their standard deviation. The formula used for the Pearson correlation is Equation 4.4. This formula is implemented in Excel and the coefficient r was determined. One speaks of a strong relation when the r values are close to 1. In the formula, x and y stand for the different data sets that are used:

$$r = \frac{n(\sum(xy)) - (\sum(x))(\sum(y))}{\sqrt{[n\sum(x)^2 - (\sum(x))^2][n\sum(y)^2 - (\sum(y))^2]}} \tag{4.4}$$

The second analysis uses the difference between the estimated model and the data, which will be used to calculate the Root mean square error (RMSE). A smaller RMSE value means that the model is closer to the observed data. RMSE is calculated with Equation 4.5. The parameters used in this equation are: n is the number of data points, z_{fi} is the predicted data and z_{oi} is the measured data.

$$RMSE_{fo} = [\sum_{i=1}^{n}(z_{fi} - Z_{oi})^2/n]^{\frac{1}{2}} \tag{4.5}$$

The final analysis uses the scatter index (SI). The scatter index shows the distribution of the tidal gauge data with the simulated data. The SI is found by dividing the RMSE with the absolute mean of the observed data Equation 4.6. Lower values for SI indicate a better model performance. In this formula xi is the value of the data and $m(X)$ is the average value of the data set.

$$SI = \frac{RMSE}{\frac{1}{n}\sum_{i=1}^{n}|x_i - m(X)|} \tag{4.6}$$

The sensitivity analysis is used for the model formulation and calibration. The data of EMODnet also includes the influence by wind, waves and pressure changes. These parameters are not included in the model, hence a deviation is expected. The time-series tidal gauge data of the DDB does not include the influence due to the wind, waves and pressure changes. Meaning that the model and the tidal gauge data of DDB will have a higher correlation. It is however still impossible for the model to have a 100% correlation due to the fact that the flow is modelled over nodes that reflect the real world. Furthermore, many assumptions had to be made regarding the flow, such as the consistency of the bottom friction over the entire model and the exact effect of the shore.

4.3. Telemac and Delft 3D

The Telemac model is the first model used and the second 2D model that is used is the Delft 3D model. The following subsection explains the equations behind the models.

4.3.1. Telemac 2D model

Telemac 2D is an open source program that is able to solve shallow water equations by using a finite element model. Telemac is the abbreviation for TELEMAC-MASCARET, the program was developed by Laboratoire National d'Hydraulique et Environnement (LNHE) and the *R&D* group of Électricité de France (EDF) [30]. The program is able to include wind stress, heat exchange, density, Coriolis effect and barometric pressure. Telemac 2D is a tool that has been widely used and has been validated by comparing its results to different areas of interest [77, 81, 80, 19].

Telemac 2D works by solving four formulas at the same time. These formulas are based on the conservative Navier-Stokes equations. The Saint-Venant equations are used to solve the shallow water equation for Navier-Stokes. The Saint-Venant equations express the conservation of water mass, the continuity equation, and the conservation of momentum in both the u and v direction. These equations are the continuity Equation 4.7 and the moment Formula along the v (lateral) axis 4.8 and u (longitudinal) axis Equation 4.9:

$$\frac{\partial h}{\partial t} + u * \overrightarrow{\nabla}(h) + h div(\overrightarrow{u}) = S_h \tag{4.7}$$

$$\frac{\partial u}{\partial t} + \overrightarrow{u} * \overrightarrow{\nabla}(u) = -g\frac{\partial Z}{\partial x} + S_x + \frac{1}{h} div(h\nu_t \overrightarrow{\nabla} u) \tag{4.8}$$

$$\frac{\partial v}{\partial t} + \overrightarrow{u} * \overrightarrow{\nabla}(v) = -g\frac{\partial Z}{\partial y} + S_y + \frac{1}{h} div(h\nu_t \overrightarrow{\nabla} u) \tag{4.9}$$

h is the water depth, u and v are the velocity components, g is the gravity acceleration, Z is the free surface elevation and t is the time. The other components are known components, S_h and S_x, y are the source terms. These source terms account for the wind, Coriolis force, bottom friction, sink of momentum and effective diffusion parameter.

As Telemac calculates these formulas, it is also calculating the conservation equation of tracers. With this it is for example possible to determine the variation in salinity of a tracer in an estuary. For the thesis the conservation equation for a tracer is not used and will therefore not be further elaborated on, because tracers are mainly used to see the variation in salinity which is out of scope.

The simulation looks into the energy extraction by the turbine. The model simulates the transport of turbulent flows.The model includes turbulent kinetic energy (k) and the turbulent dissipation (ϵ). The inclusion of these parameters is given in the following equations:

$$\frac{\partial k}{\partial t} + \overrightarrow{u} * \overrightarrow{\nabla}(k) = \frac{1}{h} div(h\frac{V_t}{\sigma_k}\overrightarrow{\nabla} k) + P - \epsilon + P_k v \tag{4.10}$$

$$\frac{\partial \epsilon}{\partial t} + \overrightarrow{u} * \overrightarrow{\nabla}(\epsilon) = \frac{1}{h} div(h\frac{V_t}{\sigma_\epsilon}\overrightarrow{\nabla}\epsilon) + \frac{\epsilon}{k}(c_{1\epsilon}P - c_{2\epsilon}\epsilon) + P_{\epsilon v} \tag{4.11}$$

The right side of the formulas give the energy dissipation and generation. The simulation should include a period of at least 1 tidal cycle in order for the model to reach the steady state. This is needed because the model determines the flow conditions on the nodes from the boundary. It takes time for the whole model to be influenced by the tidal force and therefore have the correct tidal flow.

4.3.2. Delft 3D model

Delft 3D is a program that is created by Deltares [21]. The Delft3D-flow method is able to do both 2D and 3D hydrodynamic simulations. The program uses finite difference modelling, that use shallow water and the Boussinesq assumption to solve the Navier-Stokes equations. The program is able to compute river, coastal and estuary areas. The 2D model is able to solve depth averaged solutions, and so the continuity Equation 4.12, momentum Equation 4.13 and the advection diffusion transport Equation 4.14:

$$\frac{\partial \zeta}{\partial t} + \frac{\partial[(\zeta + d)\overrightarrow{U}]}{\partial y} + \frac{\partial[(\zeta + d)\overrightarrow{V}]}{\partial y} = S \tag{4.12}$$

$$\frac{\partial u}{\partial t}+U\frac{\partial U}{\partial x}+V\frac{\partial U}{\partial y}-fV=-\frac{1}{\rho_0}P_x+F_x+M_x+\frac{1}{h^2}\frac{\partial}{\partial\sigma}(\upsilon_v\frac{\partial U}{\partial\sigma} \tag{4.13}$$

$$\frac{\partial V}{\partial t}+U\frac{\partial V}{\partial x}+V\frac{\partial V}{\partial y}-fV=-\frac{1}{\rho_0}P_y+F_y+M_y+\frac{1}{h^2}\frac{\partial}{\partial\sigma}(\upsilon_v\frac{\partial V}{\partial\sigma} \tag{4.14}$$

In these formula's, ζ is the water level, d is the water depth, S is the discharge term, f is the Coriolis effect, u and v are the velocity components for sigma. F_x F_y are the Reynolds stress components, P_x P_y are the pressure terms and M_x M_y are the source terms. The σ is used for a 3D model where the depth is represented by multiple layers, for a 2D model the σ is always 1.

With the use of the equation the resource assessment for The Netherlands can be done. The simulation needs at least part of a tidal cycle to reach steady state conditions.

4.4. Model set-up

In the following subsections a general model set-up is given for both the Telemac and Delft 3D model.

4.4.1. Telemac 2D set-up

Telemac 2D works together with Blue Kenue (BK) and Fudaa PrePro (Fudaa). BK is a mesh generator and a post processor program. The program was developed by the Canadian hydraulics centre of the national research council Canada[67]. Fudaa is a software program that is developed by the Institute for maritime and inland waterways France (CETMEF) [51]. The program is able to generate the steering file that describes to Telemac 2D the required configuration for the simulation. The steps that need to be taken in BK, Fudaa and Telemac are shown in Figure 4.2 below.

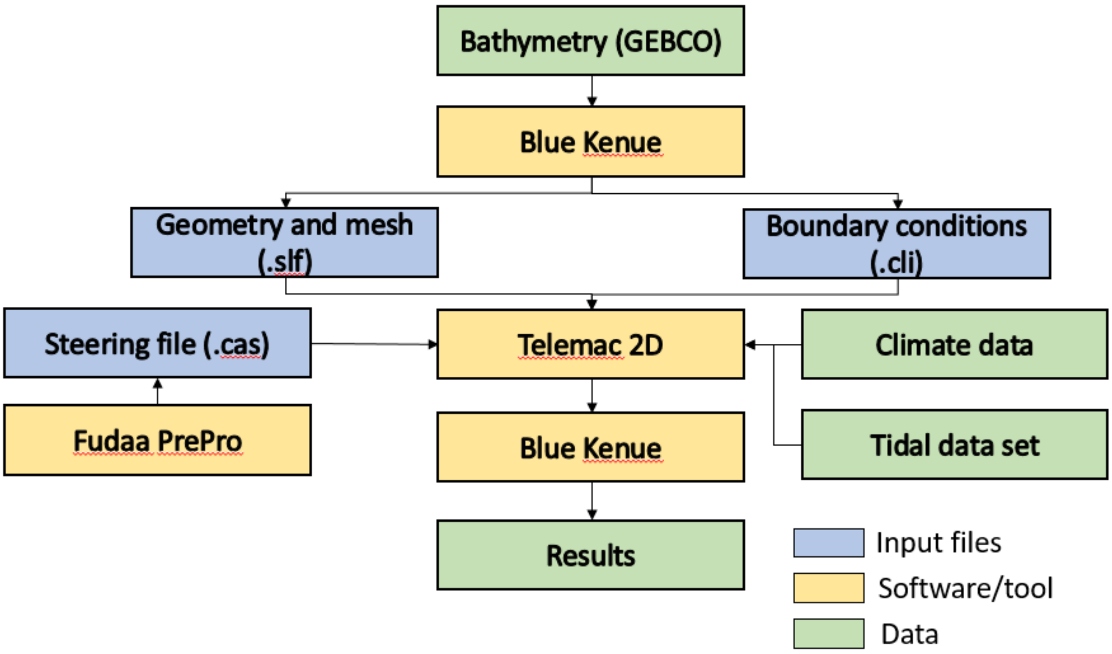

Figure 4.2: Resource assessment process for Telemac 2D

The first step in BK is to get the bathymetry data. As explained before, the GEBCO data is used because it uses mean sea level to determine the water depth. Determining the depth averaged velocity requires the mean sea level, meaning that when using GEBCO no extra steps need to be taken to get the correct water depth.

A problem with using GEBCO is that the data provided is in Latitude and Longitude decimal degrees. In BK the data used are in Latitude and Longitude meters, according to universal transverse mercator zone

(UTM 31N). The coordinates of the data are changed with the use of ArcMap, where the latitude and longitude degrees can be modified to latitude and longitude meters according to WGS 1984 UTM zone 31U. In Appendix B it is shown how this modification is applied.

After the coordinates system is changed it is possible to generate a mesh in BK that has the correct size. Once the bathymetry data is correctly implemented in BK, the geometry of the model can be determined. The model is looking at the entire Dutch coastal zone, meaning that a complex geometry needs to be created in BK. The first step is to create the outline of mesh. For models it is possible to change to grid size for different locations. This modification is done by resampling the outline. By doing so it is possible to generate a smooth and consistent outline over the entire model. The mesh that is generated by BK and used in Telemac consists of unstructured triangular mesh. This mesh makes it possible to have more data points at certain locations which can in turn increase the accuracy of the model.

Furthermore, Telemac reduces the chance of having too many points near a nodes and will produce constant triangle areas. However, a risk is that resampling the outline changes the coastline of the mesh. Therefore extra attention needs to be paid to make sure the coastline remains as close as possible to the original. Resampling can be performed by using the equal distance function between each point. By using this method it is possible to have different step sizes for coastal areas and for areas that have sea boundaries, resulting in a varying mesh size (see Figure 4.3).

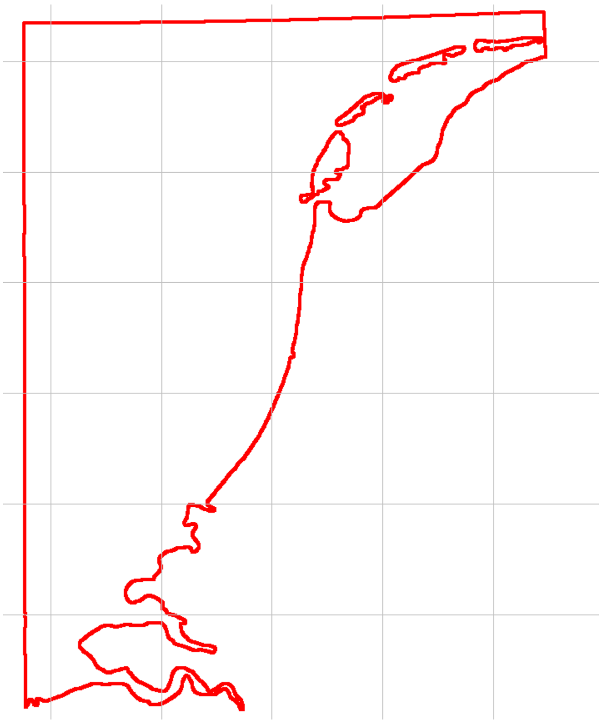

Figure 4.3: Outline used for the mesh generation in Blue Kenue

The number of nodes determines the computational time of both the mesh in BK and in Telemac. The mesh size is linked to the Courant-Friedrichs-Lewy (CFL) conditions [78, 109]. This condition makes sure the time step is not greater than the time it takes for the fluid to travel between nodes, which is important because if the time step is too large the model will not be able to run. Moreover, with the use of the CFL condition it is possible to reduce the time step by reducing the mesh size. The formula used for the CFL, links the mesh size with the time step of the simulation Equation 4.15:

$$CFL = U\frac{\Delta t}{\Delta x} \tag{4.15}$$

In this equation Δ is the time step of the simulation and Δx is the grid size. The CFL value for Telemac is between 0.1 and 1. The next step in BK is to define the boundary conditions of the model. In BK it is possible to set the boundaries to open or solid. The initial conditions in BK is that all boundaries are solid. If open boundaries need to be considered, it is possible to edit the boundaries, by stating the different conditions that occur at the boundaries. This includes a predefined water depth, velocity, flow or combination of the variables. It is also possible to let Telemac compute the boundary conditions, which is done by using Thompson boundary conditions. BK is only capable of determining the location and type of boundary conditions, while the data used for the boundaries are defined in Telemac.

When the mesh has been completed and the required boundaries conditions have been defined the steering file for the simulation in Telemac needs to be determined. In Fudaa the steering file is generated. The steering file tells Telemac what to do and what to consider during the simulation, thereby steering Telemac in the by the user defined direction. In Fudaa it is possible to include and edit different criteria in the simulations, including:

1. Internal conditions, language etc.
2. Initial conditions and boundary conditions
3. Physical parameters, like the density, friction, turbulence and Coriolis effects.
4. The solver specifications, like accuracy and iterations amount
5. Tidal conditions, like tidal flats
6. Sediment transport
7. Tracers
8. Turbulence

Telemac can accommodate different laws of bottom friction. Literature showed that either Chezy's or Manning's formulation gave the best solution for the European shelf [77, 81, 99]. By entering different values into these two formulations, one can determine which formulation gives the most accurate solution when compared to the tidal gauge data. In order to reduce computational time, a time frame of 31 days is used to determine the best roughness value. Although this is a somewhat limited timeframe, it still provides an accurate indication of the model. Moreover, this time frame also includes a 5 day period which represents part of a tidal cycle to make sure that the model has reached a steady state before comparing the data.

In addition, it is possible to edit sub routines in Telemac. For example it is possible to modify the friction coefficient in the time dimension, space dimension and to include the energy extraction in the model. Once the simulation has run, BK can provide a visualisation of the results. Here, data from the model are extracted and compared with tidal gauge data which makes it possible to assess the accuracy of the model and determine whether more modifications are required.

4.4.2. Delft 3d model set-up

Delft 3D works together with the Delft dashboard (DDB). DDB is also a program created by Deltares, and is able to generate a mesh for given UTM coordinates. Figure 4.4 shows the steps that need to be taken by DDB and Delft 3D.

The first step is to make sure the bathymetry data in DDB are correct. In DDB it is possible to use GEBCO 19 bathymetry data, the same bathymetry data is used as in Telemac. It is therefore possible to generate a grid over a certain area where there is a prescribed depth, from which a grid that only reflects the coastal area can be generated. The Netherlands has many areas that are below sea level, so that these areas are initially also included in the mesh generation by DDB. To make sure only the coastal and estuary locations are included, the grid was modified in RFGRID, which is an extension of Delft 3D. In this extension it is possible to delete certain grid points that do not need to be included in the model.

The grid that is generated in DDB and Delft 3D is a structured grid. The structured mesh makes it more difficult to change the mesh locations at different points, for example at monitoring stations. The monitoring stations will be located at the centre of the cell. The mesh on the other hand can be generated relatively quickly due to the simplicity of the mesh. The computational time is therefore relatively small as well. The CFL value for Delft 3D needs to be between the 0.1 ad 1, to make sure that the fluid moves between the nodes within the given time step. In DDB there is a function that determines the ideal time step with regards to the mesh size, this is based on the CFL condition, see Equation 4.15. Once this has been done, it is possible to put the new grid back into DDB to generate the open boundary conditions. Here it can be decided what forcing occurs at the open boundaries.

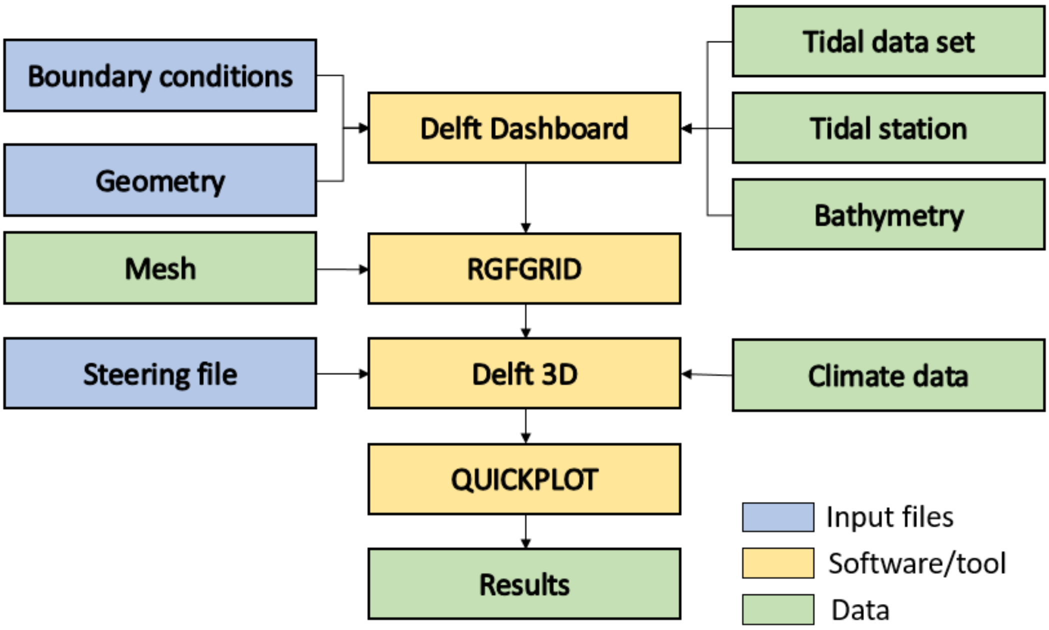

Figure 4.4: Resource assessment process for Delft 3D

For both Telemac and Delft 3D astronomical forcing is used. The boundary conditions used are based on the European shelf (ES) data set from the TPXO database. The ES is included in the DDB routines. The initial conditions can be described in Delft 3D. In Delft 3D the water level is assumed to be constant. The bottom roughness parameters used are the same as used in Telemac. The same iteration as with Telemac will be done to determine which value gives the most accurate solution. The time frame of the simulation needs to be determined as well. As the simulation needs time to reach a steady state, the chosen time span should include part of the tidal cycle. In Delft 3D the tidal data can only be generated over a single year, so that the time frame is consists of an entire year excluding the first four days. For the simulation of the bottom friction the simulation runs from 5 January till 3 February.

Tidal force is used to force the model, to get the most accurate simulation of the tidal flow. In Delft 3D it is only possible to use tidal forcing when the WGS 84 coordinate system is used, while it does not work for the UTM coordinate system. Once the forcing has been decided the physical parameters can be edited to make sure the model reflects the real life conditions as realistically as possible. The last step in DDB is to use monitoring stations. DDB is a worldwide tide stations database incorporated in the software. The measurement data of these stations only include the astronomical input. An important variable to take into account is the distance of a monitoring point to the centre of the cell. Making sure the monitoring stations are close to the centre will increase the accuracy of the data compared to the model outcome. After these parameters are determined, the model is run. The model shows the results of the water elevation and the U (lateral) and V (longitudinal) velocity components. It is possible to immediately examine the difference between the model and the data by using the QUICKPLOT extension.

4.5. Model set-up for the Dutch coastal area

In the following subsection the models for the Dutch coastal area will be elaborted on.

4.5.1. Telemac 2D for the Dutch coastal area

A solution for the creation of a Telemac 2D model of the Dutch coastal area is provided in this section.

The first step is to import the bathymetry in BK. Because this research incorporates and compares the two models it is important that the same area is considered for both these models. The GEBCO data is downloaded for the area bounds.

Table 4.1: The coordinates of the area of interest of The Netherlands

	West	East	South	North
Coordinate	3.15	6.1	51.3	53.5

Then, the data is modified in ArcMap to get the correct coordinate system. The next step is to implement the bathymetry data in BK. With the bathymetry data ready, it is possible to determine where the outline of the mesh will be placed. The step size between the outline points of the Dutch coastal line has been set to 200 meters, while the step size between the outline points for the rest of the outline has been set to 750 meters. It is important to keep a relatively small step size for the coastal area, because the coast will have more interaction with the waterflow, [3] while the rest of the outline will have less of an influence on this flow. Therefore, increasing the accuracy of the model along the coastal areas is preferred, which can be ensured by making the mesh near the coast relatively small. However, in order to decrease the computational time, it is preferred to set the step size higher for less influential areas. More specifically, the spacing for the rest of the outline is set at 750 meters because it is just a little larger than the resolution provided by GEBCO and therefore keeps the correct bathymetry data for the simulation.

After the outline of the model has been generated, the islands in the Wadden sea also need to be added to the model. This is done by generating separate closed lines and resampling these to a spacing of 200 meters. After adding the islands to the model, it is possible to generate the mesh. In Figure 4.5 the mesh is mapped for the Dutch coastal area. This figure also shows that the mesh is a little finer along the coastal areas.

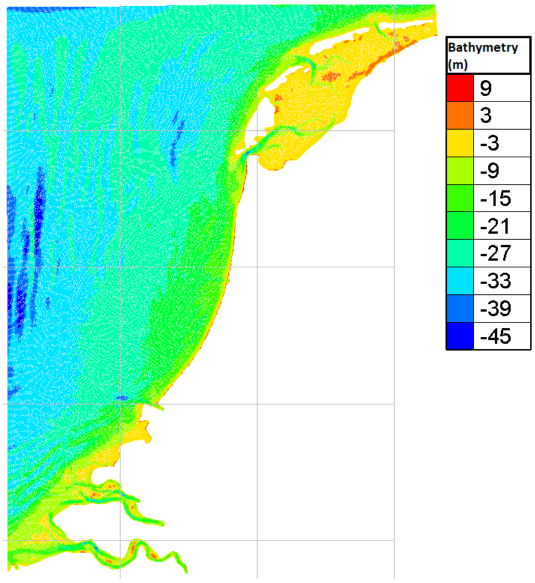

Figure 4.5: Geometry and mesh mapped of the bathymetry of The Netherlands

In the model there is a single liquid boundary that surrounds the computational mesh. The liquid boundary runs from the southern west side to the northern west side. In between this liquid boundary a solid boundary exists, which is the mainland of The Netherlands. Furthermore, in the model the Wadden islands are also shown to have solid boundaries. In Figure 4.6 these boundary conditions are presented. Here, the orange boundary condition reflects an open boundary condition for velocities and water depth.

The velocities and water depth at the boundaries are derived from a harmonic tidal database, namely the European shelf (ES). Using Fudaa, it is possible to create a steering file. With this steering file it is possible to calibrate the model. This calibration is possible by changing certain parameters that have a large influence on the model outcome. From the literature about hydrodynamic modelling it was possible to deduct the relevant input parameters, such as the friction coefficient, initial elevation, Coriolis effect and tidal conditions.

---

[3] At these areas, the actual flow changes regularly, this is due to beach, waterworks and other geometry changes in the water.

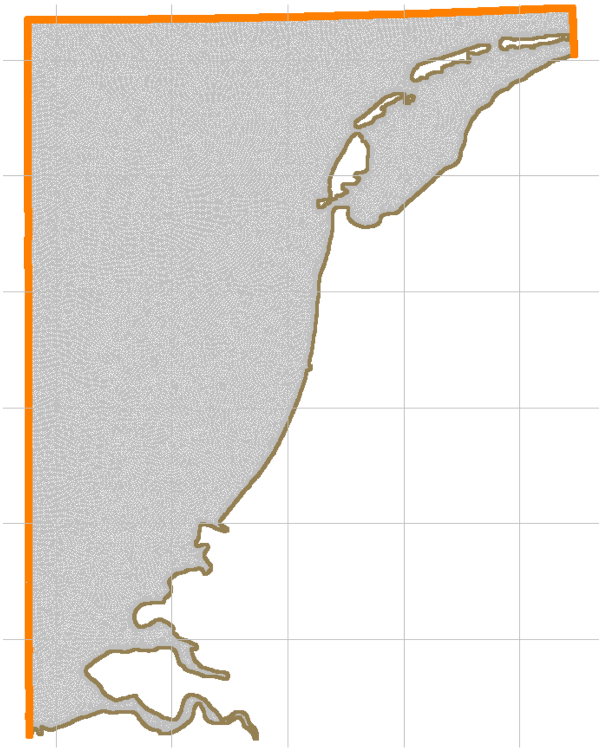

Figure 4.6: Boundary conditions of The Netherlands model, the liquid boundaries are shown in orange and the solid boundaries of The Netherlands mainland and the Wadden islands are shown in grey

The TPXO altimetry data is then used to set the initial conditions of the water depth. Next, different friction coefficients are used to determine the accuracy of the model. This can be done by running multiple simulations, which can point to the most accurate model. These data are compared to the tidal gauge date provided by the DDB. The tidal gauge data is used because it only takes into account the water level change by tidal constituents, meaning that the data is an average reflection of the exact water level elevations provided by buoys that are shown in EMODnet [37]. The filtering of the data is done by using the exact tidal constituents at the location and water depth of the tidal station. When comparing these to different data sets, one can observe that they are in phase but that the buoys data has more extremes. This is also shown in Figure 4.7. The data provided by DDB are assumed to be correct and do not include any errors.

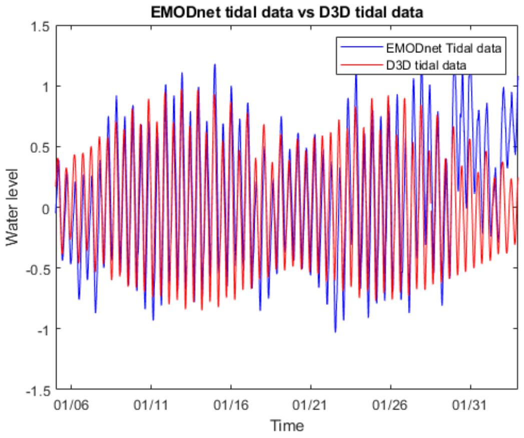

Figure 4.7: The data comparison between EMODnet and DDB tidal data for the tidal location Terschellinger BAIHO

Telemac also facilitates the use of different turbulence models. From Telemac [30] it was found that the difference between the available turbulence models was very small. The default Telemac option, the Prandtl model, can be used in the simulation. In the Fudaa file the Coriolis effect is included. The Coriolis effect occurs due to the rotation of the Earth and influences the weather patterns and ocean currents. This effect on the Dutch coast is relatively small in the model, because small spatial resolution is used in the model. The steering file also includes tidal flats, which are areas that periodically change from wet to dry and vice versa during tides, because the model also incorporates estuaries. In Appendix C the table with the parameters of the steering file is presented.

The steering file also presents some parameters which were not taken into account, such as weather conditions like wind, waves and barometric effects. The influence of these conditions is not consistent over time, which makes it more difficult to estimate the potential of a tidal farm more accurately. Furthermore, more boundary conditions result in more computational time without providing extra value. Secondly, the model also disregards the flow into the estuaries, because the flow of water into the estuaries from the rivers has a very small impact on the tidal flow, thus unaffecting the accuracy of the model. Thirdly, because the simulation is run for shallow water it can be assumed that there is no high non-linear flow. Therefore, a constant viscosity of $1 * 10{-}6$ can be used, which is also the default option in Telemac.

The last step is to calibrate and validate the model. Calibration of the model is the process to assign the correct values to the parameters such that the computational model will produce the most accurate outcomes. Observed data is needed to validate the model. This data is obtained from DDB, which provides sea level elevation data for different tidal stations. In the following subsection the analysis for the Telemac model is shown. From this analysis it is possible to determine the most suitable parameters for the model compared to the data and to perform a year-long resource assessment.

4.5.2. Delft 3D for the Dutch coastal area

In this section a solution is provided for the creation of a Delft 3D model for a 2D simulation for the coastlines of The Netherlands. DDB makes it possible to generate a geometry over the same area, as downloaded with GEBCO 19. DDB facilitates generating a mesh over this area, after which the Dutch areas that are below sea level that are not coastal areas need to be excluded again. To make sure both Telemac and Delft 3D can be compared, the mesh size in Delft 3D is (following the Telemac approach) set at 750 meters, see Figure 4.8.

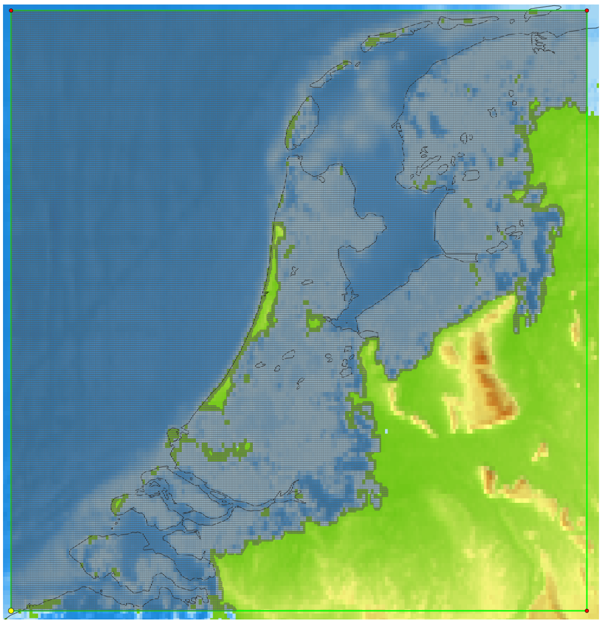

Figure 4.8: Mesh generated by BK, where for all areas below the 0 meter sea level a grid is generated

Using RGFGRID, the mesh only includes the required areas as can be seen in Figure 4.9a. Because in Delft 3D it is only possible to use tidal forcing data by using the latitude/longitude at decimal degree, the edge length of the mesh could not be set in meters. Therefore, a conversion from meters to decimal degrees is applied, which means that the edge length of the mesh will be 0.007 decimal degrees. This conversion is based on the WGS 1984 UTM zone 31U.

After the mesh has been completed the boundaries conditions can be provided. The Wadden islands

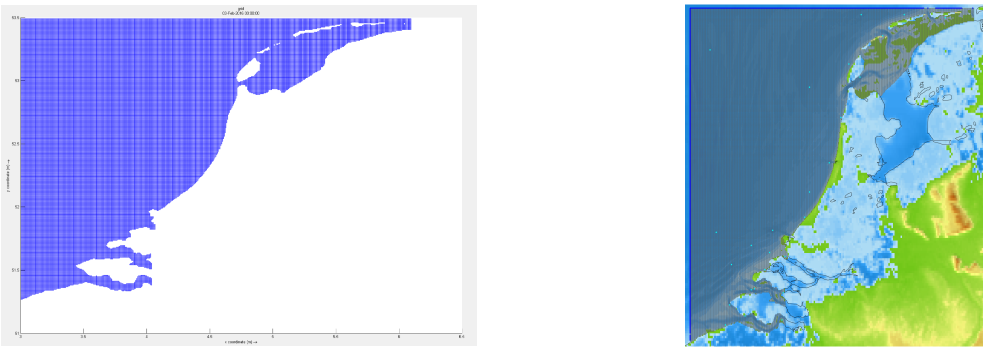

(a) Grid added with the use of the RGFGRID

(b) Mesh used for the Delft 3D simulations

Figure 4.9: Grids used for the Delft 3D model

and the general Dutch coast line have solid boundary conditions. The western and northern boundaries have open boundary conditions and are astronomical forced. These conditions are provided by the TPXO European shelf. In Delft 3D it is also possible to change multiple parameters, such as the friction coefficient and viscosity. The value of the friction coefficient is found with the calibration and validation of the model. The Coriolis's effect is included in the model, while wind, wave and barometric effects were neglected. Flows from rivers into the estuaries are not been taken into account because of the small impact this has on the tidal flow. With the build in function in DDB it is possible to get water surface elevation from tidal gauges. The assumption is made that the data from these stations are correct and do not have any errors.

Delft 3D is widely used for creating hydrodynamic models and has been validated [86, 2, 108, 114, 1]. After the sensitively analysis of the parameters, the accuracy of the results can be determined and from this the resource assessment is concluded. A difference between the tidal gauges and the model is expected, because the model consists of just a few conditions while the tidal gauge data uses the exact tidal data of that location.

4.6. Analysis models

In the following subsections an sensitivity analysis is done for both the model of The Netherlands

4.6.1. Telemac 2D analysis

In this subsection the analysis of the Telemac 2D model for the resource assessment is described. Intuitively, bottom friction is an important parameter for the modelling of tidal flow. There are different drag coefficients that can be used, like Chezy and Manning. Literature shows that for a 2D simulation at the location Pentland firth, a Manning coefficient of 0.035 is suitable [77]. Other research showed that a roughness coefficient based on the Chezy principal between 0.025 and 0.086 was appropriate. For the analysis, a Chezy coefficient of 34, 44 and 60 as well as a Manning coefficient of 0.03, 0.035, 0.04, 0.05 and 0.06 are initially compared to the tidal gauge data. For this comparison different locations were used to get a good understanding of the difference between these values. The roughness coefficient that gives the highest accuracy is then used for the analysis of the tidal resource, see Table 4.2.

One can notice from Table 4.2 that more Manning coefficients were investigated than initially planned. This is due to the fact that during the sensitivity analysis it was found that the best friction parameters were outside the range suggested in literature. Additional simulations showed that the best friction coefficient was Manning 0.11. The time step used for the simulation was set at 10 seconds.

A time step of 10 seconds was opted to meet the CFL constraint. The results of the simulation were given for every 10 minutes. The tidal gauge data used from the DDB dashboard and the water level data from EMODnet are given for every 10 minutes as well. The simulation runs from January 1st 2016 till February 3rd 2016. For the comparison between the simulation and the tidal gauge data a 5 day time span was given for Telemac to reach a steady state.

For comparison the RMSE, SI and Pearson are determined. With the different tidal gauge locations the overall best roughness coefficient can be determined. In Table 4.3 the average score of the friction parameters for the different tidal stations are presented.

In Figure 4.10 till Figure 4.12 the tidal gauge data and the simulated data are compared with each other for different locations and for different bottom roughness parameters. Figure 4.10 till Figure 4.12 shows that

Table 4.2: Roughness coefficient and their values used in the analysis

Roughness component	Value
Chezy	34
Chezy	44
Chezy	60
Manning	0.03
Manning	0.035
Manning	0.04
Manning	0.045
Manning	0.05
Manning	0.06
Manning	0.08
Manning	0.08
Manning	0.09
Manning	0.1
Manning	0.11
Manning	0.12
Manning	0.13

Table 4.3: The average RMSE, Pearson and SI score of the different bottom roughness, Telemac

Average	Ch: 34	Ch: 44	Ch: 60	Ma: 0.03	Ma: 0.035	Ma: 0.04	Ma: 0.045	Ma: 0.05	Ma: 0.06	Ma: 0.07	Ma: 0.08	Ma: 0.09	Ma: 0.1	Ma: 0.11	Ma: 0.12	Ma: 013
RMSE	0.309	0.312	0.315	0.315	0.313	0.311	0.310	0.308	0.304	0.301	0.298	0.295	0.294	0.294	0.294	0.295
Pearson	0.875	0.866	0.859	0.859	0.863	0.866	0.870	0.875	0.884	0.893	0.902	0.909	0.915	0.920	0.924	0.927
Scatter	57.059	57.715	58.332	58.324	57.965	57.655	57.347	57.018	56.335	55.724	55.245	54.915	54.734	54.691	54.775	54.971

there is a underestimation of the water level difference. Furthermore, the figure shows that for some locations the Chezy coefficient seems to have a stronger correlation with the data. Upon examining the data in more detail, for example Chezy 34, it follows that for the Chezy the correlation with smaller water level change is less accurate, while the correlation of Chezy with the peaks is much better. The peaks for these coefficients seem to strongly coincide, yet the overall correlation of the data is low. Therefore, the sensitivity analysis gives a worse outcome for these Chezy coefficients. This can also be observed when comparing the RMSE of Chezy 34 with the RMSE of Manning 0.11 for Texel Noordzee tidal station for example. The difference in performance is illustrated in the scatter plot shown in Figure 4.13 and Figure 4.14.

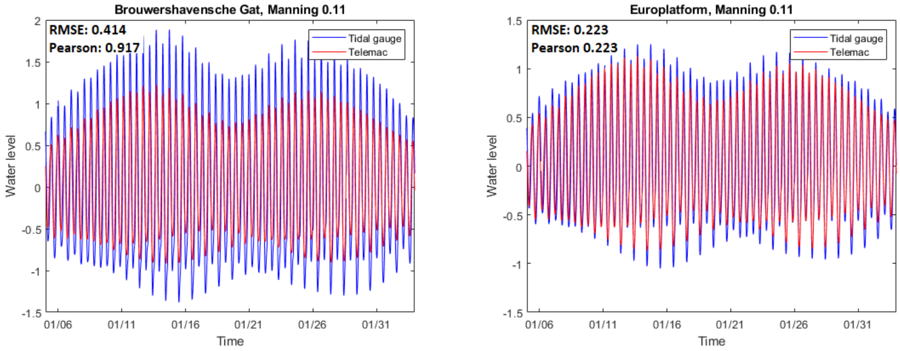

(a) Comparison between Brouwers Havensche Gat and tidal gauge data and Telemac Manning 0.11

(b) Comparison between Euro platform tidal gauge data and Telemac Manning 0.11

Figure 4.10: The comparison between Telemac and the tidal gauge data, Brouwers Havensche Gat and Euro platform

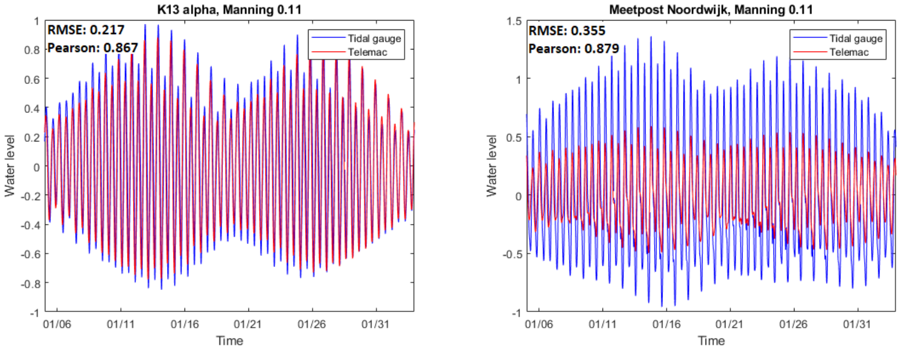

(a) Comparison between K13 alpha tidal gauge data and Telemac Manning 0.11

(b) Comparison between Meetpost Noordwijk tidal gauge data and Telemac Manning 0.11

Figure 4.11: The comparison between Telemac and the tidal gauge data, K13 alpha and Meetpost Noordwijk

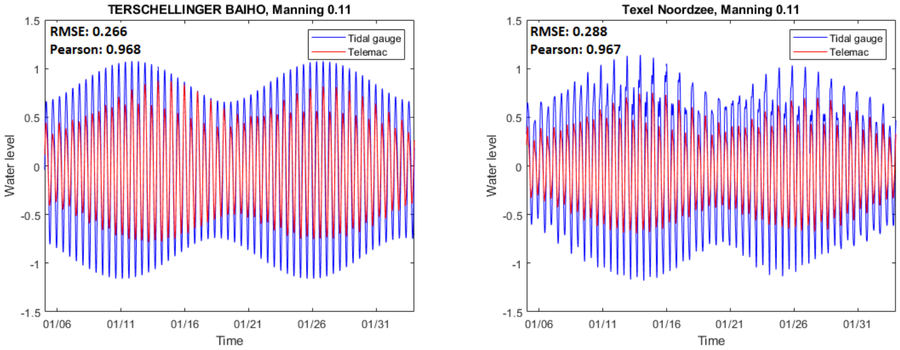

(a) Comparison between Terschellinger BAIHO tidal gauge data and Telemac Manning 0.11

(b) Comparison between Texel Noordzee tidal gauge data and Telemac Manning 0.11

Figure 4.12: The comparison between Telemac and the tidal gauge data, Terschellinger BAIHA and Texel Noordzee

The plot shows that Manning 0.11 is not consequently the best fit at each data point, but overall still provides the best fit when checking the RMSE, Pearson and SI analysis, see Table 4.3. For location Meetpost the best bottom friction is Manning 0.03 but for the other locations this bottom friction does not have a good comparison. [4]

This finding is presented in more detail in Appendix C, which shows that Manning 0.11 is not the best fit for all tidal stations, while the average error indicates that it is the best fit for the overall model.[5]

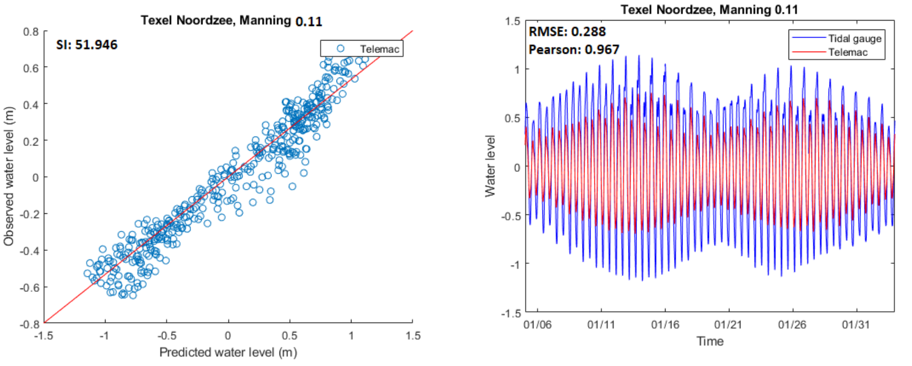

(a) Scatter plot for Manning 0.11, Texel Noordzee station

(b) Comparison between Texel Noordzee gauge data and Telemac Manning 0.11

Figure 4.13: Scatter plot and difference plot of Chezy 34 and Manning 0.11, for tidal station Texel Noordzee

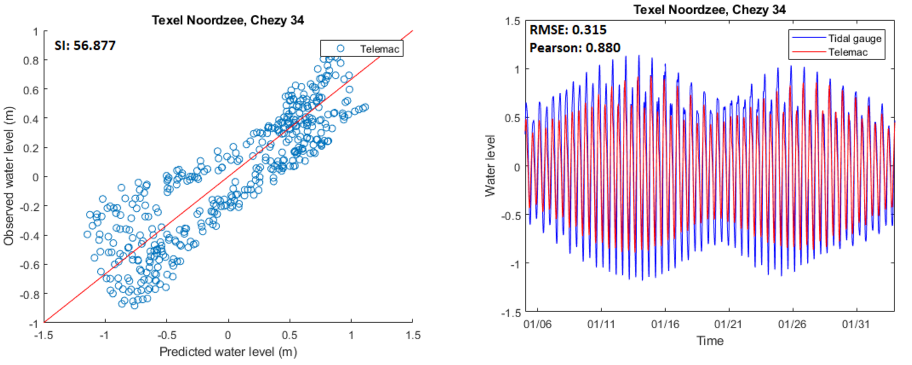

(a) Scatter plot for Chezy 34, Texel Noordzee station

(b) Comparison between Texel Noordzee gauge data and Telemac Chezy 34

Figure 4.14: Scatter plot and difference plot of Chezy 34 and Manning 0.11, for tidal station Texel Noordzee

A reason why the Manning coefficient was superior over the Chezy coefficient, is because the Chezy coefficient is highly dependent on the velocity of the flow. Due to the low velocity and the shallow water conditions the Chezy coefficient underestimates the water level compared to the Manning coefficient [64]. Furthermore, due to the shallow water conditions the velocity taken in the simulation is a depth averaged velocity, which means that at the bottom of the sea the water velocity is the same as at the surface.

However, using a Manning coefficient of 0.11 is quite a high friction coefficient, so that the velocity in the model could be underestimated. The current speed will be reduced due to this high friction. Because there is no current data available for the area of interest it is assumed that the best friction coefficient is determined by water level correlation. This means that Manning 0.11 will be used for the resource assessment of an entire year.

4.6.2. Delft 3D analysis

In this subsection the analysis of the Delft 3D model for 2D resource assessment will be described. Delft 3D sets the roughness formula to Chezy by default. The default values for horizontal- and vertical viscosity

---

[4] The figures show that the Manning 0.11 for some locations underestimates the peaks but has a very good correlation with the lower elevation data.

[5] In Appendix C the scatter plots and error plots of the different friction coefficients and locations can be found.

and diffusivity are used. The default value of the viscosity is $1 m^2/s$, which previous research shows is a good estimation [108, 8]. The vertical eddy viscosity is based and the k - ϵ method. Due to the fact that a 2D model is used, the vertical eddy viscosity and vertical eddy diffusivity have less influence on the outcome. A detailed description of these methods to determine the viscosity is beyond the scope of this paper.[6] For the viscosity the default value of 1 m^2/s is used.

The time step for the simulation was set to 1 minute, so that the CFL condition is met, see Equation 4.15. The results file will give results for every 10 minutes, as the tidal data from EMODnet and DDB is given for every 10 minutes. The simulation is done from the January 1st till February 3rd.

In Delft 3D it is possible to change multiple parameters. There are several options for the roughness formula. In line with literature and as was the case in Telemac, Chezy and Manning are used in Delft 3D as well. Delft 3D also facilitates varying bottom roughness for the U and V component. However, because Telemac does not facilitate such varying bottom roughness, it is preferred to keep these components at an unvarying value in Delft 3D as well for comparison reasons. It would be very interesting to see the effect of varying bottom friction in the U and V direction and to see the effect of varying bottom friction over the model. The seabed is not constant over the entire Dutch coastal area so to see the effect of the varying bottom friction on the accuracy of the model would be interesting.

Furthermore, in Delft 3D it is possible to determine the forcing at the boundary, which is set to astronomical forcing. It is also possible to determine the type of open boundary, which influences how waves and flow propagate from the boundary. For a tidal model the boundary is set open for water level, which means that a change in water level is allowed at the boundary. Furthermore, for the boundary conditions the reflection coefficient α needs to be determined. The reflection coefficient determines the amount of reflection of the short waves at the boundaries. Meaning that the higher reflection coefficient, the less the waves are reflected in the model. To determine the influence of the reflection coefficient, three simulations with the same conditions are run with the reflection coefficient only set to 0 and 1000. Table 4.4 shows the effect of using different reflection parameters is. It is evident that a reflection coefficient of 1000 gives better results for both the Chezy and Manning bottom friction coefficients.

Table 4.4: The influence of using an α of 0 and a α of 1000

Brouwers Havensche Gat	Chezy 44, alpha 1000	Chezy 44	Manning 0.05, alpha 1000	Manning 0.05
RMSE	0.353	0.422	0.285	0.339
R^2 (Pearson)	0.915	0.875	0.957	0.929
SI (%)	45.545	54.414	36.769	43.678
Euro platform				
RMSE	0.254	0.302	0.261	0.308
R^2 (Pearson)	0.901	0.860	0.895	0.854
SI (%)	49.816	41.387	51.184	60.362
K13				
RMSE	0.206	0.236	0.203	0.232
R^2 (Pearson)	0.889	0.851	0.891	0.857
SI (%)	57.109	65.559	56.480	64.389

---

[6] For background, see amongst others [86]

The sensitivity analysis for the different bottom coefficients require multiple simulations to be run. The different bottom frictions that are examined are shown in Table 4.5. These values are based on the bottom coefficients found in the literature [77].

Table 4.5: The influence of using an α of 0 and a α of 1000

Roughness component	U component	V component
1	Chezy 34	Chezy 34
2	Chezy 44	Chezy 44
3	Chezy 60	Chezy 60
4	Manning 0.03	Manning 0.03
5	Manning 0.035	Manning 0.035
6	Manning 0.04	Manning 0.04
7	Manning 0.045	Manning 0.045
8	Manning 0.05	Manning 0.05
9	Manning 0.06	Manning 0.06

In Appendix D the comparison between the Delft 3D model and the tidal gauge data is presented in more detail. From Figure D.1 till Figure D.12 the different bottom frictions for all tidal stations are shown.

These different simulations were compared to measure data that was extracted from the DDB. From this, it is possible to deduce the water level changes at certain tidal stations. After this, the water level changes between the modelled and observed data can be compared. In this comparison, the RMSE, Pearson coefficient and the Scatter index are analysed. The scatter plots show the comparisons of the observed and simulated data of a tidal station, see Figure D.13 till Figure D.24 in Appendix D. In these plots every 10th time step is shown to make it easier to visualize the difference between the two data sets. Table 4.6 shows the results of the analysis of the different parameters for the different locations.

Table 4.6: The average RMSE, Pearson and SI score of the different bottom roughness, Delft 3D

Average	Chezy 34	Chezy 44	Chezy 60	Manning 0.03	Manning 0.035	Manning 0.04	Manning 0.045	Manning 0.05	Manning 0.06
RMSE	0.265	0.266	0.269	0.26	0.257	0.255	0.254	0.253	0.255
Pearson	0.903	0.9	0.899	0.9032	0.904	0.905	0.907	0.909	0.913
SI	49.732	49.84	50.394	49.18	48.713	48.454	48.332	48.305	48.49

This analysis shows that the best bottom friction for the Delft 3D simulation is a Manning coefficient of 50. This could be determined by calculating the average errors of the different parameters for all tidal stations. The Manning coefficient 50, α 1000 was found to be the overall best bottom roughness coefficient, and thus these parameters are used for the resource assessment of an entire year. Due to the fact that in the Delft 3D simulation there is a change in velocity over depth, the velocity used by Chezy is too high. From Equation 4.1 it follows that if the velocity is high, the Chezy coefficient become smaller and thus the Chezy will underestimate the water level change and the current velocity. Just as explained in subsection 4.6.1.

In Figure 4.15 below the Manning coefficient 0.05 is compared to the different tidal gauge data. The figure shows that the simulation still underestimates the water level compared to the tidal gauge data. This is due to the fact that in the simulation not all parameters that occur in real life can be exactly modelled. Appendix D shows the comparison for each of the different bottom coefficients in more detail.

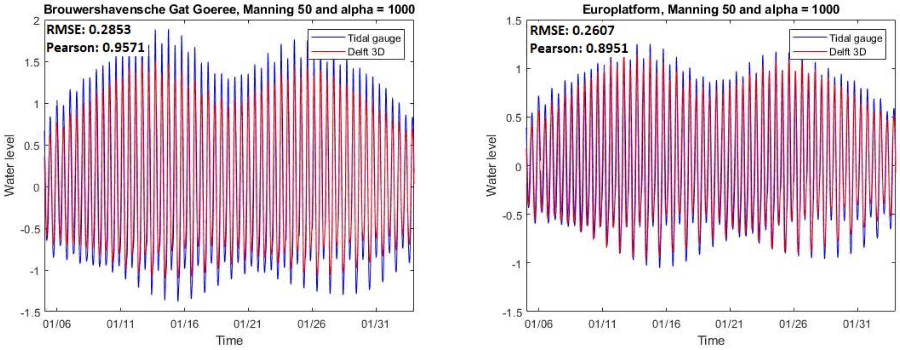

(a) Comparison between Brouwers Havensche Gat tidal gauge data and Delft 3D Manning 0.05

(b) Comparison between Euro platfrom tidal gauge data and Delft 3D Manning 0.05

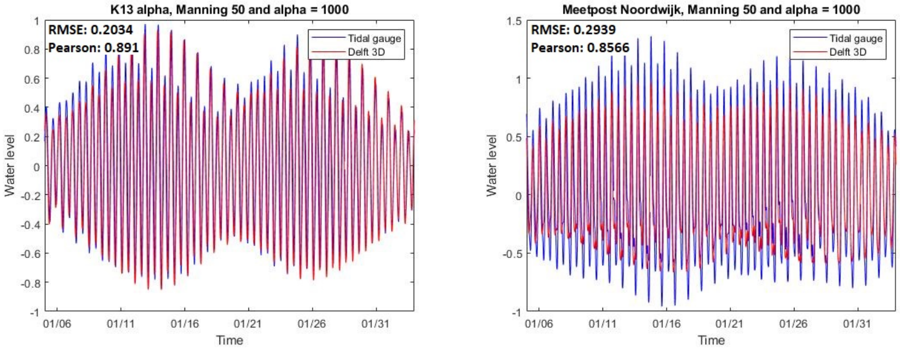

(c) Comparison between K13 alpha tidal gauge data and Delft 3D Manning 0.05

(d) Comparison between Meetpost Noordwijk tidal gauge data and Delft 3D Manning 0.05

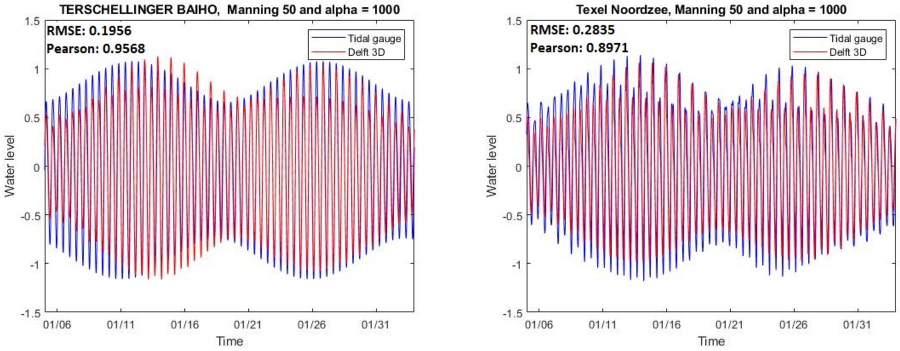

(e) Comparison between Terschellinger BAIHO tidal gauge data and Delft 3D Manning 0.05

(f) Comparison between Texel Noordzee tidal gauge data and Delft 3D Manning 0.05

Figure 4.15: The comparison between the Manning 0.05 coefficient simulated by Delft 3D and the tidal gauge data

5

Tidal resource assessment

In this chapter the resource assessments of both Delft 3D and Telemac are constructed. In this assessment it is also determined which program is best suited for the MCDM assessment and energy extraction. section 5.1 and section 5.2 discuss the resource assessments of Delft 3D and Telemac, respectively. In section 5.3 a comparison between Delft 3D and Telemac will be made to see which program best fits the tidal gauge data provided by DDB. In the last section it is determined which program will be used for remainder of the thesis.

5.1. Telemac

This section discusses the resource analysis of The Netherlands by using Telemac. For the resource assessment the metrics determined in subsection 4.6.1 are used. Using these metrics, it is possible to find the velocities, potential power and capacity factors for the different locations.

5.1.1. Telemac resource analysis

The previous chapter identified the Westerschelde, Oosterschelde and the area between Texel and Vlieland as the preferred tidal farm locations. Because these areas include multiple grid points, it is important to determine the exact resource potential of the multiple locations within these areas. For this evaluation, multiple metrics are relevant, such as tidal current, capacity vector and maximum tidal current.

For the resource assessment the RMSE, SI and Pearson metrics are used to determine the fit of the model regarding the tidal gauge for a period of a year. These are the tidal current, capacity vector and max tidal current. From this metrics it is possible to compare different locations with each other. In Figure 5.1 the locations that have been evaluated are shown.

The RMSE, SI and Pearson are determined for a full year analysis of Telemac. In Table 5.1 each of these parameters is shown per tidal station. The overall score of the RMSE is determined for a year. It can be seen that the scores are slightly higher compared to the month analysis in subsection 4.6.1. This mean that the accuracy of the water elevation over a year is slightly less than the sensitivity analysis of a month.

Table 5.1: The RMSE, Pearson and SI for the different location for Telemac

Telemac	Terschelling	Brouwer	Euro	k13	Meet	Texel	Average
RMSE	0.416413	0.230812	0.224535	0.369139	0.271946	0.307501	0.303391
Pearson	0.925653	0.922219	0.860117	0.877976	0.962646	0.955573	0.917364
Scatter index	53.40423	44.95001	61.79541	75.75633	47.26695	55.08188	56.3758

5.1.2. Assessment of velocity and water level for Telemac

For the assessment of tidal resources in The Netherlands, the predetermined locations have been evaluated. The evaluation consists of determining the velocities at multiple grid points in the areas of interest, selecting the location with the highest velocity. In Appendix E this evaluation is conducted.

After selecting the most suitable grid point, it is possible to obtain data regarding the water level elevation and velocity range over a year. These ranges are presented in Figure 5.2 to Figure 5.6.

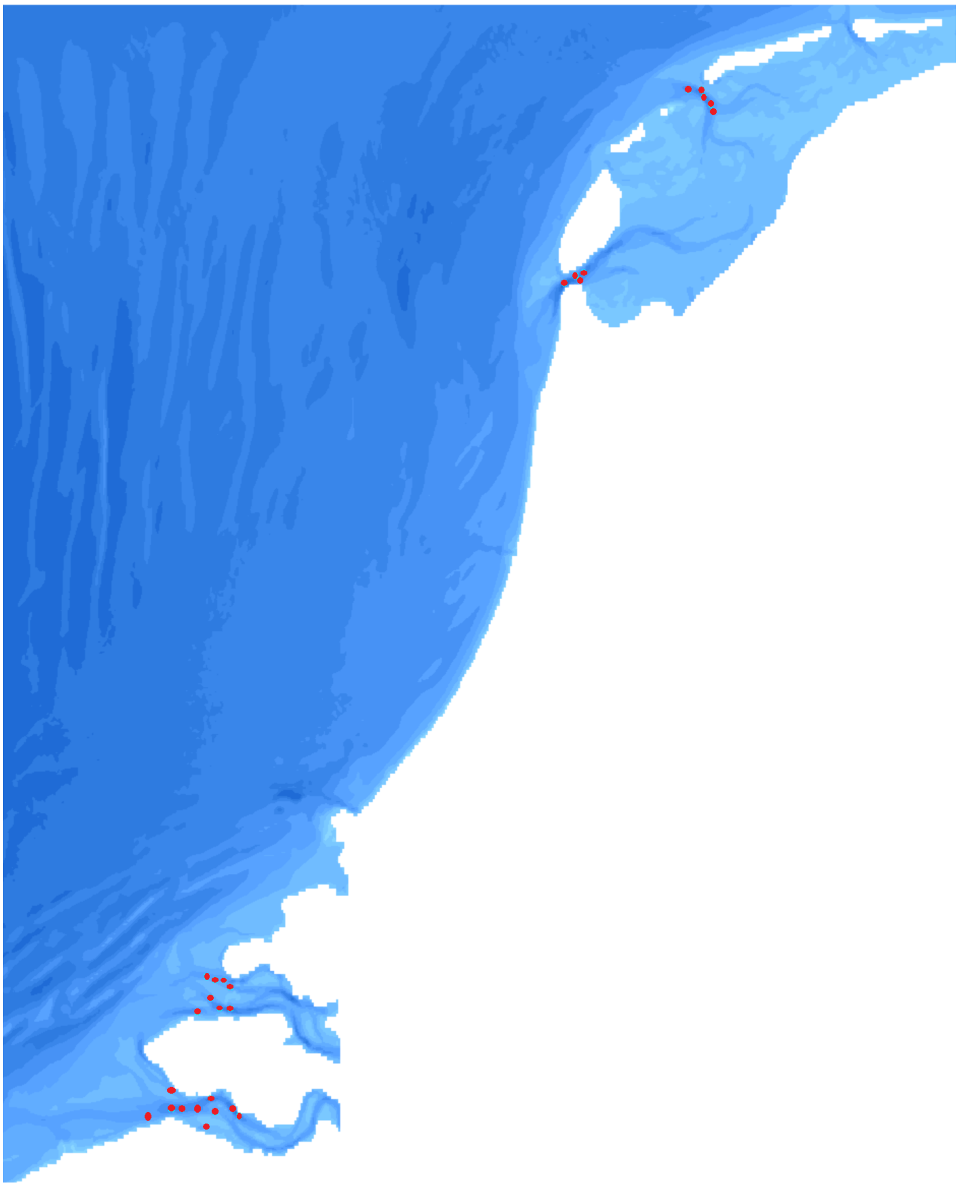

Figure 5.1: Location for resource assessment of The Netherlands

Next, the maximum and mean velocities at different locations are obtained, see Table 5.2. The figures also shows the velocity ranges during the different seasons, thus showing the effect of the different constituents. Table 5.2 shows that the maximum velocity occurs in Spring and the minimum velocity in Winter.

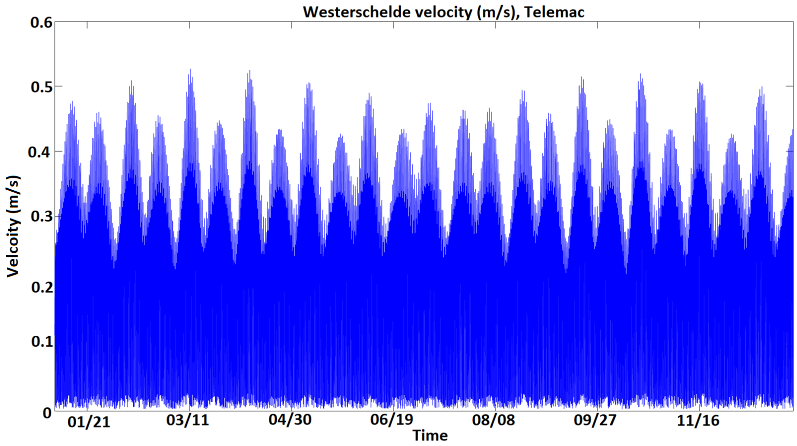

Figure 5.2: Westerschelde velocity (m/s)

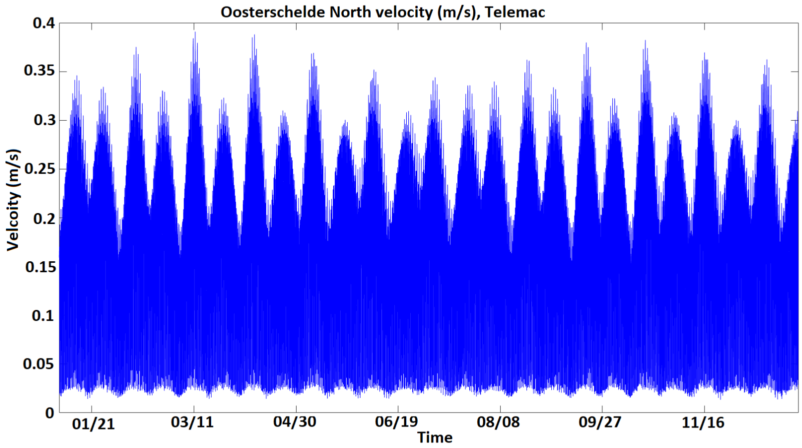

Figure 5.3: Oosterschelde North velocity (m/s)

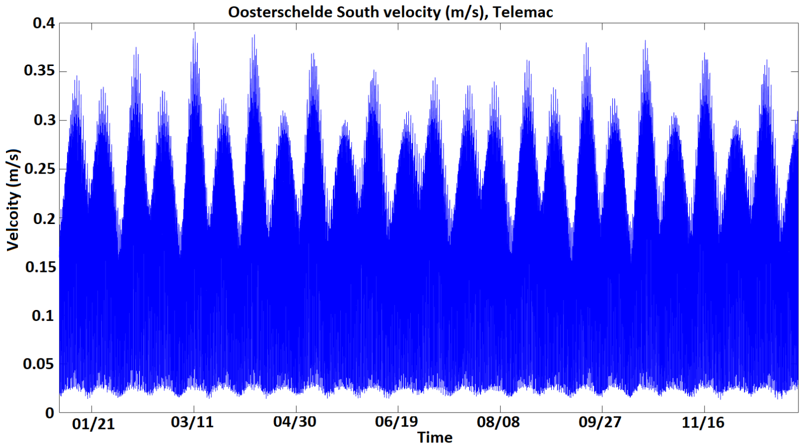

Figure 5.4: Oosterschelde South velocity (m/s)

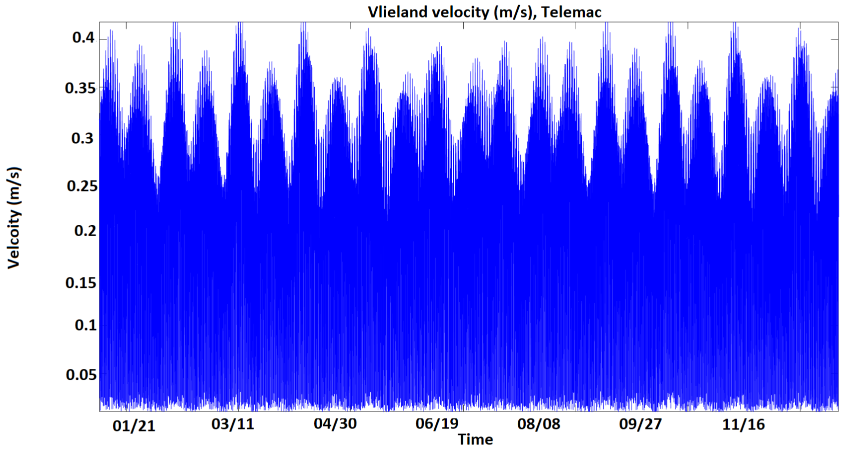

Figure 5.5: Vlieland velocity (m/s)

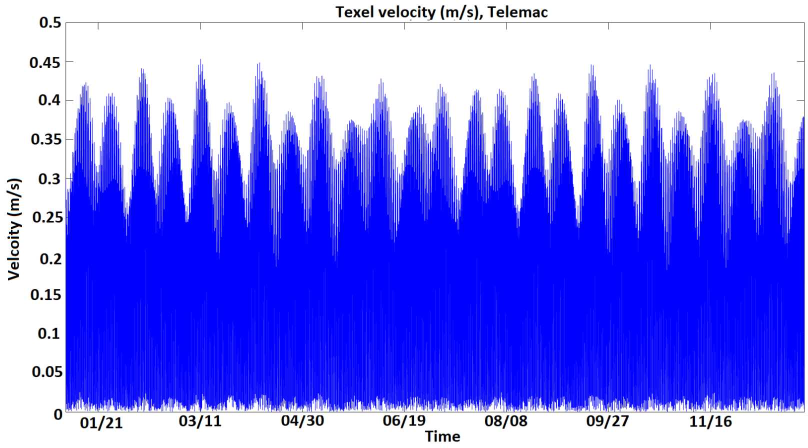

Figure 5.6: Texel velocity (m/s)

Table 5.2: The max and mean velocity of the different locations.

Delft 3D		Westerschelde	Oosterschede North	Oosterschelde South	Vlieland	Texel
Year	Max	0.503899	0.492345	0.390878	0.434615	0.452911
Year	Average	0.231877	0.242176	0.193195	0.224625	0.207823
Spring	Max	0.503899	0.492345	0.390878	0.434615	0.452911
	Average	0.230264	0.240123	0.191553	0.223438	0.206827
Summer	Max	0.472904	0.457732	0.362033	0.419401	0.43458
	Average	0.231899	0.242503	0.19348	0.22459	0.207301
Autumn	Max	0.497552	0.482196	0.382312	0.42944	0.445944
	Average	0.232335	0.242634	0.19356	0.22488	0.208317
Winter	Max	0.487085	0.473952	0.375169	0.42852	0.441167
	Average	0.233081	0.243521	0.19425	0.225651	0.208912

Next, it is important to determine the frequencies in which the different velocities occur. The frequency is found by determining how often a certain velocity range occurs over a year. In Figure 5.8, the histograms of the different locations are presented.

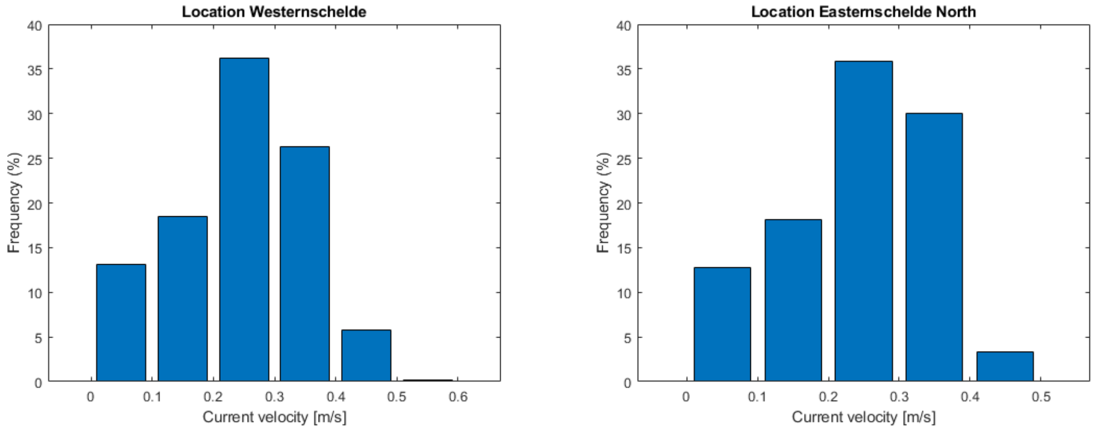

(a) Frequency of velocity occurrence for Westerschelde.

(b) Frequency of velocity occurrence for Oosterschelde North.

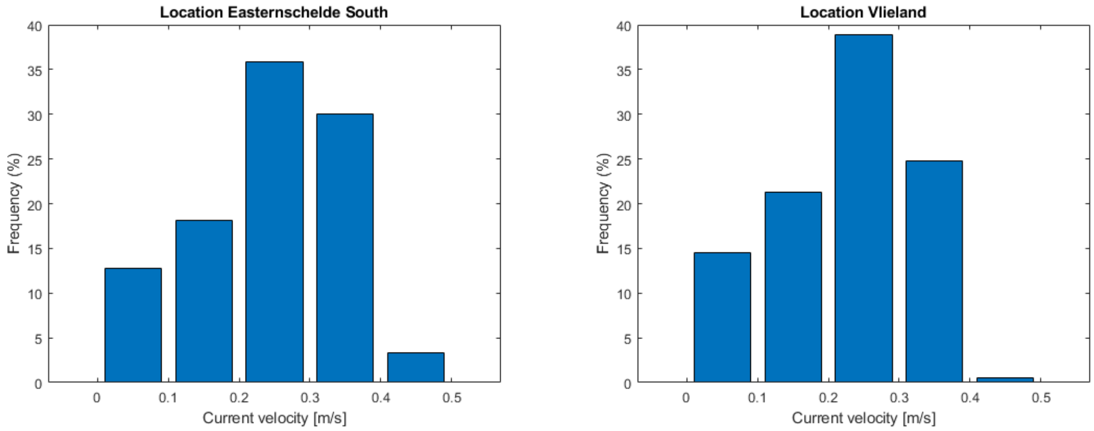

(c) Frequency of velocity occurrence for Oosterschelde South.

(d) Frequency of velocity occurrence for Vlieland.

Figure 5.7: Frequency of velocity occurrence

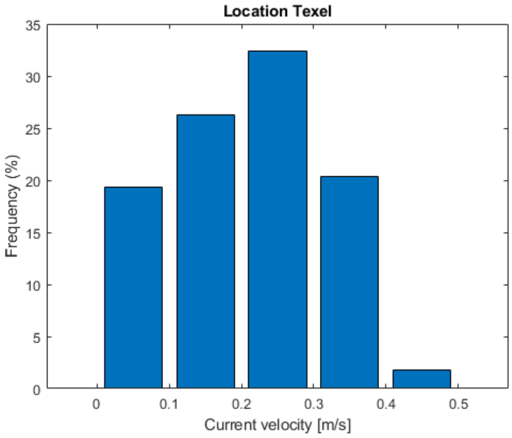

Figure 5.8: (e) Frequency of velocity occurrence for Texel.

The histograms use a step size of 0.1 m/s, and make it possible to determine the cut-in, cut-out and rated velocity. As can be seen in the figures the most common velocity range is between 0.2 and 0.3 m/s.

Furthermore, the cut-in velocity can be determined by investigating what velocity occurs the least, which in this case are velocities between 0 and 0.1 m/s.

The identified parameters will be used in the MCDM analysis to determine the most suitable location, while the cut-in and cut-out ranges found from the histogram will be used for the turbine assessment in chapter 6.

5.1.3. Mapping tidal, Telemac model

The maximum and mean velocity of the entire Dutch coastal area are presented in Figure 5.9 and Figure 5.10, in which the areas around the boundaries report a higher velocity. The higher velocity is due to the fact that the forcing of the model comes from the boundary. If the model would be extended over a larger area, this effect would fade out. Furthermore, as expected, the areas with the largest resource potential are the areas between Texel and Den Helder, between Vlieland and Terschelling, the Oosterschelde and Westerschelde. Furthermore, the maximum and mean velocity of the tidal ranges are determined for each season, in order to show the influence of the different constituents. In Appendix E the maximum and mean velocities of the different season are shown.

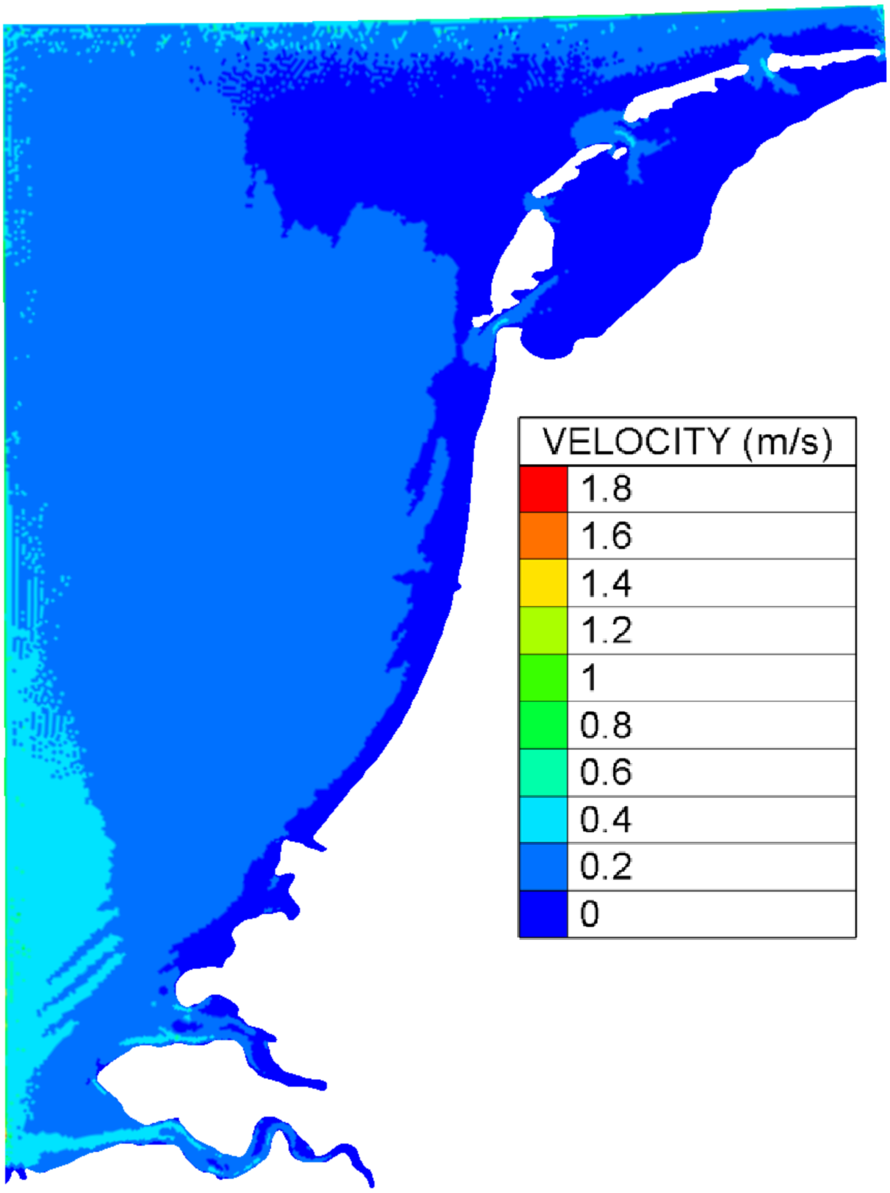

Figure 5.9: Max velocity for each grid point for a time span of a year.

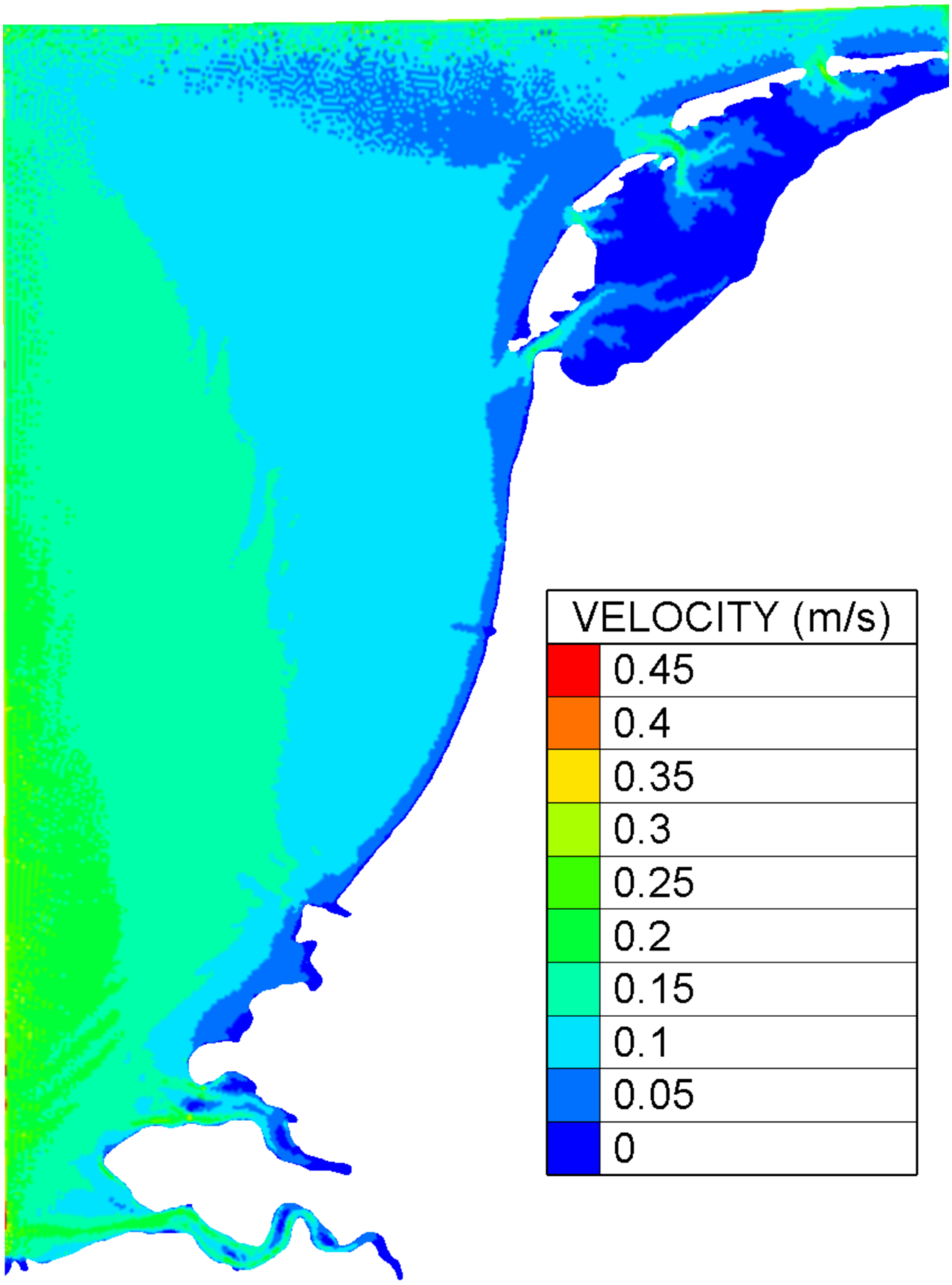

Figure 5.10: Mean velocity for each grid point for a time span of a year.

5.2. Delft 3D resource analysis

In the following section the resource analysis of The Netherlands with the use of Delft 3D will be explained. For the resource assessment the physics that have been determined in subsection 4.6.2 will be used. From this it is possible to find the velocities, potential power and capacity factors for the different locations.

5.2.1. Resource assessment Delft 3D for 2016

The same regions that were tested in Telemac are investigated. For the resource assessment the RMSE, SI and Pearson metrics are used to determine the fit of the model with the tidal gauge data for a period of one year. These are the tidal current, capacity vector and maximum tidal current. From this metrics it is possible to compare different locations with each other. In Figure 5.1 the locations that have been evaluated are shown.

First the RMSE, SI and Pearson are determined for the year-based analysis of Delft 3D. In Table 5.3 each of these parameters is shown for each tidal station. The overall score of the RMSE is 0.007 higher than for the monthly analysis. This shows that a bottom friction of 0.05 has a slightly worse outcome compared to the monthly analysis constructed in subsection 4.6.2.

Table 5.3: The RMSE, Pearson and SI for the different location

Delft 3D	Terschelling	Brouwer	Euro	k13	Meet	Texel	Average
RMSE	0.190693	0.303054	0.262311	0.214004	0.286292	0.316381	0.262123
Pearson	0.957835	0.943339	0.89691	0.878473	0.863567	0.864493	0.90077
SI	33.05343	38.75962	50.94437	58.73573	58.59312	56.51711	49.43389

5.2.2. Assessment of velocity and water level for Delft 3D

Next, it is possible to determine the tidal range, mean velocity, maximum velocity and the frequency in which certain velocities occur for the different locations. This provides a good estimation for what the best location is for the placement of tidal turbines. For each of the different locations, the grid point with the highest potential is used. In Appendix E the analysis between the different grid points is presented in more detail. After determining the most suitable grid point, it is possible to extract the velocity and water level range for this point over an entire year, see Figure 5.11 to Figure 5.15

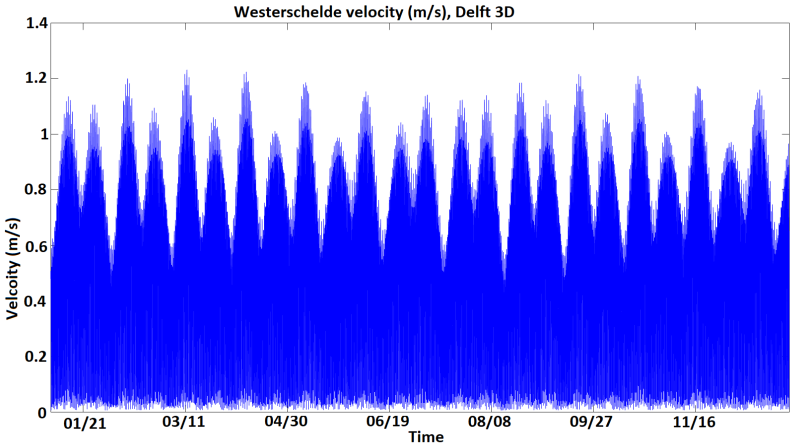

Figure 5.11: Westerschelde velocity (m/s)

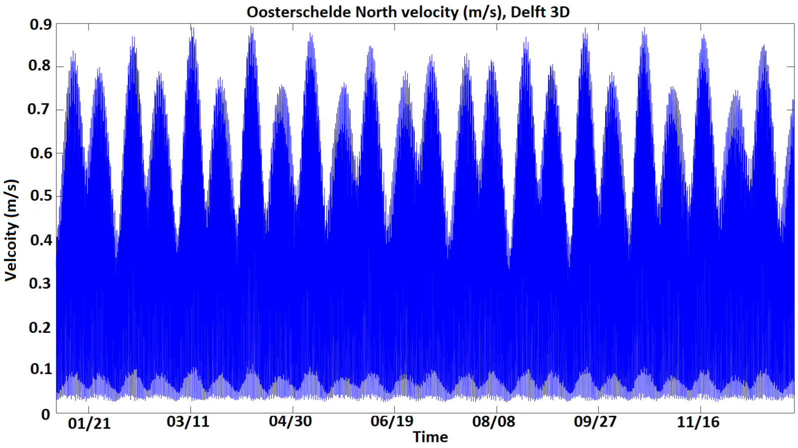

Figure 5.12: Oosterschelde North velocity (m/s)

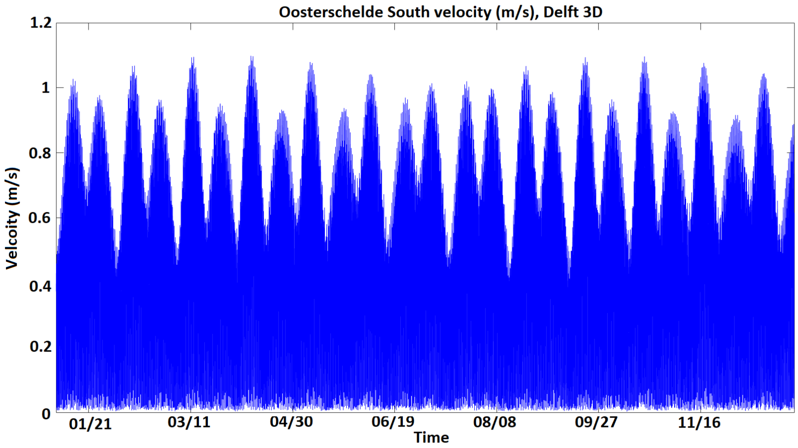

Figure 5.13: Oosterschelde South velocity (m/s)

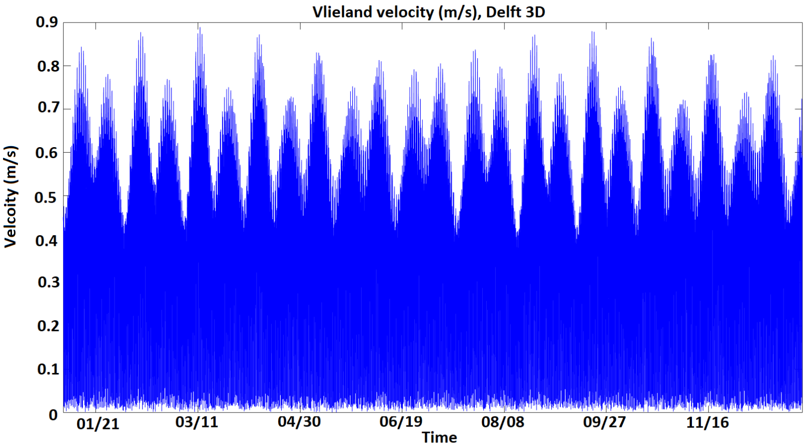

Figure 5.14: Vlieland velocity (m/s)

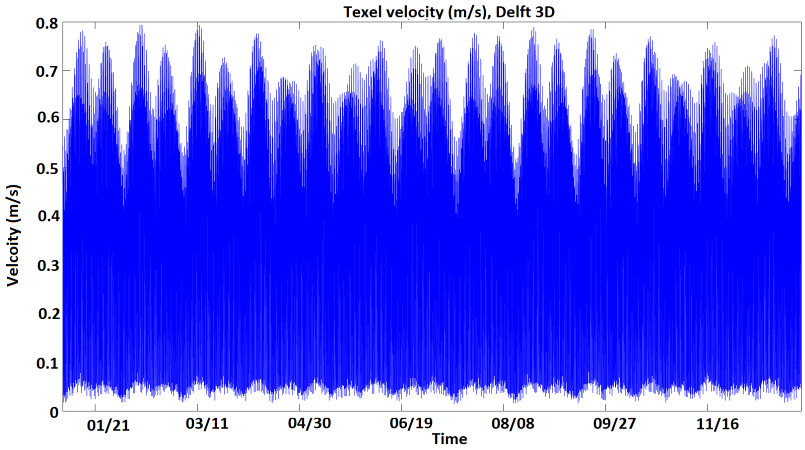

Figure 5.15: Texel velocity (m/s)

The maximum and average velocities are determined for each of these grid points, see Table 5.4. Furthermore, Table 5.4 includes the maximum velocity per month and season in order to show the effect of all tidal cycles over a full year. The data shows that the current velocity is the highest during Spring, while it is the lowest during Summer.

Table 5.4: The max and mean velocity of the different locations.

Delft 3D		Westerschelde	Oosterschede North	Oosterschelde South	Vlieland	Texel
Year	Max	1.23096	0.894629	1.09843	0.888947	0.872071
Year	Average	0.57427	0.424195	0.505295	0.426828	0.420264
Spring	Max	1.23096	0.894629	1.09843	0.888947	0.868402
	Average	0.570896	0.421449	0.501969	0.425538	0.419576
Summer	Max	1.18432	0.868799	1.0669	0.871479	0.867382
	Average	0.574809	0.42498	0.50613	0.426609	0.420029
Autumn	Max	1.21522	0.891265	1.09637	0.879519	0.860145
	Average	0.57517	0.425203	0.506641	0.427525	0.420532
Winter	Max	1.1999	0.869959	1.06797	0.877354	0.872071
	Average	0.576348	0.425228	0.506534	0.427705	0.420969

Another important parameter is the frequency in which certain velocities occur. With the frequency of occurrence known, it can be determined what percentage of time the turbine will operate at a certain location. Figure 5.17 shows the histograms per location, which provide information on the velocities for a step size of 0.1 m/s.

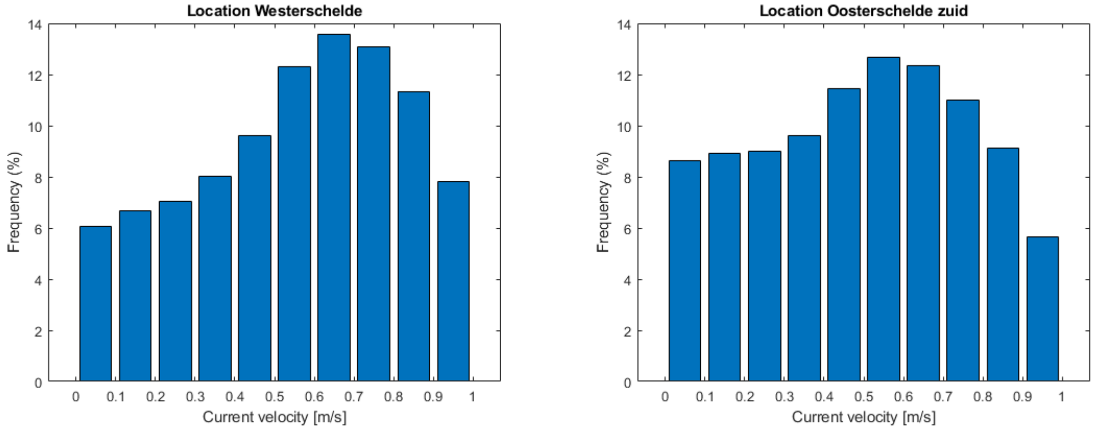

(a) Frequency of velocity occurence for Westerschelde.

(b) Frequency of velocity occurence for Oosterschelde North.

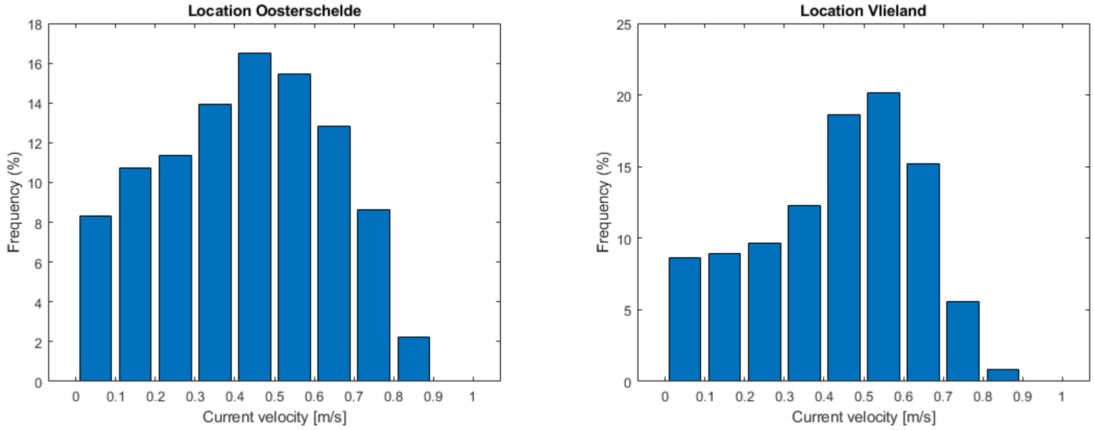

(c) Frequency of velocity occurence for Oosterschelde South.

(d) Frequency of velocity occurence for Vlieland.

Figure 5.16: Frequency of velocity occurence

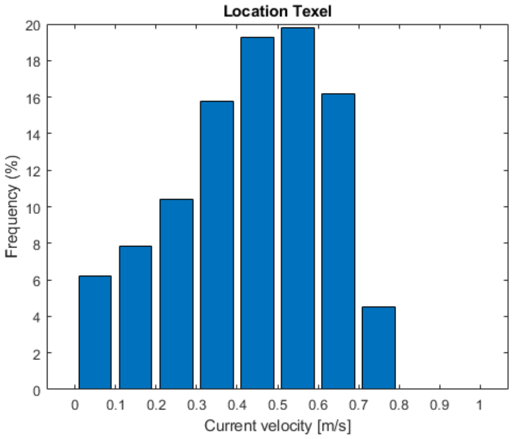

Figure 5.17: (e) Frequency of velocity occurence for Texel.

Knowing the velocities and frequencies, it is possible to determine the cut-in, cut-out and rated velocities of the turbines. The figures show that the most occurring velocity is in the range of 0.5 to 0.6 m/s, meaning that this would be a good rated velocity for the turbines. Furthermore, for all areas velocities below the 0.2 m/s do not occur often, which means that the velocity of 0.2 m/s would be a good cut-in velocity.

These parameters will be used in the MCDM analysis to determine the most suitable location, and the cut-in and cut-out ranges found from the histogram will be used for the turbine assessment in chapter 6.

5.2.3. Mapping tidal, Delft 3D model

This section provides a visual analysis of the maximum and mean current velocities and power potential of The Netherlands, to see if the area which shows the so far greatest potential also presents the highest velocity. In Figure 5.18 and Figure 5.19 the maximum current velocities of a year are presented. It was not possible to get the time independent maximum and mean velocities of the entire grid. Therefore, for different locations the maximum and mean velocities were calculated and the most common time step was used to visualise this. The figure shows that the areas that were thought to be optimal, also shows the highest potential. Furthermore, in Figure 5.18 the boundary forcing is pictured and present a high velocity. Due to the fact that the model covers a relatively small area, the boundary forcing at the boundaries is an overestimation. In Appendix E the maximum and mean velocities of the different seasons are presented in more detail.

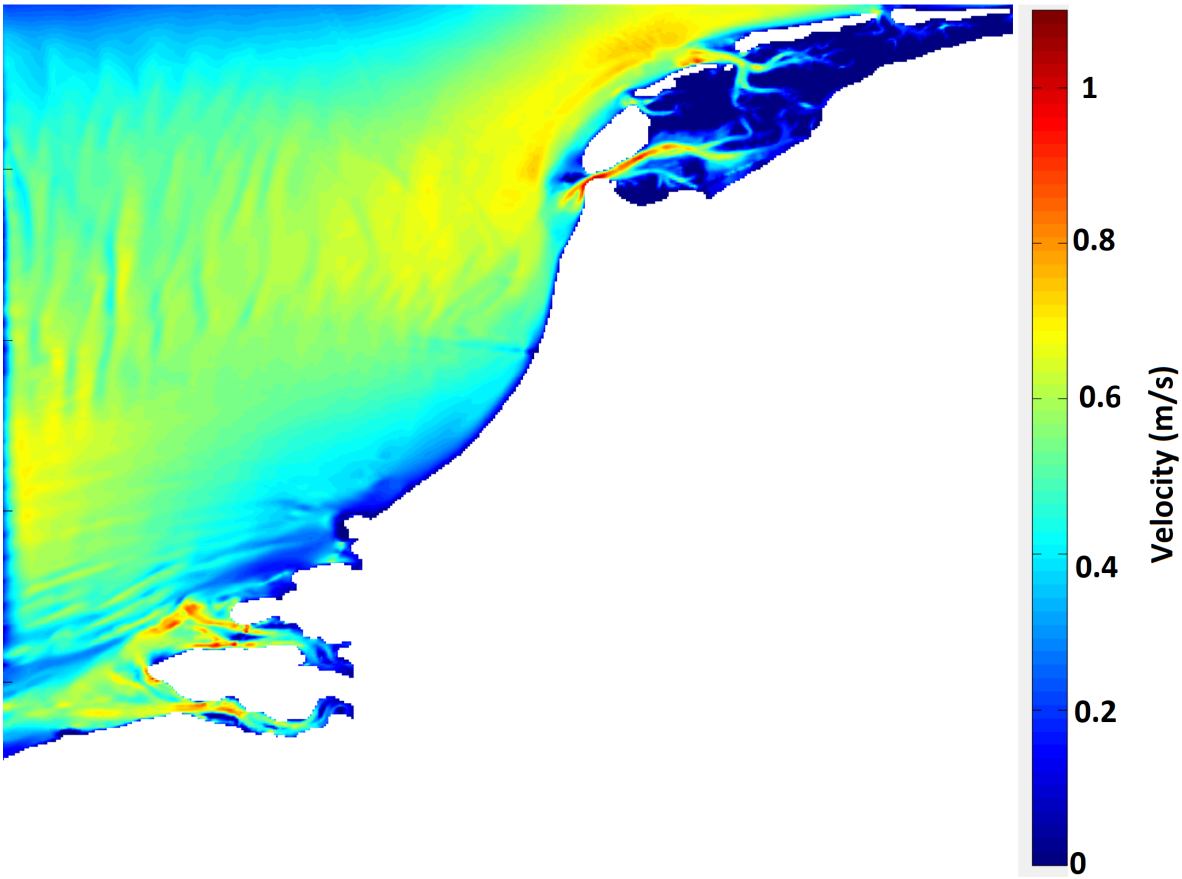

Figure 5.18: Max velocity for each grid point for a time span of a year.

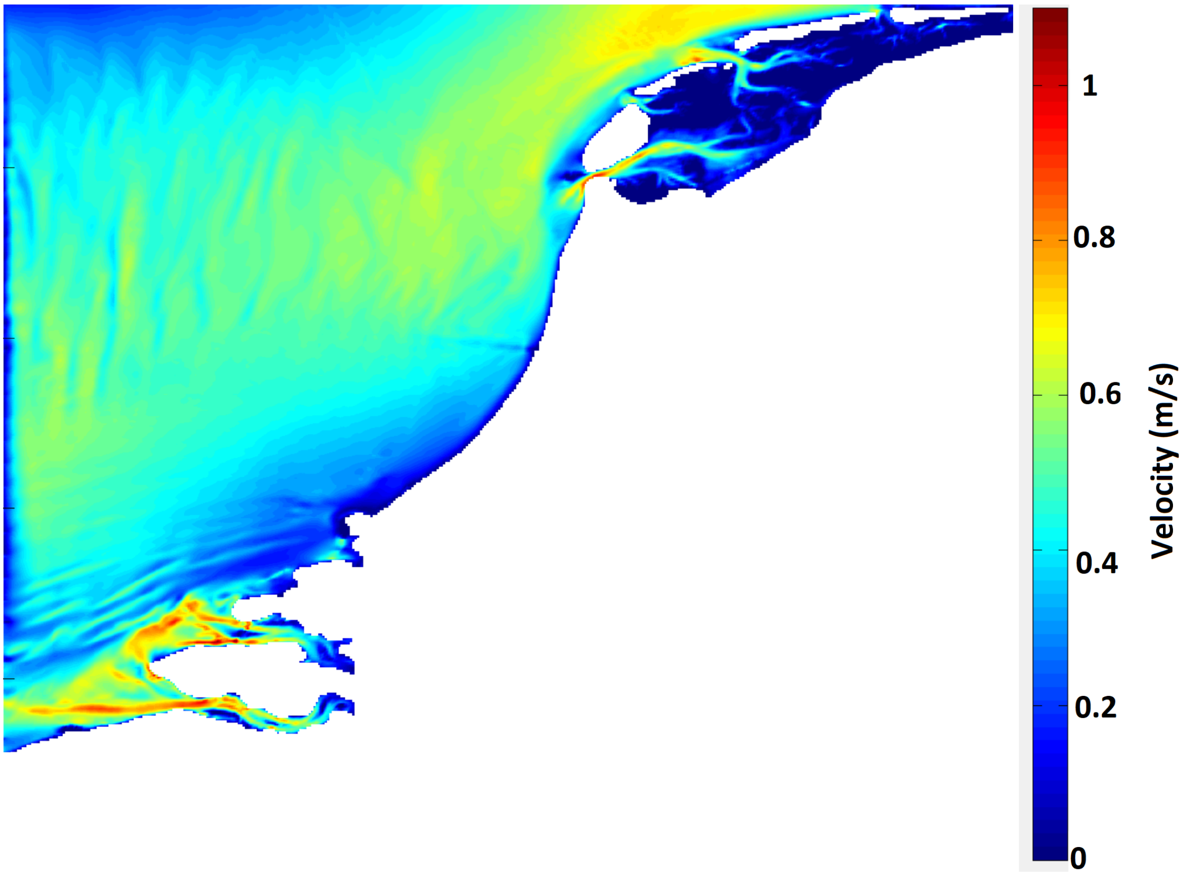

Figure 5.19: Mean velocity for each grid point for a time span of a year.

5.3. Comparison between Delft 3D and Telemac

The main difference between the models is that Telemac uses an unstructured grid and Delft 3D uses a structured grid. In Delft 3D it is not possible to increase or decrease the grid size in certain areas, while Telemac can provide for such an adjustment. This feature is for example useful around tidal stations, where a decreased mesh size results in the distance between the grid point and tidal station being decreased. Moreover, Telemac uses a triangular mesh and therefore has a larger computational time, while Delft 3D uses a rectangular mesh.[1] However, Telemac can use multiple processors within one computer to calculate the results, thus decreasing the computational time significantly depending on the amount and type of processors.

The accuracy of Telemac was expected to be higher than the accuracy of the Delft 3D model, due to the increased amount of node points and the inclusion of a finer mesh along the coastal areas. However, it was found that the model has a less accurate fit than the Delft 3D model. The main reason for this is that the Telemac model was more out of phase with the tidal gauge data than the Delft 3D model and therefore had a worse correlation with the data. A difficult part of Telemac, however, is the TPXO tidal data base not being implemented as was the case in the Delft 3D dashboard. When comparing the results of both Delft 3D and Telemac, the RMSE and SI show that Delft 3D provides a better fit with the tidal data compared to Telemac. For the Pearson index, however, Telemac shows a slightly better comparison.

Another big difference is visible when looking at the velocity range models of both programs. Due to the fact that the sensitivity analysis showed that the best comparison between Telemac and the tidal gauge data occurred at a Manning coefficient of 0.11, the velocity is very slow. With the increase in bottom friction, the velocity profile decreases. For Delft 3D the best bottom friction occurred at a Manning coefficient of 0.05, meaning that the velocity profile found by Delft 3D is much higher. For Telemac, in order to get the optimal model with regards to the RMSE, SI and Pearson, a high bottom friction was required. Due to this the peaks of the Telemac model for the water level were reduced and so the velocity was significanty underestimated.

Lastly, in Delft 3D it is harder to change and implement new variables into the model compared to Telemac. Telemac is an open source program were it is possible to change a lot of features to get the ideal model.

5.4. Conclusion

With the simulations completed and the data compared, it is argued that for the rest of the thesis Delft 3D is better suited for determining the location and energy extraction. The main reason for this is that in the Telemac simulation, there is a large underestimation of the velocity compared to the Delft 3D model. Evidently, the velocity range is a very important factor for calculating the energy production. Furthermore, when looking at the sensitivity analysis between both models, the Delft 3D model has a slightly better fit with the tidal gauge data. The main explanation for this is that the comparison between Telemac and Delft 3D showed that the lower friction coefficient better fits the peaks of the tidal gauge data, while the overall comparison was the best for the larger bottom coefficient.

---

[1] The main reason for this is that the amount of grid points for the same area is larger when using the triangular mesh, thus resulting in a longer computational time.

6

Power curve

In order to determine the optimal tidal farm, it is paramount to calculate the best size of the tidal turbine with respect to the resources available. The optimal size can be calculated by creating a power curve for the different tidal turbine sizes.

Literature shows that there are tidal turbines in construction, which are solely designed for areas with an extremely high tidal potential, such as the Rathlin sound location. Because higher tidal locations can exploit bigger tidal turbines, these turbines are designed as big as 20 meters in diameter. However, The Netherlands is considered to have a low tidal resource and these turbines would simply be too big to be operational. Using turbines that are to big would result in a cut-in, rated, and cut-out speed that is too high with respect to the tidal speeds in The Netherlands.

It is therefore important to determine, dependent on the resource assessment, the best design for the turbine. But not only the optimal diameter needs to be calculated, also the power coefficient, thrust coefficient and rated power production will need to be determined. The designed turbine can be compared to an already excisting turbine, which will show how important it is to design the turbine for a specific location. The two different turbines that will be compared to the new design are the AR1500 from Atlantis [5] and the M100-D from Nova [73]. Table 6.1 below presents the characteristics of the turbines.

Table 6.1: Specifications of turbines AR1500 and M100-D

Specifications	AR1500	M100-D
Rated speed [m/s]	3.0	2.0
Cut-out speed [m/s]	5.0	6.0
Cut-in speed [m/s]	-	0.5
Blade diameter [m]	18	8.5
Rotor speed [rpm]	7-15	10 - 27
Rated capacity [kW]	1500	100
Design life [years]	25	20
Number of blades [-]	3	2
Rotor swept area [m^2]	254.47	56.75
Power coefficient [-]	0.42	0.43

From the information in Table 6.1 the power curve can be constructed for these two tidal turbines. The power curve is constructed by developing custom in-house matlab codes, that take into account the resource and structure interaction. Figure 6.1 and Figure 6.2 present the power curves.

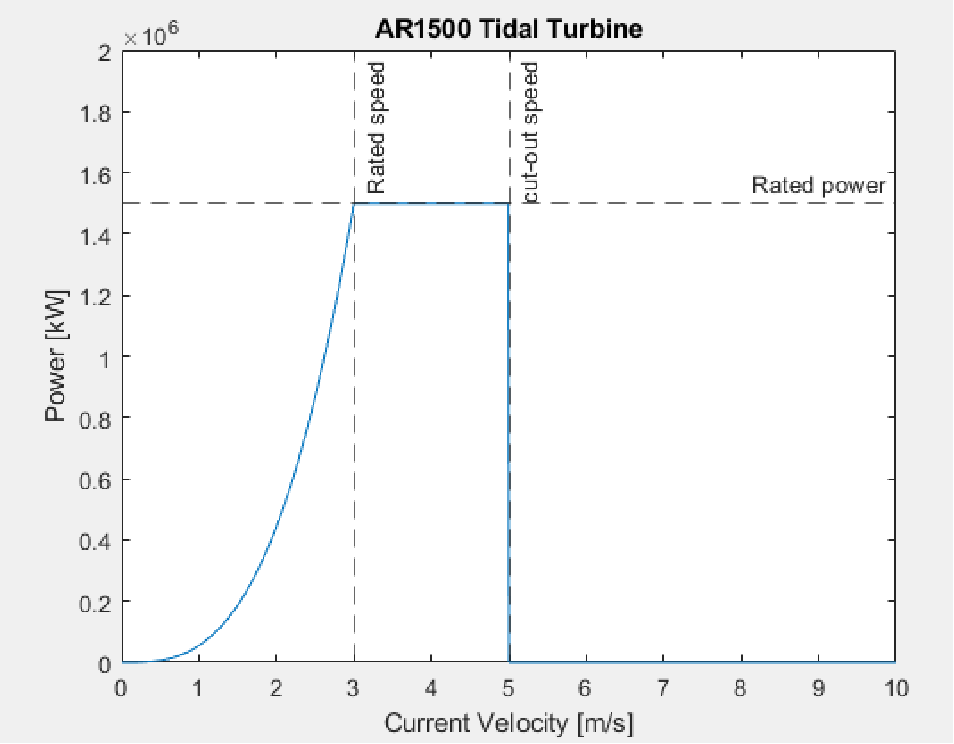

Figure 6.1: Power curve AR1500

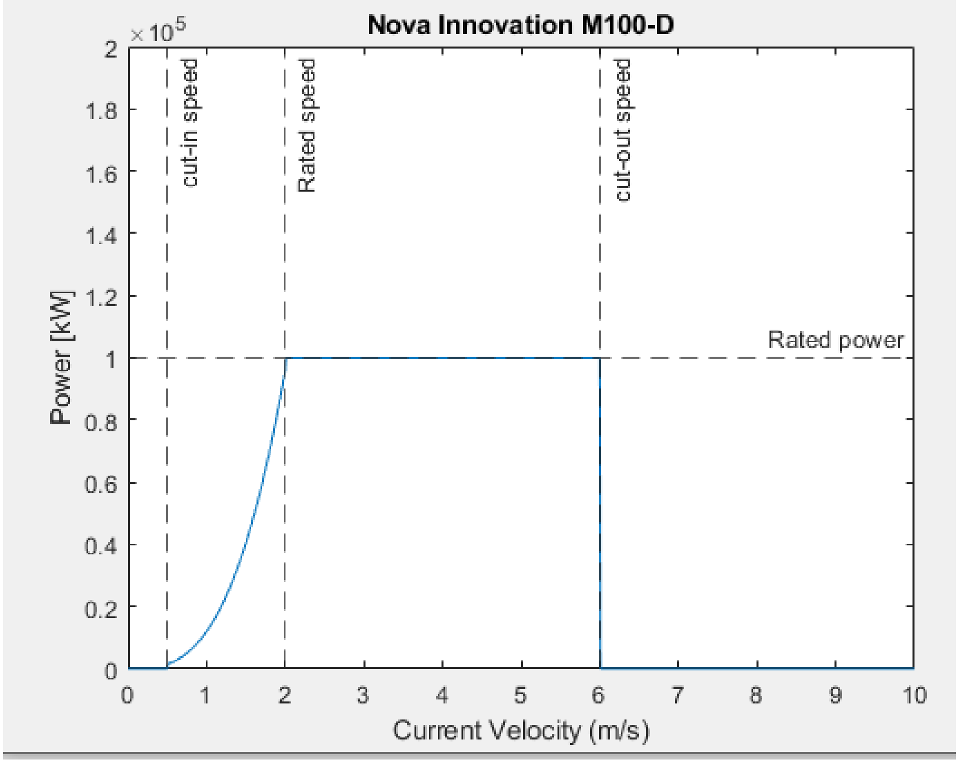

Figure 6.2: Power curve M100-D

6.1. Developing a turbine for low resource regions

The ideal turbine size is determined by using the AD theory. From the resource assessment a histogram of the available tidal currents is created. The histogram makes it possible to determine what the ideal cut-in speed, cut-out speed and rated speed are. These speeds are dependent on the velocities of the water flow. Figure 6.3 shows the cut-in speed should be around 0.2 m/s. Speeds lower than 0.2 m/s are too low to create a sufficient amount of power. The rated speed of the turbine should be around 0.6 m/s and the cut-out speed should be 1.3 m/s. These speeds do not occur very often but can generate a good amount of energy.

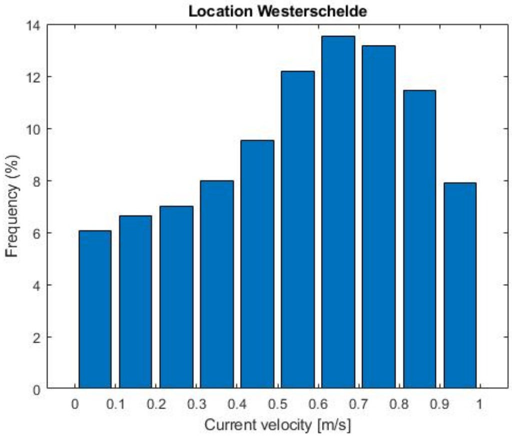

Figure 6.3: Frequency of occurrence of the different current velocities of the Westerschelde location

To determine the power curve from these speeds, an AD should be placed in the Delft 3D simulation. Some assumptions need to be made for the implementation of the turbine in Delft 3D, because Delft 3D does not have a build in function to add a tidal turbine into the model. To add the tidal turbine into the model a porous plate, representing an AD, is placed in the required location. This plate represents the AD, because of the fact that the porosity of the plate determines the amount of flow let through. The changed geometry of the AD does not significantly influence the model outcome of the turbine and gives accurate results [101, 103].

Logically, this is also the case for the support structure of the turbine [108, 9]. It is also possible to increase the friction to represent a drag force caused by a tidal turbine. The method is mostly used in Telemac [53]. Due to the fact the usage of the AD theory with a porous plate has been validated [108], this method is used to determine the production of the turbine.

The first step is that the grid where the turbines are placed needs to be sufficiently small. Because the size of the turbine is between the 3 and 8 meters, the grid should also be in this range. The grid size where the turbines are placed is around the same size as the diameter of the turbine. From here on, the production of a farm can be determined. However, the individual wake effect of the turbine in these farms is not represented, meaning the wake effect between these turbines is neglected. To include this effect, the turbines will be placed in the smaller grid where each individual turbine is represented.

The porosity is determined by the energy loss coefficient C_{loss}. The coefficient of a porous plate is determined by the Equation 6.1:

$$M_{\xi} = -C_{loss-U} \frac{Um,n|U_{m,n}|}{\Delta x} \tag{6.1}$$

To determine the C_{loss} the difference between the free flowing velocity u_{fs} and the velocity at the porous plate u_{cell}. The Equation 6.1 can be rewritten from vector components to scalar components for simplification:

$$M = -\frac{C_{loss}}{\Delta x} u_{cell}^2 \tag{6.2}$$

In order to determine the drag on the porous plate, the water depth must be divided into vertical layers. The depth averaged velocity is a 2D simulation, meaning the model has one vertical layer, so that the drag force on the turbine is assumed to be:

$$F = N\frac{1}{2} C_t \rho A_t u_{fs}^2 + F_{support} \tag{6.3}$$

The thrust on the support structure needs to be implemented into the drag of the turbine. In this Equation 6.3 c_t is the thrust coefficient. To keep the calculation time to a minimum it is important to simplify the support structure of the turbine. This can be achieved by assuming that the support structure will be a single horizontal cylinder. Other than for the tidal turbine the supporting structure will have a fixed drag coefficient for the different velocities. The equation for the thrust on the support structure will be:

$$F_{support} = \frac{1}{2} * \rho * c_D * A_{support} * V_0^2 \tag{6.4}$$

In this Equation 6.4 c_d is the thrust coefficient of the support structure, $A_{support}$ is the projected area of the turbines supporting structure. The turbine supporting structure is considered to be 10% of the turbine swept area. The drag coefficient of a smooth cylinder is depended on the Reynolds number.

$$Re = \frac{\rho u D}{\mu} \tag{6.5}$$

In this Equation 6.5 u is the flow speed, D is the diameter of the fluid and μ is the viscosity of the fluid. From this the Reynolds number can be found. The Reynolds number can determine the drag coefficient of the cylinder with the use of the graph found in Figure 6.4.The graph shows the relation between the drag coefficient and the Reynolds number for a cylinder. In Table 6.2 the Reynolds number for the different diameters is shown.

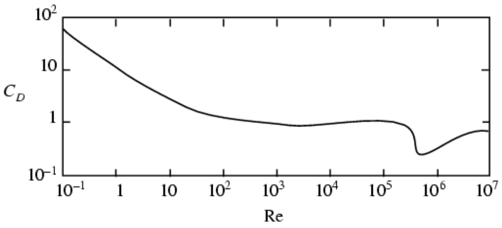

Figure 6.4: Drag force relation with the Reynolds number for a cylinder, [110]

Table 6.2: Drag coefficient of the supporting structure

Diameter (m)	velocity (m/s)	A_{disk} (m^2)	$A_{support}$ (m^2)	Diameter (m)	Reynolds	c_d
3	0.6	7.0686	0.707	0.949	534.82	1.1
4	0.6	12.566	1.257	1.265	713.094	1.05
5	0.6	19.635	1.963	1.581	891.367	1
6	0.6	28.274	2.827	1.897	1069.64	0.97
7	0.6	38.485	3.8485	2.2136	1247.914	0.95
8	0.6	50.265	5.0265	2.5298	1426.171	0.934

With the drag coefficient of the support structure known it is possible to rewrite Equation 6.6, because force is the momentum change per second. The energy loss Equation will become:

$$M = \frac{F}{\rho \Delta x \Delta y * H} \tag{6.6}$$

In this Equation 6.6 F is the combination of the drag cost by the turbine and by the support structure. The C_{loss} for a 2D simulation can now be determined with the use of the AD theory. The parameter γ represents the portion of momentum passing through the cell. This gives the Equation 6.7, Equation 6.8 and Equation 6.9:

$$C_{loss} = \frac{\gamma}{2} * \alpha \tag{6.7}$$

$$\gamma = \frac{C_{dt} A_e}{\Delta x H} \tag{6.8}$$

$$\alpha = \frac{4}{(1 + \sqrt{(1-\gamma)})^2} \tag{6.9}$$

Where Δx is the grid size, H is the water depth, A_e is the turbine size and C_{dt} is the thrust coefficient and drag coefficient combined.

Unfortunately, it is not possible in Delft 3D to have a velocity varying thrust coefficient which means that the rated-speed thrust coefficient should be used. However, because the turbines used in the analysis are not yet designed, it is unknown what the thrust coefficient of such turbines are at certain speeds. From [108] it was found that a turbine with a diameter of 20 m and a rated speed of 2.5 m/s has a thrust coefficient of 0.85. It is therefore assumed that the turbines used in this analysis will have a thrust coefficient that is 20 % of the thrust coefficient of the 20 meter turbine, so that a thrust coefficient of 0.17 is used to represent the turbines.

In Table 6.3 the different C_{loss} values of the different diameters are presented.

Table 6.3: The C_{loss} calculated for the different tidal turbine diameters

Diameter (m)	Depth (m)	Grid size (m)	A (m^2)	C_{dt}	C_{loss}
3	10	3	7.775	1.27	0.1773
4	10	4	13.823	1.22	0.2405
5	10	5	21.598	1.17	0.3052
6	10	6	31.102	1.14	0.3805
7	10	7	42.333	1.12	0.4693
8	10	8	55.2915	1.104	0.5749

The table shows the combination of the support structure with the tidal turbines (Cd). With the C_{loss} values of the different turbines known, it is possible to place the turbines into a grid and determine the power curve for the different turbines.

6.2. Power curve determination

The power curve must be calculated and a loading estimation must be made to determine which turbine is optimal. In Delft 3D, the free flowing velocity u_{fs} and the velocity at the porous plate u_{cell} can be determined for different speeds, and with that the power curve can be created.

The exact power produced by a turbine is dependent on the current velocity (u), the rotor swept area (A), the turbine power coefficient (C_p) and the seawater density, which is assumed to be 1025 kg/m^3 (ρ). See Equation 6.10 [62, 11]:

$$P = \frac{1}{2}\rho C_p A u^3 \tag{6.10}$$

For calculation of the power curve, the power (C_p) and thrust coefficient (C_t) are required and can be determined by using Equation 6.11 and Equation 6.12:

$$C_t = \frac{2F}{\rho A u^2} \tag{6.11}$$

$$C_p = \frac{2P}{A\rho u^3} \tag{6.12}$$

Both the power coefficient and thrust coefficient are dependent on the power production. For the power coefficient it is important that the value will be below the Betz limit, which is 59 % [69]. The value is created for the situations in which there is no loss in rotor speeds. However, this cannot be the case in a real life scenario.

The power curve for the AD can be determined by using the momentum theory. With the momentum theory the swept area of the blades is assumed to be a disk, the AD. To determine the pressure on the AD, Bernoulli's equation is used upstream and downstream of the AD. Bernoulli's equation cannot be used at the location of the AD, because at the AD there is a big pressure difference, which goes against the laws of the Bernoulli equations. Therefore, the velocity at the AD needs to be determined using the upstream and downstream velocity. The input variables are determined using the resource assessment and the placement of the AD in the model. The equation for the upstream part is:

$$p_0 + \frac{1}{2} * \rho * V_0^2 = p + \frac{1}{2} * \rho * u^2 \tag{6.13}$$

The equation for the downstream part is:

$$(p-\Delta p)+\frac{1}{2}*\rho*u^2=p_0+\frac{1}{2}*\rho*u_1^2 \tag{6.14}$$

In Equation 6.14 $\Delta\ p$ is the pressure drop at the AD, p is the pressure just upstream of the AD, p_0 is the pressure downstream of the turbine, V_0 is the velocity upstream, u_1 is the velocity downstream and u is the velocity at the AD. The Equation 6.14 can be rewritten so the pressure drop can be determined:

$$\Delta p=\frac{1}{2}*\rho*(V_0^2-u_1^2) \tag{6.15}$$

The velocity at the AD is found by:

$$u=\frac{1}{2}*(V_0+u_1) \tag{6.16}$$

From this the axial induction factor must be used to determine the thrust and power:

$$u=(1-a)*V_0 \tag{6.17}$$

$$u_1=(1-2a)*V_0 \tag{6.18}$$

In these Equation 6.17 and Equation 6.18 a is the axial induction factor and can be determined by combining Equation 6.17 and Equation 6.18. The Equation 6.19 for the axial induction factor is given by:

$$a=\frac{V_0-u}{V_0} \tag{6.19}$$

The thrust and power equation for the turbine can be rewritten as:

$$T=2*\rho*V_0^2*a*(1-a)*A=\frac{1}{2}*c_t*\rho*A*V_0^2 \tag{6.20}$$

$$P=2*\rho*V_0^3*a*(1-a)^2*A=\frac{1}{2}*c_p*\rho*A*V_0^3 \tag{6.21}$$

To find total thrust on the tidal stream turbine the supporting structure must be included. Meaning that the thrust of the tidal stream turbine is given by:

$$T=2*\rho*V_0^2*a*(1-a)*A=\frac{1}{2}*c_t*\rho*A*V_0^2+\frac{1}{2}*\rho*c_d*A_{support}*V_0^2 \tag{6.22}$$

The power coefficient and power curve will be calculated with the use of a matlab script, which takes into account the different current velocities. Due to the fact that multiple assumptions are made about the thrust coefficient and the drag coefficient, the Power coefficient is smaller than expected.

A single turbine is placed in Delft 3D and velocities in the tidal range are flowed into the turbine to determine the power coefficient of the different turbines. From this it is possible to the find the velocity changes behind the turbine.

Figure 6.5 shows that behind the turbine there is a wake effect. The wake effect is dependent on the size of the turbine. From this analysis it is possible to determine the power coefficient and power curve of the different turbine diameters. Table 6.4 presents the power coefficients relating to the different diameters.

Due to the fact that the rated velocity is 0.6 m/s, the rated power can be determined by Equation 6.21. For this velocity the thrust force on the turbine can also be deducted. The thrust force includes both the turbine and the supporting structure. Table 6.5 shows these parameters.

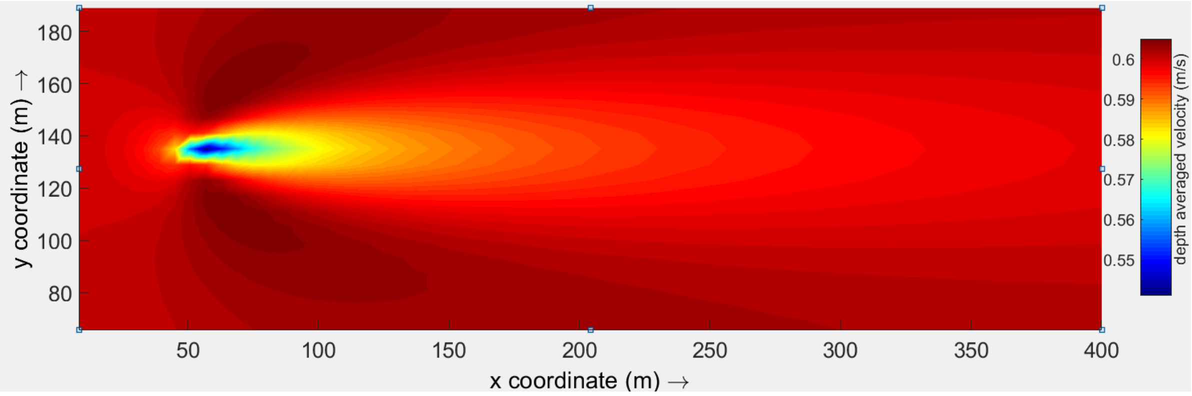

Figure 6.5: The wake effect of a single 6m turbine

Table 6.4: The power coefficient determined for the different turbine

Velocity	Turbine diameter: 3m		4m		5m		6m		7m		8m	
	a	c_p	a	c_p	a	c_p	a	c_p	a	c_p	a	c_p
0.2	0.019	0.0731	0.0305	0.118	0.0475	0.172	0.062	0.218	0.082	0.275	0.104	0.334
0.3	0.0243	0.0927	0.0400	0.148	0.0596	0.211	0.077	0.261	0.100	0.324	0.126	0.386
0.4	0.0293	0.110	0.0463	0.168	0.0695	0.241	0.089	0.294	0.114	0.359	0.143	0.421
0.5	0.0334	0.125	0.0520	0.187	0.0774	0.264	0.098	0.320	0.126	0.385	0.157	0.446
0.6	0.0370	0.137	0.0573	0.204	0.0845	0.283	0.107	0.340	0.136	0.405	0.168	0.465
0.7	0.0404	0.149	0.0621	0.219	0.0906	0.299	0.114	0.357	0.144	0.422	0.177	0.480
0.8	0.0436	0.159	0.0664	0.231	0.096	0.314	0.120	0.372	0.149	0.497	0.185	0.492
0.9	0.0468	0.170	0.0136	0.248	0.101	0.326	0.126	0.384	0.158	0.447	0.192	0.502
1	0.0495	0.179	0.0145	0.256	0.105	0.337	0.131	0.395	0.163	0.457	0.199	0.510
1.1	0.0525	0.188	0.0773	0.263	0.109	0.347	0.135	0.405	0.168	0.357	0.204	0.517
1.2	0.0547	0.195	0.0808	0.273	0.113	0.356	0.140	0.414	0.173	0.474	0.209	0.523
1.3	0.0577	0.205	0.0838	0.282	0.117	0.365	0.144	0.422	0.177	0.480	0.214	0.529

Table 6.5: The rated power and total thrust for the different turbine diameters

Diameter (m)	P_{sat} (W)	$T_{turbine}$	$T_{support}$	T_{total} (N)
3	107.398	221.706	1434.57	1656.28
4	283.429	394.144	2550.345	2944.489
5	615.759	615.85	3984.914	4600.764
6	1064.483	886.825	5738.276	6625.101
7	1725.69	1207.067	7810.431	9017.498
8	2586.88	1576.58	10201.4	11778

The wake effect is the last parameter that is relevant for the single turbine. For the different velocities there is a slight variation in the wake effect. From this it can be determined how fast the flow is recovered, which is important for the placement of a turbine array. The impact of the wake influences the power production of the other turbines in the array by reducing the flow velocity. The power curves of the different diameters are presented in Appendix F. Figure 6.6 shows the wake effect of the different tidal turbines, and shows that the larger the turbine the longer it takes for the flow to recover and thus the larger the impact on the flow is.

In chapter 8 these different turbine diameters will be analysed and the power coefficient found in this chapter will be used for the analysis of the best array configuration.

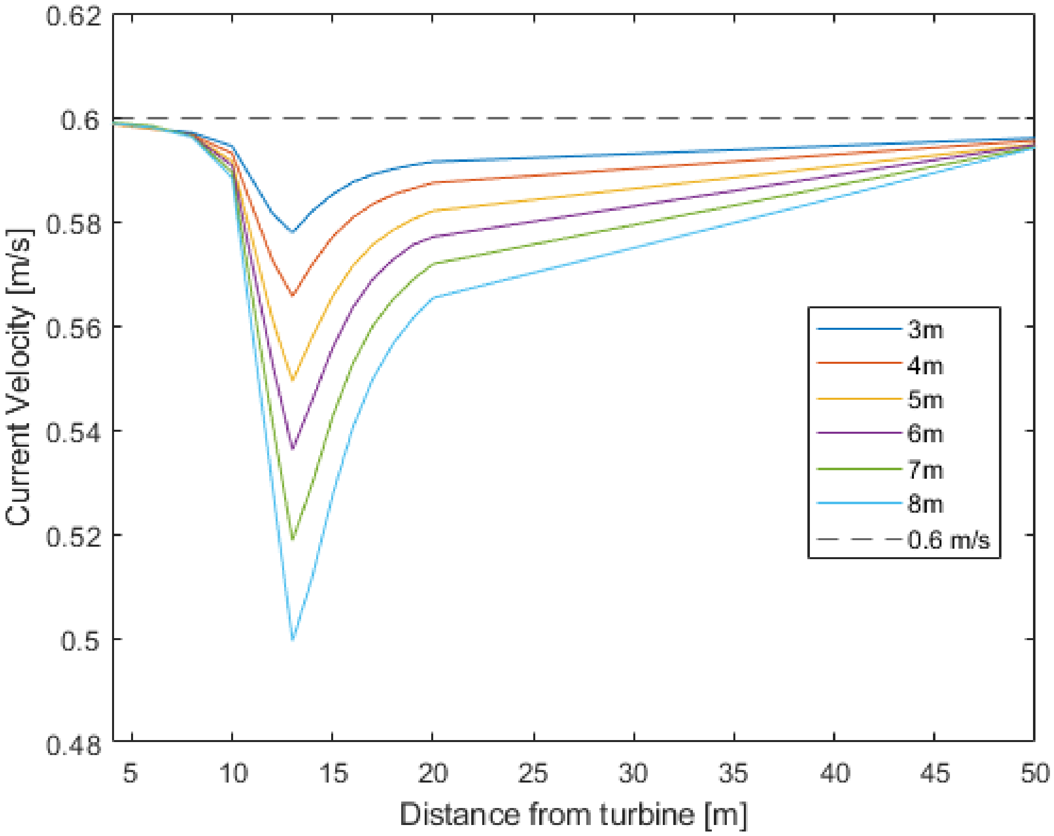

Figure 6.6: The wake effect of the different diameters for a 0.6 m/s flow speed.

7

Multi-Criteria Decision Making (MCDM) for tidal arrays

Tidal stream energy is an upcoming technology that in the coming years can become commercially available. The current tidal stream turbines that are being used, are constructed in areas with high tidal energy potential. For The Netherlands, which has low tidal areas, there has never been an investigation on a possible location for tidal farms. To determine the best location to place such a tidal farm a Multi-criteria decision making (MCDM) has to be developed. In this chapter the following sub-question will be answered:

1. ***"What is the best location in The Netherlands to generate tidal energy?"***.

7.1. Methodology

There are multiple methods for solving a MCDM model. The base for the MCDM is geographic information system (GIS) based data and the Analytic hierarchy process (AHP). Combining these two makes it possible to assign weight to the criteria required to find the most suitable location. The advantages of determining the MCMD this way is that with GIS it is possible to store, manage and visualise the data. Together with the AHP it is possible to create a model to evaluate, structure and prioritize the different options. The MCDM consists out of two phases and multiple steps to determine the values for the potential locations of the tidal farm.

The values of the AHP are normally determined with the use of expert's opinions. With the use of interviews and questionnaires the values of the different criteria can be determined [25, 38, 113, 6]. Due to the scope of the thesis it is not possible to include a full analysis of different stakeholders and experts to determine the values. The criteria and their weights will therefore be determined with the use of an extensive literature research. The AHP models that have been found during the literature review will be modified to fit the demands of a tidal farm. The first phase of the MCDM method is to determine restricted areas within the study area. The second phase of the MCDM consists of multiple steps. The first step is to determine criteria and generate a pairwise comparison between these criteria with the use of the AHP. The second step is to analyse these criteria with respect for the different locations, which is done with the aid of GIS. Figure 7.1 presents a flowchart to determine the best location. The third step is to determine the consistency ratio and rank the different locations. With the AHP model it is possible to only determine the weight of the different criteria compared to each other but also to compare the different locations. The method is used to give the criteria quantitative and reproducible values.

Unfortunately, this also brings along uncertainties with respect to the distributions between the scores.[1] The criteria are determined based on existing literature and a pairwise comparison square matrix build. The analysis is performed in Excel and is included in the documentation of the thesis, see Appendix D

7.2. Area of study

The Netherlands is located at the North sea around the 52^{nd} degree latitude. The coastal area is around 325 kilometers long, including the Wadden islands and multiple rivers and estuaries like the Schelde, Maas and

---

[1] A solution would be to also use expert's opinions to rank the location, but as stated before it is not possible to include such opinions in the thesis.

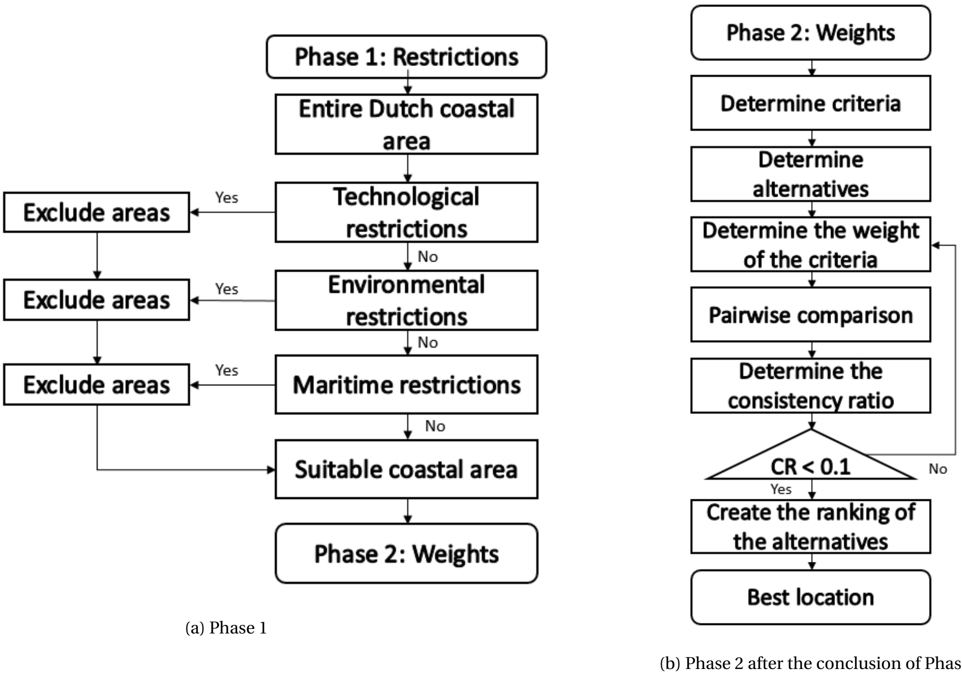

(a) Phase 1

(b) Phase 2 after the conclusion of Phase 1

Figure 7.1: Methodology flowchart for the MCDM analysis

Rijn. The coastal area of The Netherlands is mostly comprised of beach areas with dunes.

Figure 7.2: Map of The Netherlands.

The average population density of The Netherlands is around the 508 inhabitants per km^2. The main populated area is the Randstad, an area compiling parts of North- and South- Holland with cities like Amsterdam, Rotterdam and The Hague. Less populated areas near the coast are Zeeland and the top of North-Holland. The main economic driver of the Randstad is service industry-based, which also includes the exploitation of the Port of Rotterdam. The economy of Zeeland is mostly focused on tourism, but Zeeland also houses a big industrial area around Vlissingen. Most of the coastal regions are also looking to expand their production of green energy, and because of the geographical locations of these areas they focus on offshore energy, from for example offshore wind projects [15].

The climate of the coastal area is a mild sea climate according to the Köppen classification, indicating that both the Winter and Summer have mild conditions and during the entire year there is precipitation. The temperature in the Summer is around the 17.3 degrees Celsius and in Winter around the 3.9 degrees Celsius. Because of the location of The Netherlands at the North sea the wind speed can become very high, around the 120 km/hour. The highest wind speeds occur during storms, which are most common during the Winter months. The wave conditions are also more extreme during these periods due to the higher wind speeds.

Tidal conditions in The Netherlands are considered to be low, which is due to the underwater geology of The Netherlands and because there is not a large congestion of flow. The Netherlands has a relatively low tidal range and low tidal velocities. The potential for tidal stream energy in The Netherlands is dependent on the currents velocities. Therefore, geographical areas in The Netherlands where the water flow goes through a smaller area, for example estuaries or islands, have a higher potential for beneficial currents velocities.

Along the Dutch coast there are a variety of factors that can influence the possibility of using the area for the tidal stream farm, such as marine traffic, military activities and environmentally protected areas. Furthermore, land availability for the tidal stream energy facilities needs to be investigated as well, which can be done by looking at the destination plans applicable to the different areas. Other important parameters are technological and economic constraints, like water depth and distance to land facilities. Meaning that the entire economic zone of The Netherlands can be reduced by factoring in the restricted areas.

The most suitable location for a tidal farm in The Netherlands needs to be identified by determining the restriction criteria and weighted criteria. First, the restrictions of the spatial layout need to be determined, after which the weights of the different criteria can be determined. The restriction criteria are all criteria that would make it impossible or prohibited to build offshore constructions, therefore reducing the spatial layout. The weighted criteria are criteria that can be graded, and therefore indicate the suitability of a certain location.

7.3. Restriction criteria

First, the restriction criteria are discussed, which are also summarised in Table 7.1. The first restriction is set by the boundaries of the exclusive economic zone of The Netherlands, as this boundary surrounds the area in which the Dutch government has sovereignty. The second restriction relates to the size of the tidal turbine. Because the size of the tidal turbine is dependent on the resources available, such as the depth at a certain location, the size of the optimal turbine will be different per location. Hence, an estimation of the turbine size is made from the information following the resource assessment. It is argued that the average depth velocity is around the 0.5 m/s,[2] indicating an optimal turbine size between the 3 and 8 meters. This in turn means a minimum water dept of 10 meters is required. [3]

With the information about the usage of the different regions in the EEZ of The Netherlands, the restriction of the spatial layout can be analysed. Such restrictions could include technological, environmental or other maritime restrictions. Technological limitations can influence the productivity of the turbines, the energy output and determine the lifetime of the turbine. Water depth, remoteness and resource potential are considered technological limitations.[4]

Military areas, which are used for military exercises or for the destruction of explosive devices, are also considered hard restrictions. Areas near the location of underwater cables and pipes are also not suitable for the placement of tidal stream turbines, because of the risk that the construction and placement of the tidal stream farm damages these structures. Areas where sand extraction takes place are also restricted, as the bottom of these areas is already claimed.

---

[2] An average velocity can be used, as the model is a 2D model so that there is no difference made within the vertical column.

[3] With the turbines having a maximum size of 8 meters, a minimum dept of 10 meters is necessary so as to ensure the turbines can remain safely under water.

[4] Presently, only larger tidal turbines are constructed, with a diameter of around 18 to 20 meters. The technological feasibility of designing and building a significantly smaller turbine of around 3 to 8 meters is not further assessed.

Table 7.1: Restriction criteria, [85, 25, 38, 113, 6, 14]

Type	Constraint	Description	Data	Restricted threshold
Techno-economics	Water depth	The tidal turbine size is between the 3 and 7 meters, so a minimum low low spring tide of 10 meters is required for ships to be able to sail above the turbine the water depth must be 15 meters	GEBCO	≤ 10 m
Environmental	Protected areas	Area that are reserved for recreation or conservation of its nature and ecosystem	Natura 2000	Full
Marine	Military excercise	Areas that are used for military training	NoordzeeLoket	Full
	Marine traffic	Areas of high density ship traffic or commercial routes	EMODnet	≤ 10 km
	Underwater lines cables	Electric cables, gas/oil pipes, communication lines	NoordzeeLoket	≤ 0.5 km
	Oil - and gasfields	Underwater marine areas for oil and gas mining	NoordzeeLoket	Full
	Sand Mining	Underwater marine areas for sand extraction	NoordzeeLoket	Full
	Exclusive economic zone	The area where The Netherlands is allowed to build offshore	NoordzeeLoket	Full

Figure 7.3 visualises the data from the Noordzeeloket, which is a destination plan (bestemmingsplan) for the Dutch part of the North Sea. The spatial layout of the Dutch coastal area has been determined by the Noordzeeloket for the years 2022 till 2027 [63]. In the document, no specific area has been allocated for building tidal stream farms, as this is a relatively new way of generating energy. In the document however, all spatial restrictions for the Dutch coastal areas that have been considered are described. With this information about the restricted areas and the bathymetry data of the coastal area, it is possible to remove the none viable areas from the spatial layout, to reduce the areas that will be investigated in the AHP phase. Therefore, Figure 7.3, Figure 7.4a and Figure 7.4b provide a clear overview of the restricted, partially restricted and non-restricted areas. In Figure 7.4b, the red areas show the restricted areas of the Dutch coast and the (partially) green areas show the remaining possible suitable locations. The figure shows that most areas are already declared unsuitable at this point.

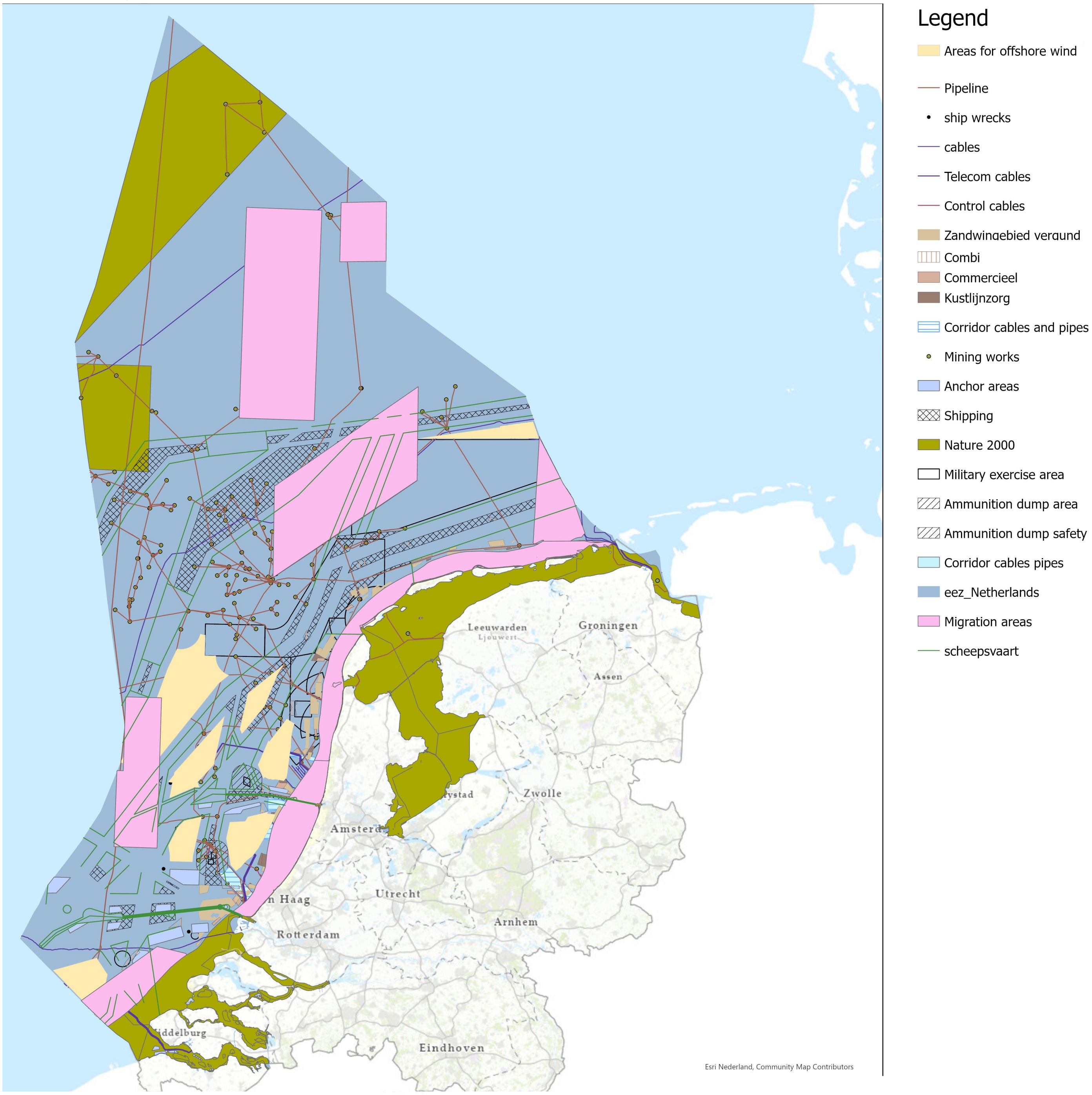

Esri Nederland, Community Map Contributors

Figure 7.3: Usage per region in the EEZ of The Netherlands

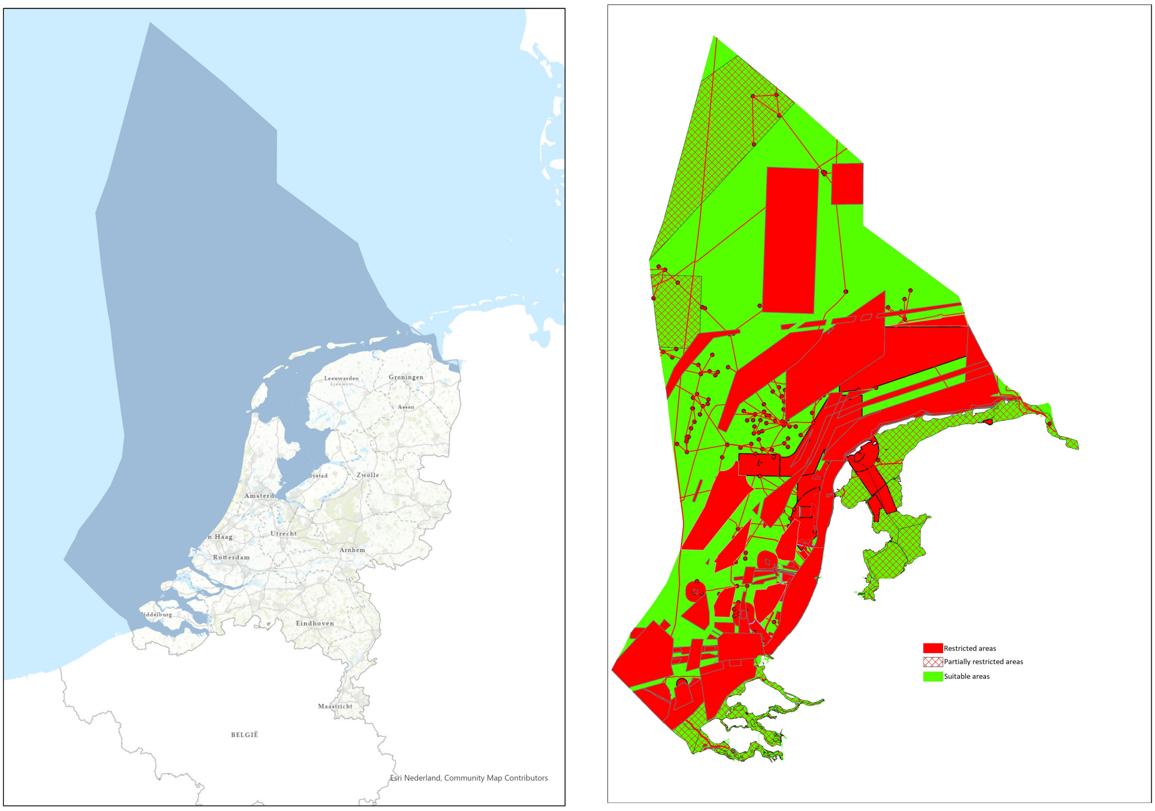

Esri Nederland, Community Map Contributors

(a) Offshore Exclusive Economic Zone (EEZ) of The Netherlands [63]

(b) The restricted areas of The Netherlands, with red the restricted areas are noted

Figure 7.4: The EEZ and restricted areas of The Netherlands

7.4. Weighted criteria

This leaves open the question what areas remain suitable. Using AHP, it is possible to determine the best location among the remaining locations, which is done by evaluating different criteria regarding the placement of the tidal stream turbine and subsequently determining the weight of these criteria. Table 7.2 shows the definitions of these criteria and explains what kind of data is required to determine the score for the different locations. The four main criteria are met ocean, logistics, marine environment and politics.

Table 7.2: Weighted criteria used for the MCDM

Type	Constraint	Description	Data	Restricted threshold
Met ocean (C1)	Tidal range (C11)	Areas were the current velocity is higher, are more suitable	Hindcast	Maximize
	Capacity factor (C12)	Depending on the cut-in and cut-out speed the amount of time the turbine can operate	Hindcast	Maximize
	Water depth (C13)	The water depth influences the installation cost and determine where the turbine can be placed	GEBCO	Maximize
Logistic (C2)	Distance from electrical grid (C21)	Shorter distance to existing transmission time or power station will reduce costs	NoordzeeLoket/Tenet	Minimize
	Distance from ports (C22)	Shorter distance from port will reduce the O & M costs	NoordzeeLoket	Minimize
Marine environment (C3)	Distance from protected areas (C31)	Higher distance away from protected areas will reduce environmental impact	NoordzeeLoket	Minimize
	Distance from maritime routes (C32)	Higher distance away from maritime traffic will reduce the risk of collision	NoordzeeLoket	Minimize
Politics (C4)	Area for the tidal farm (C41)	The total area size available for the tidal stream farm	GIS Data	Maximize
	Proximity to industrial cluster (C42)	Closer to areas with electricity demand can increase the need for the tidal stream farm	GIS Data	Minimize

After identifying these criteria, the next step is to quantify them, after which they are analysed with the use of ArcGis. Such an analysis can be performed with the use of the BUFFER tool, which makes it possible to create a study area in which each criterion is weighted individually. From this analysis it is possible to use GIS data to determine the ranking of the different locations. Table 7.3 and Table 7.4 present the grades awarded to each criteria. The criteria are divided into main criteria and sub-criteria. In subsection 7.4.1 to subsection 7.4.9 give a more detailed explanation of these different criteria.

Table 7.3: Criteria and value scores used in the MCDM, part 1

AHP criteria	linear	linear	non-linear	inverse linear	inverse linear
Value score	Tidal current(m/s)	Capacity factor(%)	Water depth(m)	Distance from electrical grid (km)	Distance from port (km)
1	<0.2	<70	<8.0	>25.000	>5.5
2	0.25-0.3	70-72.5	8.0-10.0	22.500-25.000	5.0-5.5
3	0.3-0.35	72.5-75	10.0-12.0	20.000-22.500	4.5-5.0
4	0.35-0.4	75-77.5	12.0-14.0	17.500-20.000	4.0-4.5
5	0.4-0.45	77.5-80	14.0-16.0	15.000-17.500	3.5-4.0
6	0.45-0.5	80-82.5	16.0-18.0	12.500-15.000	3.0-3.5
7	0.5-0.55	82.5-85	>22.0	10.000-12.500	2.5-3.0
8	0.55-0.6	85-87.5	20.0-22.0	7.500-10.000	2.0-2.5
9	0.6-0.65	87.5-90	18.0-20.0	5.000-7.500	1.5-2.0
10	>0.65	>90	16.0-18.0	<5.000	<1.5

Table 7.4: Criteria and value scores used in the MCDM, part 2

AHP criteria and score	Linear	Linear	inverse linear	linear
Value score	Distance from shipping (m)	Distance from protected areas (km)	Distance from industrial hub (km)	Area size suitable for tidal turbines (km^2)
1	<4.0	<5.0	>50.000	<5.0
2	4.0-8.0	5.0-10.0	45.000-50.000	5.0-7.5
3	8.0-12.0	10.0-15.0	40.000-45.000	7.5-10.0
4	12.0-16.0	15.0-20.0	35.000-40.000	10.0-12.5
5	16.0-20.0	20.0-25.0	30.000-35.000	12.5-15.0
6	20.0-24.0	25.0-30.0	25.000-30.000	15.0-17.5
7	24.0-28.0	30.0-35.0	20.000-25.000	17.5-20.0
8	28.0-32.0	35.0-40.0	15.000-20.000	20.0-22.5
9	32.0-36.0	40.0-45.0	10.000-15.000	22.5-25.0
10	>36.0	>45	<10.000	>25.0

7.4.1. Tidal current

The average current velocity in a specified area is a key criterion which influences the economic performance of a tidal turbine. In papers which investigate wind energy potential, which is a neighbouring subject, current velocity is argued to be one of the most important criteria [85, 59, 38, 25]. The average current velocities can be computed for the different locations when the hindcast is in a steady state, for which the formula is given in the following Equation 7.1:

$$U_{average} = \frac{1}{N}\sum_{i=1}^{N} U_i \tag{7.1}$$

In this formula U is the velocity and N is the number of time steps. It also possible to determine the potential kinetic powerW/m^2 of the different locations for a hindcast period of a year. This is done by using the Equation 7.2:

$$P_{average} = \frac{1}{N}\sum_{i=1}^{N} \frac{1}{2}\rho U_i^3 \tag{7.2}$$

With this formula it is possible to determine the potential kinetic power at different locations and hence make a good estimation of the value per location. Using TELEMAC and Delft 3D, the current velocity along the Dutch coast is determined. The analysis of both these models has been explained in chapter 5. From this data the average current velocity, potential power and the tidal range is determined.

In chapter 5 the average current velocity was determined, and it was shown that velocities below 0.2 m/s and above 0.9 m/s rarely occur. Because the size of the turbine will be substantially smaller that the currently available tidal turbines, the cut-in and cut-out speed of our turbine will also have dissimilar values. If the current velocity is below 0.2 m/s, the current velocity is considered too small for the farm to be economically feasible. The ideal average current velocity needs to be around 0.6 m/s, meaning that the lower current velocities score a value between the 1-3, average current velocities between the 5-7 and high current velocities score around the 8-9. With current speeds above 1.2 m/s, this criteria is awarded a 10.

7.4.2. Capacity factor

The capacity factor is a criterion that relates to the economic performance of the turbine [85, 25]. The capacity factor can be determined using the power curves for the turbine. The capacity factor indicates the percentage of time the turbine is operating at full power. Equation 7.3 shows the formula for calculating the capacity factor:

$$C_f = \frac{T_{equivalent}}{T_{actual}} = \frac{T_{equivalent}}{\Delta T * MW_{installed}} \tag{7.3}$$

In this formula T_{actual} is the production that is achieved by coupling the turbine information and the resource data, while the $T_{equivalent}$ is the equivalent production to achieve the same production if the turbine is constantly at full power for a given time period ΔT year. Due to the fact that the exact power production of a tidal farm is not yet known, the capacity factor cannot be calculated at this point. But what can be determined is the percentage of time a certain location is within the cut-in speed. For the MCDM, the capacity factor has the definition of the percentage of time the current velocities are within the cut-in and cut-out velocity of the turbine. The more time the velocity is within the operating window of the turbine, the higher the capacity factor is.

From the data a histogram is created which shows the number of time steps that are within a velocity field and with this the frequency of different velocity ranges can be determined. Here, the higher the capacity factor, the more electricity can be produced. Table 7.3 provides the ranges and subsequent scores for this criteria. [5]

7.4.3. Water depth

Water depth is a criterium that consists of multiple factors. Firstly, the water must have a minimum water depth for a certain tidal turbine to be placed. Because of the possible size of the turbine, the minimal depth at low tides must be above the 10 meters, as was discussed in section 7.4. However, it is not necessarily the case that such depths are deep enough so that ships can sail over these turbines. That being said, the size of the turbines is relatively small, so that it could be possible to place turbines in certain areas where there is marine traffic. This is due to the average draft of a ship which is around the 8.3 meters [17], while the turbine sizes will be set between 3 and 8 meters. Secondly, the costs of the foundation of the turbine increases when the turbine is placed deeper. Considering these factors, it is evident that the scoring of this criteria is non-linear.

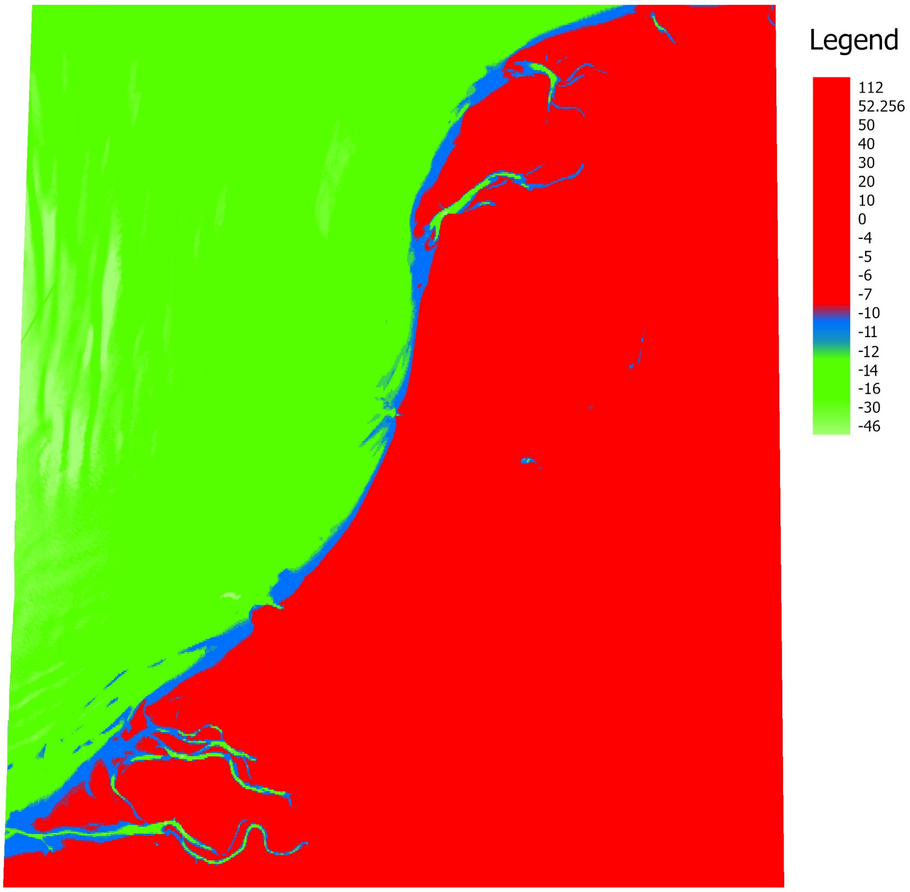

Figure 7.5: The elevation and water depth along The Netherlands coastlines

This Figure 7.5 shows that both the blue and green areas are suitable for the placement of the turbines. Moreover, for the green area it is also possible to place the turbine under a marine route because the water is deep enough. Subsequently, the scores are determined by the possibility of a ship sailing over the turbine on the one hand, and the higher costs of the foundation on the other hand. A score of 1-3 is given for water depths between 10 and 12 meters, as ships cannot sail over such farms. For a water depth which is deeper than 20 meters, a score between 4-5 is assigned. The optimal water depth is between 16 and 18 meters and will be awarded a score between 7-10. Table 7.3 provides an overview of these values.

---

[5] In chapter 5 the histogram figure of the different locations is shown.

7.4.4. Distance from the electrical grid

The distance form electrical lines or connection points influences the Capital Expenditure (CAPEX) of the project. The mean driver for this is the high price of transmission cables [85, 65, 50, 106]. The electrical network of The Netherlands consists of underground and above ground transmission cables. In ArcGIS, a feature layer consisting of the high voltage network of Tennet can be seen [100]. The current available tidal turbines have a voltage output of around 4.16 kV [5]. Because the size of the turbine that will be used is much smaller, the voltage the turbine generates will also be smaller. A medium voltage network is required for the transportation of the energy, meaning that the transmission line required needs to be able to transport 110 kV.

Multiple studies focus on the importance of the distance to the electrical grid [85, 65]. Because the transmission lines will be placed below sea level a minimum distance is included, because the turbine can interfere with or damage the transmission line. The score for this criteria decreases when the distance is increasing. Because of the study area and the spatial dimensions the areas within a range of 5 kilometers within an existing and suitable electrical grid will get the highest score of 10. Areas with a distance that exceeds the 25 kilometers get a score of 1., due to the higher costs of the increased cable length. In the appendix the scores of all locations are presented.

7.4.5. Distance from port

The distance from a port strongly influences the costs of installation, operation and maintenance of the tidal farm. A location closer to a port will result in a lower CAPEX and Operational Expenditure (OPEX). Moreover, the ports included in this analysis feature infrastructures that are able to support the installation, operation and maintenance of a tidal farm. Due to the small size of the turbines, small ports with shallow water depths can also provide a suitable location. In the spatial analysis small ports are included, for which the absolute distance from the location to a port will be limited.

The evaluation of this criterium is achieved using the port maps created in GIS, after which the BUFFER tool was used to determine the scores per suitable location. Figure 7.6 presents the suitable ports along the Dutch coast. Consequently, the most preferred areas for the tidal farm are those with the smallest distance to the ports. According to Murphy J. et al.[65] a minimum required port draft for installation of offshore renewable energy projects is equal to 10–15 meters. After determining the restricted area, the port with the smallest distance to the remaining areas remained. For evaluating eligible locations in terms of distance to a port, the value score for distance less than 2.5 kilometers are assigned the highest score of 10. Distances exceeding 10 kilometers are given the lowest score of 1. It is important to note that the weight of this criterium compared to the other criteria is smaller, because the absolute distance from a port for all locations is relatively small. Figure F.6 shows a layer created in ArcGIS that contains the distance of each location to the nearest port.

7.4.6. Distance from protected areas (NATURA2000, UNESCO)

Environmental restrictions also need to be taken into account. These restrictions concern the environmental conditions and ecosystems of different locations. Protected areas include amongst others the national parks, UNESCO areas, areas for migrating sea life, bird reserves. NATURA2000 indicates protected regions, in which turbines are not allowed to be built as they could damage the ecosystem. Furthermore, there are also UNESCO protected areas like the Wadden sea. In this step of the MCDM, the NATURA2000 areas with regards to wildlife protection and breeding areas are not as a whole excluded from potential farm sites, because such exclusion would significantly reduce the number of potential areas for the tidal farm.[6] In addition, because the tidal turbine is placed completely underwater, while no extensive research on the effect of tidal stream turbines on flora and fauna exists yet, [7] these areas will be used as a weighted criteria [61, 20].

Although the impact on wild life should never be underestimated, it is the hope that the impact of a tidal farm on the wild life would be limited because of the configuration, rotation speed and size of the turbines. When looking at conventional hydro power turbines, the tidal stream turbines are believed to be less harmful because they have unenclosed turbines meaning that marine life cannot get stuck. Furthermore, the operating speed of tidal turbines is much lower than of conventional hydro power turbines so the impact and change of contact is smaller. Moreover, slender blades are used and so the swept area of the turbine is smaller than that of conventional hydro power turbines.

---

[6] Later in the analysis, locations near these areas will receive lower grades in the quantification step.

[7] Tidal energy is mentioned in the Noordzeeloket, but it is stated that because of the current state of the technology for tidal energy no specific area has been designated. Meaning that no investigation into the site selection method or into the impact of tidal energy has been concluded yet.

Figure 7.6: Ports suitable for offshore renewable projects

Therefore, marine life is less likely to be hit by the turbine [61, 20, 104]. It is even possible that a tidal farm could influence the wild life population in a positive manner. Around the tidal turbine a no-phishing zone will need to be implemented, meaning that marine life can seek shelter in these areas. The foundation and transmission lines can also shelter marine life and be a suitable structure for the creation of reefs. However, it is still important that during construction and maintenance the impact on the ecosystem is limited as much as possible. The noise during construction could for example influence breeding- and migration patterns of the marine life. It is important to carefully determine the timing of the construction of the tidal farm in order to reduce the impact.

Because of these possible mitigations and the turbine configuration, it is assumed to be possible to place the turbines in certain areas that are now considered protected areas as far as offshore wind farms are concerned. Unsurprisingly however, the locations that are the furthest away from protected areas will be rewarded with the highest score. Table 7.4 presents the distribution of the scores.

7.4.7. Distance from maritime routes

As explained in the previous subsection 7.4.3, it is possible under certain ship drafts and water depths for the ship to sail over the turbine [61, 20, 23]. However, influences the power extraction from the turbine, due to the fact that the flow will be influenced by the ships.[8] Moreover, parts from the passing ships could become detached from the ship and potentially damage the tidal farm. In areas with a large number of shipping routes or heavily used routes, the placing of the tidal farm is also more complicated. Lastly, there is also

---

[8] This influence will not be investigated, because in order to give a good estimation of the influence of the ship, a 3D model must be created.

the possibility that the placing of the tidal farm influences the shipping route all together. For this reason, proximity to maritime routes is considered to be disadvantageous.

In other words, the further away from the shipping routes, the better [20] [9]. For this criterium, maritime routes are considered to be areas with intense maritime freight and passenger traffic. Recreational traffic is not taken into account, because the size and draft of these vessels is relatively small compared to freight vessels and large passenger vessels.

7.4.8. Area size suitable for tidal turbines

The last criterium relates to the size of the area available for the placement of the tidal farm. The area that is available for the tidal farm has an important impact on the tidal farm capacity and the potential economics of the project [25, 6].

Multiple array configurations can be placed in the given area. Furthermore, this criterium examines whether there is enough space for the ideal configuration, also in terms of staggered or non-staggered and distance between the turbines. For assigning the value to this criterion, a larger area is awarded a higher grade. The scores for this criterium are presented in Table 7.4.

7.4.9. Distance from industrial hubs

Industrial hubs are considered to be industrial areas that have a substantial need for energy. This is an important criterion that relates to social and political acceptance of the tidal farm. If the project can help with the energy transition or reduce carbon emission, the government and people will be more likely to accept the project and provide the required permits.

In The Netherlands there are six areas with a strong concentration of heavy industry, namely Vlissingen, the Port of Rotterdam, the Port of Amsterdam, Eemshaven, Limburg and Emmen. Clearly, not all of these areas have a close proximity to the possible locations for the tidal farm. Logically, the score assigned for this criteria is dependent on the distance from suitable industrial hubs. This quantification does not take into account the energy consumption of these hubs, which is less relevant as the amount of energy generated by a tidal farm could be used in full by all these industrial hubs [15, 59, 105, 25]. A score of 1 is assigned to the location that is the farthest away and a score of 10 is assigned to the location that is the closest to an industrial hub.

7.5. The AHP model

The literature used for identifying the relevant criteria and their subsequent weights is presented in Table 7.5. By using different sources for the determination of the weights, it is attempted to reduce the subjectiveness of the weights assigned.

Table 7.5: Literature review of different criteria weights

Criteria	Literature
Met ocean	[85, 38, 25, 14, 106, 105, 25, 113, 6, 36, 112, 50]
Logistics	[85, 25, 106, 105, 25, 36, 50]
Marine environment	[85, 38, 25, 106, 105, 25, 113, 112, 50, 36]
Politics	[25, 105, 25, 113, 6, 36, 50]

7.5.1. The ratio of the AHP model

With the literature found it is possible to create the AHP model and determine the hierarchy of the different criteria. The AHP model was first used by Saaty [91]. to decompose complex problems consisting of multiple variables by using a hierarchy system. The hierarchy system consists of multiple layers, with at the bottom of the hierarchy the criteria and alternative locations and at the top the final goal of the AHP model. At each level a pair-wise comparison of the different elements in the layer is performed. This comparison is executed with regards to the criteria divided at the prior level. Furthermore the AHP model is used because it considers both tangible and intangible criteria, making it also suitable for more complex and undefined problems.

---

[9] subsection 7.4.3 discusses that if it is impossible to avoid shipping routes, enough clearance should be provided between the tip of the rotor blade and the draft of the vessel at the low astronomical tided [23, 61]

In the AHP model each of the criteria is first paired against all other criteria to determine the most important criterium. The results of this comparison are compiled in a matrix. The dimensions of the matrix are determined by the amount of criteria that are used in the AHP model. In the AHP model a 9 point scale is used to quantify the different options. These numbers are 1, 3, 5, 7, 9 and correspond to: equal direct influence, weak direct influence, moderate direct influence, strong direct influence and very strong direct influence. The number 2,4, 6 and 8 are used as intermediate numbers, see Table 7.6.

Table 7.6: Saaty's scale for pairwise comparison

Intensity of importance on a absolute scale	Explanation	
1	Equal importance	Element **x** and **y** contribute equally to the objective
3	Moderate importance of one over another	Experience and judgment strongly favor **x** over **y**
5	Essential or strong importance	Experience and judgement strongly favor **x** over **y**
7	Very strong importance	Element **x** is favored very strongly over **y** and its dominance demonstrated in practice
9	Extreme importance	The evidence favoring element **x** over **y** is of the highest possible order of affirmation
2, 4, 6, 8	Intermediate values between two adjacent judgments	When compromise is needed
Reciprocals	If activity **x** has one of the above numbers assigned to it when compared with **y**. Then **y** has the reciprocal value when compared with **x**	
Rationals	Ratios arising from the scale	If consistency were to be forced by obtaining **n** numerical values to span matrix

After the weights of the criteria are determined, a pairwise comparison between the different locations can be conducted. From this, the relative importance of the criteria and of the different locations are determined. The AHP pairwise comparison is divided into 4 criteria which are decomposed out of 9 sub criteria. The locations that will be investigated are determined after the restriction criteria are subtracted from the entire area and from this smaller area the most suitable locations are taken into account.

7.5.2. The formulation of the AHP model

The AHP model of Saaty has been simplified over the years [91, 90]. Matrix A 7.4 shows the preference between the different criteria that determine the selection of the different locations. The matrix is generated for n criteria, where a_{ij} is the importance of criteria i over criteria j. This also means that the $a_j i$ is the inverse of element a_{ij}. From Matrix 7.4 the relative weight of the criteria can be determined.

The values in each column of matrix A are summed and a normalised matrix is constructed. The normalized matrix is made by dividing each element in the matrix by the sum of the columns of that matrix. The priority vector W can be found by calculating the average of the elements in each row of the normalised matrix. The priority vector shows the hierarchy ranking of the different criteria and the level of contribution of that criteria to the end goal. These calculations are done for each criteria:

$$A = \begin{bmatrix} a^{11} & a^{12} & ... & a^{1n} \\ a^{21} & a^{22} & ... & a^{2n} \\ ... & ... & ... & ... \\ ... & ... & ... & ... \\ a^{n1} & a^{n2} & ... & a^{nn} \end{bmatrix} \tag{7.4}$$

$$\begin{aligned} &[A_{ij}],\ where\ i,j = 1,2,...,n \\ &A_{ij} = 1\ for\ 1 = j \\ &A_{ij} = \frac{1}{A_{ji}}\ for\ i \neq j \end{aligned} \tag{7.5}$$

An important restriction that comes with the AHP model is that a reasonable level of inconsistency regarding the criteria is to be expected. The inconsistency of the matrix can be determined with the use of the Saaty Consistency index (CI) and the consistency ratio (CR). The CI can be calculated using Equation 7.6:

$$CI = \frac{(\lambda_{max} - n)}{n-1} \tag{7.6}$$

In this equation λ is the maximal eigenvalue [34, 90], n is the number of criteria. The eigenvalue of the matrix is calculated with the use of Equation 7.7:

$$\lambda_{max} = \frac{1}{p}\sum_{i=1}^{p}\frac{A_{ij}xW_i}{W_i} \tag{7.7}$$

By solving the equations above it is possible to calculate the CR. This can be done with Equation 7.8:

$$CR = \frac{CI}{RI} = \frac{(\lambda_{max} - n)}{RI(n-1)} * 100\% \tag{7.8}$$

In this equation RI is the random index value that depends on the size of the matrix, see Table 7.7.

Table 7.7: Random index based on matrix dimensions

n	1	2	3	4	5	6	7	8	9
CR	0	0	0.52	0.89	1.11	1.25	1.35	1.40	1.45

For a matrix to be considered good, the CR must be below a certain threshold. In Table 7.8 these thresholds are shown. This AHP model uses 9 criteria, meaning that the CR must be below 0.10 to be within the requirement of consistency. If the matrix has a higher CR, the matrix must be modified. This modification is based on the maximum deviation between the weights used in the matrix.

Table 7.8: Consistency ratio threshold based on matrix dimensions

n	3	4	n ≥ 5
CR	0.05	0.08	≤ 0.1

If the matrix is within the required CR range, the preference percentage can be determined. The preference percentage is able to determine the final ranking of the different alternatives. The formula to determine the preference percentage is given in Equation 7.9:

$$PP_p = \sum_{i=1}^{n} W_i x W_{pi}, \quad where \;\; p = 1, ..., m \tag{7.9}$$

After the AHP model has been completed for the different criteria, a similar AHP model is conducted to determine the preference percentage of the different locations.

7.6. Results

In the following section the results of the GIS based analysis are shown and discussed. This analysis is divided into two phases. The first phase is to subtract the restricted areas from the total study area. The second phase is to examine the results of the AHP model and determine whether the CR is below 0.1.

7.6.1. Restricted areas in The Netherlands

The areas that are restricted for the placement of tidal farms are found by using the restriction criteria in ArcGIS. In Figure 7.7 all the restricted criteria are presented. The red colour represents the areas that are restricted and the green colour represents the areas that are suitable for placing tidal turbines.[10]

Now the restricted criteria results are discussed, it is possible to find the locations with the highest potential for tidal farms along the Dutch coast. This can be done by combining the restriction criteria with the

---

[10] Waters with a depth starting at 16 meters are suitable for building tidal stream farms. This depth is used to ensure that most ships can sail over the turbines.

depth averaged velocity along the Dutch coast. Figure 7.8a below presents the average current velocity. The figure shows that the best locations for the placement of tidal stream turbines are The Westerschelde estuary (L1), The Oosterschelde estuary south (L2), The Oosterschelde estuary north (L3), the opening between Texel and Den Helder (L4) and the opening between Vlieland and Terschelling (L5). The locations are shown in Figure 7.8b

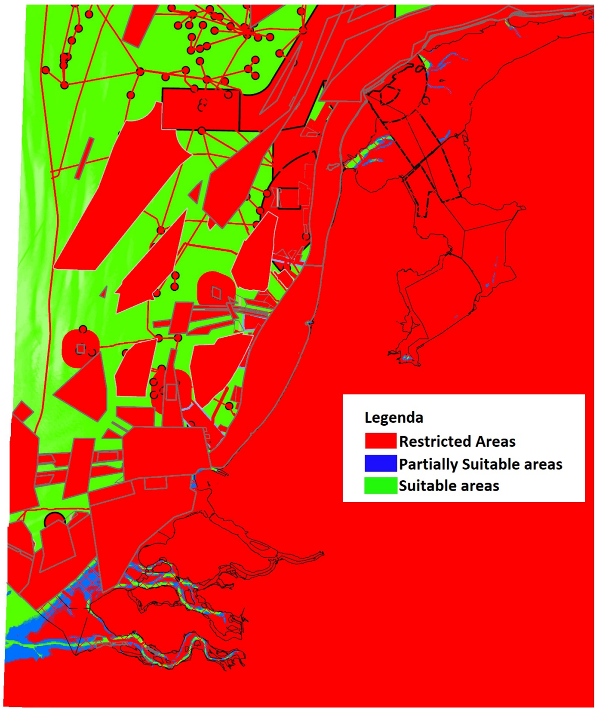

Figure 7.7: Restricted area including water depth

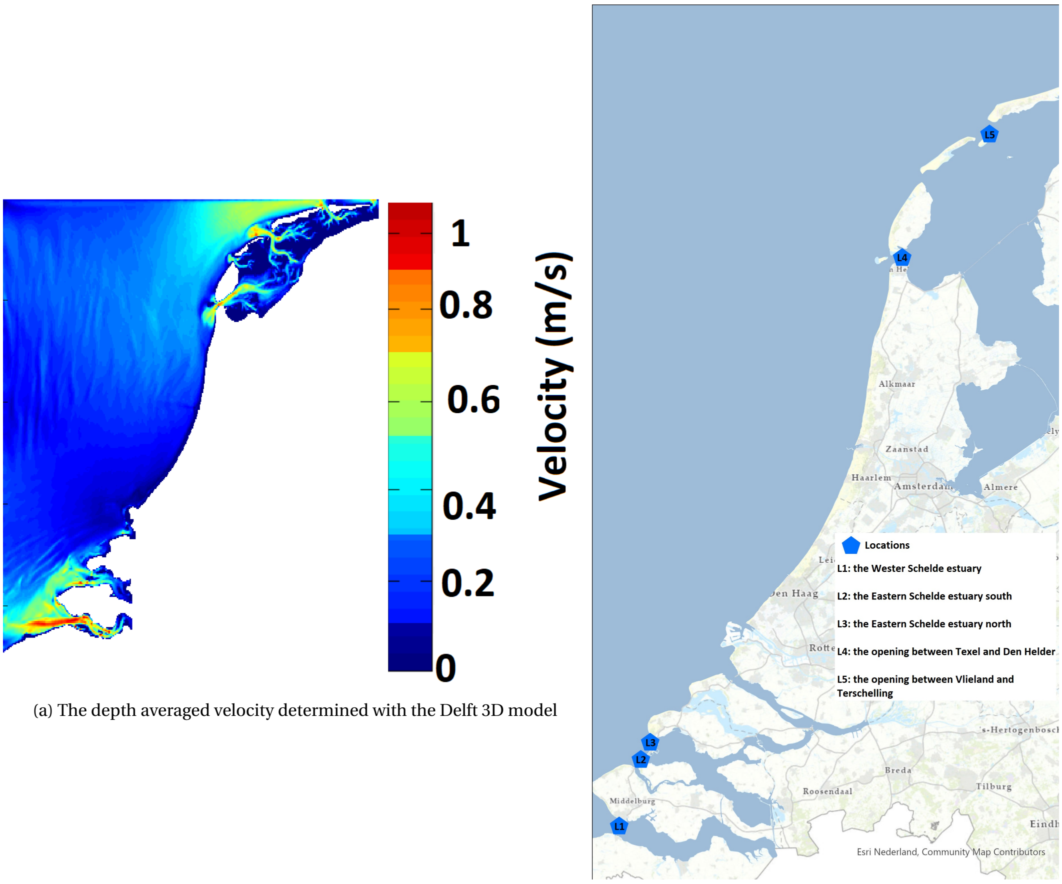

(a) The depth averaged velocity determined with the Delft 3D model

(b) Suitable location for tidal energy

Figure 7.8: Most suitable locations and the depth averaged velocity from Delft 3D

7.6.2. Weighting the criteria

Table 7.9 presents the pairwise comparison between the criteria. In this analysis the priority vectors of the different criteria are determined. With the matrix, the CR can be calculated. Table 7.10 shows that the CR is below 0.1, meaning that the consistency of the matrix passes the requirement. Furthermore, the most important criteria are the tidal current and the capacity factor.

Table 7.9: Pairwise comparison of the criteria

Criteria	C11	C12	C13	C21	C22	C31	C32	C41	C42	priority vector
C11	1.00	1.00	5.00	5.00	9.00	7.00	3.00	5.00	9.00	0.27
C12	1.00	1.00	5.00	5.00	9.00	7.00	3.00	5.00	9.00	0.27
C13	0.33	0.33	1.00	3.00	5.00	7.00	5.00	3.00	5.00	0.15
C21	0.20	0.20	0.33	1.00	5.00	3.00	5.00	3.00	3.00	0.10
C22	0.11	0.11	0.14	0.20	1.00	0.33	0.20	0.20	1.00	0.02
C31	0.14	0.14	0.20	0.33	3.00	1.00	0.33	0.33	3.00	0.04
C32	0.33	0.33	0.20	0.20	5.00	3.00	1.00	1.00	3.00	0.07
C41	0.20	0.20	0.33	0.33	5.00	3.00	1.00	1.00	5.00	0.07
C42	0.11	0.11	0.20	0.33	1.00	0.33	0.33	0.20	1.00	0.02
CR	0.095									

Table 7.10: Priority vector of the different criteria

Criteria	Weight	Sub criteria	Weight
Met ocean (C1)	0.68	Tidal current (C11)	0.27
		Capacity factor (C12)	0.27
		Water depth (C13)	0.15
Logistics (C2)	0.12	Distance from electrical grid (C21)	0.1
		Distance from ports (C22)	0.02
Marine environment (C3)	0.11	Distance from protected areas (C31)	0.04
		Distance from maritime routes (C32)	0.07
Politics (C4)	0.09	Area of territory (C41)	0.07
		Proximity to industrial clusters (C42)	0.02
CR	0.095		

The preference percentage shows that these 2 criteria have the highest importance in support of the feasibility of the project. The least important criteria are the distance to ports and to industrial clusters. The weights of the different criteria are pictured in Figure 7.9. The AHP determined that the most important criteria is C1, the met ocean data, which is also the criteria that determines the power output of the tidal farm.

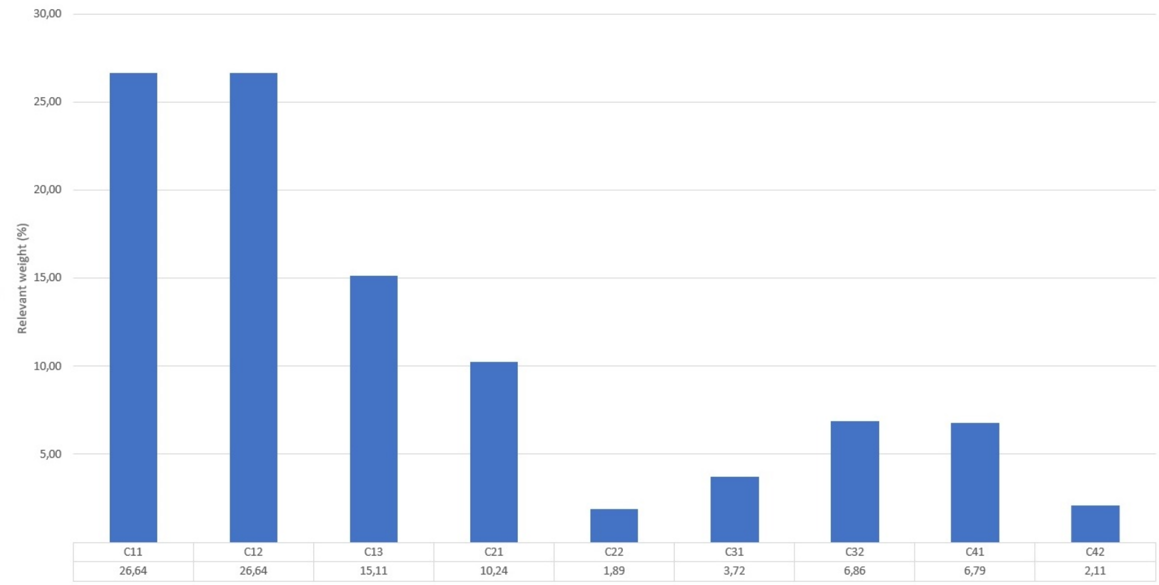

Figure 7.9: The relevant weight of the different criteria

7.6.3. Scoring the locations through MCDM

The five locations are evaluated and ranked by using the criteria described in Table 7.3 and Table 7.4. The method of evaluation used was described in section 7.5. The priority weight of the different locations in respect to the different criteria will be determined. The capacity factor and current velocity are determined with the use of chapter 5

In Figure 7.10a and Figure 7.10b the distance to both electrical networks can be seen. These figures show the scores of the criteria for each location. Appendix G presents the scores of these locations and the AHP model is constructed.

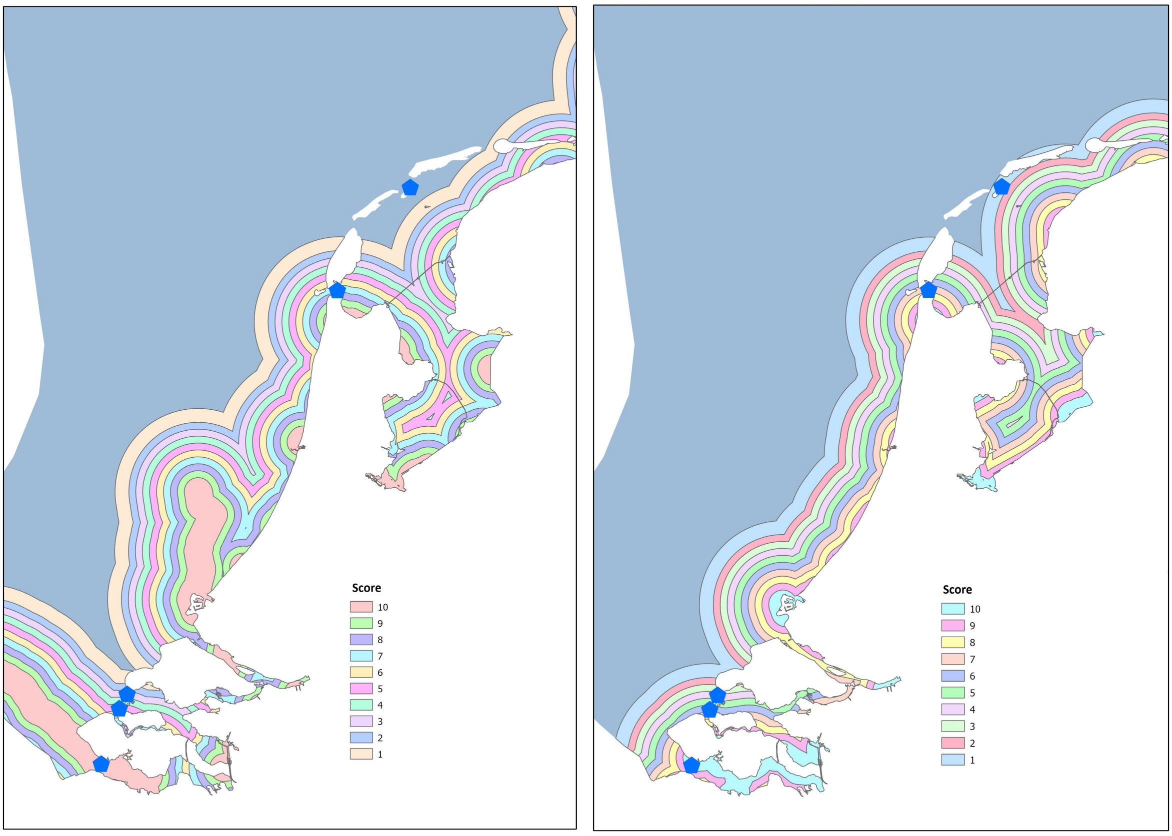

(a) C21: Distance to electric grid, high voltage cable above ground

(b) C21: Distance to electric grid, high voltage cable under ground

Figure 7.10: C21: Distance to electric grid, high voltage

Figure 7.11 shows the distance from specific locations to a port. It can be observed that each location has a port close by, resulting in relatively small weights. From Figure 7.11 the scores for the different locations can be determined. In Appendix GF the exact scores of these locations can be seen and the AHP model is constructed.

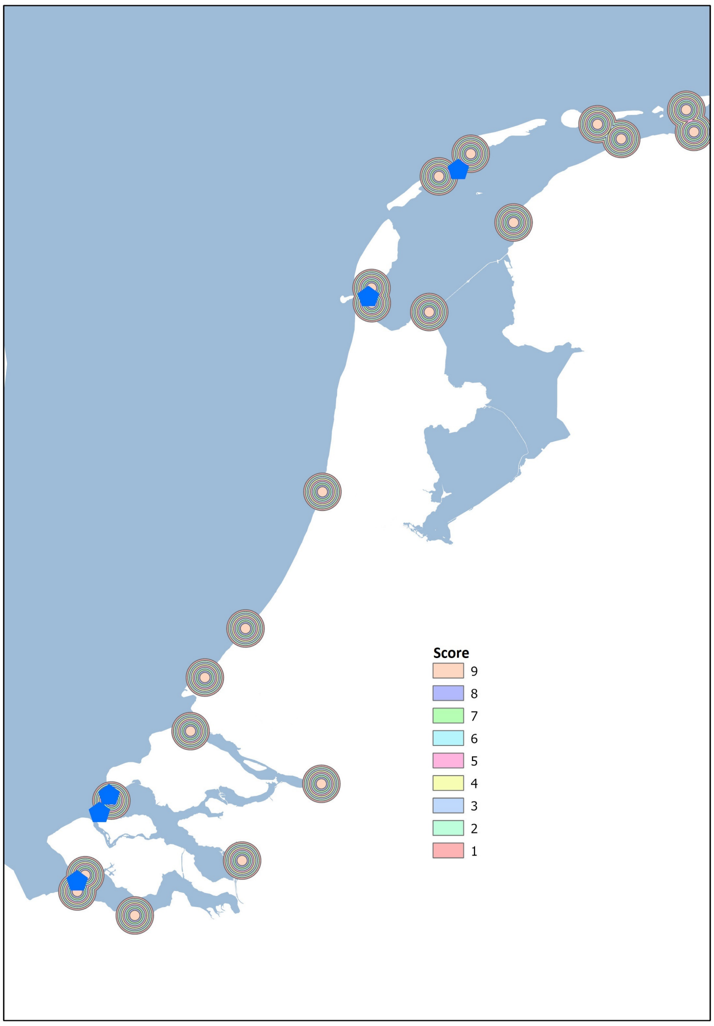

Figure 7.11: C22: Distance from suitable ports

In Figure 7.12 the distance to protected areas can be observed. As explained before, due to the limited environmental impact it is possible for the turbines to be placed inside of protected areas, but the further away from these areas the higher the score. The figure shows that for the two location around the Wadden sea the score is low, because the Wadden sea is a protected area. The Locations in Zeeland have a slightly higher score, due to the fact that the protected areas are further away. In Appendix G the exact scores of these locations can be seen and the AHP model is constructed for this criterium and locations.

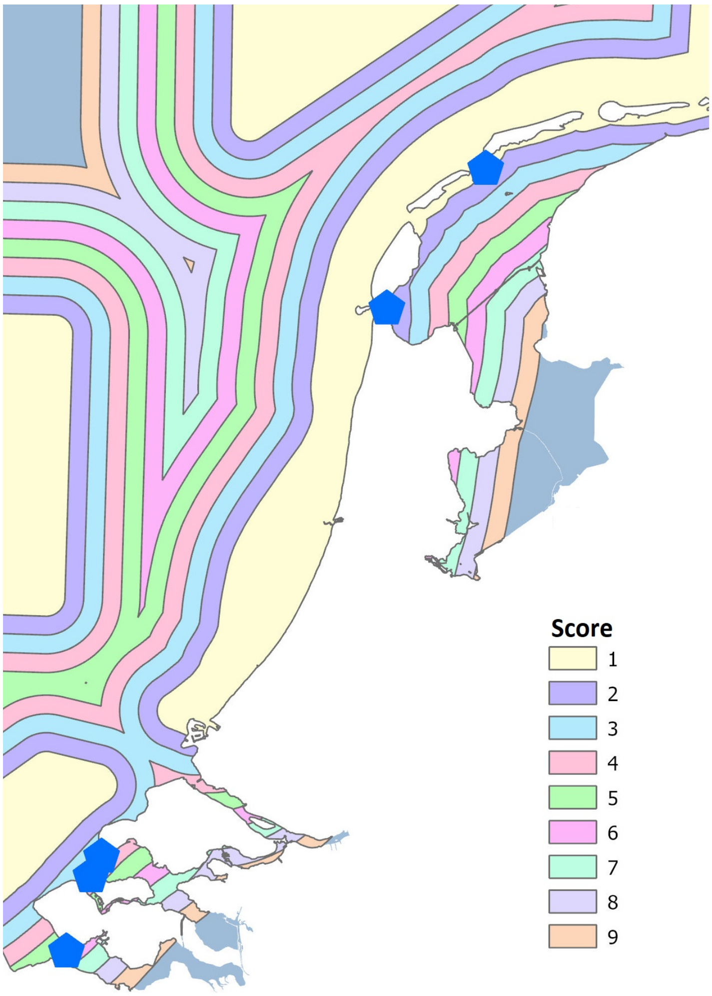

Figure 7.12: C31: Distance from environmental protected areas

Figure 7.13 shows the distance from the locations to the marine routes. The figure is cropped down to increase the visibility of the figure. Furthermore, the data that is cropped out is further away from the locations that will be considered. [11] Figure 7.13 shows that all locations are close to marine routes. This can also be seen in the assigned scores and AHP model in Appendix G.

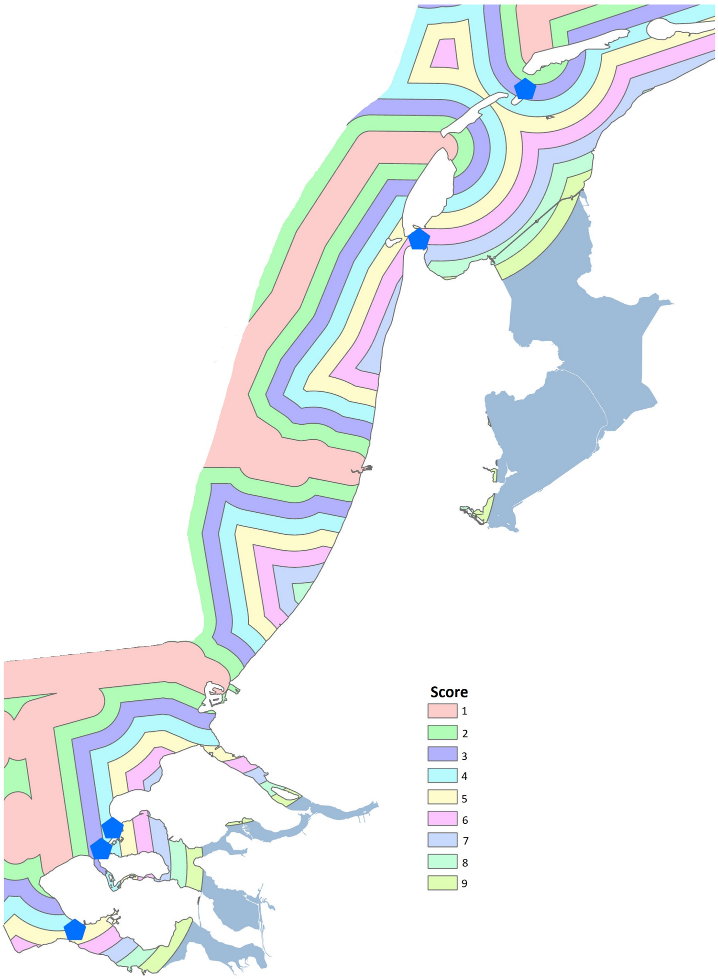

Figure 7.13: C32: Distance from marine shipping routes

Table 7.11 presents the turbine sizes available for the different locations. The size available is determined by the water depth and its consistency. If there is a large change in depth at these locations, the suitable area will reduce. Using ArcGIS, the area available at these locations is calculated. In Appendix G the AHP model for this criterium can be seen.

Table 7.11: C41: Area size suitable for tidal stream turbines

Area size suitable for tidal turbines	Size (km)	Value score
L1	16.24	6
L2	17.14	6
L3	14.04	5
L4	39.8	10
L5	15.36	6

---

[11] Showing this data does not increase the accuracy of the analysis.

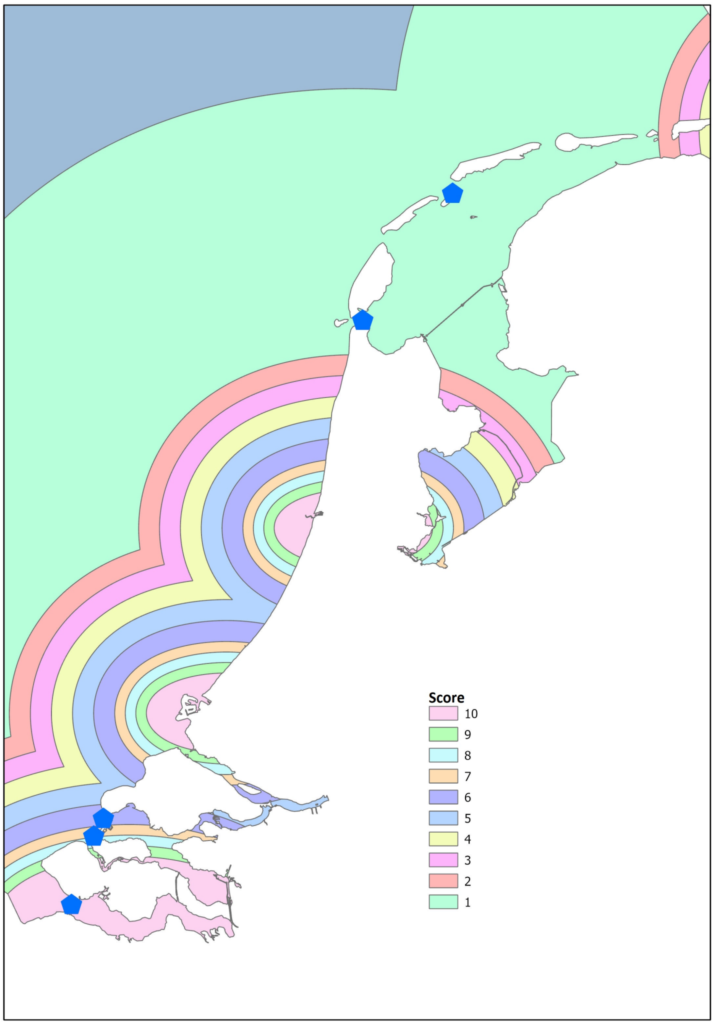

Figure 7.14: C42: Distance from industrial hub

Figure 7.14 shows the distance from the five identified locations to industrial hubs. The figure shows that most industrial hubs reside along the North Sea coastal area, namely around Rotterdam, Amsterdam and Zeeland. Therefore, the scores for the locations in Zeeland are relatively high. For the locations around the Wadden sea the closest industrial hub is Amsterdam, which is quite far away. Therefore, the score of these locations is low. Appendix G presents the scores and AHP model for this criterium.

7.6.4. Location selection

Using the above deducted scores, the AHP matrix for the different locations can be constructed. The CR scores of the matrix show that the inconsistency is within the required range, as all five CR matrix values are below the 0.1. Furthermore, the scores have a high accuracy, because the values of these scores are based on GIS data. In Figure 7.15 the scores of the different locations against the criteria are shown.

The figure shows that the most suitable location regarding energy resource (C11) is the Westerschelde, this is mainly due to the average tidal current at the third location: 0.58 m/s. In regards to the capacity factor (C12), the most suitable locations are Texel and Vlieland. At these locations the capacity factor is around 80%. Moreover, over time these locations have the lowest fluctuation in current velocity and have a high capacity factor.

As for the water depth (C13), all locations except L2 are suitable for placing the turbine. The most suitable locations in respect to the water depth are L3, L4 and L5, because the water depth at these locations is between 16 and 20 meters.

For the logistics (C2), there is a large variation between the different locations. When looking at the distance to a local grid it can be seen that L1 is very close to an existing grid compared to the other locations.

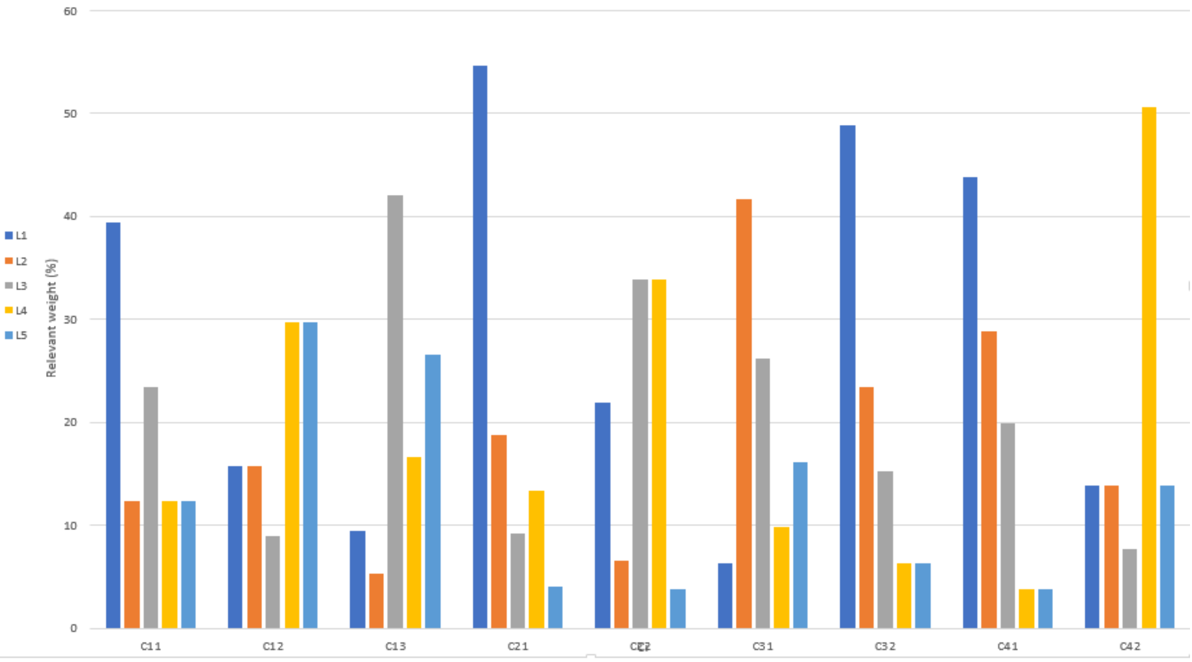

Figure 7.15: The relevant weights of the different locations with respect to the criteria

This can be explained by the fact that location L1 is the closest to an industrial area.

For the distance to a port it can be noticed that the best locations are L3 and L4. Because also relatively small ports are suitable for the installation of these tidal stream turbines, all the locations are relatively close to a port.

For the marine environment (C3) L1 seems to be the most suitable location, because it is both relatively far away from shipping routes and also far away from migration marine life. For the Politics (C4) L5 is superior, see Appendix G. This is because the water depth is more than 16 meters over a large area.

Table 7.12: Ranking of the alternatives

Ranking	Alternative	Preference percentage (%)
1	L1	27.6
2	L2	24.5
3	L3	18.4
4	L4	15.6
5	L5	13.9

With the scores determined, it is possible to calculate the preference percentage of the different locations. The procedure for determining the preference percentage was described in subsection 7.5.2. The ranking is presented in Table 7.12. This table shows the best location is L1, the Westerschelde, with a preference percentage of 27.6%. With this information the answer to the sub question stated at the beginning of the chapter is provided.

Now the most suitable location for tidal stream turbines is identified, it is possible to design the array configuration and use this location to determine the power output over a tidal cycle.

8

Tidal arrays in the Dutch tidal hot-spots

With the preferred Dutch tidal farm location selected, the ideal array design for this location can be determined. In this chapter the different array designs will be explained. Furthermore, the best array design with regards to the different diameters will be selected. The maximum turbine diameter, which cannot have a diameter exceeding the 8 meters, is determined by the depth of the water at the location of the tidal farm. This chapter aims to answer the following sub-questions:

1. ***"Which design for tidal stream energy generation is most suitable for The Netherlands?"***
2. ***"What is the best configuration of tidal stream generators to generate the highest amount of energy?"***
3. ***"What will be the loads on the tidal stream generators, and how does that influence the design of the generators?"***

8.1. Array configuration in Delft 3D

The objective of this section is to compare different tidal stream turbines and array configurations, to find the best set up for the tidal farm. The array design of the tidal farm depends on the spacing, alignment, turbine diameter and number of turbines. Because of the low tidal resource, the turbines are much smaller compared to the turbines used in previous research.

Multiple assumptions have been made in the analysis of the different array configurations regarding the flow and depth. Due to the small tidal resource it is assumed that the suitable tidal turbine ranges from 3 to 8 meter. Furthermore, for placement of the tidal array it is important to take into account the dominant flow direction. Due to the limitations of Delft 3D it is not possible to rotate the turbines. A constant flow of 0.6 m/s is assumed for the array configuration, which is the rated flow speed, and the flow is directed perfectly in the direction of the array. The different array designs will have the same velocity conditions which makes it possible to make a good comparison between the different designs.

The literature argues that the best configuration of turbines depends on the resource and the spacing of the turbines [101]. This literature finds that if the spacing between the rows is too small, the flow is not able to recover well enough and thus the performance of the turbines decreases. The best power production occurs when the spacing between the turbines is small and the spacing between the rows is large. A negative effect of a small spacing between the turbines is the increased blockage ratio. The blockage ratio is the amount of free following current in the model, and this ratio influences the flow by reducing the free flow available.

The aligned layout results in a significant drop in production between the first and second row. The drop occurs because of the wake effect between the turbines. If the spacing is increased significantly, the power production is also increased because the wake effect has more time to recover. After a loss occurs in current velocity between the first and second row, the production of the rows after the second row remains fairly constant over time. The production of these rows is smaller than the production of the first two rows.

The staggered layout consists of turbines that are not placed right behind each other. Because of this, the flow has more time to recover between the different rows. The production loss in the first two rows will therefore be smaller compared to the production loss in the aligned layout. The study from Thiebot et al. [101] finds that there was an increased power production between the first and second row when the turbines were placed in a staggered layout. The power production increased when the spacing between the turbines was 5D and the spacing between the rows was 5D. The increased production occurred due to the increased flow velocity between the turbines. In this gap, the flow velocity increased slightly and when reaching the second row of turbines, the velocity was still slightly higher than the flow velocity measured at the first row.

In the literature [75, 3, 101] it was found that the most important factor in the design of the ideal array configuration are:

1. The spacing between the turbine.
2. The spacing between the rows.
3. Staggered or aligned layout.
4. Diameter of the turbine.

These factors all influence the wake effect of the turbines and the array. It is important that the wake effects of the turbines do not overlap, because this would decrease the power production significantly. It follows that the increased distance from the staggered layout causes turbulence and therefore results in a smaller wake effect. The lateral spacing influences the blockage ratio, which is determined by the size of the turbine and the size of the mesh. The mesh size in which the arrays are tested is 0.25 by 1 kilometers. Nguyen et al. [70] find that when the blockage ratio is lower than 5%, it is not needed to include a blockage correction. Because the global blockage of the tidal farm is much smaller than 10%, the tidal farm will not influence the hydrodynamics of the channel.

The analysis considers 13 different layout configurations. These layouts include both staggered and aligned configurations. Furthermore, the spacing between the turbines and in between the rows vary. The different arrays are analysed in a grid with a mesh of 5 meters and with two boundary conditions from which a 0.6 m/s current velocity flows. The current velocity of 0.6 m/s is used because this is the rated velocity of the turbines. After finding the best array configuration, the array is nested into the model to determine the exact energy extraction for a full tidal cycle.

Due to the low tidal resource, the hypothesis is that the turbulence of the turbine will increase the production of the turbines when they are placed closer together. This is especially the case for the aligned layout where the influence of the spacing between the turbines has much less influence and the turbulence develops much faster. It is assumed that due to the small size of the turbines it is possible for the turbulence to have a positive impact, unlike the case is for larger turbines. Table 8.1 presents the 13 different layouts that are tested.

Table 8.1: The 13 array layout used for the assessment

Run	Layout	Spacing, turbine	Spacing, rows	Number of turbines	Blockage ratio
1	non-staggered	2 D	4 D	9	0.1
2	non-staggered	2 D	6 D	9	0.1
3	non-staggered	2 D	8 D	9	0.1
4	non-staggered	1 D	4 D	9	0.1
5	non-staggered	4 D	4 D	9	0.1
6	non-staggered	4 D	6 D	9	0.1
7	staggered	2 D	4 D	9	0.1
8	staggered	2 D	6 D	9	0.1
9	staggered	2 D	8 D	9	0.1
10	staggered	4 D	4 D	9	0.1
11	staggered	4 D	6 D	9	0.1
12	staggered	1 D	4 D	9	0.1
13	staggered	5 D	10 D	9	0.1

Each of these configurations are simulated for the turbine diameters of 3, 4, 5, 6, 7 and 8 meters. The literature showed that the array 13 configuration was the best configuration for high tidal resource areas [101].

8.2. Results of the Delft 3D array simulations

The velocities before and after the turbines are measured for the different arrays. The wake effect and the power production can be determined by using the AD theory. These velocities are measured in 2D before and

1D after the turbine. The porous plate holds back the flow which means that right in front of the turbine and right behind the turbine the flow is influenced by the turbulence around the porous plate.

The power production is determined for each of the turbines in the array. From this the total power production is determined and the best array configuration is identified. The wake effect of the different array configurations is also determined and presented in Figure 8.1b. The wake effect shows the influence of the array configurations on the flow, and gives a clear image of what the best configuration is. The model uses a velocity equal to the mean velocity measured at the Westerschelde. Next, the power production and thrust force for the mean velocity can be determined which gives the best array configuration for the average velocity of 0.6 m/s. With the optimal array configuration identified, it is possible to determine the capacity factor for this configuration, which will be discussed in chapter 9.

The configurations that are tested were selected on the base of the smaller turbines and the low current velocity measured at the Westerschelde. First, the non-staggered configurations are examined. It is hypothesized that a staggered layout yields a higher power production than a non-staggered layout. However, with the non-staggered layout the wake effect of the turbines as well as the effect of the wake effect on the spacing of the turbines can be shown clearly. The staggered layouts are tested to determine what the ideal spacing is. With the ideal spacing for high tidal resource areas known, it can be determined if it is better to decrease the spacing in the search for an increased power production. The array configurations are further elaborated on in the following subsections.

8.2.1. Non-staggered tidal arrays with varied distances

The first non-staggered layout used is presented in Figure 8.1a.The array configuration consists of 9 turbines, each with a spacing of 2D between the turbines and 4D between the rows. Figure 8.2 shows the flow around the turbines. Here, the flow around the array increases due to the water only partially passing through the AD.

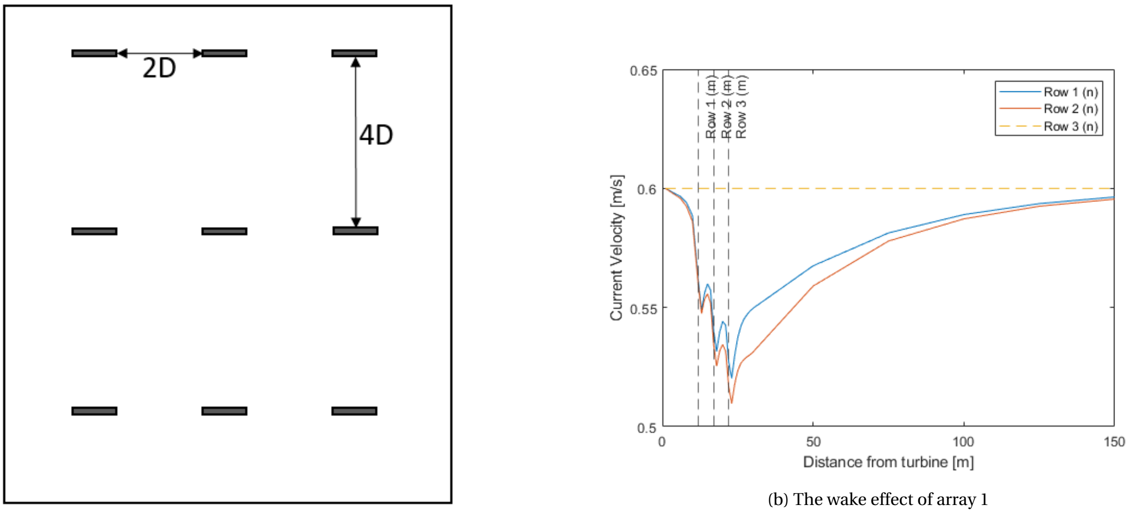

(b) The wake effect of array 1

(a) Array 1 configuration

Figure 8.1: Array configuration and wake effect of array 1

The flow is compressed around the turbines and increases in velocity. Immediately behind the first row of turbines, the flow decreases for the first time due to the AD. The flow is then partially recovered before hitting the second row of turbines. The figure illustrates that after each row the flow takes a longer distance to recover from the placement of the AD. The wake effect of this array configuration is determined for the different diameters, and for the middle and the outer rows of the array. In order to visualise the difference between the wake effect measured for the different array configurations and rows, only the wake effect for a 5 diameter turbine is presented.

Figure 8.1b pictures the wake effect for the middle and outer rows. The figure shows that the current velocity is more strongly reduced at the middle row than at the outer row. Therefore, the power production for the middle turbines is smaller in the first row than the power production in the outer rows. The wake effect of the turbine increases the power production of the middle turbine.

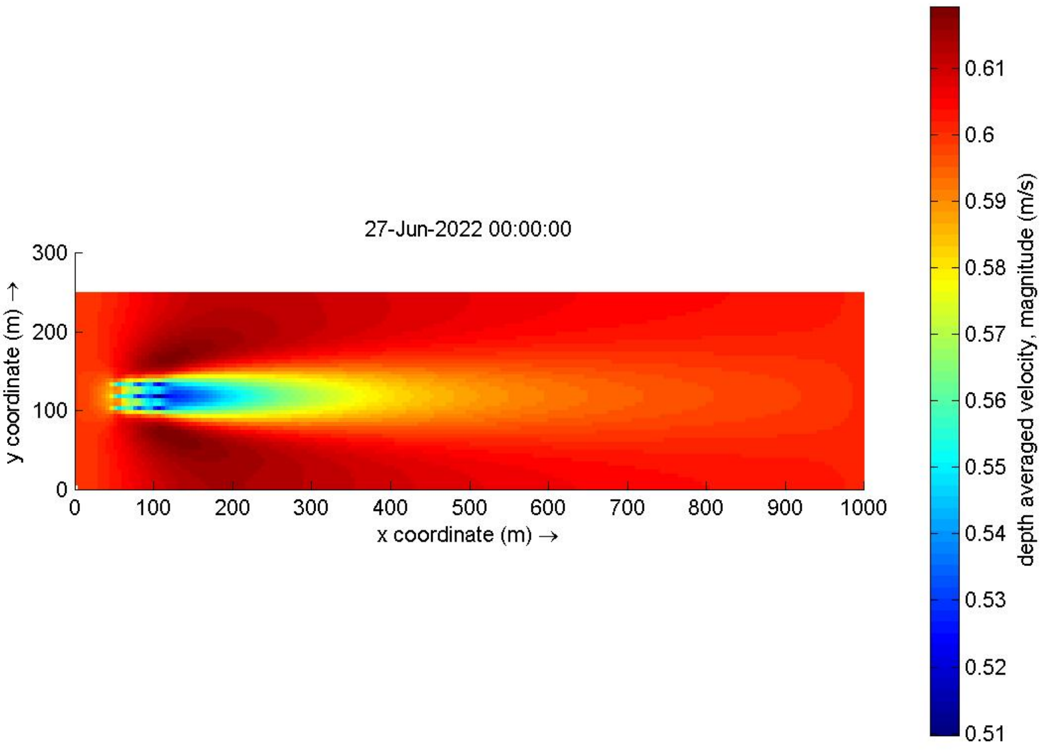

Figure 8.2: Current flow around array 1

In Table 8.2 the power production and the thrust of the different turbines can be seen. The table shows that the power production decrease for each row. The percentage of reduction between the second and third is 70% for the outer and 80.65% for the middle turbine, and the percentage of reduction between the first and second row is 67.24% for the outer and 72.29 % for the middle turbine. This also indicates that placing turbines closer together increases the power production.

Table 8.2: Thrust (N) and electricity production (W) of the different rows and turbines for array 1

	Row 1		Row 2		Row 3	
	P	T	P	T	P	T
Outer	480.2478	4426.092	322.9302	4006.346	260.429	3784.814
Middle	465.7355	4390.065	336.6716	3946.465	259.3371	3651.093
Outer	480.2478	4426.092	322.9302	4006.346	260.429	3784.814

The second non-staggered layout is presented in Figure 8.3a. The array configuration consists of 9 turbines, each with a spacing of 2D between the turbines and 6D between the rows. In Figure 8.2 the flow around the turbine is pictured. Here, the flow around the array increases due to the water only partially flowing through the AD. For this array configuration it is interesting to see what the effect of the wake effect is on the flow recovery between the turbines compared to the first array configuration. In Figure 8.4 the wake effect of this configuration can be seen. The figure clearly shows that the flow has a better flow recovery than the first array. The percentage of flow reduction between the first row and the second row is 82 % and between the second and third row is 84 % for the outer and 78 % for the middle turbine. Due to the better wake recovery for the non-staggered layout the power production is reduced less, so that the total power production is 8 % higher.

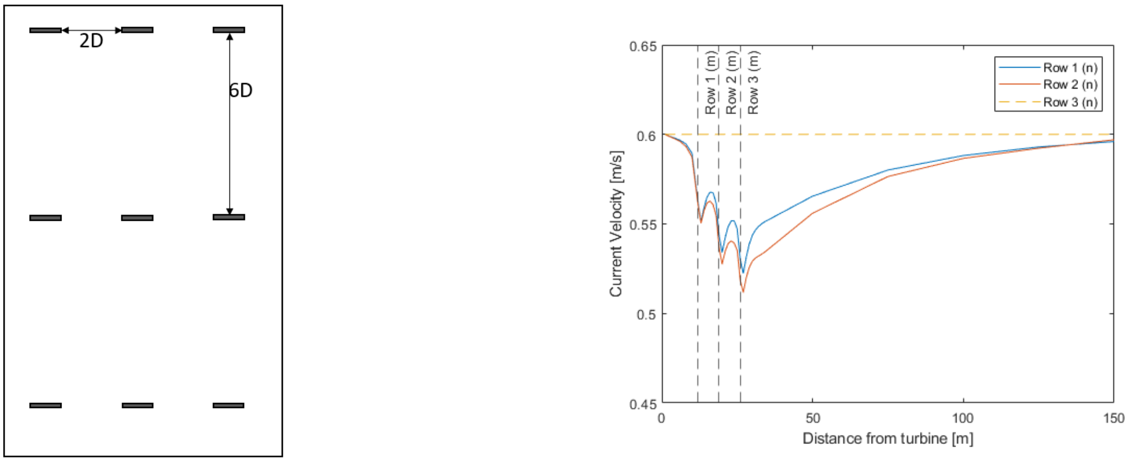

(a) Array 2 configuration

(b) The wake effect of array 2

Figure 8.3: Array configuration and wake effect of array 2

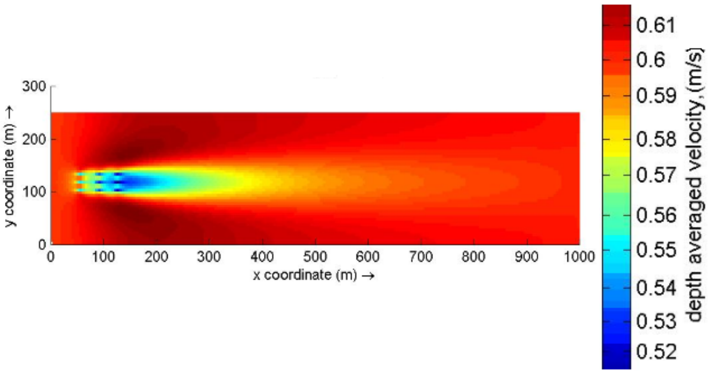

Figure 8.4: Current flow and wake effect of array 2

Table 8.3 provides the power production and thrust on each of the turbines in the grid. The power and thrust are determined for each of the different turbines to see the effect of the array. The table shows that there is a consistent reduction in power production over the rows.

Table 8.3: Thrust (N) and electricity production (W) of the different rows and turbines for array 2

	Row 1		Row 2		Row 3	
	P	T	P	T	P	T
Outer	468.383	4441.147	382.217	4112.946	323.926	3891.266
Middle	451.172	4409.561	371.849	4017.803	291.826	3716.964
Outer	468.383	4441.147	382.217	4112.946	323.926	3891.266

The third non-staggered layout is pictured in Figure 8.5a. The configuration has a spacing of 2D between the turbines and 9D between the rows. In Figure 8.6 the flow around the turbine is visualised. The difference with the first and second layout is the increased spacing between the rows, which results in an increase in wake recovery before hitting the new row of turbines. Table 8.4 presents the power production of the turbines in each row. It shows that the power reduction between the rows is smaller, so that increasing the spacing in a non-staggered layout increases the power production. The percentage of power reduction between the first and second row is 85 % for the outer and 82 % for the middle turbines. The difference between the second and third row is 86% for the outer and 80% for the middle turbines. The total power production compared to array 3 is just 2.3%, which means that increasing the spacing further than 6D does not significantly increase the power production of the array. Furthermore, increasing the spacing results in decreasing the number of rows that can be placed. Keeping the turbine rows at a spacing of 6D gives the better overall power production.

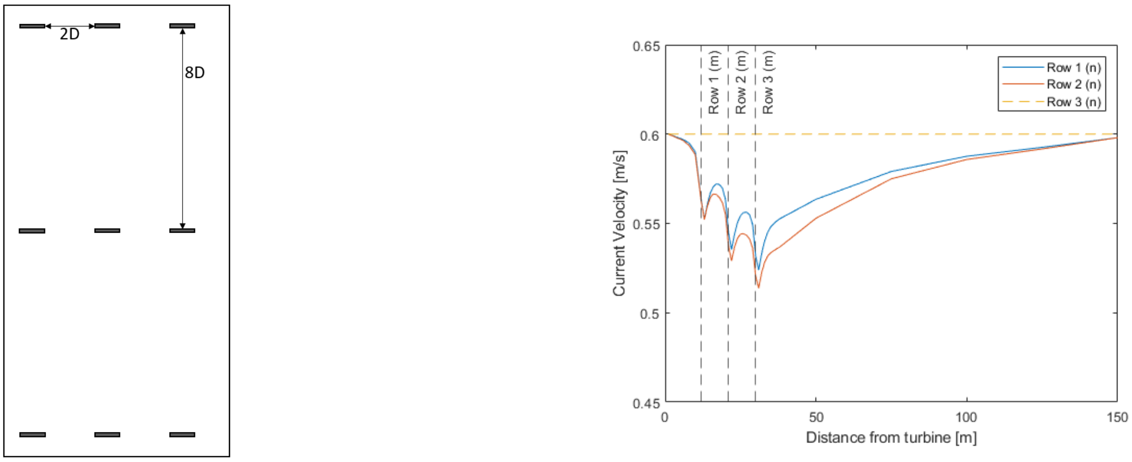

(a) Array 3 configuration

(b) The wake effect of array 2

Figure 8.5: Array configuration and wake effect of array 3

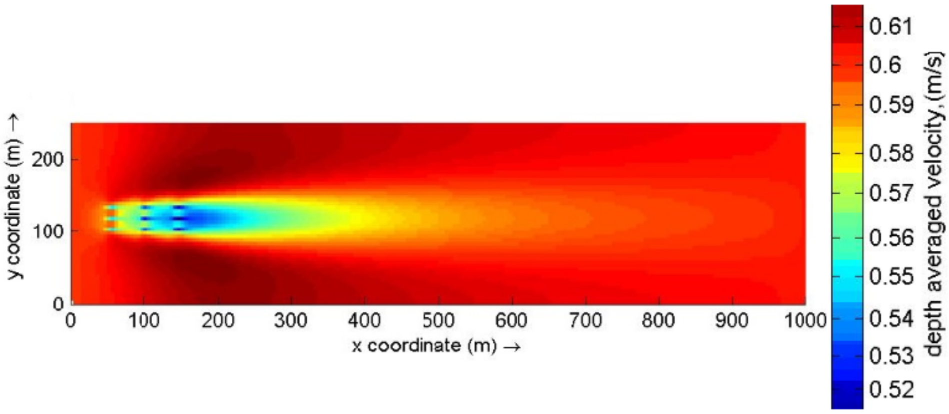

Figure 8.6: Current flow and wake effect of array 3

Table 8.4: Thrust (N) and electricity production (W) of the different rows and turbines for array 3

	Row 1		Row 2		Row 3	
	P	T	P	T	P	T
Outer	464.115	4450.192	395.762	4147.820	341.381	3933.692
Middle	446.602	4426.092	366.082	4029.276	293.165	3744.584
Outer	464.115	4450.192	395.762	4147.820	341.381	3933.692

The fourth and fifth array configurations change the spacing between the turbines compared to the first array configuration. In Figure 8.7a and in Figure 8.9a the array configurations can be seen. The difference is the spacing of respectively 1D and 4D between the turbines. With these three configurations presented, the effect of the turbine spacing can be looked into. The wake effect of these configurations is shown in Figure 8.8 and Figure 8.10, respectively. The figures show that the wake effect in array configuration 4 is higher, while the width of the wake is smaller compared to array 5.

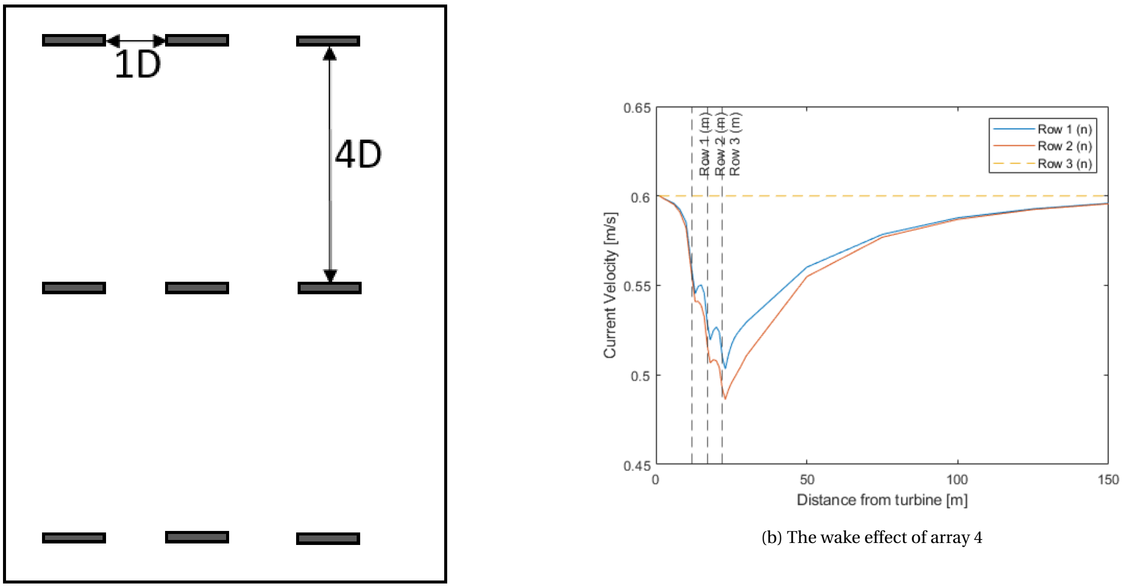

(b) The wake effect of array 4

(a) Array 4 configuration

Figure 8.7: Array configuration and wake effect of array 4

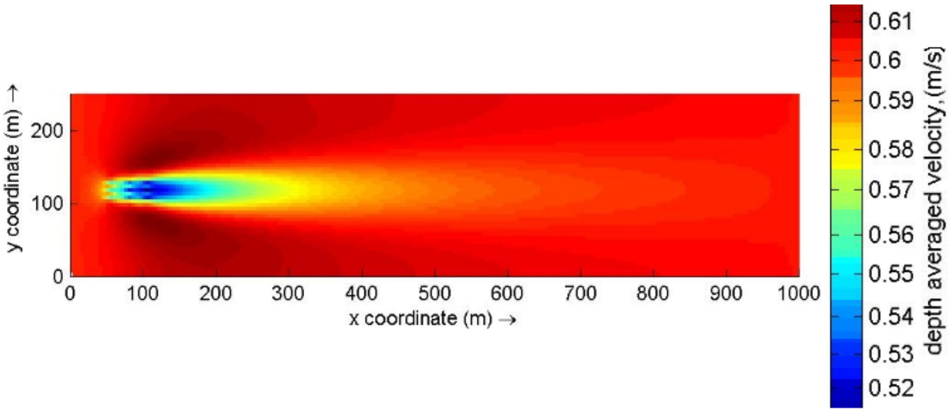

Figure 8.8: Current flow and wake effect of array 4

In Table 8.5 and Table 8.6 the power and thrust for each of the nine turbines is determined. For the 4e array configuration the percentage of power reduction between the first and second row is 68.3 % for the inner turbine and 70% for the outer turbine. The percentage of power reduction between the second and third row is 62.3% for the middle turbine and 71.3% for the outer turbine. The fifth array configuration comes with a percentage of power reduction of 62.5% for the middle turbine and 61% for the outer turbine for the first and second row. For the second and third row the reduction in power is 85.8% for the middle turbine and 82.6% for the outer turbine. The data show that the total power production for the spacing of 4D is just a little higher than for a spacing of 2D, while both are higher than the 1D spacing. The difference in total power production between these configurations is relatively small and the effect of the spacing between the turbines can almost be neglected compared to the spacing between the rows, which effect is stronger and more visible.

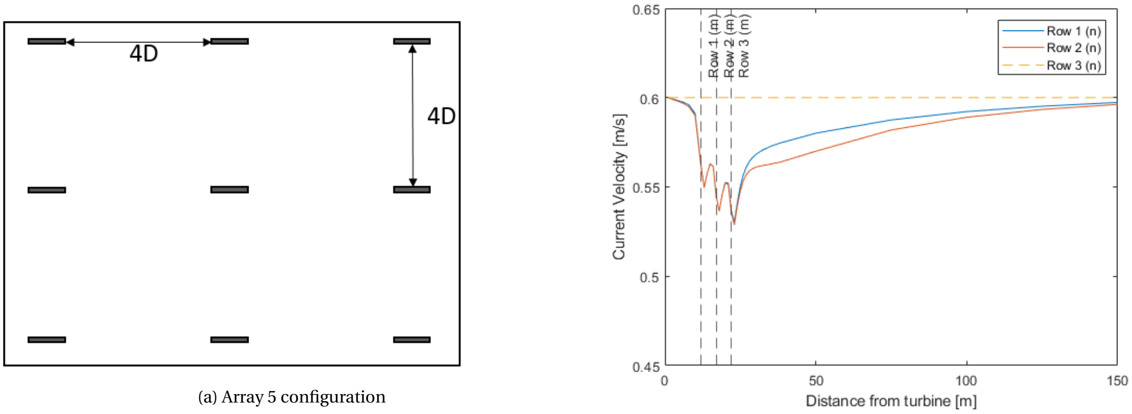

(a) Array 5 configuration

(b) The wake effect of array 5

Figure 8.9: Array configuration and wake effect of array 5

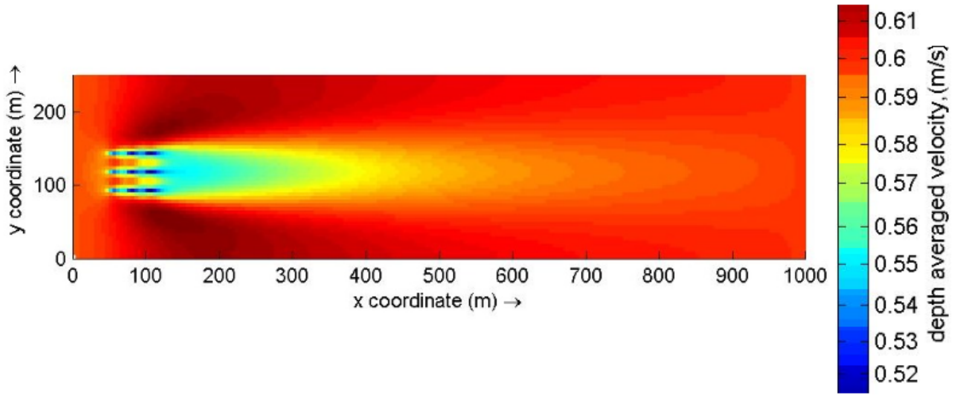

Figure 8.10: Current flow and wake effect of array 5

Table 8.5: Thrust (N) and electricity production (W) of the different rows and turbines for array 4

	Row 1		Row 2		Row 3	
	P	T	P	T	P	T
Outer	494.2437	4378.0884	334.5843	3870.1385	238.6855	3546.6556
Middle	485.1935	4330.3468	331.7345	3710.0747	206.5628	3298.0323
Outer	477.7348	4378.0884	334.5843	3870.1385	238.6855	3546.6556

Table 8.6: Thrust (N) and electricity production (W) of the different rows and turbines for array 5

	Row 1		Row 2		Row 3	
	P	T	P	T	P	T
Outer	503.5418	4465.2872	306.9073	4049.3935	253.3654	3901.1446
Middle	491.2002	4448.6834	307.0217	4050.8324	263.3798	3896.9092
Outer	503.5418	4465.2872	306.9073	4049.3935	253.3654	3901.1446

The sixth array configuration is pictured in Figure 8.11a. In this configuration the spacing between the turbines is set at 4D and the spacing between the rows is set at 6D. To see the effect of the spacing between the turbines, this array is compared to the third array configuration for which the spacing between the rows is 4D. The wake effect of the configuration is pictured in Figure 8.12, which shows that the two wake effects look very similar. However, compared to the power production of array 3, the total power production is about 150W higher. The spacing between the rows combined with the spacing between the turbines increases the power production of the turbines.

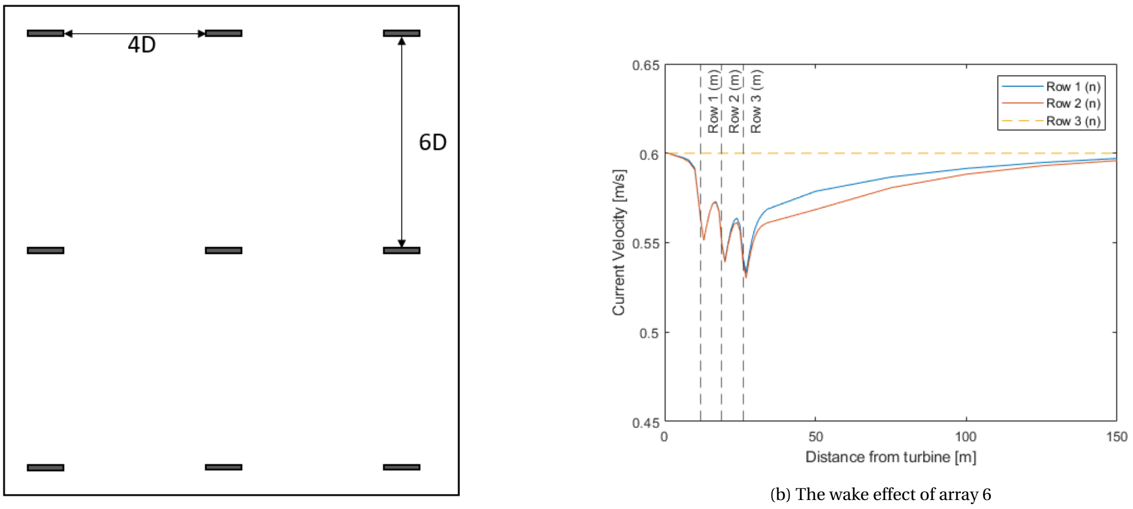

(a) Array 6 configuration

(b) The wake effect of array 6

Figure 8.11: Array configuration and wake effect of array 6

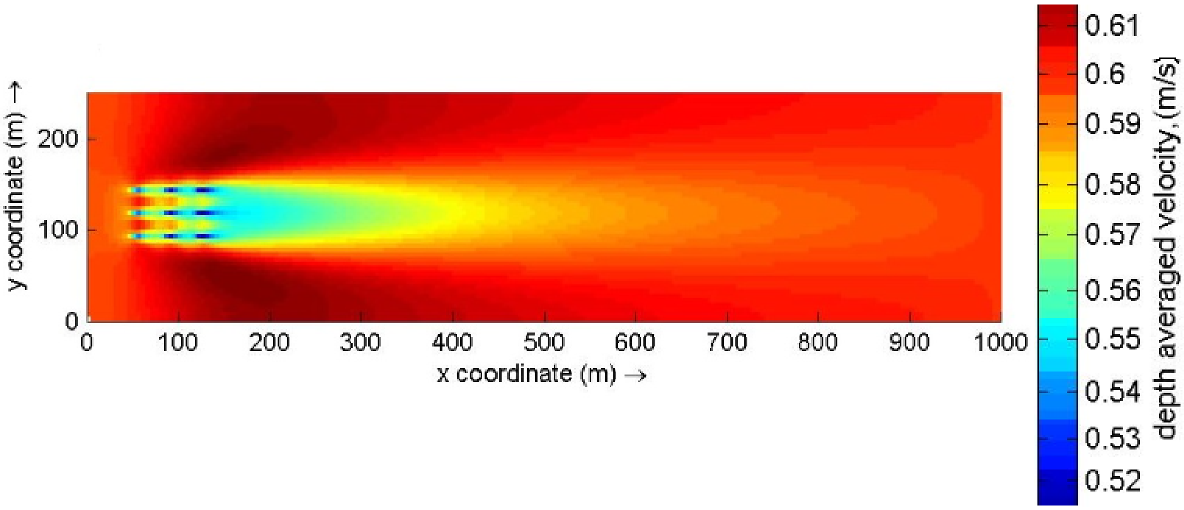

Figure 8.12: Current flow and wake effect of array 6

Table 8.7: Thrust (N) and electricity production (W) of the different rows and turbines for array 6

	Row 1		Row 2		Row 3	
	P	T	P	T	P	T
Outer	494.2437	4474.3569	389.3925	4196.0120	352.1996	4062.3527
Middle	482.1848	4460.7559	391.7474	4188.6923	352.9019	4026.4060
Outer	494.2437	4474.3569	389.3925	4196.0120	352.1996	4062.3527

Overall, the sixth array configuration has the highest total power production which generates as much as

3698.5W. For each of the other turbine diameters (3m, 4m, 5m, 6m, 7m and 8m), the power of the turbines and thrust on the turbines is determined. In Table 8.8 the total power production, minimum and maximum thrust is determined. The data show that for each of the different diameters, the best array configuration is the sixth configuration. It can therefore be concluded that when looking at the power production of non-staggered array designs, the most important parameter is the spacing between the rows, where a larger spacing results in a higher power production.

Table 8.8: Max thrust and total production of the different rows and turbines for all non-staggered layouts

		8m	7m	6m	5m	4m	3m
array 1	P tot	12754.05	8665.939	5451.917	3188.9581	1488.903	565.2156
	Max T	9530.203	7642.719	5725.049	4426.0918	2731.357	1604.785
	Min T	6775.8	5759.164	4544.458	3651.0930	2376.78	1456.746
array 2	P tot	14654.24	9731.28	6045.122	3463.9002	1620.794	586.7474
	Max T	9552.908	7663.523	5742.567	4441.1465	2739.702	1609.68
	Min T	7177.92	5998.463	4666.568	3716.9637	2401.91	1466.081
array 3	P tot	15082.06	10056.92	6171.417	3508.3654	1571.039	583.9145
	Max T	9569.142	7679.144	5750.361	4450.1916	2745.273	1612.947
	Min T	7313.59	6090.906	4717.631	3744.5836	2414.96	1472.32
array 4	P tot	11849.41	8008.537	5299.341	3125.5000	1492.813	581.2367
	Max T	9404.201	7544.288	5630.141	4378.0884	2706.399	1593.935
	Min T	5678.948	4956.837	3885.748	3298.0323	2216.237	1392.744
array 5	P tot	12952.93	8707.426	5491.953	3189.2309	1468.259	547.5734
	Max T	9575.639	7697.389	5769.87	4465.2872	2752.709	1616.218
	Min T	7172.295	6104.833	4847.399	3896.9092	2507.302	1517.426
array 6	P tot	15602.49	10444.01	6288.232	3698.5056	1675.541	783.133
	Max T	9601.651	7710.434	5777.683	4474.3569	2757.361	1619.492
	Min T	7975.365	6614.394	5099.359	4026.4060	2553.675	1531.197

Another important characteristic is the thrust. The difference in thrust between the different turbines impacts the CAPEX of the project. When all the turbines have approximately the same thrust, the costs for the design and production of the support structure can be reduced, due to the fact that manufacturing multiple foundation with the same layout reduces the costs compared to using multiple designs.

Table 8.9: Production of the different turbines for all non-staggered layouts

Max thrust		8m	7m	6m	5m	4m	3m
array 1	Row 1	9530.203	7642.719	5725.049	4390.064727	2731.357	1604.785
	Row 2	7713.631	6486.884	5035.314	4006.345651	2553.675	1537.042
	Row 3	7060.252	5980.06	4710.572	3784.814123	2449.057	1492.167
array 2	Row 1	9552.908	7663.523	5742.567	4441.147	2739.702	1609.68
	Row 2	8256.546	6809.211	5224.945	4112.946	2594.148	1550.367
	Row 3	7585.847	6320.378	4899.439	3891.266	2489.58	1505.823
array 3	Row 1	9569.142	7679.144	5750.361	4450.192	2745.273	1612.947
	Row 2	8475.213	6937.358	5292.05	4147.820	2607.71	1554.643
	Row 3	7839.542	6472.528	4978.927	3933.692	2489.58	1511.092
array 4	Row 1	9404.201	7544.288	5630.141	4378.0884	2706.399	1593.935
	Row 2	7387.608	6209.796	4705.28	3870.1385	2485.159	1504.77
	Row 3	6372.01	5414.816	4064.007	3546.6556	2333.762	1442.284
array 5	Row 1	9575.639	7697.389	5769.87	4465.2872	2752.709	1616.218
	Row 2	7734.058	6510.848	5082.852	4049.3935	2584.226	1555.178
	Row 3	7217.359	6142.051	4859.935	3901.1446	2516.187	1526.953
array 6	Row 1	9601.651	7710.434	5777.683	4474.3569	2757.361	1619.492
	Row 2	8408.095	6942.311	5327.64	4196.0120	2642.225	1575.035
	Row 3	7978.331	6628.907	5123.25	4062.3527	2577.921	1547.163

The data from Table 8.9 show that the maximum thrust difference between the rows is much higher for the larger than for the smaller turbines. This difference is the result of the fact that the wake effect for larger turbines is stronger, because more of the flow is influenced by the wake and therefore the between the row difference in tidal production will also be more visible.

The installation costs of the different turbine diameters are dependent on the thrust. Due to the wake effects, there is a substantial difference in thrust force between different turbines. For the larger turbines each turbine requires a specific foundation, or the total costs of the foundation is relatively higher because using uniform foundations is sub optimal for the second and third row. However, it needs to be said that in this analysis the flow only comes from the West. In real life the flow in the Westerschelde will originate from both the West and East, meaning that when looking at the maximum thrust on the turbine, array 6 has the highest thrust.

Therefore, taking the wake effect into account, an increase in the distance between the rows and increasing the distance between the turbines has a positive effect on the energy production of the array.

8.2.2. Staggered tidal arrays with varied distances

According to the literature [101], staggered layouts yield a higher power production compared to non-staggered layouts. These array configurations compare the spacing between the turbines and rows and see the effect of both these changes in the configuration. Array configuration 7 can be seen in Figure 8.13a, where the spacing between the turbines is 2D and is 4D between the rows. In this configuration the same spacing is used as was used for array configuration 1. Comparing the two facilitates determining what the effect of the staggered versus non-staggered layout is.

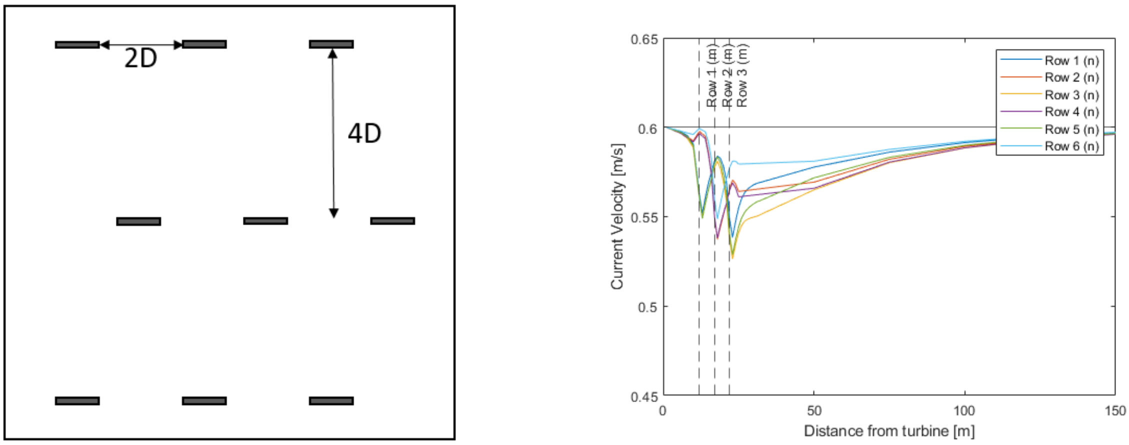

(a) Array 7 configuration

(b) The wake effect of array 7

Figure 8.13: Array configuration and wake effect of array 7

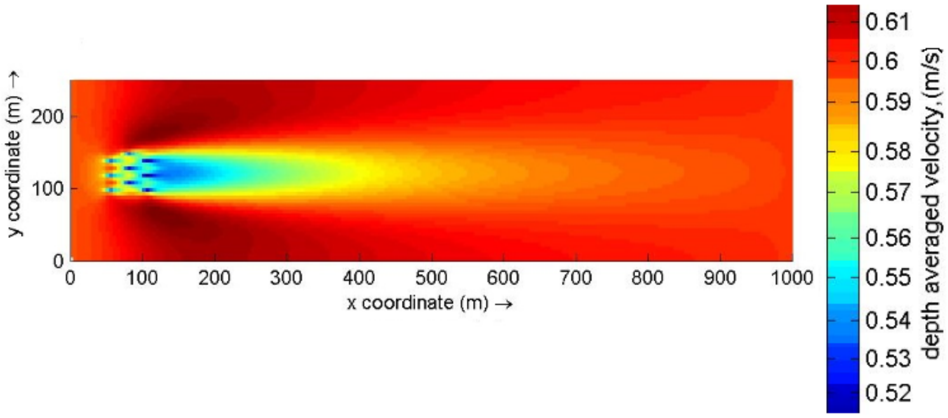

Figure 8.14: Current flow and wake effect of array 7

In Table 8.10 the power production of the different turbines and rows is shown. Comparing both power production tables, it is evident that the staggered layout has a higher energy production. The staggered layout produces up to 30 % more energy for the given conditions. Looking into the power reduction of the different rows, the second row experiences in fact an increase in power compared to the first row of turbines. This can be explained by the fact that the first row of turbines is compressing the flow between the turbines and with that is creating a higher free flow velocity for the second row of turbines. The thrust difference between the maximum and minimum thrust is around the 95 kW. The thrust difference is relatively small, which could mean that the foundation costs for the different turbines can be mitigated by designing one single foundation.

Table 8.10: The power production(W) and thrust (N) of the different rows of array 7 for a 5 diameter turbine

Array 7	Row 1		Row 2		Row 3	
	Power	Thrust	Power	Thrust	Power	Thrust
Outer	477.809	4459.245908	569.39482	4459.245908	463.216862	4271.037843
Middle	474.178443	4427.5961	547.781793	4427.5961	478.489932	4141.997652
Bottom	493.767896	4444.160513	523.524991	4444.160513	497.683399	4197.476734

The array configuration of array 8 is presented in Figure 8.15a. The spacing of the turbines and rows means that this array can be compared to array 6, in order to see the effect of the staggered versus non-staggered set up. Moreover, array 8 can be compared to array 7 to see the effect of the spacing for a staggered layout.

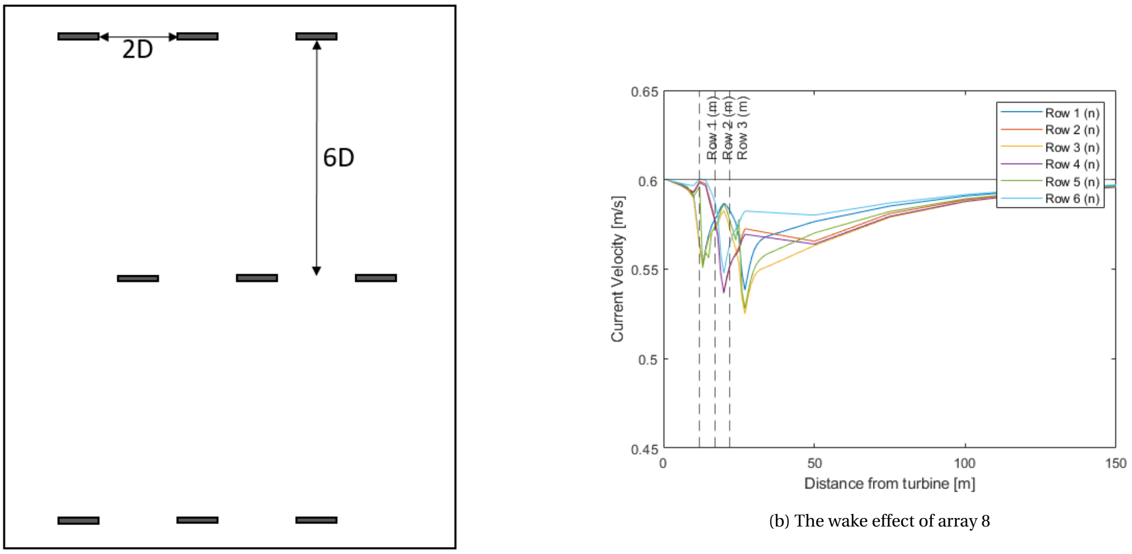

(b) The wake effect of array 8

(a) Array 8 configuration

Figure 8.15: Array configuration and wake effect of array 8

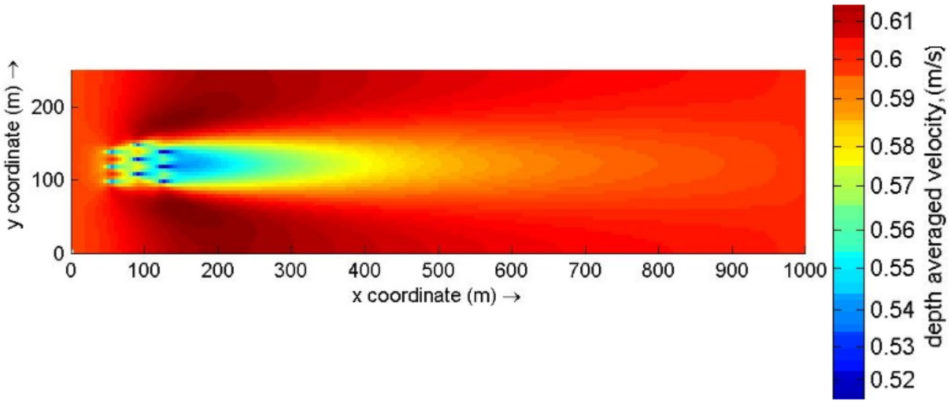

Figure 8.16: Current flow and wake effect of array 8

In Table 8.11 the power production and thrust of the different rows and turbines can be seen. Comparing it to array 2, the increase in production is around 16%. Comparing it to array 7, the production of the second row is much smaller, around the 12%. This difference is due to the fact that the increased flow velocity, which is produced by the first row, is reduced when hitting the second row of turbines. Therefore, increasing the spacing between the rows will reduce the production of the turbines. For minimum and maximum thrust on the turbine for array 8 a difference around the 0.5 kN is calculated, which is considered relatively high when looking at the total thrust on the turbine.

Table 8.11: The power production(W) and thrust (N) of the different rows of array 8 for a 5 diameter turbine

Array 8	Row 1		Row 2		Row 3	
	Power	Thrust	Power	Thrust	Power	Thrust
Outer	477.794001	4468.309413	486.6	4276.95	437.384893	4237.12037
Middle	466.444268	4442.653379	468.7615	4259.225	400.506492	4023.537173
Bottom	487.064862	4457.736218	487.934	4420.077	429.784125	4098.459086

The power production and array configuration of array 9 are pictured in Figure 8.17a The array configuration can be compared to array 3 (staggered versus non-staggered) and to array 7 and 8 (spacing between the rows). Figure 8.18 clearly pictures the effect of the array on the flow.

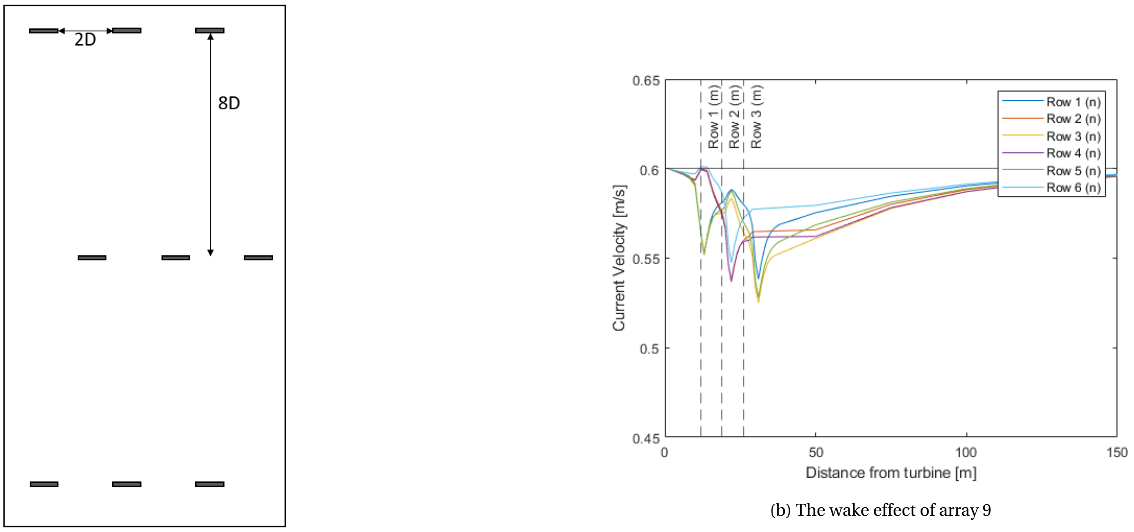

(b) The wake effect of array 9

(a) Array 9 configuration

Figure 8.17: Array configuration and wake effect of array 9

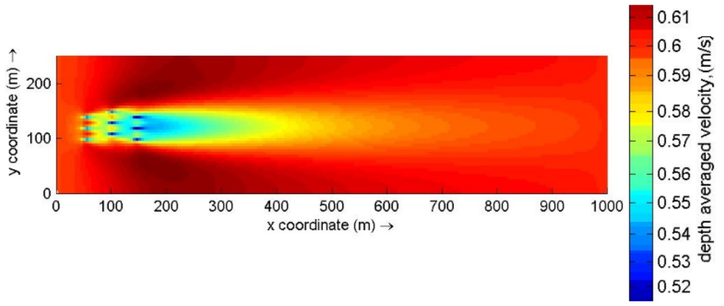

Figure 8.18: Current flow and wake effect of array 9

The production and thrust of the different turbines are shown in Table 8.12. A comparison between array 3 and 8 shows that using a staggered layout would increase the production of the turbine by 11%. Comparing array 3 to array 7 and 8 can show the effect of using a 4D, 6D and 8D spacing between the rows. A 8D spacing between rows will decrease the production of the second row compared to a spacing of 6D with 7% and compared to a spacing of 4D with 18%. From this it can be concluded that with the low velocities it is possible to increase the production of the turbines by decreasing the spacing between the rows. Determining the difference in total array production between array 7, 8, and 9 shows that when using array 7, the production is 8% higher than array 8 and 12% higher than array 9. The third array has a slightly higher production with the increased spacing. The thrusts on the different turbines in array 9 are far apart compared to array 10, meaning that for the design of the foundation either the foundation is over designed for some turbines or the foundation needs to be designed individually.

Table 8.12: The power production(W) and thrust (N) of the different rows of array 9 for a 5 diameter turbine

Array 9	Row 1		Row 2		Row 3	
	Power	Thrust	Power	Thrust	Power	Thrust
Outer	476.198361	4472.844617	447.542462	4229.764898	428.054015	4225.354682
Middle	460.03558	4451.700015	425.461396	4210.670576	367.363312	3982.053999
Bottom	481.659016	4465.287222	470.389852	4394.560057	399.637362	4060.911738

The array configuration of array 10 is shown in Figure 8.19a. Here, the spacing between the turbines and rows is 4D. The array can be compared to array 5 (staggered versus non-staggered) and to array 7 (spacing between the turbines). Figure 8.20 clearly shows the effect of the array on the water flow. The figure also shows the array-specific velocity changes.

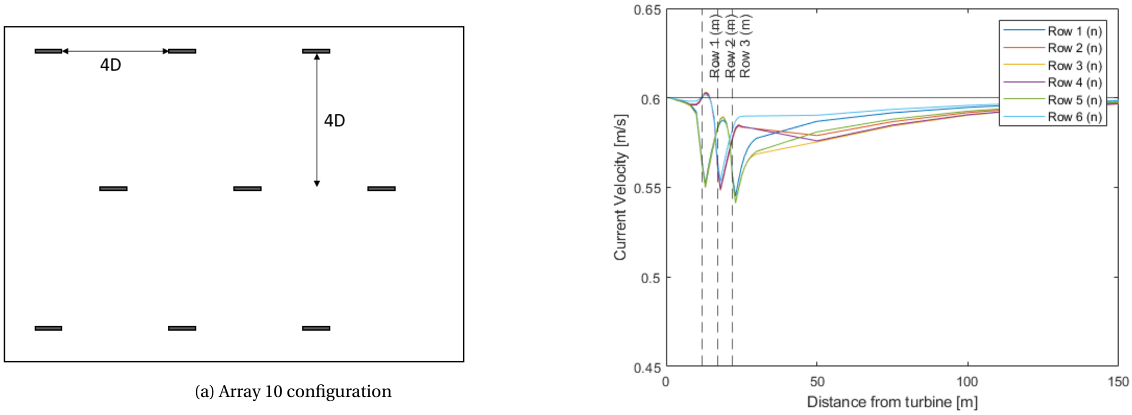

(a) Array 10 configuration

(b) The wake effect of array 10

Figure 8.19: Array configuration and wake effect of array 10

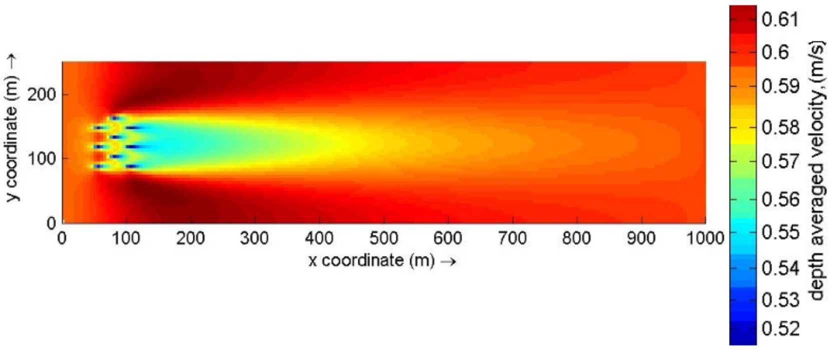

Figure 8.20: Current flow and wake effect of array 10

The production and thrust of the different turbines are documented in Table 8.13. The comparison between array 7 and 8 shows that the production of array 10 is around 33% higher. This can be clearly seen in the increased production of rows 2 and 3. When looking at the production of the different rows, the first two rows both produce around the same amount of electricity, while the second row of array 10 has a 46% higher production than the second row of array 5. The third row of array 10 produces 49% more than the third row of array 5. When comparing the production of array 10 to that of array 7 to see the effect of the spacing between the turbines, the overall production of array 10 turns out 6% higher than the production of array 7. This difference is the result of each row having a higher production of around 3%. It can therefore be concluded that increasing the spacing between the turbines has a positive effect on the overall production. The data also shows that for array 10 the thrust difference between the turbines is relatively small, meaning that when designing the turbine one single foundation can be designed.

Table 8.13: The power production(W) and thrust (N) of the different rows of array 10 for a 5 diameter turbine

Array 10	Row 1		Row 2		Row 3	
	Power	Thrust	Power	Thrust	Power	Thrust
Outer	495.140566	4481.921925	594.157707	4560.977368	484.207797	4381.080968
Middle	491.769071	4462.266054	581.329219	4554.871643	526.788494	4393.061358
Bottom	501.473983	4465.287222	543.233674	4559.450553	528.369596	4390,064727

The array configuration of array 11 can be seen in Figure 8.21a. The spacing between the turbines and rows is 4D and 6D respectively. In Figure 8.22 the effect of the array on the flow and the wake effect are pictured. Array 11 can be compared to array 6 (staggered versus non-staggered) and to arrays 8 and 10 (spacing between the turbines and between the rows). The power production and thrust on the turbines of array 11 are presented in Table 8.14.The overall production of array 11 is 4276,78 kW, which is an increase of 13% compared to the production of array 6. This can again be explained by the fact that the flow has more time to recover between the rows and thus has a higher free flowing velocity when the flow hits the turbine. Comparing the production to array 8 and 10, the data show that array 11 has a 3% higher production than array 8 and a 11% smaller production than array 10. The production difference between array 10 and 11 can be explained by the fact that the increase in flow velocity after the first row of turbines is higher with at a spacing of 4D than with a 6D spacing. Again, the production of the third row of turbines is higher for the 6D spacing, but this finding is not so substantial that it can counteract the increased production measured at the second row. Furthermore, it is interesting to see that the maximum thrust on the turbine in array 10 and 11 are almost the same, while the minimum thrust on the turbines in array 11 is much smaller. The same is found when comparing the array to array 8 and to array 6. The lower thrust can be explained by the fact that the velocity on the second row in array 11 has already been decreased, meaning that the thrust - which is mainly dependent on the velocity - has also decreased more than for the other configurations. It can thus be concluded that when a design for the foundation of array 11 is made, either a higher cost occurs due to the fact for each turbine a specific foundation needs to be designed or because the foundation for the turbines in row 2 is much stronger than required and therefore has a higher cost.

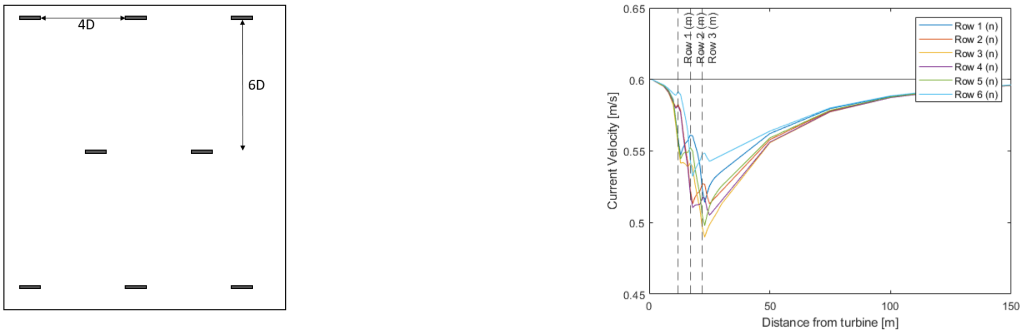

(a) Array 11 configuration

(b) The wake effect of array 11

Figure 8.21: Array configuration and wake effect of array 11

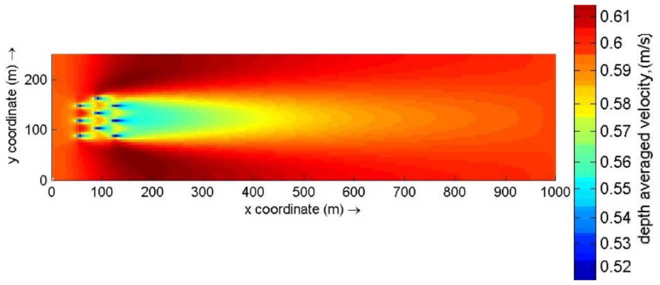

Figure 8.22: Current flow and wake effect of array 11

Table 8.14: The power production(W) and thrust (N) of the different rows of array 11 for a 5 diameter turbine

Array 11	Row 1		Row 2		Row 3	
	Power	Thrust	Power	Thrust	Power	Thrust
Outer	494.452175	4484.949739	437.188971	3802.918258	488.631271	4384.074532
Middle	490.751513	4471.332627	429.406066	3815.477194	504.383404	4333.32299
Bottom	501.349077	4472.844617	420.603915	3889.855322	510.009005	4346.728467

The array configuration of array 12 is pictured in Figure 8.23a. In this configuration the spacing between the turbines is extremely small, as to see whether the effect shown in array 10 is stronger when the turbines are placed closer together Figure 8.24. A comparison for array 12 can be made with array 5 (staggered versus non-staggered) and with array 10 (to see if decreasing the spacing between the turbines has a positive effect).

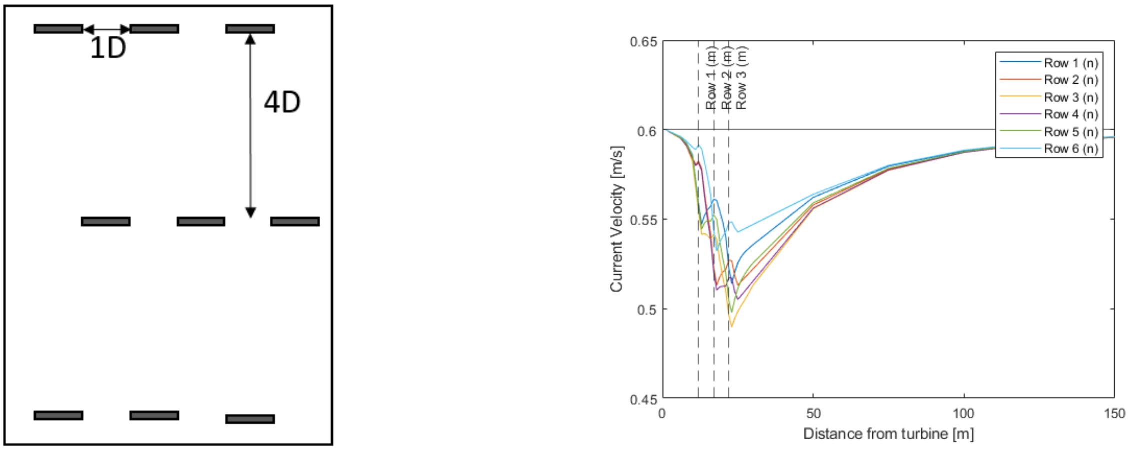

(a) Array 12 configuration

(b) The wake effect of array 12

Figure 8.23: Array configuration and wake effect of array 12

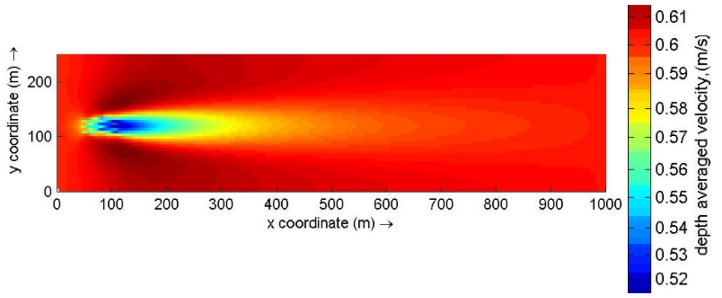

Figure 8.24: Current flow and wake effect of array 12

The power production and thrust on the turbines in the array 12 configuration are presented in Table 8.15. The overall production of array 12 is calculated to be around the 3701.71W. Comparing this to array 5, the production of array 12 is 14% higher. Looking at the production difference between the different rows of array 12 and array 10, it can be seen that the first row of array 11 has a 4% production decrease compared to array 10. When comparing the second rows, array 12 also produces 10% less compared to array 5. Moreover, when comparing the third rows, array 12 produces 37% less compared to array 5. When placing the turbines so close together, the positive effect of increased velocity fades out.

Table 8.15: The power production(W) and thrust (N) of the different rows of array 12 for a 5 diameter turbine

Array 11	Row 1		Row 2		Row 3	
	Power	Thrust	Power	Thrust	Power	Thrust
Outer	465.055179	4384.074532	415.407035	3898.320728	365.963187	3844.861892
Middle	480.369121	4331.83477	411.046685	3860.298862	268.451669	3423.86014
Bottom	484.335183	4373.601531	470.85105	4203.338108	340.224764	2890.66

Figure 8.25a presents the array configuration of array 13. As explained before, according to the literature found [101], this array configuration has the highest production for high tidal resource areas. Array 13 is built using a spacing of 5D between the turbines and 10D between the rows. With this it can be determined if placing the turbines closer together has a positive effect on the production of the tidal farm. So far it has been found that array 10 has the highest overall production.

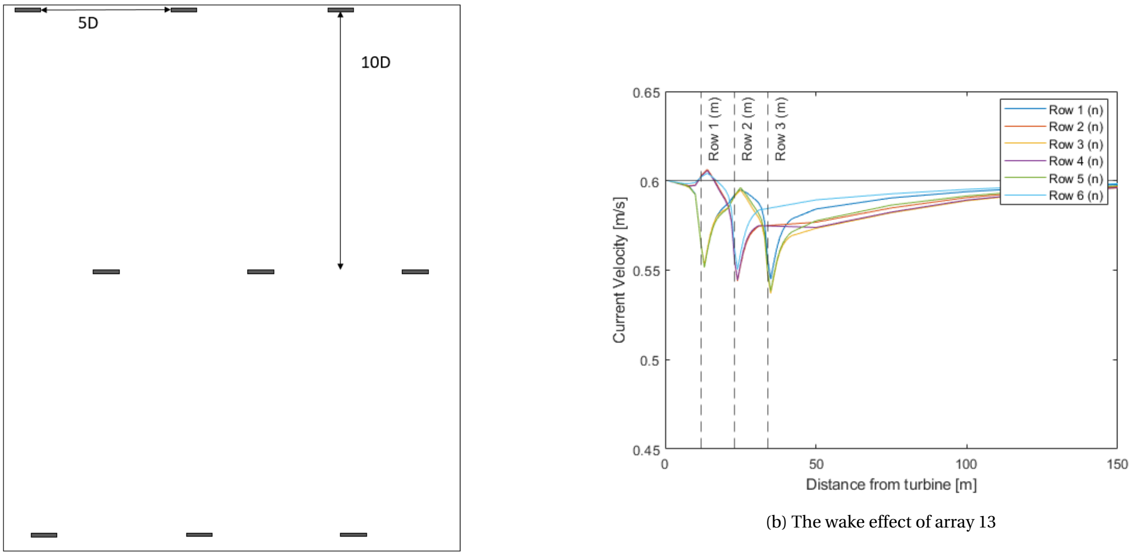

(a) Array 13 configuration

(b) The wake effect of array 13

Figure 8.25: Array configuration and wake effect of array 13

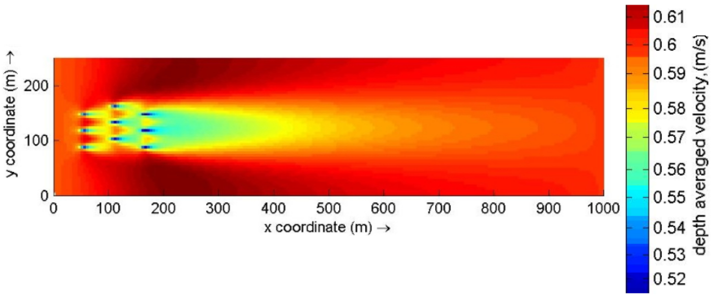

Figure 8.26: Current flow and wake effect of array 13

The power production and thrust on the turbines of array 13 is shown in Table 8.16. When looking into the wake effect of this array configuration, it can be seen that the flow has recovered more after hitting a new row of turbines than was the case in other configurations. However, the first row-increased flow has less effect due to the higher spacing between the turbines. Comparing the production of array 13 to the production of array 10, array 10 provides an 8.5% higher production. This can be mainly credited to the production of the second row, which is 14% higher for array 10. Again, the first and third row of array 13 have a slightly higher production but overall the production of array 10 is higher.

Table 8.16: The power production(W) and thrust (N) of the different rows of array 13 for a 5 diameter turbine

Array 11	Row 1		Row 2		Row 3	
	Power	Thrust	Power	Thrust	Power	Thrust
Outer	493.761409	4487.978575	495.353458	4381.080968	473.273898	4366.128484
Middle	486.920283	4483.435704	483.31975	4373.601531	448.042928	4234.177414
Bottom	497.231118	4481.921925	499.947566	4469.820892	464.211166	4271.037843

8.3. The optimal array design

Table 8.17 presents the calculated power production for each of the turbine diameters. In Appendix H the individual power and thrust calculated per turbine is presented. In Table 8.18 the maximum thrust of the different rows can be seen. These tables show that for each of the different diameters, the highest energy production is generated in array 10. This is due to the fact that for array 10 there is an ideal combination between wake recovery and the wake increased velocity.

Table 8.17: The power production and max and min thrust of the different diameters for each of the staggered layouts

Max thrust		8m	7m	6m	5m	4m	3m
array 7	P tot	20,567.33	13,413.25	7763.195	4525.847137	2006.005	717.7627
	Max T	9906.629	7857.296	5832.522	4477.382121	2749.919	1614.582
	Min T	8955.652	7161.975	5126.93	4141.997652	2579.721	1531.728
array 8	P tot	19,152.97	12,417.29	7458.143	3858.204735	2308.004	651.0444
	Max T	9660.307	7710.434	5775.73	4468.309413	2733.211	1617.309
	Min T	8551.807	6873.135	5178.596	3678.467585	2437.665	1514.785
array 9	P tot	18,140.71	11,866.54	7106.818	3956.341355	2209.684	708.5124
	Max T	9611.414	7715.655	5781.592	4472.844617	2736.919	1618.946
	Min T	8277.68	6735.823	5097.523	3982.053999	2419.318	1511.619
array 10	P tot	21209.36	13647.97	8402.457	4746.470109	2110.012	758.1503
	Max T	10,226.45	8072.173	5962.81	4560.977368	2790.976	1629.881
	Min T	9304.644	7497.886	5639.789	4381.080968	2706.399	1588.523
array 11	P tot	21,047.49	13,761.83	8263.771	4276.775396	1924.098	801.4766
	Max T	10,015.99	7939.191	5887.62	4484.949739	2839.89	1623.315
	Min T	9452.564	7567.543	5633.999	3802.918258	2200.408	1571.806
array 12	P tot	15,408.06	9930.157	6365.371	3701.703873	1701.629	644.8877
	Max T	9423.532	7559.787	5668.783	4384.07	2710.089	1595.018
	Min T	6311.192	5351.568	4239.567	2890.66	2264.907	1409.5
array 13	P tot	20,235.13	13,473.63	7819.046	4342.061577	1901.473	669.0682
	Max T	9814.306	7802.061	5807.029	4487.978575	2768.543	1624.955
	Min T	9247.08	7339.151	5490.22	4234.177414	2628.574	1556.783

However, determining the ideal turbine diameter is more difficult. Looking at Table 8.17 it becomes clear that the 8 meter turbine has the highest production, while having a very large thrust difference between the turbines, compared to the 6 diameter turbine for example. To further determine which of these diameters is optimal, both will be placed in Delft 3D for a full tidal cycle at the Westerschelde. This is because the thrust difference is the most optimal for the 6 diameter turbine and the 8 diameter turbine because of the production score.

To implement the mesh with the turbines into Delft 3D, a nested model needs to be created. This nested model needs to be created because a mesh with the 6 meter turbines has a grid size of 6 meters and a mesh for the 8 meter turbines has a grid size of 8 meters. The grid made for the resource assessment has a grid size of 750 meters, so the model is nested using a much smaller grid. In Delft 3D for the location of the turbines a new boundary condition needs to be implemented, which is forced by a time series of currents. This time series is created with the use of observation points around the boundary. With the current velocities found the model can be run, using a time step of 0.1 to make sure the CFL coefficient is still accurate.

Before running the simulation with the turbines implemented, the water depth at this locations as well as the most common flow direction need to be determined. Because the flow is well aligned for both flood and ebb, the tidal turbines can be designed as a bi-directional system. The AD in Delft 3D is in a fixed position and the thrust is calculated by the axial velocity. Using a year-based resource assessment, it follows that the most common direction of water flow in the Westerschelde is 5.86 degree with respect to the North. The direction in which the turbines are placed is pictured in Figure 8.27. With the exact depth of this location being 16 meters, it is possible to determine the C_{loss} for Delft 3D, which represents the turbines. The results show that the 6m turbine corresponds with a C_{loss} of 0.2038, while the 8m turbine corresponds with a C_{loss} of 0.2823.

Table 8.18: The max thrust of the different rows for each of the diameters and array staggered layouts

Max thrust		8m	7m	6m	5m	4m	3m
array 7	Row 1	9608.159	7702.606	5767.918	4459.245908	2749.919	1614.582
	Row 2	9906.629	7857.296	5832.522	4477.382121	2694.423	1609.68
	Row 3	9091.282	7313.707	5431.334	4271.037843	2579.721	1571.806
array 8	Row 1	9608.159	7689.567	5775.73	4468.309413	2736.919	1617.309
	Row 2	9660.307	7689.567	5734.778	3833.654431	2682.473	1602.069
	Row 3	9002.849	7245.231	5452.192	4237.12037	2572.523	1565.359
array 9	Row 1	9611.414	7715.655	5781.592	4472.844617	2754.569	1618.946
	Row 2	9530.203	7614.16	5692.032	4394.560057	2790.976	1599.355
	Row 3	8668.89	7219.951	5433.228	4225.354682	2712.858	1563.213
array 10	Row 1	9614.67	7723.49	5787.457	4481.921925	2773.209	1622.222
	Row 2	10,226.45	8072.173	5962.81	4560.977368	2825.737	1629.881
	Row 3	9536.687	7627.135	5697.851	4390.064727	2839.89	1599.355
array 11	Row 1	9617.926	7726.103	5791.369	4472.844617	2773.209	1623.315
	Row 2	10,015.99	7939.191	5887.62	3889.855322	2825.737	1622.222
	Row 3	9569.142	7601.197	5661.044	4384.074532	2839.89	1595.56
array 12	Row 1	9423.532	7559.787	5593.554	4384.074532	2710.089	1595.018
	Row 2	8946.228	7202.281	5404.844	4203.338108	2620.4	1553.573
	Row 3	7635.091	6308.567	4865.313	3844.861892	2456.959	1486.931
array 13	Row 1	9627.698	7723.49	5795.282	4487.978575	2768.543	1624.955
	Row 2	9814.306	7802.061	5807.029	4469.820892	2753.639	1615.672
	Row 3	9465.482	7541.706	5643.651	4366.128484	2699.026	1591.228

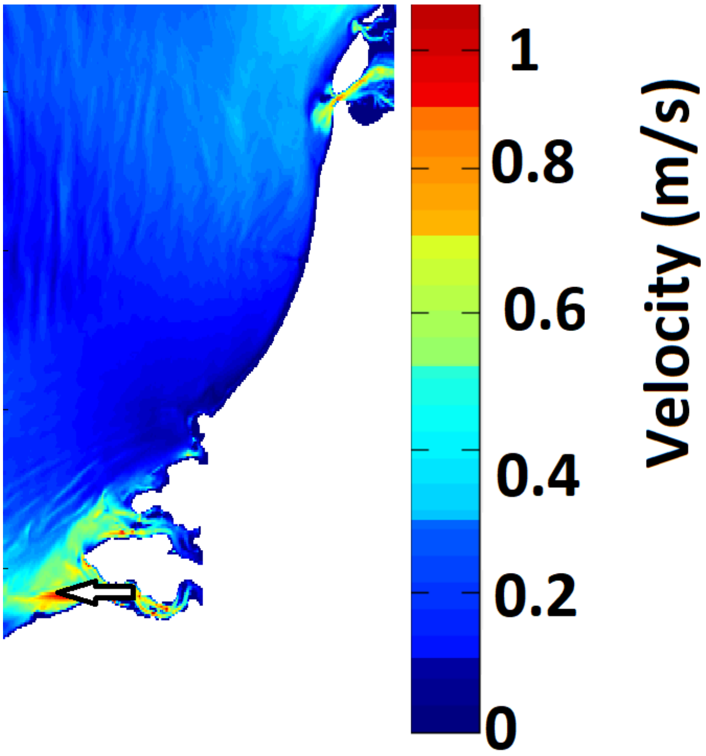

Figure 8.27: Turbine alignment with respect to the most common flow direction in the Westerschelde is shown with a arrow

Next, it is possible to determine the power production of an tidal cycle of 14 days. In Table 8.19 and Table 8.20 the average power production per hour is determined. With the power curves of the turbine known it is then possible to determine the capacity factor, which indicate the percentage of time the turbine is operating at full power. The formula for this is Equation 8.1:

$$C_f = \frac{T_{equivalent}}{T_{actual}} = \frac{T_{equivalent}}{\Delta T * MW_{installed}} \tag{8.1}$$

In this formula T_{actual} is the production that is achieved by coupling the turbine information and the resource data, while the $T_{equivalent}$ is the equivalent production to achieve the same production if the turbine is constantly at full power for a given time period ΔT year.

With this information it is possible to determine the generated amount of energy over a longer period of time. It is important for calculating the economics of the project and the levelized cost of energy. In Table 8.19 the capacity factor of the 6m turbine and in Table 8.19 the capacity factor of an 8m turbine are given.

Table 8.19: Power production and capacity factor of a tidal cycle for a 6 diameter turbine

8 m diameter	Potential (W)	Tot power (Wh)	Capacity factor	Thurst max (N)
Turbine 1	15,524.6451	6118.761	0.394132	6485.56
Turbine 2	15,524.6451	6291.226	0.405241	6428.78
Turbine 3	15,524.6451	6328.583	0.407647	6426.48
Turbine 4	15,524.6451	7043.483	0.453697	6675.04
Turbine 5	15,524.6451	6854.191	0.441504	6650.41
Turbine 6	15,524.6451	6558.116	0.422433	6624.89
Turbine 7	15,524.6451	6208.069	0.399885	6176.41
Turbine 8	15,524.6451	6194.243	0.398994	6215.99
Turbine 9	15,524.6451	6192.67	0.398893	6180.99
Total		57,789.34	0.413603	

Table 8.20: Power production and capacity factor of a tidal cycle for a 8 diameter turbine

6 m diameter	Potential (W)	Tot power (Wh)	Capacity factor	Thurst max (N)
Turbine 1	6385.136	2105.494	0.329749	3732.32
Turbine 2	6385.136	2187.533	0.342598	3720.10
Turbine 3	6385.136	2213.468	0.34666	3730.58
Turbine 4	6385.136	2478.165	0.388115	3797.45
Turbine 5	6385.136	2403.115	0.376361	3798.84
Turbine 6	6385.136	2235.944	0.350179	380.93
Turbine 7	6385.136	2100.598	0.328982	3640.05
Turbine 8	6385.136	2142.692	0.335575	3665.16
Turbine 9	6385.136	2159.295	0.338175	3665.73
Total		20,026.3	0.348488	

The tables show that the capacity factor of an 8m turbine is almost 8% higher than of that of a 6m turbine. Furthermore, when looking at the difference between the maximum thrust force on the turbine and support structure, it follows that for the 8m turbine there is a difference of 498.6N and for the 6m turbine there is a difference of 160.88N. This corresponds to a percentage difference for the 8m turbine of 7.47% and for the 6m turbine of 4.23%. Regarding the installation and construction costs of the different foundations, the 6 diameter turbine has the smallest difference between the turbines and therefore an optimal foundation can be designed for each turbine. Due to the fact that the difference in percentage between the turbine is so small the capacity factor has a much higher importance for the determination of the turbine diameters. The last parameter is the overall production of the farm. The 8m turbine produces almost 3 times more than the 6m turbine.

Looking at the average wake effect of the 8m turbine it can be clearly seen that before the second row of turbines the velocity actually increases and so the production of these turbines increases. In this figure the average velocity over time has been used to asses the wake effect. Due to the fact that an actual tidal cycle is used it can also be seen that the average velocity from the right to left direction is higher than from the left to right direction. The figure shows that with the use of the array configuration their is an increased production.

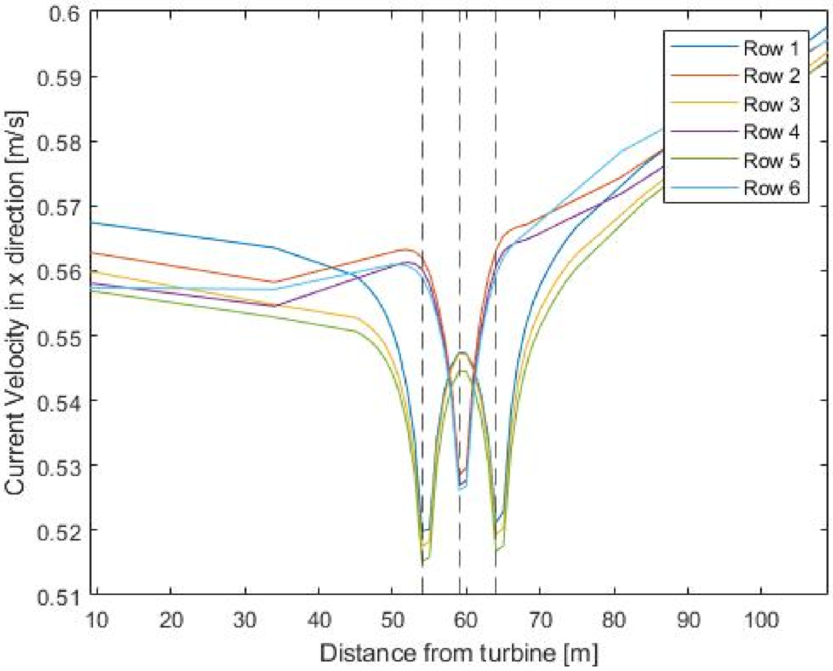

Figure 8.28: The average wake effect for a tidal cycle for a 8 m turbine (velocity is in magnitude)

8.4. Conclusion

Taking all these parameters into account, it can be concluded that the 8m turbine is the best turbine for the given location. Combined with array 10, this results in the highest energy production. Due to the fact that the location in the Westerschelde is a heavily traffic shipping route, the maximum turbine size that can be placed in this location is 8m. Increasing the size of the turbine will lead to a higher production, but it would mean that the turbine could not be placed at this location. In chapter 9 the economics of this farm are determined to see if the project is economically viable.

9

Economics for tidal arrays in The Netherlands

The economic feasibility of a Dutch tidal farm can be examined by calculating the capital expenditure (CAPEX), the operational expenditure (OPEX) and the decommissioning Cost (DECEX) cost of the tidal farm. From this, it is possible to calculate the levelized cost of energy (LCoE), Internal Rate of Return (IRR), Net Present Value (NPV) and Payback Period (PP). These calculations will show whether the tidal farm is a feasible investment. In this chapter the following subsection will be answered: ***"What are the economics of the project, is it possible to make the project economically viable?"***.

9.1. CAPEX

CAPEX stands for capital expenditures. With CAPEX it is possible to calculate the total initial costs required for designing and manufacturing the farm. This includes the design and definitions of the project, together with the development and construction of the project.

As for the installation, not only the foundation cost should be included, but also the vessel required for the installation at the location of the farm and the infrastructure for the cables' connection to the electrical grid. The costs are estimated based on literature about the costs of offshore wind farms and offshore tidal farms [92, 69]. Because the concept includes tidal turbines that have not yet been designed, the associated costs are also based on costs per MWh identified in the literature for tidal farms.

The manufacturing process for the tidal farm includes the manufacturing of the turbines and the foundation. Due to the small size of the turbines and thus for the foundation, it is possible to construct these two components and install the turbines on their foundation on the mainland. This will significantly reduce the total installation costs while only slightly increasing the manufacturing costs. The costs for the turbine, including the design and manufacturing, are estimated to be between €2 - 5 million Pounds according to [40, 42, 5, 73]. However, these costs are associated with turbines that have a diameter between 18 and 20 meters. Using these numbers for the smaller tidal farm it is important to calculate the cost per MWh. For the tidal turbines as used in Segura et al. [94] the CAPEX of the farm was around the 100 million. This farm includes 42 turbines each with an installed capacity of 1.2 MW. Using the CAPEX of this larger farm the price per MWh of this farm is €2 million. The CAPEX of the tidal farm designed in this thesis can therefore be calculated to be €300,000 for the entire farm, this is based on a linearly approach of costs.

Due to the fact that the scaling of the cost is not linear [97], when reducing the size of the turbines in the farm the cost per MW will be higher compared to that of larger farms. Therefore an estimation needs to be made. No literature was found with regards to the scaling effect on a tidal stream farm. From Smart et al. [97] the LCOE/per MWh can be determined with the use of the LCOE/per MWh cost for different sized farms. It is possible to determine the cost of the tidal farm designed of 0.1395 MW farm by calculating the slope in found in [97]. According to this source for a 1 MW farm the LCOE is 510 pounds per MW and for a 5 MW farm the LCOE is 425 pounds per MW. Using these numbers and Equation 9.2 is was calculated that the LCOE of a 0.1395 MW farm is around the 550 pound per MW in 2012.

$$Y = ax + b \tag{9.1}$$

Using the cost calculated above, the inflation rated since 2012 and the difference between the pound and euro, the LCOE of a 0.1395 MW farm in 2022 would:

$$550 * 1.03^{10} * 1.2 = \text{£}886 \tag{9.2}$$

In this formula the historical exchange rate between the pound and euro is 1.20 [32] and that the average inflation over the last 10 years was around the 3%.

With the LCOE known it is possible to determine the CAPEX of the farm. The CAPEX was estimated to be around the €5.5 million.

The installation process for the tidal farm requires a special vessel that is typically used for the installation of offshore wind farms. This vessel needs to be adjusted in order to perform installation and maintenance (O&M) tasks for the tidal farm. If such moderation's are not possible, the costs of the project will be significantly higher. Due to the fact that the size of the turbines and foundations is smaller than those of other tidal turbine vessel. The installation vessel for this farm will have a higher capacity, meaning that the installation vessel can transport and install multiple turbines. The transport vessel will therefore be used less often, which results in less shipping costs associated with the installation. The costs for the installation and transport of the turbines and under water cables are estimated to be around the €21,000,000 for 43 tidal turbines with a diameter of 20 meters [94]. Due to the smaller size of the turbine and the lower number of turbines used (9 turbine), the cost for adjusting and operating the installation vessel is therefore estimated to be around €1,200,000.

The turbines are constructed at the port of Vlissingen, which is 4 kilometers away from the site. [1] For the economics, the distance from the site to the port is an important cost indicator. Furthermore, the weather conditions influence the installation of the farm. It is important that the weather conditions are monitored and a good planning is required to make sure installation and finalization is possible at the location. Possible delays can occur due to weather conditions, which could increase the costs.

Other costs include the cost for securing an area to build the tidal farm, the design of the farm, research and project management costs. These different costs are presented in Table 9.1 This table also provides the calculation of the total CAPEX.

Table 9.1: The CAPEX of the tidal farm

Capex				Cost	Total cost
Concept and definition	Area used (m^2)	16	Cost per m^2	3,000	48,000
			Conception and design	100,000	100,000
			Project requirements specification cost	102,000	102,000
				Total	250,000
Manufacturing	Number of Tidal turbines	9	Cost per Tidal turbines	300,000	2,700,000
			Cost per foundation	50,000	450,000
	Length of cable (km)	5	Cost per km for array cable	90.000	450,000
				Total	3,600,000
Installation			Cost per port	450,000	450,000
	Days	2	Vessel cost per day	600,000	1,200,000
				Total	1,650,000
				Total	5,500,000

9.2. OPEX

OPEX stands for the operating expenditures. OPEX include the costs associated with operating the tidal farm on an ongoing base. First, the average lifetime of a tidal turbine needs to be estimated. Because not much investigation has been done on the OPEX costs of a tidal stream farms, most data has to be derived from literature about offshore wind farms.

The average lifetime of a wind turbine is 20 years, but can be extended to 25 years or more depending on the environmental conditions. For offshore bottom founded platforms the average lifetime is around 30 years. Tidal turbines have a life cycle quite similar to the life cycle of offshore wind turbines as well as of offshore

---

[1] In chapter 7 the viable ports for the tidal farms were included.

bottom founded platforms. It is therefore assumed that the lifetime of the tidal farm will be around 25 years. The exact estimation of the lifespan can be made when a full scale analysis of the turbines is performed. Testing and simulations of tidal turbines have shown that they are able to operate consistently over a period of 5 years.

A part of the OPEX are the maintenance costs, which need to be made to keep the turbines in a good state during its lifespan. The maintenance of the tidal farm consists of planned maintenance, preventive maintenance and corrective maintenance. The planned maintenance include blade cleaning, painting, checking systems. The actions are planned and are consistent over a certain time period. The preventive maintenance looks at replacing parts of the turbine that reach their end of life and inspecting the turbines and substructures. This type of maintenance occurs less often but is needed to extended the working life of a turbine. The last type of maintenance is corrective maintenance and relates to reparations of turbines when unexpected problems occur. This type of maintenance occurs the least, but the material costs will be the highest because more repairs need to be done.

Next, the operation and maintenance costs of the tidal farm need to be calculated. The array configuration and the size of the farm affect these costs significantly, because the spacing determines the costs of maintenance and operation. If the spacing between the turbine increases, the amount of exposed cables and manoeuvrability of the maintenance craft increases. But as determined in chapter 8, if the spacing is too small the wake of the turbines influences the power production of the turbines behind it. However, because this thesis focuses on the ideal configuration of the turbines, the operational and maintenance costs will not be a factor that influences the configuration of the turbines. Yet, these costs will of course be included in the calculations.

A number assumptions need to be made regarding the maintenance and operational costs. The first assumption is that the turbine will experience degradation over its lifetime, meaning that the energy production will decrease every year. As for costs associated with maintenance, the following is taken in to account. The distance the maintenance ship has to sail is not included in the calculations. This is because all possible farm locations were chosen within a certain distance from a port, meaning these costs can be neglected. It is also assumed that all maintenance costs are incurred constant over time, so that no unforeseeable costs occur during these operations. Moreover, it is assumed that when new parts are needed the replacement time is constant for all parts. Furthermore related to the smaller size of this tidal farm, it is assumed that economies of scale will arise so that the costs of maintenance per turbine will decrease. These costs are based on the estimation made by Segura [94] for a tidal farm consisting of 43 turbines. Knowing that the OPEX of a project is normally 10% of the CAPEX [76], the OPEX is determined using this percentage, as can be seen in Table 9.2.

Table 9.2: The OPEX of the tidal farm

OPEX			
Number of TEC	9	Cost	Total Cost
	Planned maintenance	33,000	297,000
	Preventive maintenance	23,375	210,375
	Corrective maintenance	9625	86,625
		Total	594,000

9.3. DECEX

Next, the decommissioning costs, also known as DECEX, need to be calculated. For this, some assumptions need to be made. The disposal costs together with the recycling income of the different parts of the farm are assumed to be equal to zero. The reason for this is that it is very difficult to predict these costs due to the uncertainties of the project, which are the result of lacking precedents. Similarly, the costs for the removal of the tidal farm are also hard to predict, as there has not yet been a tidal farm removal. Therefore, these costs are determined using offshore wind farm literature. This literature finds that the costs for site clearance for a farm are around the €0.9 million. Due to the much smaller size of the turbines and a smaller impact of the site, the costs will be much less. [40] assumes that the decommission costs are around €200,000 per turbine of 20m. From this, it is assumed that a cost of around €100,000 per 8 m turbine is proportional. There is also the possibility that with the renewal or modification of the turbines after the end of service the service life of the farm can be extended. The cost of energy will be divided by a longer time period, which would increase the income of the project. It needs to be mentioned that there are still lots of uncertainties around the costs of dismantling a tidal farm. In tab: DECEX the estimated decommissioning costs are shown.

Table 9.3: The DECEX of the tidal farm

DECEX			
Number of TEC	9	Cost	Total cost
	Decommissioning cost per TEC	100,000	900,000

9.4. Power production

The total power production per tidal cycle was determined in chapter 8. For the 8m turbine and array configuration 10, the total production generated by the 9 turbines over a tidal cycle is on average 57789.3 Wh or 57.79 kWh. This calculation does not take into account all the different tidal constituents that occur during the year. However, due to the computational time for a tidal cycle of 14 days and the consistency of the tidal cycles, it is assumed that the power production of 57.79 kWh is representative for the power production of an entire year. Table 9.4 presents the total energy production per turbine in kWh. Knowing the total energy production, it is possible to calculate the CAPEX, OPEX and DECEX, for which the calculations are presented in Table 9.5.

Table 9.4: The power production of the individual turbines

Turbine	production (Wh)
1	6,118.761
2	6,291.226
3	6,328.583
4	7,043.483
5	6,854.191
6	6,558.116
7	6,208.069
8	6,194.243
9	6,192.67
SUM	57,789.34
Cp	0.413603

Table 9.5: The CAPEX, OPEX and DECEX of the tidal farm

Cost in \euro	
CAPEX, total	5,500,000
OPEX, per year	594,000
DECEX, total	900,000

9.5. Feasibility analysis

After calculating the life cycle costs of the project and the annual energy production, a viability analysis can be performed. This analysis is done by using several economic and technical formulas, including calculating the break-even power, the Net Present Value (NPV), Payback Period (PP), the Internal Rate of Return (IRR) and the Levelized cost of energy (LCoE). The NPV and IRR are dependent on the market conditions, while the LCOE is not, which makes it the LCOE a robust tool to use for renewable energy projects. These parameters will be further explained in the following subsections.

9.5.1. Break even power

Break-even Power is the average power that the turbines must generate over their lifetime in order to make sure the project makes a break even over time. Break-even power can be calculated with Equation 9.3

$$ {}_{i=0}^{L} P_{BE} * T_e * t_i * n_t - Ex_i = 0 \tag{9.3} $$

$$P_{BE} = \frac{\sum_{i=0}^{L} Ex_i}{n_t * \sum_{i=0}^{L} (T_e * t_i)} \tag{9.4}$$

P_{BE} is the break even power, T_e is the electricity tariff, the price per kWh electricity is sold, t_i is the number of hours generating power throughout a year, L is the lifetime of the project,Ex_i is the sum of all the expenditure in a single year. At the moment the T_e is around the €0.70 according to [82]. The production determined is the average electricity production per hour over a 14 day period. The number of hours the turbine operates can be assumed to be 365*24. The total costs per year are the OPEX and the CAPEX and DECEX, divided over the lifetime.

If the P_{BE} reflects all of the costs associated with the project, it is possible to determine if adding an additional turbine would increase the profitability of the project. From this, the optimal amount of turbines can be determined. However, due to the fact that increasing the number of turbines decreases the production per turbine, an assumption needs to be made. When looking at Table 9.4, it can be seen that increasing the number of turbines in a row does not significantly decrease the production of the turbines. When increasing the number of turbine in a row the production of these turbines will be on average 6400 Wh, not taken into account the different rows.

9.5.2. Net Present Value (NPV)

Because the construction and placement of a tidal farm is a long term investment, it relies heavily on the discounted cash flow analysis that determines whether the worth of the money today is higher than the worth of the money in the future. Meaning that investors need to adjust the cash flows for time to compare the costs and revenues incurred at different time periods. This adjustment is done by using the NPV. The NPV is a measurement that sums all the incoming and outgoing cash flow for each year. The costs are then adjusted for the value of the cash at a certain time, also known as the discount rate over time. The NPV can be determined with the Equation 9.5

$$NPV = -C_0 + \sum_{t=1}^{n} \frac{C_t}{(1+r)^t} \tag{9.5}$$

In this formula C_0 is the initial investment, C_t is the net cash flow during a period t, r is the discount rate and n is the number of time periods. The discount rate r is the interest rate charged to determine the present value of future cash.

With the NPV it is possible to see what the value of money generated over time is. This is an important matrix to determine if an investment can give a positive return. Furthermore, the NPV can also include the effect of degradation on the turbine performance.[2] However, in this analysis the degradation of the performance of the turbine over time has not been taken into account. The metrix uses the average power generate per year, with uncertainties about installation and downtime it is assumed that the production for the NPV is constant.

9.5.3. Payback Period (PP)

The payback period (PP) metrics can be calculated from the NPV. The PP is the amount of years it will take to recover the investment, and therefore to break even. It is a useful characteristic that determines the risk of the project, because a project with a shorter payback period is considered to be a safer investment. The payback period is found by the following Equation 9.6.

$$PP = \frac{NPV_{cr}}{NPV_{cr} - NPV_{cr+1}} + i_{cr} \tag{9.6}$$

In the formula the NPV is determined for each year, this is done until the NPV becomes positive. The year the NPV becomes positive is the critical year (i_{cr}) and is the project break even year.

9.5.4. Internal Rate of Return (IRR)

The internal rate of return can be used to estimate the profitability of an investment. IRR determines a discount rate for the project. If the IRR is higher than the projected discount rate of the project, the investment will likely become profitable over the lifetime of the tidal farm. The IRR is not the euro value of the project, but the annual return that makes the NPV equal to zero and therefor looks at the profitability of the project.

---

[2] Due to for example downtime or reduced efficiency (algae).

The IRR can only be calculated with the use of an iterative process. The IRR is found by Equation 9.7. Excel is used to find the IRR value of the project.

$$0 = NPV = \sum_{t=1}^{t} \frac{C_t}{(1+i)^t} - C_0, i = IRR \tag{9.7}$$

The calculation of the IRR takes more computational time than the calculation of the NPV, PP or break even Power. For this thesis the computational difference is negligible. But it may become significant when there is an increase in the number of parameters and a larger number is required for the optimisation.

9.5.5. Levelized cost of energy (LCOE)

The LCoE is a tool that is often used to determine the suitability of renewable energy projects. This is done by comparing the costs of different projects over their economic life. This can help in ranking projects with different technologies and different economic life spans. The LCoE is the life cycle cost of the project divided by the lifetime of the energy production. The LCoE is the main metric of the feasibility analysis. This is due to the fact that many projects and organisations use this metric to estimate the lifetime cost of energy for a project. A problem with the other metrics is that they are highly influenced by uncertain parameters, such as the discount rate and the price of energy. The LCoE takes away these uncertainties, because the price of energy is not included. The formula for calculating the LCoE is given in Equation 9.8,

$$LCoE = \frac{LC_{total}}{LP_{total}} \tag{9.8}$$

$$LC_{total} = \sum_{t=1}^{n} \frac{CAPEX + OPEX}{(1+r)^t} \tag{9.9}$$

$$LP_{total} = \sum_{t=1}^{n} \frac{E_t}{(1+r)^t} \tag{9.10}$$

In this equation CAPEX are all the initial investment costs required for the project, and OPEX are the operation and maintenance cost during the life cycle of the project.[3] E_t is the annual energy production. Both CAPEX and OPEX are denoted as €and E_t is denoted as kWh

9.6. Results

With the above parameters discussed, the viability of the project can be assessed. First of the Break-even Power. In Table 9.6 the different parameters are shown and the Break-even Power is determined. The calculations show that the total energy production of the array must be 627.13 MWh in order to break even. This is higher than the total amount of energy produced by the farm, which was calculated to be 506.24 MWh in section 8.3.

Table 9.6: The power production of the individual turbines

Break even power		
T_e kWh	0.7	
L (years)	25	
t_i (hours)	8,760	
Ex_i (cost)	10,974,828.17	
P_{BE} (MWh)	69.68	Per turbine
P_{BE} (MWh)	627.13	Per array

Secondly, the NPV is discussed. The parameters required for the determination of the NPV can be seen in Table 9.7. With the Break-even Power metrics determined, it can be predicted that the NPV of the project will be negative. The data in Table 9.7 shows that the NPV has a value of €-2.28 million. The main reason for the negative NPV is because of the relatively high CAPEX of the project (compared to that of larger tidal farms).

The PP of the project shows how long it takes for the project to payback its initial investment (CAPEX). The OPEX and DECEX are not taken into account in the calculation of the PP. This metrics shows whether it

Table 9.7: NPV of a 8 m diameter turbine farm

NPV	
C_0 (£)	10,974,828.17
C_t (£)	354,364.43
n	25
Discount rate	0.1
i (years)	25
NPV ((€)	-2,283,419.88

Table 9.8: The PP of the tidal farm

PP	
CAPEX (€)	5,500,000
Cash flow (€)	354,364.43
PP (years)	15.52

is possible for the project to break even over its life time. In Table 9.8 it can be seen that the PP is 15.5 years, meaning that the initial investment is recovered within the total life time of the project, which is 25 years.

With the IRR it is possible to determine the ideal discount rate is. In Table 9.9 the IRR determined was 0.0406, which means that the IRR found is lower than the discount rate of 0.1. From this it can be concluded that according to the IRR metrics investing in this project will not economically viable. In this table, the same production is generated from year 3 till year 25.

Table 9.9: The IRR of the tidal farm for the break even power

Year 0	-5,500,000
Year 1	354,364.43
Year 2	354,364.43
Year 3	354,364.43
Year 25	354,364.43
IRR	0.0406

In Table 9.10 the LCOE of the project can be seen. From this, the income per kWh that would break even the project is determined. As can be seen in Table 9.10 for a price of €0.867 per kWh the project can break even. At the moment the cost per kWh is at the historically high point of €0.70 per kWh and the price is still rising at the moment. Meaning that the project with the current market environments would not economically viable.

Table 9.10: The LCoE of the tidal farm

LC0E	
r	0.1
t (year)	25
CAPEX (€)	5,500,000
OPEX (€)	594,000
DECEX (€)	900,000
$E_t(kW$	139.72
LC total (€per kWH)	10,974,828.17
LP total (kWh)	12,655,872
LCOE (€)	0.867

---

[3] A problem with the OPEX data is that because of the lack of data of tidal farms, these values have a high uncertainty.

9.7. Conclusion

Looking at all the above metrics, it can be concluded that placing a tidal stream farm in The Netherlands without subsidies is not economically viable in the current environment. The main reason for this it that the amount of electricity that can be produced is not high enough for the farm to be viable.

However, although the farm may not be economically viable, it is still important to acknowledge the upsides from constructing such a tidal farm. Looking into the effect of the electricity produced by the tidal farm on the electricity network, it potentially provides a big positive impact. Therefore, when assessing the viability of a tidal farm not only the economics should be considered.

Unlike other sustainable energy resources, the electricity produced by the tidal farm is very predictable over time. Looking at the energy transition, the tidal farm could be used to fill in the gaps that are created due to the unpredictability of the other sustainable energy sources. Furthermore, the current geopolitical landscape is making it increasingly clear that it is important for nations to become more self-sufficient and therefore independent in generating their own electricity. Due to the fact that tidal energy is so consistent and predictable, it can be used to become more self-sufficient and make The Netherlands less reliant on fossil fuels. Tidal energy could indeed be a good addition to the energy transition, but increased production is needed to make it viable in the long run. Furthermore, government subsidies would be needed to make the profitable with the current price per kWh. Unfortunately, the break-even point without subsidies is slightly higher at this moment, if the current price per kWh will stay at this level or even rise further with relatively small amounts of subsidies a tidal farms at low tidal resource areas could be built in the near future.

With the information gathered in this chapter, the sub question as stated at the beginning of the chapter can be answered as follows. Acknowledging the positive side effect of the tidal farm and the economics the placement of a tidal farm in The Netherlands under the current circumstance would be not economically viable without government subsidies.

10

Conclusion and Discussion

In the following chapter the conclusion and discussion are described. This chapter therefore answers the main research question: ***"What is the best location and design for a Tidal farm in The Netherlands?"***.

10.1. Conclusion

In this study the resource potential of a tidal farm in The Netherlands with its low velocity currents is assessed. The first part of the study focuses on the creation of a model that can be applied to the case of The Netherlands.

Two models, namely Delft 3D and Telemac, were used to create a model for The Netherlands. An analysis was performed in both models to understand the impact of bottom friction over the whole grid. Next, the model was compared to the tidal gauge data that was gathered from DDB. This data only represents the water level elevation for a specific location. The analysis consisted of computing the RMSE, SI index and Pearson coefficients to see the effect of the different bottom friction coefficients and to determine which bottom friction coefficient is the most accurate. With Delft 3D it was found that the Manning 0.05 overall had the best comparison with the different tidal gauge stations, while Telemac indicated that the Manning 0.11 overall had the best comparison.

With these optimal bottom friction coefficients identified for both models, it was possible to perform a resource assessment, from which the velocity potential and ranges were determined. Subsequently, it was important to compare both models with each other to understand the differences and explain what caused them. The comparison included computing the RMSE, SI index and Pearson coefficient for the velocities found. The RMSE and SI index showed that Delft 3D has a slightly better overall fit with the tidal gauge data. However, the Pearson coefficient indicated that Telemac provided the better fit. As for the velocities found in both programs, the Delft 3D model reported much higher velocities than the Telemac model did. Lastly, the Delft 3D model has a better fit with the tidal gauge data. Considering the above, Delft 3D was selected as the model of choice for the remainder of the thesis.

The next phase was to determine the optimal location for the tidal farm. The methodology included the use of restricted criteria on the one hand and weighted criteria one the other hand. The restricted criteria were used to exclude certain areas within The Netherlands from the possible tidal farm locations. The weighted criteria were then used to evaluate the remaining locations, indicating what locations had the highest potential. Next, an AHP method was used to evaluate the different criteria and locations. Among the weighted criteria, the tidal current and capacity factor of the flow were identified as the most important for finding the most optimal locations. Eventually, the Westerschelde was identified to be the preferred location, because this location has the overall has the highest current velocity.

Subsequently, it was possible to determine the most ideal turbine size and array, based on the characteristics of the Westerschelde. The rated velocity at this location was used as a forcing in the model, to determine the most optimal array. Next, the wake effect and the production of the different turbines in the array were evaluated. After evaluating multiple configurations, a staggered array with a spacing of 4D between the turbines and 4D between the rows was proven to yield the highest production. Noteworthy is that literature predicted that a staggered array with a spacing of 5D between the turbines and 10D between the rows would be the most optimal turbine configuration. However, simulations for the low tidal resource showed that the smaller array has a 8.5% higher production than the larger array.

Next the forces on the tidal turbines for the different arrays were analysed. in order to reduce the costs for the foundation the ideal turbine size has a small difference between the thrusts of the different turbines in array. Using the rated velocity, the 6 and 8 diameter turbines performed best in the simulation on the factors thrust and production, respectively. When comparing these two turbines for a full tidal cycle, the 8 diameter turbine emerged as the superior turbine.

The ideal turbine diameter was identified by forcing a full tidal cycle on the array configuration for a 8- and 6 diameter turbine. Here it was found that the capacity factor of the 8 diameter turbine was 6.5 % higher. Looking into the thrust difference it was found that the 8 diameter turbine has a smaller thrust difference for a tidal cycle compared to the 6 diameter turbine. The ideal turbine size for the therefor the 8 diameter turbine, also taken into account that a larger turbine cannot be placed at the location due to the water depth at these locations.

Having determined the size and set up of the turbines, it was possible to calculate the power production for a full tidal cycle and thus to assess the economic feasibility of the tidal farm. Using a scala of economic metrics, it was found that the power production is sligtly too low for the project to become economically viable over its lifetime without subsidies. For the project to become economically viable, the price of electricity would need to reach €0.867 per kWh, with the current price increasing this price level could be reached in the near future. Furthermore, tidal energy has a number of non economical- and unquantifiable advantages over other renewable energy sources that are important to consider in the design of the future energy mix for the Netherlands. These advantages include the fact that tidal energy is sustainable and predictable. Therefore, Dutch tidal farms in low resource areas show potential but further technological-, economical- and geopolitical developments in the coming years will need to happen for them to become sufficiently beneficial to the Dutch energy transition to a sustainable energy mix.

10.2. Discussion

This section focuses on assumptions made for the thesis, and gives recommendations for further research.

Firstly, for the forcing of the model, only tidal constituents were taken into account. The constituents are very constant over time and therefore create a predictable tidal velocity over time. Only using constituents, however, is a simplification of the actual tidal flow because it does not take into account waves, wind and barometric pressure differences. Using all these factors will result in higher simulated velocities, thus resulting in a potential higher estimated electricity production. For future research it would be interesting to also take the other parameters into account.

Secondly, an extensive research focusing on varying local bottom friction coefficients could result in a more sophisticated model. Using such coefficients would most likely for some locations result in a lower bottom friction coefficients, which in turn would lead to higher simulated velocities for these locations in the model.

Thirdly, in this thesis data on water elevation was used to compare the models used. This data originated both from EMODnet, which includes wave, wind and barometric forcing, and from DDB, which only includes tidal forcing. For the sensitivity analysis of the resource assessment, the current velocity is an important parameter. However, since no data was available on the velocity profile at a certain location, a comparison between the model and the current velocity could not be conducted. It is therefore possible that both models, especially the Telemac model, overestimated the bottom friction coefficients. The velocity ranges found in the analysis were lower than velocity ranges measured in real conditions. For future research, it would be interesting to simulate the ideal bottom friction coefficients for both Telemac and Delft 3D.

Moreover, the models in the thesis are 2D models. It would be interesting to see the resource assessment using a 3D model, and in this model simulate a turbine that is also dependent on the depth of the water and to assess whether the energy production can be increased.

Also, the MCDM uses the AHP model based on criteria and scores identified in literature. For future research, a new AHP model could be created specifically for low tidal farms, in order to give a more precise insight in these criteria and weights. Such a research could be qualitative, using experts opinions to determine the scores of the criteria.

In addition, for the turbine design an assumption was made for the thrust coefficient. Because it was not possible in Delft 3D to have a time varying thrust coefficient, the C_{loss} variable was determined by thrust coefficients of an already constructed turbine. Using a time varying thrust coefficient could lead to possibility higher production of the turbine. Furthermore, due to the dependency of the C_{loss} component on the thrust coefficient, the Betz limit for the turbine was not reached. In future research the ideal C_{loss} should be determined, which would also potentially increase the production.

Furthermore, the foundation and turbines could not be simulated in detail, so that the exact effect of the design could not be assessed. A better design for the support structure could reduce the drag force of the turbine and so reduce the costs of the turbine. In Delft 3D the power production is slightly underestimated, which is due to the dependency of the C_{loss} on both the thrust coefficients and the drag force of the support structure. In future research, these effects should be further analysed to see if the electricity production could be increased by optimising the design.

Moreover, during the assessment of the economic viability no government subsidies were taken into account. Due to the positive effect that tidal energy can have on the energy transition, it would be reasonable to assume that subsidies for tidal energy would be more relatively higher than is the case for other green energy resources. With the information now available, it is not possible to include such subsidies in the analysis.

For the determination of the CAPEX the scaling of the CAPEX from larger to smaller turbine projects is not known. Due to this for the CAPEX it is assumed that the CAPEX can be determined with the use of the LCOE curve found. With the LCOE found for the size of the farm it is assumed that from this the CAPEX can calculated, while in reality the CAPEX would need to be determined by calculating the exact cost for the installation of a tidal farm.

Lastly, the most interesting finding of the thesis is that placing the turbines closer together increased the production of the tidal farm. The reason for this is that due to the turbine wake after the first row, there is an increased velocity which increases the production of the tidal farm. For future study, more in depth research should be conducted to see what the exact effect of the wake is on the turbines and to see whether there is potential in further increasing the production of the turbines.

A

Project planning

To make the thesis successful it is important to make, use and keep track of a planning. In this chapter the different choices with regards to planning and mitigation when delays occur will be explained. The planning is made with the use of a Gantt Chart A.1.

The first part of the thesis was to determination the location for the tidal converters and to determine the potential of this location. After the literature review, in which the criteria for the location were determined, the value of these criteria can be found with GIS data. The location that was found can be validated with the use of Telemac and Delft 3D. When the location has been determined and checked a model will be created with and without the AD, and the data from the model will be analysed.

Because the author has little experience with the these applications a week is used to learn the Delft 3D and Telemac. With the use of the literature report a start for the MCDM was made. Moreover, when the best locations for tidal energy in The Netherlands are determined, it will be possible to create different configurations of tidal converters to determine the loads and energy production through the use of Delft 3D and Telemac. When the energy production of the tidal farms has been determined a cost analysis must be conducted to establish whether or not the tidal energy farm is economically viable in The Netherlands.

In the project planning extra time was included for mitigation that maybe necessary. This can for example happen when problems occur with Deft 3D or Telemac. To make sure these problems are limited, a data log was created to see what steps have been taken and to easily determine the origin of errors when they occur. Writing of the thesis started after the first design is created. The time required for the writing of the thesis will increase over time when more research has been further progressed.

The weeks before the green light meeting were used to clarify the thesis and to include the feedback that will be given. If after the green light meeting additional requirements are needed a second clarification of the thesis were made. After the green light for the report has been given the presentation and defence prepared.

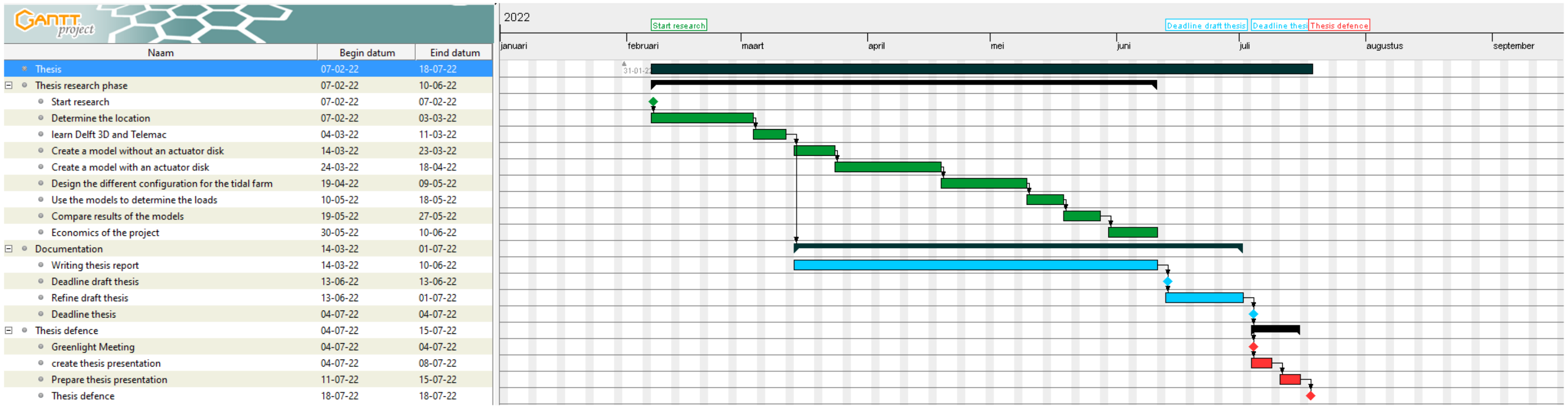

Naam	Begin datum	Eind datum
Thesis	07-02-22	18-07-22
Thesis research phase	07-02-22	10-06-22
Start research	07-02-22	07-02-22
Determine the location	07-02-22	03-03-22
learn Delft 3D and Telemac	04-03-22	11-03-22
Create a model without an actuator disk	14-03-22	23-03-22
Create a model with an actuator disk	24-03-22	18-04-22
Design the different configuration for the tidal farm	19-04-22	09-05-22
Use the models to determine the loads	10-05-22	18-05-22
Compare results of the models	19-05-22	27-05-22
Economics of the project	30-05-22	10-06-22
Documentation	14-03-22	01-07-22
Writing thesis report	14-03-22	10-06-22
Deadline draft thesis	13-06-22	13-06-22
Refine draft thesis	13-06-22	01-07-22
Deadline thesis	04-07-22	04-07-22
Thesis defence	04-07-22	15-07-22
Greenlight Meeting	04-07-22	04-07-22
create thesis presentation	04-07-22	08-07-22
Prepare thesis presentation	11-07-22	15-07-22
Thesis defence	18-07-22	18-07-22

Figure A.1: Planning of the thesis

B

Change coordinates system

The steps taken to get the correct coordinate system for BK. In ArcMap the toolbox, spatial analyst tools - extraction - sample need to be used. With this toolbox it is possible to get reform the GEBCO data to an output table in ArcMap. The data can be extracted to Excel and the columns that are required, X and Y coordinated. are found. The data is implemented back into ArcMap and needs to be displayed in the correct coordinate syste, WGS 1984. With the toolbox, projections and transformations, the projected coordinate system can be changed to the coordinate system reflecting the required location, WGS 1972 UTM zone 31N. With the new table found it is possible to calculate the geometry and set the coordinate system from degrees to meters. The columns are extracted in Excel and save as an .xyz file to be implemented into Delft 3D.

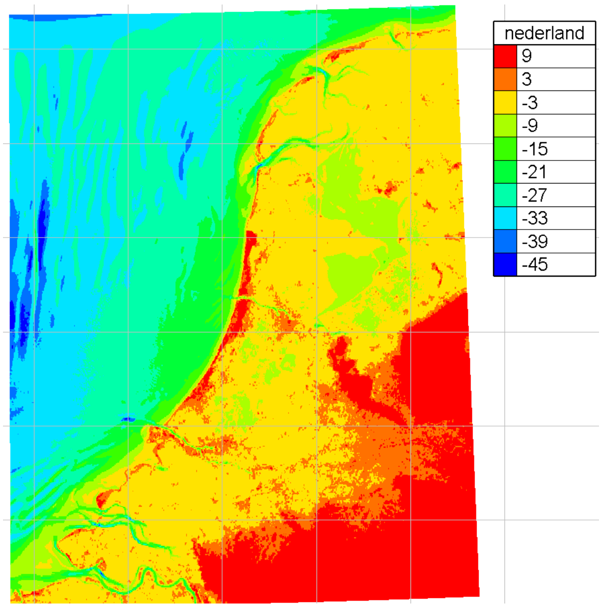

Figure B.1: GEBCO data implemented in Telemac

C

Telemac

Table C.1: All parameters used in the Telemac steering file

Telemac	Value
PARALLEL PROCESSORS	= 3
TITLE	=’Netherlands’
COMPUTATION CONTINUED	= NO
NUMBER OF TIME STEPS	= 293760
TIME STEP	= 10.0
SPATIAL PROJECTION TYPE	= 2
GEOMETRY FILE	=’mesh_nl.slf’
STEERING FILE	=’Telemac_manning40.cas’
BOUNDARY CONDITIONS FILE	=’bound_nl.cli’
RESULTS FILE	=’Manning\resultsmanning40.res’
BINARY DATABASE 1 FOR TIDE	=’hf.ES2008.out’
BINARY DATABASE 2 FOR TIDE	=’uv.ES2008.out’
INITIAL CONDITIONS	= ’TPXO SATELLITE ALTIMETRY’
OPTION FOR LIQUID BOUNDARIES	= 1
LAW OF BOTTOM FRICTION	= Chezy/Manning
INFORMATION ABOUT SOLVER	=YES
LISTING PRINTOUT PERIOD	= 60
GRAPHIC PRINTOUT PERIOD	= 60
VARIABLES FOR GRAPHIC PRINTOUTS	= U,V,H,S,F,B
/INITIAL TIME SET TO ZERO	=YES
ORIGINAL DATE OF TIME	=2016;01;01
ORIGINAL HOUR OF TIME	=00;00;00
TIDAL DATA BASE	= 2
OPTION FOR TIDAL BOUNDARY CONDITIONS	= 1
COEFFICIENT TO CALIBRATE TIDAL RANGE	= 0.9
COEFFICIENT TO CALIBRATE TIDAL VELOCITIES	= 0.95
COEFFICIENT TO CALIBRATE SEA LEVEL	= 2.52
TIDAL FLATS	= YES
OPTION FOR THE TREATMENT OF TIDAL FLATS	= 1
OPTION FOR LIQUID BOUNDARIES	= 1
BOTTOM SMOOTHINGS	=1
SOLVER	= 1
SOLVER ACCURACY	=1.E-3
MAXIMUM NUMBER OF ITERATIONS FOR SOLVER	= 500
MAXIMUM NUMBER OF ITERATIONS FOR ADVECTION SCHEMES	= 50
MATRIX STORAGE	= 3
DISCRETIZATIONS IN SPACE	= 11 ; 11
TYPE OF ADVECTION	= 1;5
FREE SURFACE GRADIENT COMPATIBILITY	= 0.9
TREATMENT OF THE LINEAR SYSTEM	= 2
SUPG OPTION	= 0;0
SOLVER OPTION	= 3
CONTINUITY CORRECTION	= true
TREATMENT OF NEGATIVE DEPTHS	= 2
WATER DENSITY	= 1025
MINOR CONSTITUENTS INFERENCE	= true
MASS-LUMPING ON H	= 1
MASS-BALANCE	= true
VELOCITY PROFILES	=1

In the following tables the analysis of different tidal stations can be seen. Here the RMSE, Pearson coefficient and the scatter index for the different bottom roughness can calculated.

Table C.2: RMSE, Pearson and Scatter index of the tidal station Brouwers Havensche Gat, Chezy 34-60 and Manning 0.03-0.05

Brouwer	Chezy 34	Chezy 44	Chezy 60	Manning 0.03	Manning 0.035	Manning 0.04	Manning 0.045	Manning 0.05
RMSE	0.4691	0.4719	0.4704	0.4701	0.4697	0.4687	0.4670	0.4646
Pearson	0.8480	0.8437	0.8437	0.8447	0.8456	0.8471	0.8493	0.8523
Scatter index	60.4538	60.8168	60.6224	60.5830	60.5332	60.4044	60.1855	59.8741

Table C.3: RMSE, Pearson and Scatter index of the tidal station Brouwers Havensche Gat, Manning 0.06-0.13

Brouwer	Manning 0.06	Manning 0.07	Manning 0.08	Manning 0.09	Manning 0.1	Manning 0.11	Manning 0.12	Manning 0.13
RMSE	0.4579	0.4495	0.4405	0.4313	0.4224	0.4141	0.4066	0.4000
Pearson	0.8603	0.8704	0.8817	0.8935	0.9055	0.9171	0.9283	0.9387
Scatter index	59.0113	57.9382	56.7692	55.5896	54.4459	53.3754	52.4038	51.5509

Table C.4: RMSE, Pearson and Scatter index of the tidal station Euro platform, Chezy 34-60 and Manning 0.03-0.05

Euro	Chezy 34	Chezy 44	Chezy 60	Manning 0.03	Manning 0.035	Manning 0.04	Manning 0.045	Manning 0.05
RMSE	0.2692	0.2874	0.3098	0.3084	0.2973	0.2877	0.2793	0.2719
Pearson	0.8887	0.8718	0.8485	0.8502	0.8621	0.8718	0.8798	0.8864
Scatter index	52.8385	56.4178	60.8047	60.5372	58.3668	56.4669	54.8161	53.3771

Table C.5: RMSE, Pearson and Scatter index of the tidal station Euro platform, Manning 0.06-0.13

Euro	Manning 0.06	Manning 0.07	Manning 0.08	Manning 0.09	Manning 0.1	Manning 0.11	Manning 0.12	Manning 0.13
RMSE	0.2597	0.2499	0.2416	0.2345	0.2282	0.2225	0.2172	0.2122
Pearson	0.8968	0.9048	0.9111	0.9163	0.9208	0.9248	0.9284	0.9317
Scatter index	50.9824	49.0469	47.4288	46.0351	44.8002	43.6772	42.6330	41.6480

Table C.6: RMSE, Pearson and Scatter index of the tidal station K13 alpha, Chezy 34-60 and Manning 0.03-0.05

K13	Chezy 34	Chezy 44	Chezy 60	Manning 0.03	Manning 0.035	Manning 0.04	Manning 0.045	Manning 0.05
RMSE	0.2262	0.2279	0.2304	0.2305	0.2292	0.2283	0.2276	0.2269
Pearson	0.8538	0.8508	0.8468	0.8467	0.8487	0.8503	0.8516	0.8528
Scatter index	62.7878	63.2680	63.9503	63.9950	63.6414	63.3849	63.1783	62.9823

Table C.7: RMSE, Pearson and Scatter index of the tidal station K13 alpha, Manning 0.06-0.13

K13	Manning 0.06	Manning 0.07	Manning 0.08	Manning 0.09	Manning 0.1	Manning 0.11	Manning 0.12	Manning 0.13
RMSE	0.2254	0.2237	0.2220	0.2203	0.2186	0.2169	0.2154	0.2138
Pearson	0.8552	0.8577	0.8602	0.8627	0.8651	0.8673	0.8695	0.8715
Scatter index	62.5661	62.1107	61.6356	61.1571	60.6857	60.2274	59.7863	59.3651

Table C.8: RMSE, Pearson and Scatter index of the tidal station Meetpost Noordwijk, Chezy 34-60 and Manning 0.03-0.05

Meetpost	Chezy 34	Chezy 44	Chezy 60	Manning 0.03	Manning 0.035	Manning 0.04	Manning 0.045	Manning 0.05
RMSE	0.3246	0.3168	0.3094	0.3082	0.3117	0.3152	0.3186	0.3218
Pearson	0.8255	0.8272	0.8339	0.8353	0.8320	0.8294	0.8279	0.8278
Scatter index	66.7683	65.1746	63.6565	63.4122	64.1146	64.8450	65.5446	66.2000

Table C.9: RMSE, Pearson and Scatter index of the tidal station Meetpost Noordwijk, Manning 0.06-0.13

Meetpost	Manning 0.06	Manning 0.07	Manning 0.08	Manning 0.09	Manning 0.1	Manning 0.11	Manning 0.12	Manning 0.13
RMSE	0.3277	0.3332	0.3386	0.3439	0.3493	0.3546	0.3600	0.3653
Pearson	0.8312	0.8382	0.8476	0.8581	0.8687	0.8787	0.8879	0.8960
Scatter index	67.4121	68.5529	69.6556	70.7507	71.8484	72.9517	74.0544	75.1463

Table C.10: RMSE, Pearson and Scatter index of the tidal station Terschellinger BAIHO, Chezy 34-60 and Manning 0.03-0.05

Terschellinger	Chezy 34	Chezy 44	Chezy 60	Manning 0.03	Manning 0.035	Manning 0.04	Manning 0.045	Manning 0.05
RMSE	0.2467	0.2387	0.2295	0.2319	0.2358	0.2398	0.2433	0.2459
Pearson	0.9541	0.9490	0.9450	0.9439	0.9460	0.9478	0.9499	0.9522
Scatter index	42.6280	41.2481	39.6482	40.0628	40.7461	41.4301	42.0288	42.4909

Table C.11: RMSE, Pearson and Scatter index of the tidal station Terschellinger BAIHO, Manning 0.06-0.13

Terschellinger	Manning 0.06	Manning 0.07	Manning 0.08	Manning 0.09	Manning 0.1	Manning 0.11	Manning 0.12	Manning 0.13
RMSE	0.2493	0.2515	0.2539	0.2570	0.2610	0.2661	0.2722	0.2792
Pearson	0.9576	0.9624	0.9660	0.9680	0.9687	0.9680	0.9660	0.9629
Scatter index	43.0699	43.4609	43.8739	44.4050	45.0983	45.9705	47.0215	48.2434

Table C.12: RMSE, Pearson and Scatter index of the tidal station Texel Noordzee, Chezy 34-60 and Manning 0.03-0.05

Texel	Chezy 34	Chezy 44	Chezy 60	Manning 0.03	Manning 0.035	Manning 0.04	Manning 0.045	Manning 0.05
RMSE	0.3154	0.3292	0.3399	0.3402	0.3349	0.3293	0.3234	0.3171
Pearson	0.8801	0.8517	0.8363	0.8358	0.8424	0.8515	0.8628	0.8757
Scatter index	56.8767	59.3661	61.3077	61.3533	60.3905	59.3977	58.3289	57.1849

Table C.13: RMSE, Pearson and Scatter index of the tidal station Texel Noordzee, Manning 0.06-0.13

Texel	Manning 0.06	Manning 0.07	Manning 0.08	Manning 0.09	Manning 0.1	Manning 0.11	Manning 0.12	Manning 0.13
RMSE	0.3048	0.2952	0.2889	0.2859	0.2857	0.2880	0.2925	0.2987
Pearson	0.9028	0.9268	0.9449	0.9570	0.9639	0.9665	0.9656	0.9617
Scatter index	54.9701	53.2340	52.1039	51.5554	51.5256	51.9460	52.7492	53.8718

Table C.14: RMSE, Pearson and SI score of the different bottom friction coefficient for the different tidal stations.

		Brouwers havensche Gat	Euro platform	K13	Meetpost	Terschellinger BAIHO	Texel
Chezy 34	RMSE (m)	0.469	0.269	0.226	0.325	0.247	0.315
	R^2(Pearson)	0.848	0.889	0.854	0.826	0.954	0.880
	SI (%)	60.454	52.838	62.788	66.768	42.628	56.877
Chezy 44	RMSE (m)	0.472	0.287	0.228	0.317	0.239	0.329
	R^2(Pearson)	0.844	0.872	0.851	0.827	0.949	0.852
	SI (%)	60.817	56.418	63.268	65.175	41.248	59.366
Chezy 60	RMSE (m)	0.470	0.310	0.230	0.309	0.229	0.340
	R^2(Pearson)	0.844	0.848	0.847	0.834	0.945	0.836
	SI (%)	60.622	60.805	63.950	63.657	39.648	61.308
Manning 0.03	RMSE (m)	0.470	0.308	0.231	0.308	0.232	0.340
	R^2(Pearson)	0.845	0.850	0.847	0.835	0.944	0.836
	SI (%)	60.583	60.537	63.995	63.412	40.063	61.353
Manning 0.035	RMSE (m)	0.470	0.297	0.229	0.312	0.236	0.335
	R^2(Pearson)	0.846	0.862	0.849	0.832	0.946	0.842
	SI (%)	60.533	58.367	63.641	64.115	40.746	60.390
Manning 0.04	RMSE (m)	0.469	0.288	0.228	0.315	0.240	0.329
	R^2(Pearson)	0.847	0.872	0.850	0.829	0.948	0.852
	SI (%)	60.404	56.467	63.385	64.845	41.430	59.398
Manning 0.045	RMSE (m)	0.467	0.279	0.228	0.319	0.243	0.323
	R^2(Pearson)	0.849	0.880	0.852	0.828	0.950	0.863
	SI (%)	60.186	54.816	63.178	65.545	42.029	58.329
Manning 0.05	RMSE (m)	0.465	0.272	0.227	0.322	0.246	0.317
	R^2(Pearson)	0.852	0.886	0.853	0.828	0.952	0.876
	SI (%)	59.874	53.377	62.982	66.200	42.491	57.185
Manning 0.06	RMSE (m)	0.458	0.260	0.225	0.328	0.249	0.305
	R^2(Pearson)	0.860	0.897	0.855	0.831	0.958	0.903
	SI (%)	59.011	50.982	62.566	67.412	43.070	54.970
Manning 0.07	RMSE (m)	0.450	0.250	0.224	0.333	0.252	0.295
	R^2(Pearson)	0.870	0.905	0.858	0.838	0.962	0.927
	SI (%)	57.938	49.047	62.111	68.553	43.461	53.234
Manning 0.08	RMSE (m)	0.440	0.242	0.222	0.339	0.254	0.289
	R^2(Pearson)	0.882	0.911	0.860	0.848	0.966	0.945
	SI (%)	56.769	47.429	61.636	69.656	43.874	52.104
Manning 0.09	RMSE (m)	0.431	0.235	0.220	0.344	0.257	0.286
	R^2(Pearson)	0.894	0.916	0.863	0.858	0.968	0.957
	SI (%)	55.590	46.035	61.157	70.751	44.405	51.555
Manning 0.1	RMSE (m)	0.422	0.228	0.219	0.349	0.261	0.286
	R^2(Pearson)	0.905	0.921	0.865	0.869	0.969	0.964
	SI (%)	54.446	44.800	60.686	71.848	45.098	51.526
Manning 0.11	RMSE (m)	0.414	0.223	0.217	0.355	0.266	0.288
	R^2(Pearson)	0.917	0.925	0.867	0.879	0.968	0.967
	SI (%)	53.375	43.677	60.227	72.952	45.971	51.946
Manning 0.12	RMSE (m)	0.407	0.217	0.215	0.360	0.272	0.292
	R^2(Pearson)	0.928	0.928	0.870	0.888	0.966	0.966
	SI (%)	52.404	42.633	59.786	74.054	47.022	52.749
Manning 0.13	RMSE (m)	0.400	0.212	0.214	0.365	0.279	0.299
	R^2(Pearson)	0.939	0.932	0.872	0.896	0.963	0.962
	SI (%)	51.551	41.648	59.365	75.146	48.243	53.872

The following figures show the comparison of the different tidal station with their respective tidal gauge data. In these figures it can be seen if the data is in phase and where the difference occurs.

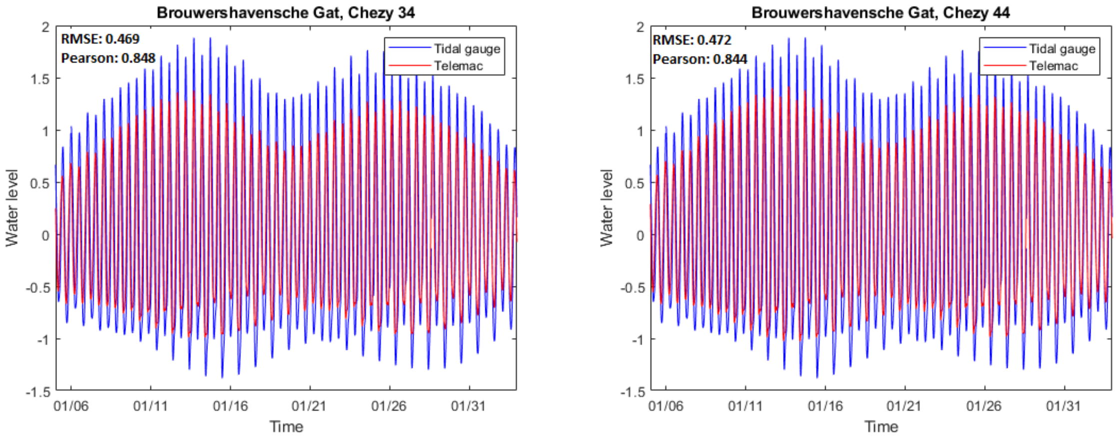

(a) Comparison between tidal gauge data and Delft 3D Chezy 34

(b) Comparison between tidal gauge data and Delft 3D Chezy 44

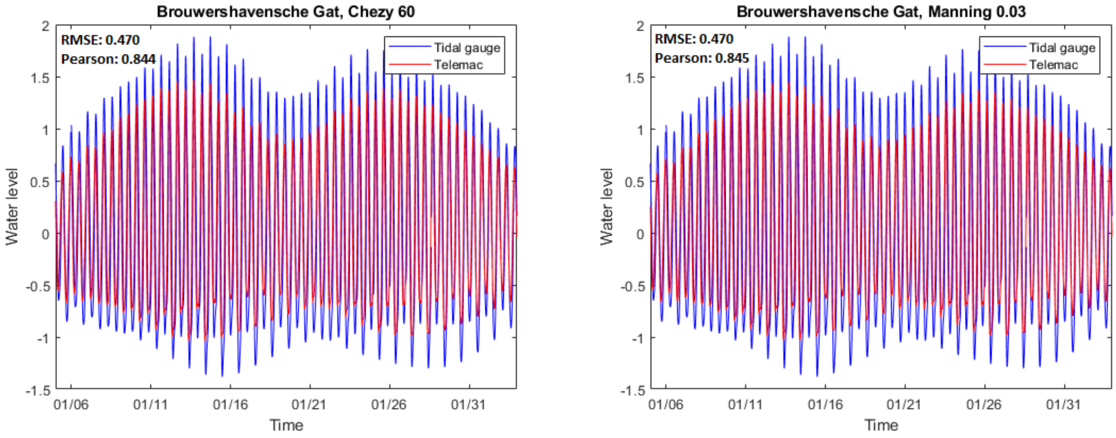

(c) Comparison between tidal gauge data and Delft 3D Chezy 60

(d) Comparison between tidal gauge data and Delft 3D Manning 0.03

Figure C.1: The comparison between the tidal station Brouwers Havensche Gat and the different Delft 3D models, Chezy 34-60 and Manning 0.03

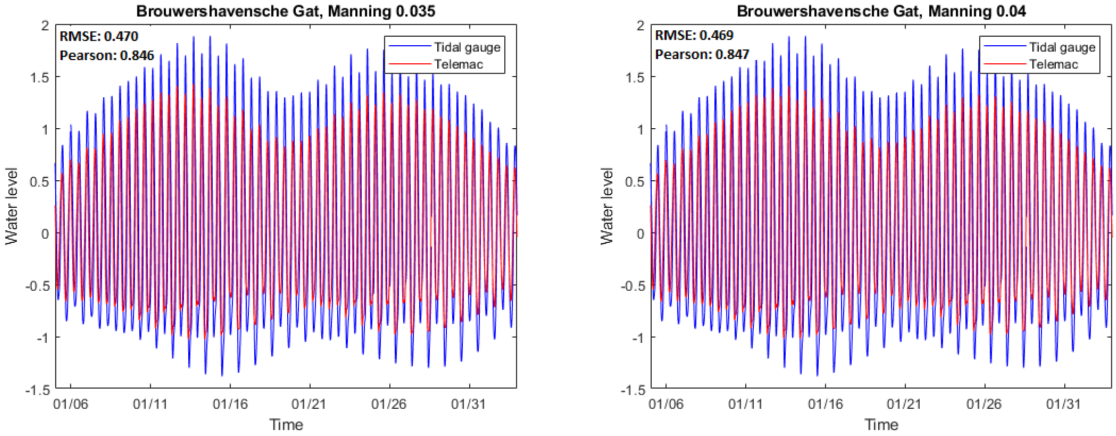

(a) Comparison between tidal gauge data and Delft 3D Manning 0.035

(b) Comparison between tidal gauge data and Delft 3D Manning 0.04

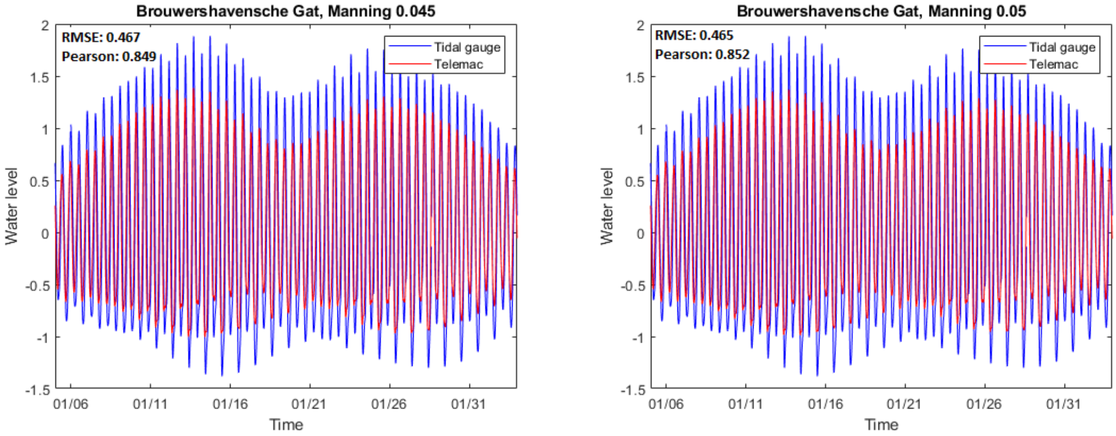

(c) Comparison between tidal gauge data and Delft 3D Manning 0.045

(d) Comparison between tidal gauge data and Delft 3D Manning 0.05

Figure C.2: The comparison between the tidal station Brouwers Havensche Gat and the different Delft 3D models, Manning 0.035-0.05

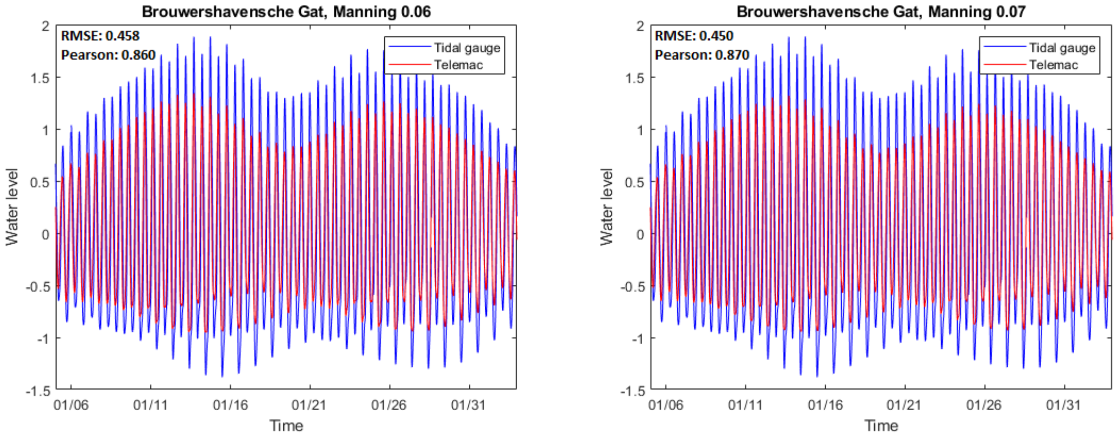

(a) Comparison between tidal gauge data and Delft 3D Manning 0.06

(b) Comparison between tidal gauge data and Delft 3D Manning 0.07

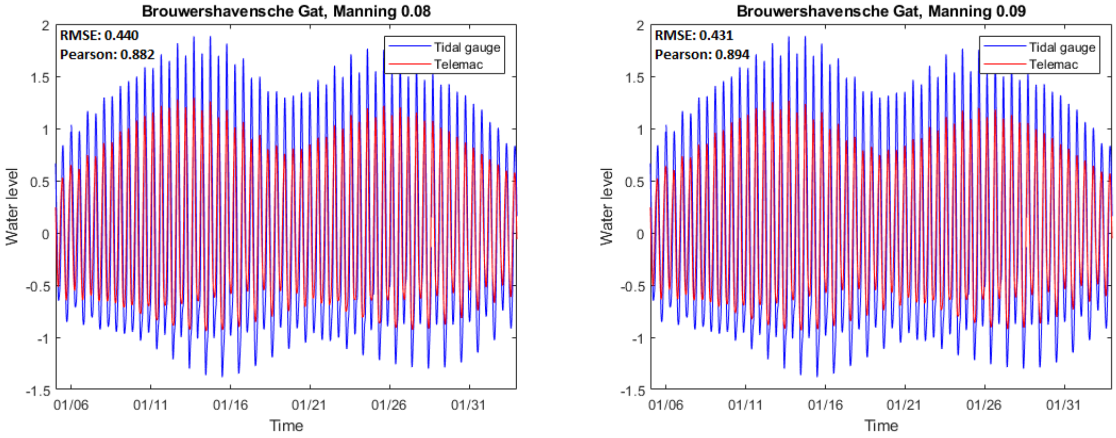

(c) Comparison between tidal gauge data and Delft 3D Manning 0.08

(d) Comparison between tidal gauge data and Delft 3D Manning 0.09

Figure C.3: The comparison between the tidal station Brouwers Havensche Gat and the different Delft 3D models, Manning 0.06-0.09

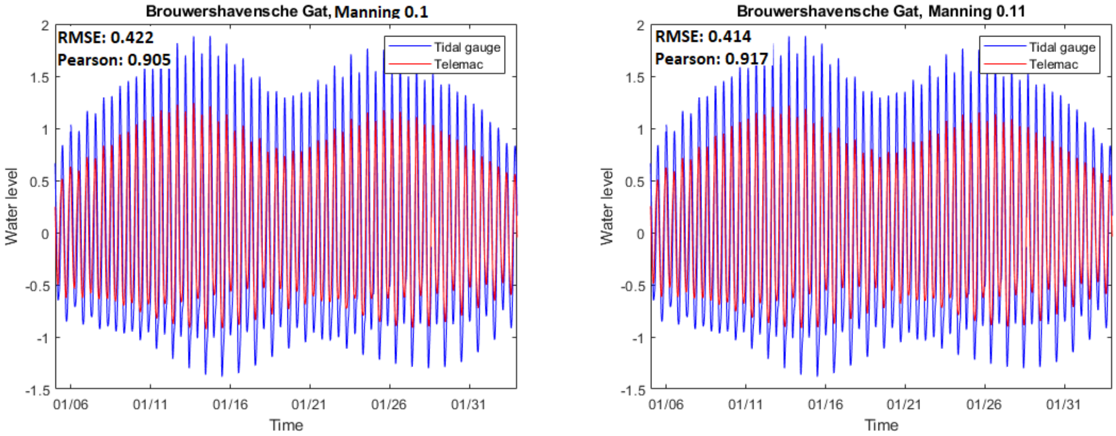

(a) Comparison between tidal gauge data and Delft 3D Manning 0.1

(b) Comparison between tidal gauge data and Delft 3D Manning 0.11

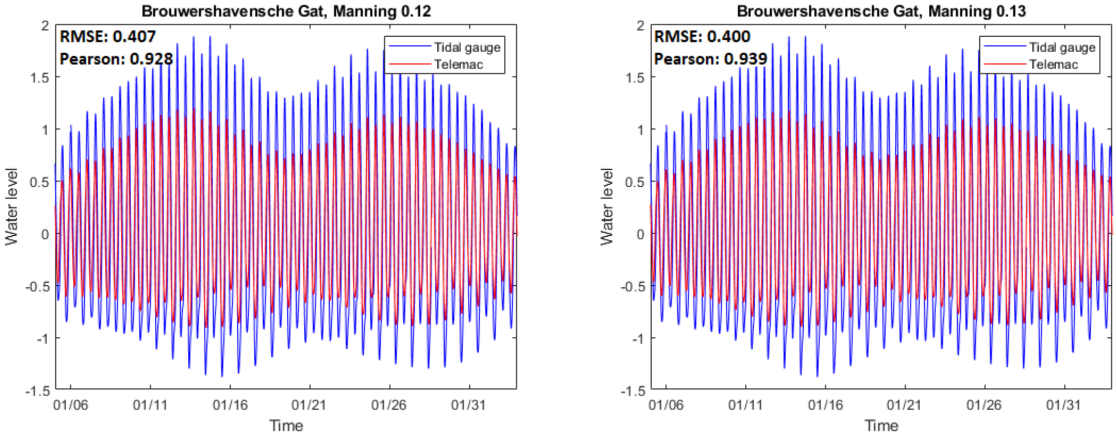

(c) Comparison between tidal gauge data and Delft 3D Manning 0.12

(d) Comparison between tidal gauge data and Delft 3D Manning 0.13

Figure C.4: The comparison between the tidal station Brouwers Havensche Gat and the different Delft 3D models, Manning 0.1-0.13

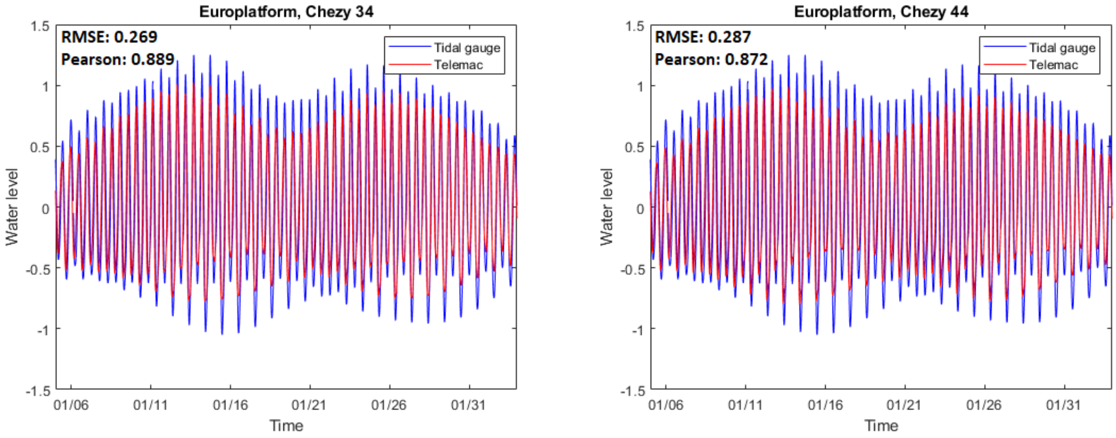

(a) Comparison between tidal gauge data and Delft 3D Chezy 34

(b) Comparison between tidal gauge data and Delft 3D Chezy 44

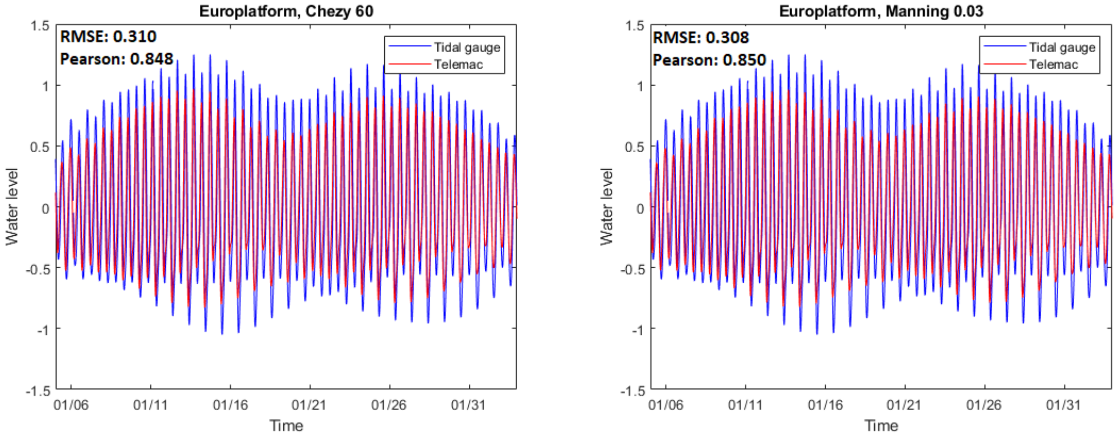

(c) Comparison between tidal gauge data and Delft 3D Chezy 60

(d) Comparison between tidal gauge data and Delft 3D Manning 0.03

Figure C.5: The comparison between the tidal station Euro platform and the different Delft 3D models, Chezy 34-60 and Manning 0.03

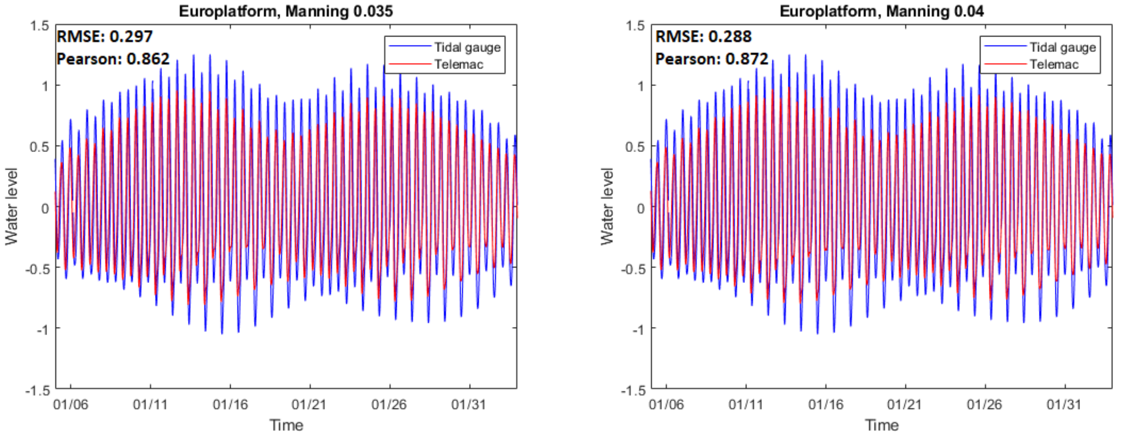

(a) Comparison between tidal gauge data and Delft 3D Manning 0.035

(b) Comparison between tidal gauge data and Delft 3D Manning 0.04

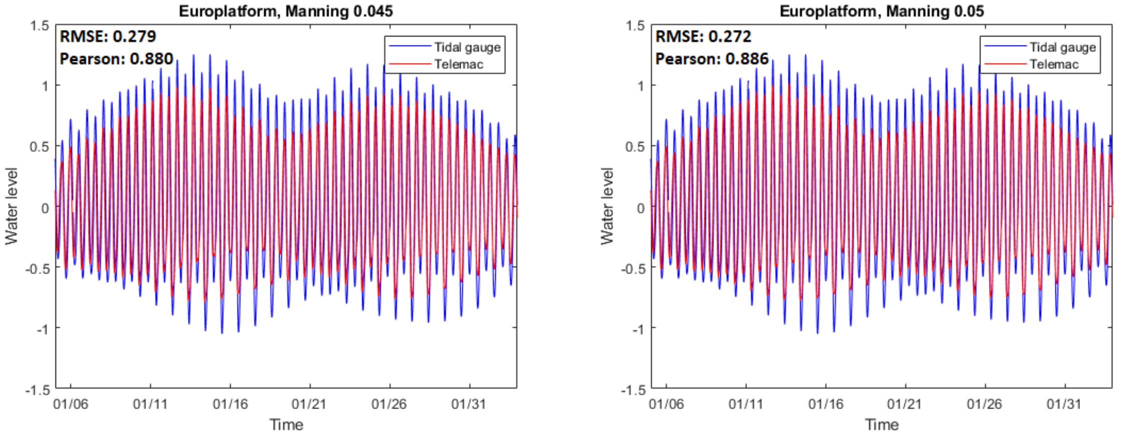

(c) Comparison between tidal gauge data and Delft 3D Manning 0.045

(d) Comparison between tidal gauge data and Delft 3D Manning 0.05

Figure C.6: The comparison between the tidal station Euro platform and the different Delft 3D models, Manning 0.035-0.05

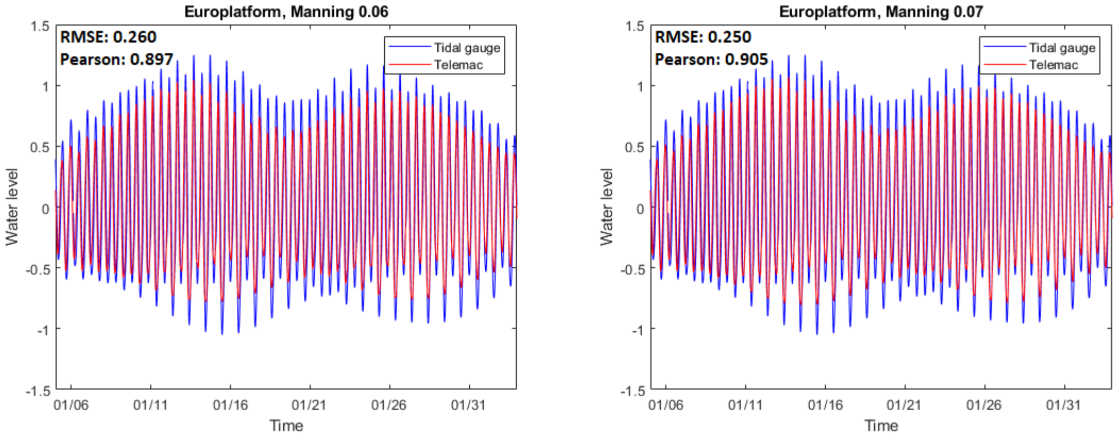

(a) Comparison between tidal gauge data and Delft 3D Manning 0.06

(b) Comparison between tidal gauge data and Delft 3D Manning 0.07

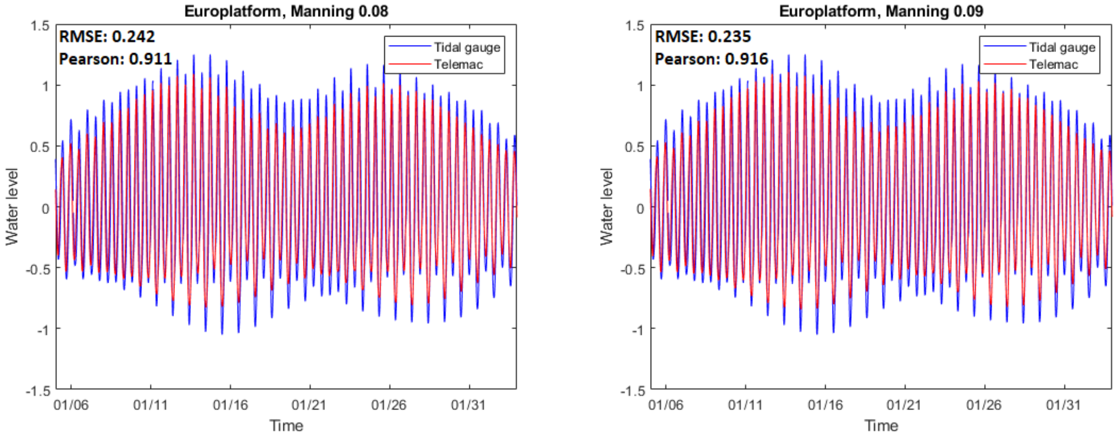

(c) Comparison between tidal gauge data and Delft 3D Manning 0.08

(d) Comparison between tidal gauge data and Delft 3D Manning 0.09

Figure C.7: The comparison between the tidal station Euro platform and the different Delft 3D models, Manning 0.06-0.09

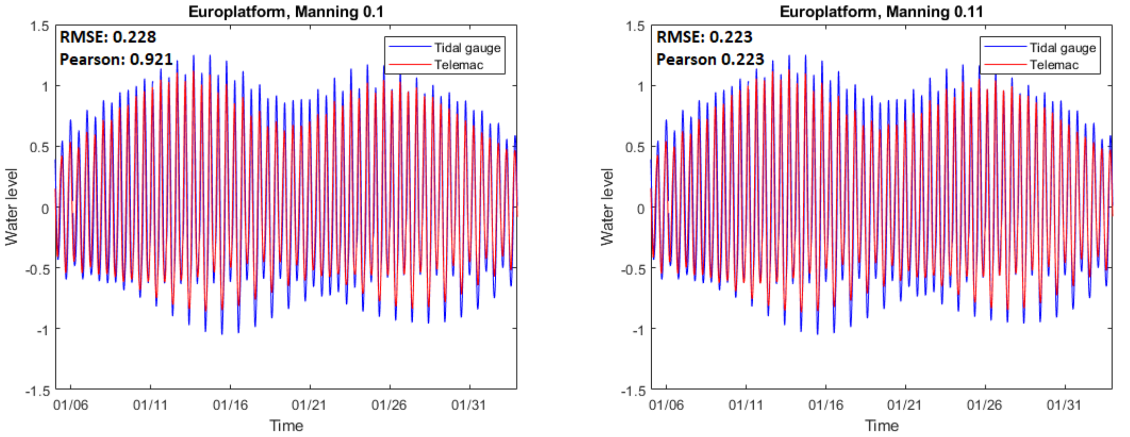

(a) Comparison between tidal gauge data and Delft 3D Manning 0.1

(b) Comparison between tidal gauge data and Delft 3D Manning 0.11

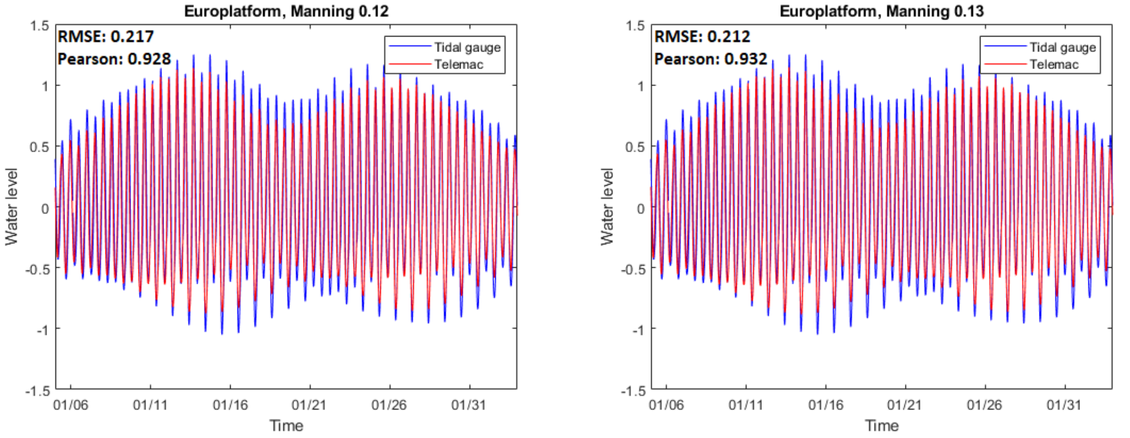

(c) Comparison between tidal gauge data and Delft 3D Manning 0.12

(d) Comparison between tidal gauge data and Delft 3D Manning 0.13

Figure C.8: The comparison between the tidal station Euro platform and the different Delft 3D models, Manning 0.1-0.13

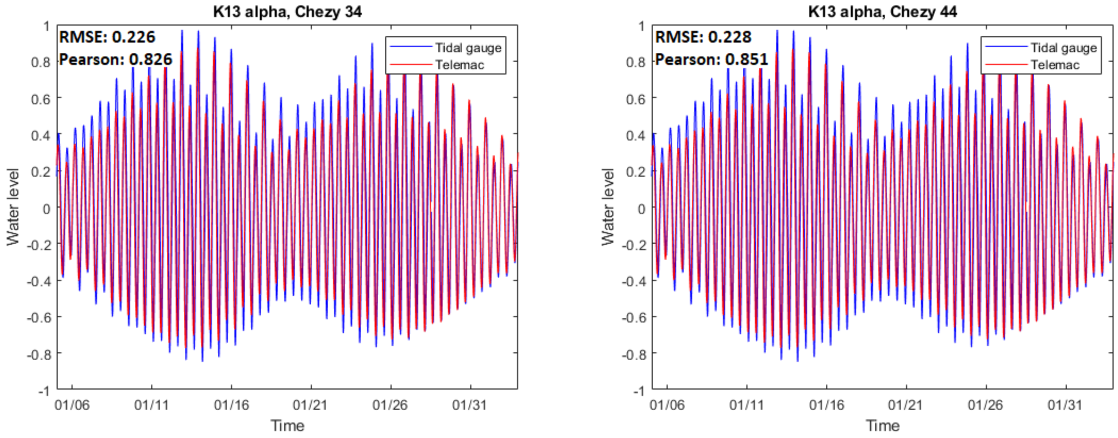

(a) Comparison between tidal gauge data and Delft 3D Chezy 34

(b) Comparison between tidal gauge data and Delft 3D Chezy 44

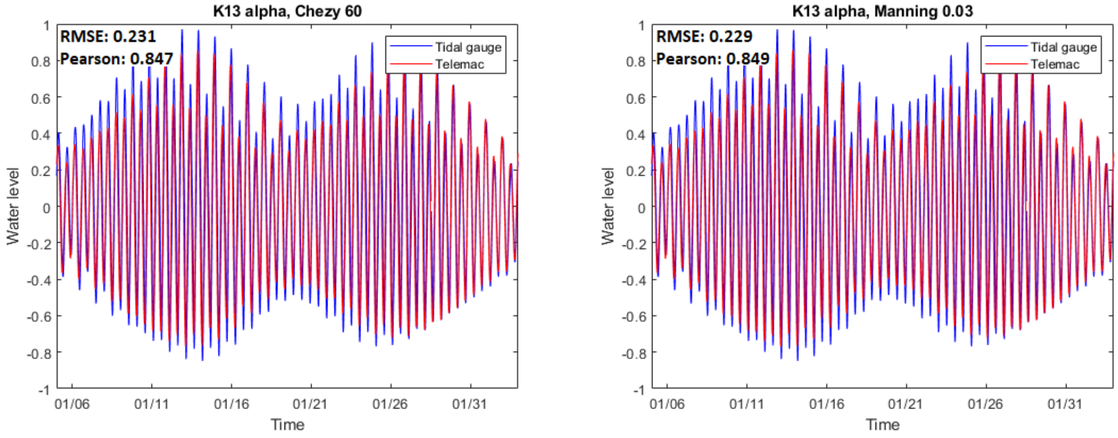

(c) Comparison between tidal gauge data and Delft 3D Chezy 60

(d) Comparison between tidal gauge data and Delft 3D Manning 0.03

Figure C.9: The comparison between the tidal station k13 alpha and the different Delft 3D models, Chezy 34-60 and Manning 0.03

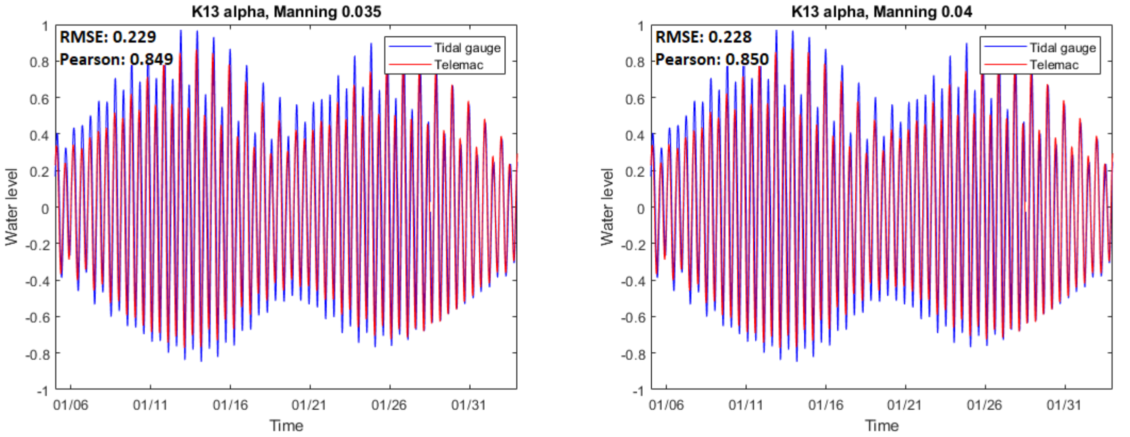

(a) Comparison between tidal gauge data and Delft 3D Manning 0.035

(b) Comparison between tidal gauge data and Delft 3D Manning 0.04

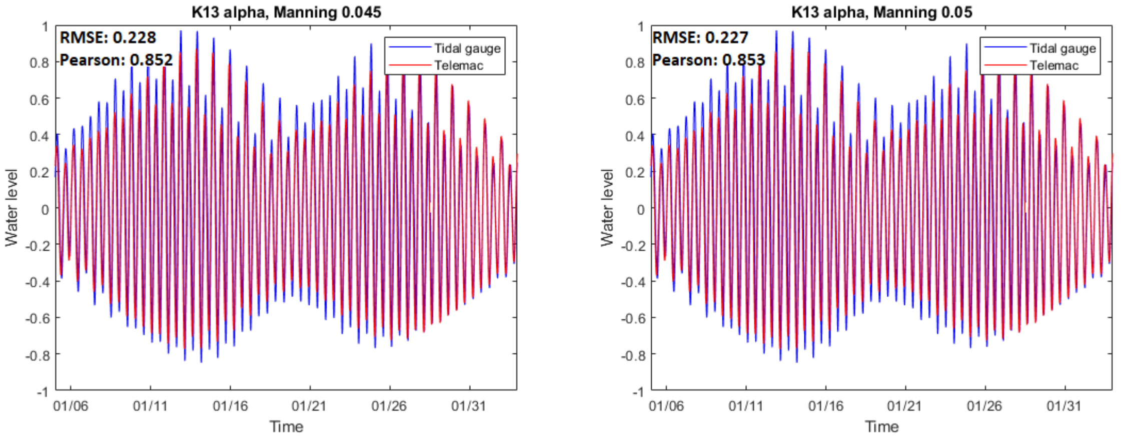

(c) Comparison between tidal gauge data and Delft 3D Manning 0.045

(d) Comparison between tidal gauge data and Delft 3D Manning 0.05

Figure C.10: The comparison between the tidal station K13 alpha and the different Delft 3D models, Manning 0.035-0.05

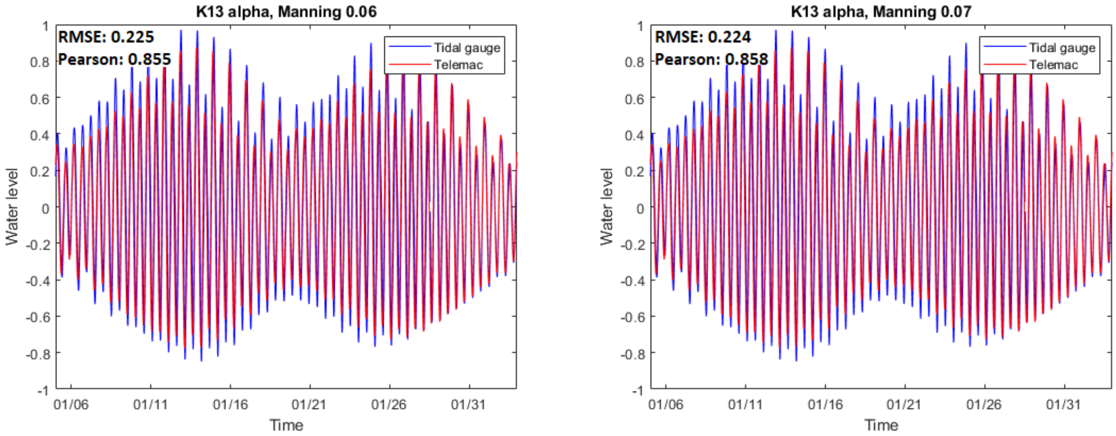

(a) Comparison between tidal gauge data and Delft 3D Manning 0.06

(b) Comparison between tidal gauge data and Delft 3D Manning 0.07

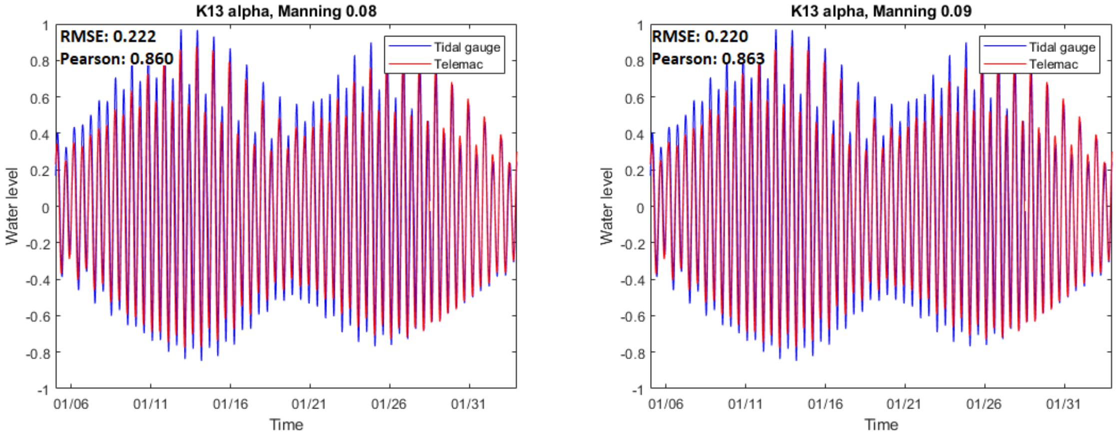

(c) Comparison between tidal gauge data and Delft 3D Manning 0.08

(d) Comparison between tidal gauge data and Delft 3D Manning 0.09

Figure C.11: The comparison between the tidal station K13 alpha and the different Delft 3D models, Manning 0.06-0.09

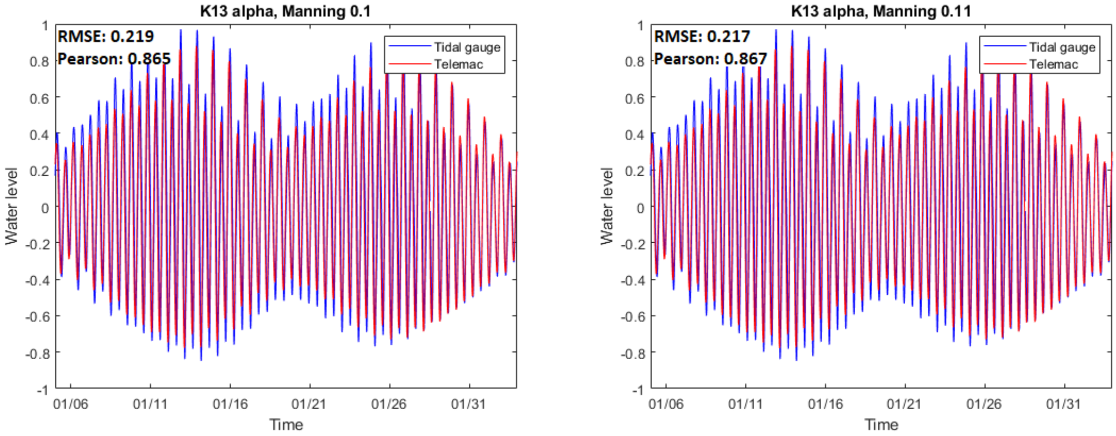

(a) Comparison between tidal gauge data and Delft 3D Manning 0.1

(b) Comparison between tidal gauge data and Delft 3D Manning 0.11

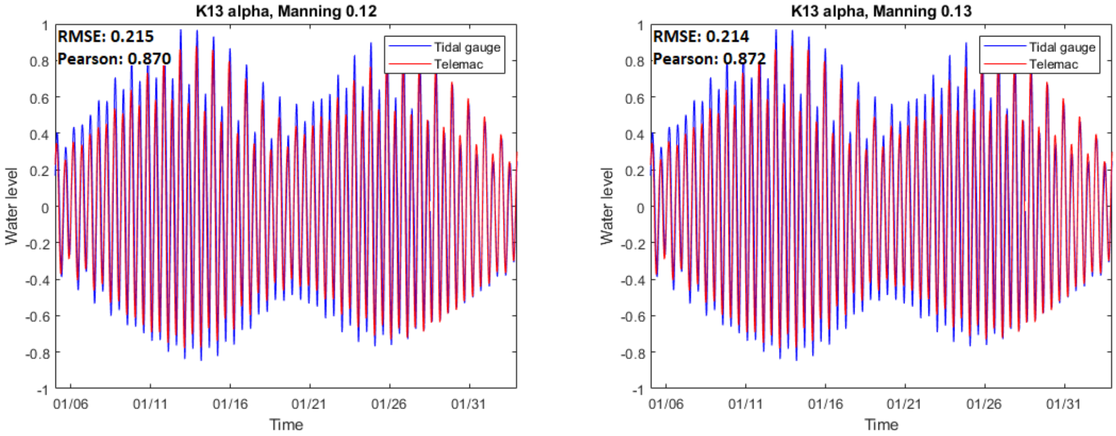

(c) Comparison between tidal gauge data and Delft 3D Manning 0.12

(d) Comparison between tidal gauge data and Delft 3D Manning 0.13

Figure C.12: The comparison between the tidal station K13 alpha and the different Delft 3D models, Manning 0.1-0.13

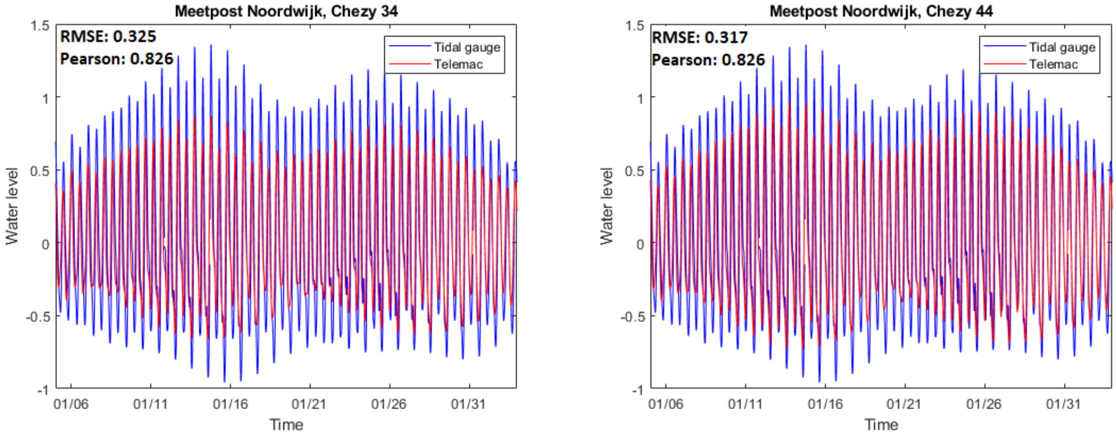

(a) Comparison between tidal gauge data and Delft 3D Chezy 34

(b) Comparison between tidal gauge data and Delft 3D Chezy 44

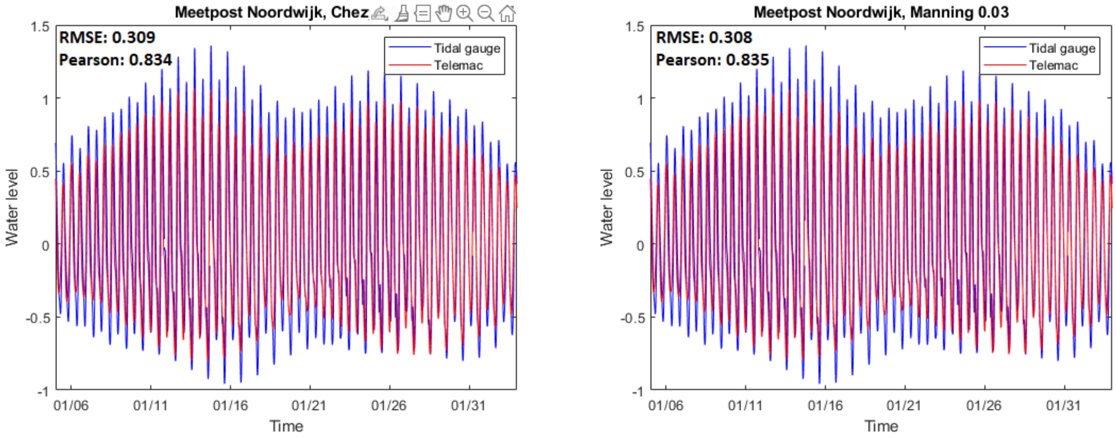

(c) Comparison between tidal gauge data and Delft 3D Chezy 60

(d) Comparison between tidal gauge data and Delft 3D Manning 0.03

Figure C.13: The comparison between the tidal station Meetpost Noordwijk and the different Delft 3D models, Chezy 34-60 and Manning 0.03

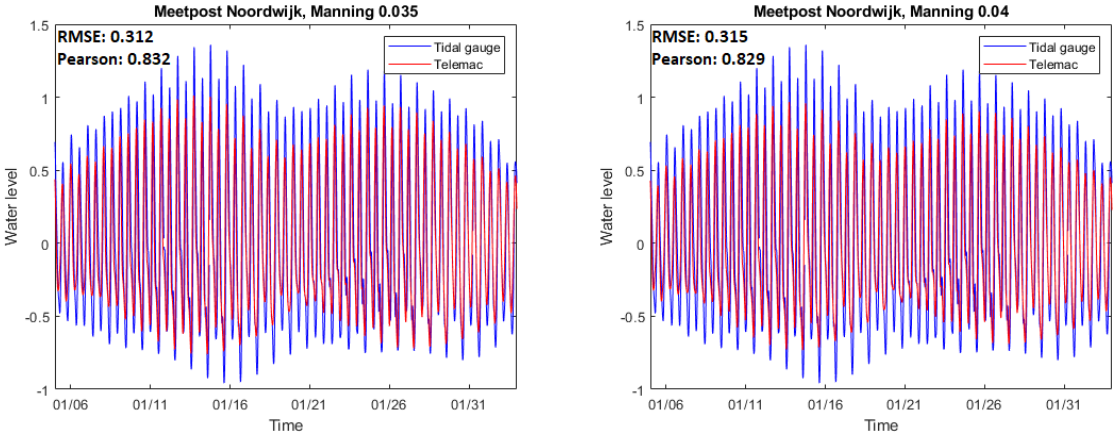

(a) Comparison between tidal gauge data and Delft 3D Manning 0.035

(b) Comparison between tidal gauge data and Delft 3D Manning 0.04

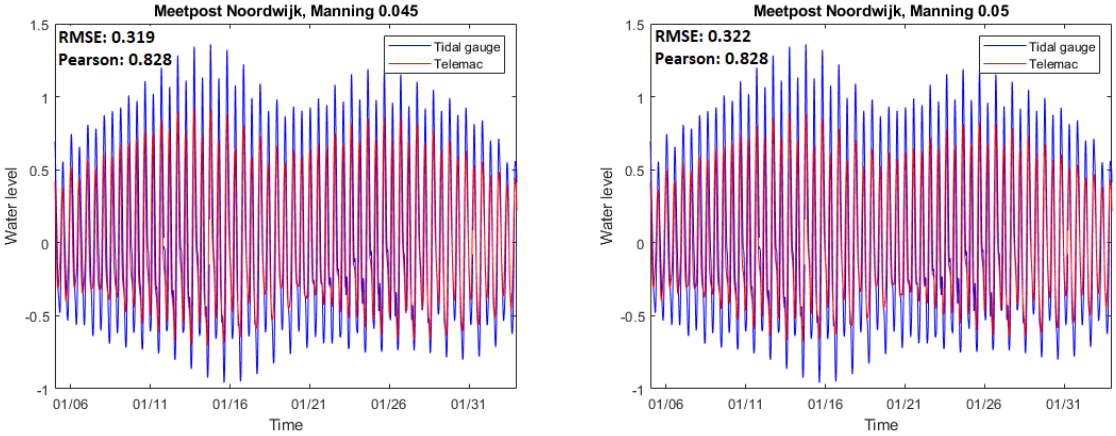

(c) Comparison between tidal gauge data and Delft 3D Manning 0.045

(d) Comparison between tidal gauge data and Delft 3D Manning 0.05

Figure C.14: The comparison between the tidal station Meetpost Noordwijk and the different Delft 3D models, Manning 0.035-0.05

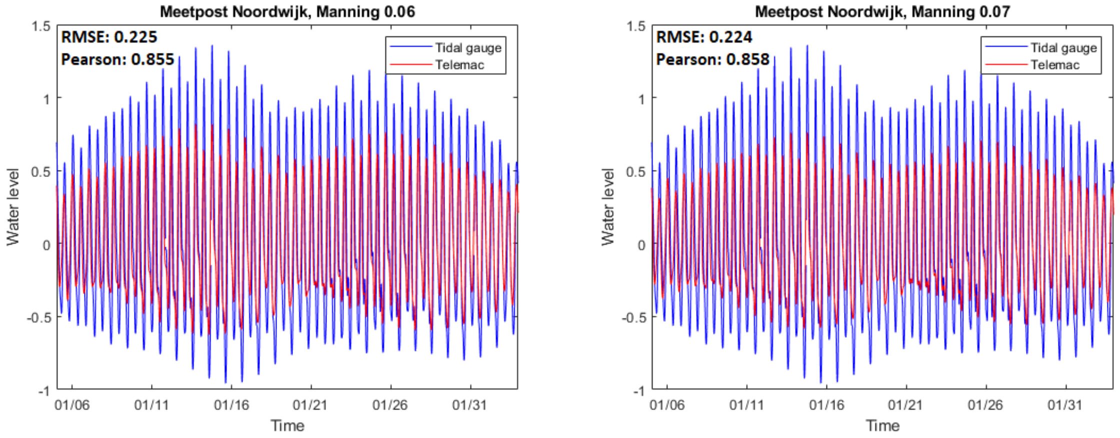

(a) Comparison between tidal gauge data and Delft 3D Manning 0.06

(b) Comparison between tidal gauge data and Delft 3D Manning 0.07

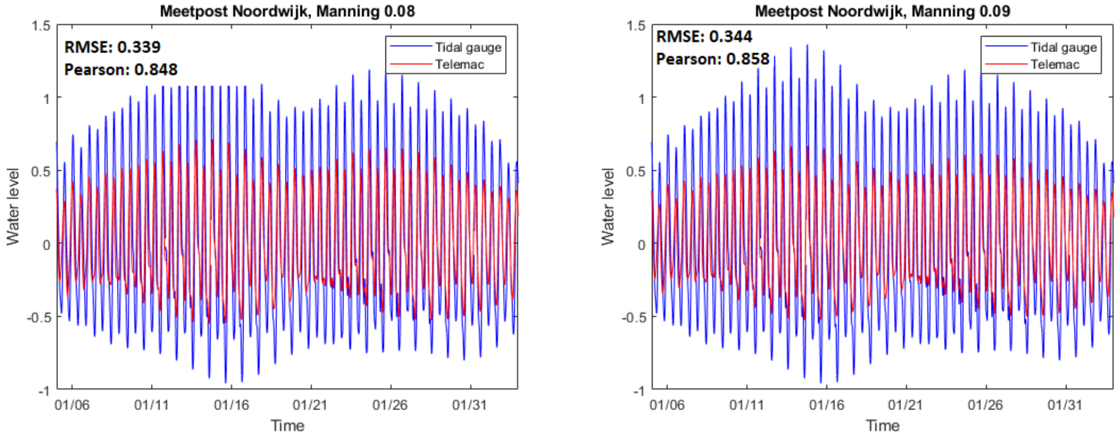

(c) Comparison between tidal gauge data and Delft 3D Manning 0.08

(d) Comparison between tidal gauge data and Delft 3D Manning 0.09

Figure C.15: The comparison between the tidal station Meetpost Noordwijk and the different Delft 3D models, Manning 0.06-0.09

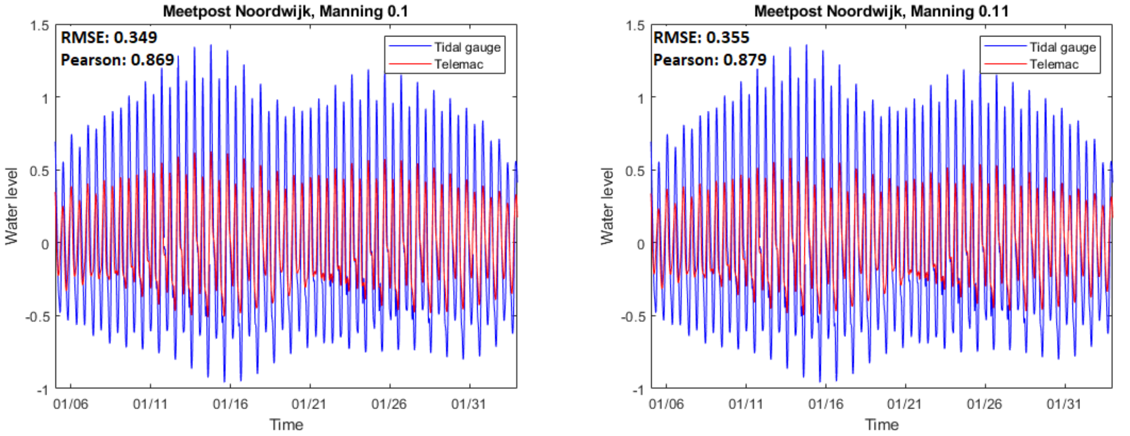

(a) Comparison between tidal gauge data and Delft 3D Manning 0.1

(b) Comparison between tidal gauge data and Delft 3D Manning 0.11

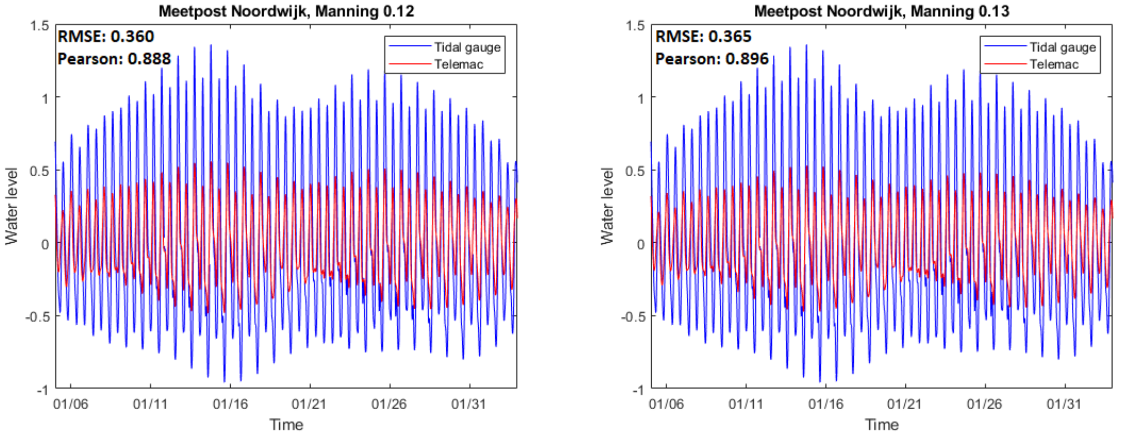

(c) Comparison between tidal gauge data and Delft 3D Manning 0.12

(d) Comparison between tidal gauge data and Delft 3D Manning 0.13

Figure C.16: The comparison between the tidal station Meetpost Noordwijk and the different Delft 3D models, Manning 0.1-0.13

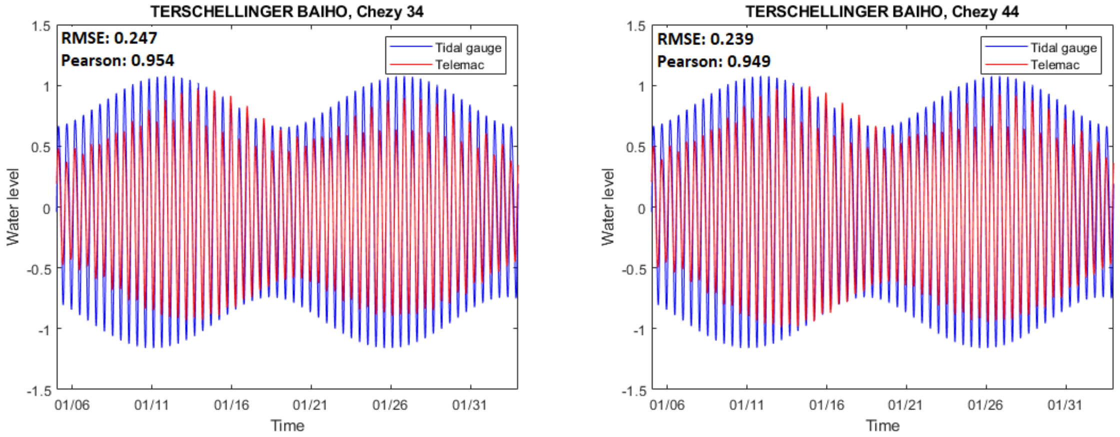

(a) Comparison between tidal gauge data and Delft 3D Chezy 34

(b) Comparison between tidal gauge data and Delft 3D Chezy 44

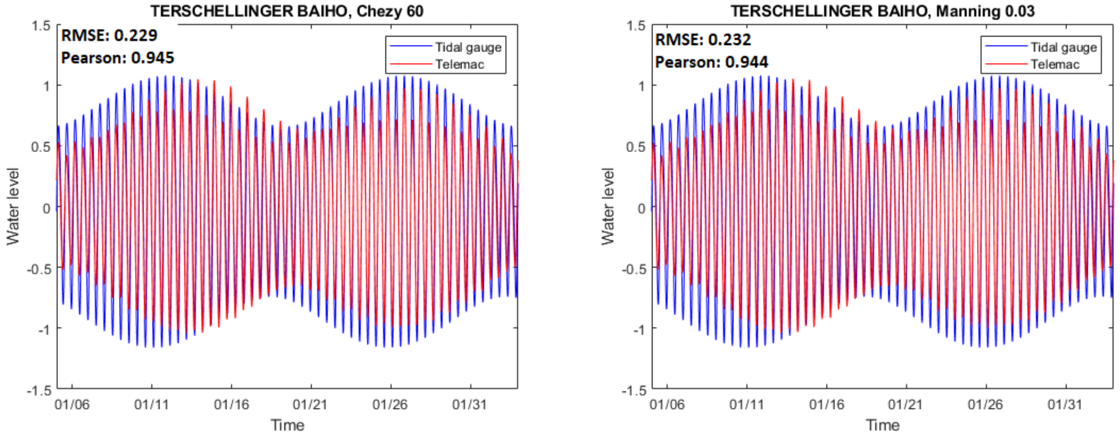

(c) Comparison between tidal gauge data and Delft 3D Chezy 60

(d) Comparison between tidal gauge data and Delft 3D Manning 0.03

Figure C.17: The comparison between the tidal station Terschellinger BAIHO and the different Delft 3D models, Chezy 34-60 and Manning 0.03

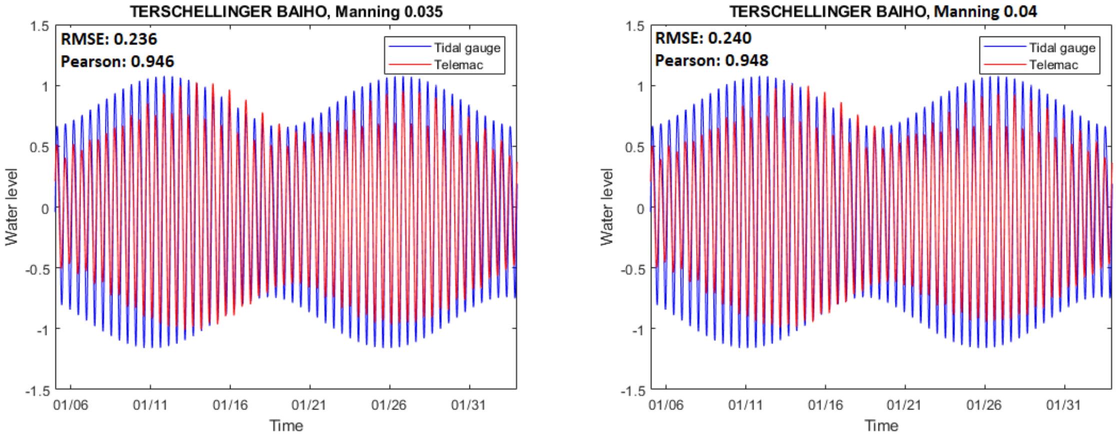

(a) Comparison between tidal gauge data and Delft 3D Manning 0.035

(b) Comparison between tidal gauge data and Delft 3D Manning 0.04

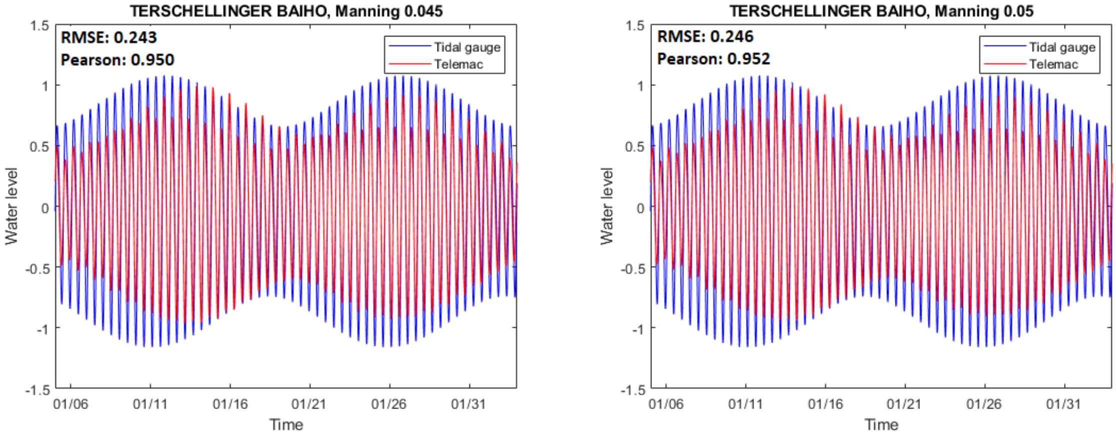

(c) Comparison between tidal gauge data and Delft 3D Manning 0.045

(d) Comparison between tidal gauge data and Delft 3D Manning 0.05

Figure C.18: The comparison between the tidal station Terschellinger BAIHO and the different Delft 3D models, Manning 0.035-0.05

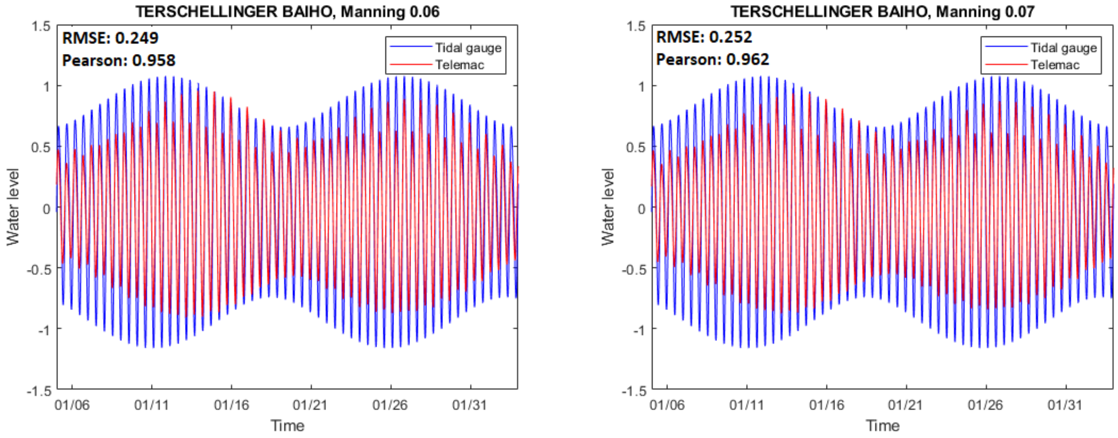

(a) Comparison between tidal gauge data and Delft 3D Manning 0.06

(b) Comparison between tidal gauge data and Delft 3D Manning 0.07

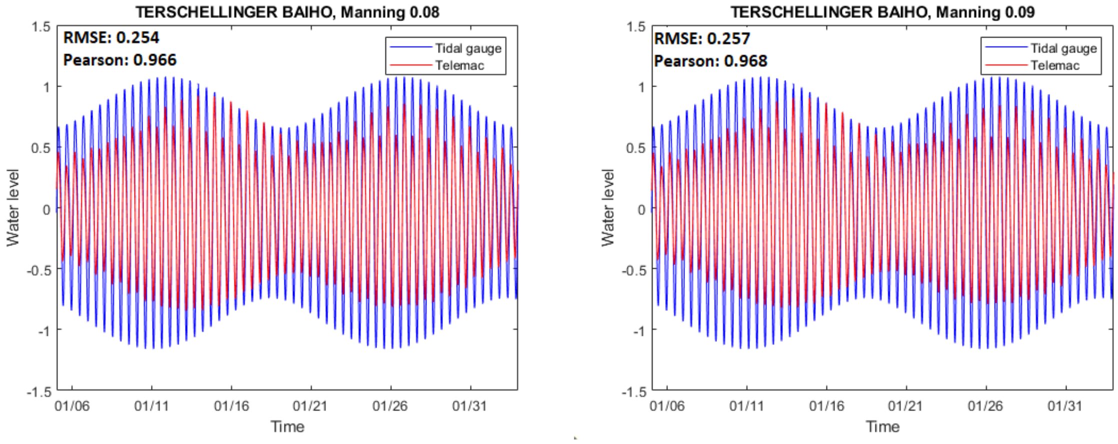

(c) Comparison between tidal gauge data and Delft 3D Manning 0.08

(d) Comparison between tidal gauge data and Delft 3D Manning 0.09

Figure C.19: The comparison between the tidal station Terschellinger BAIHO and the different Delft 3D models, Manning 0.06-0.09

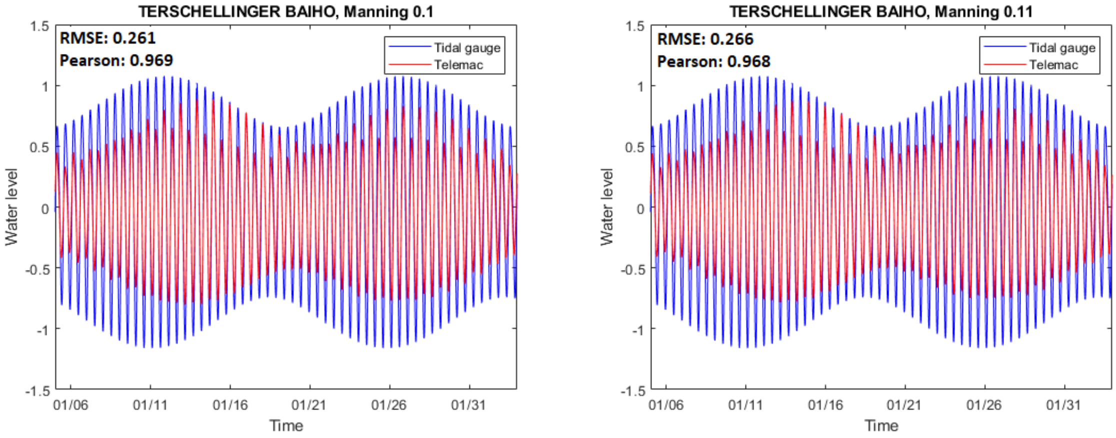

(a) Comparison between tidal gauge data and Delft 3D Manning 0.1

(b) Comparison between tidal gauge data and Delft 3D Manning 0.11

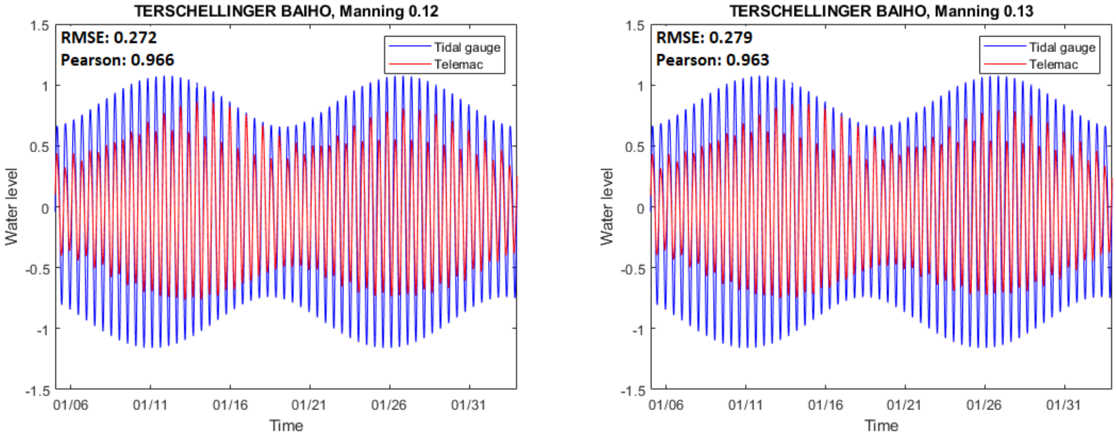

(c) Comparison between tidal gauge data and Delft 3D Manning 0.12

(d) Comparison between tidal gauge data and Delft 3D Manning 0.13

Figure C.20: The comparison between the tidal station Terschellinger BAIHO and the different Delft 3D models, Manning 0.1-0.13

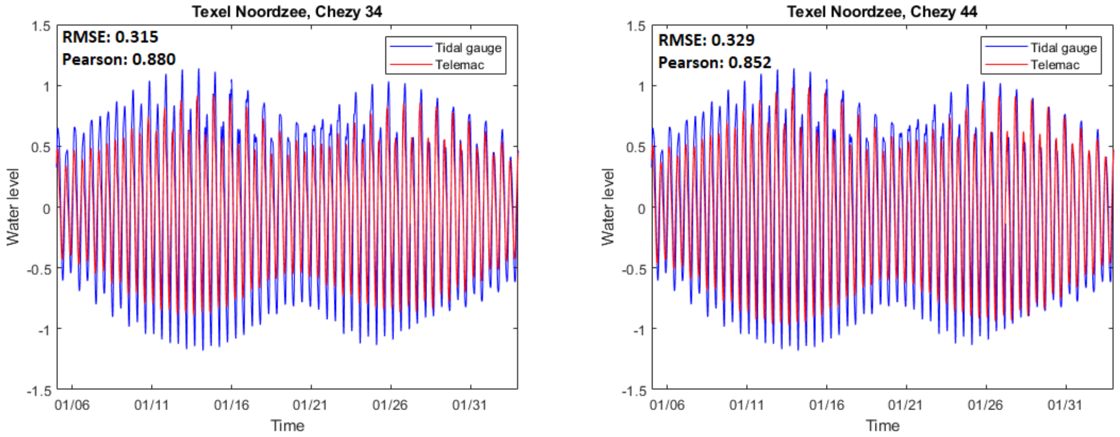

(a) Comparison between tidal gauge data and Delft 3D Chezy 34

(b) Comparison between tidal gauge data and Delft 3D Chezy 44

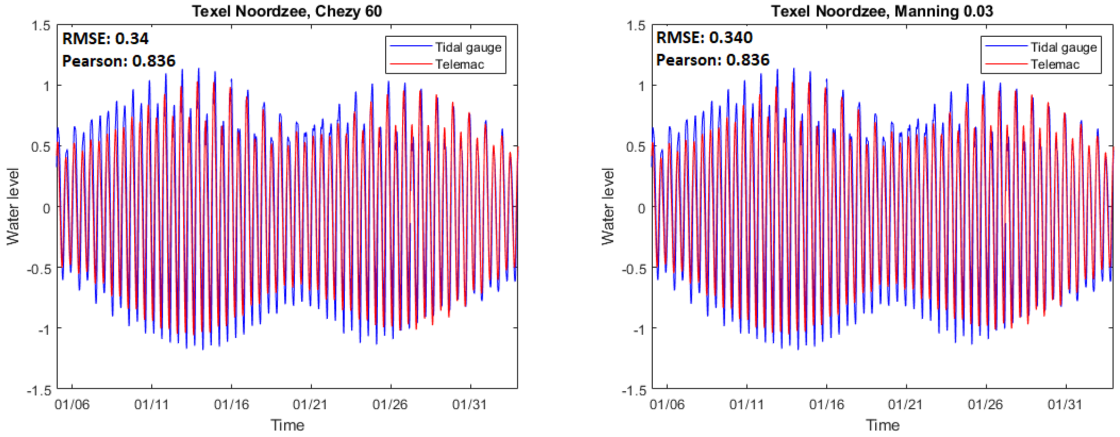

(c) Comparison between tidal gauge data and Delft 3D Chezy 60

(d) Comparison between tidal gauge data and Delft 3D Manning 0.03

Figure C.21: The comparison between the tidal station Texel Noordzee and the different Delft 3D models, Chezy 34-60 and Manning 0.03

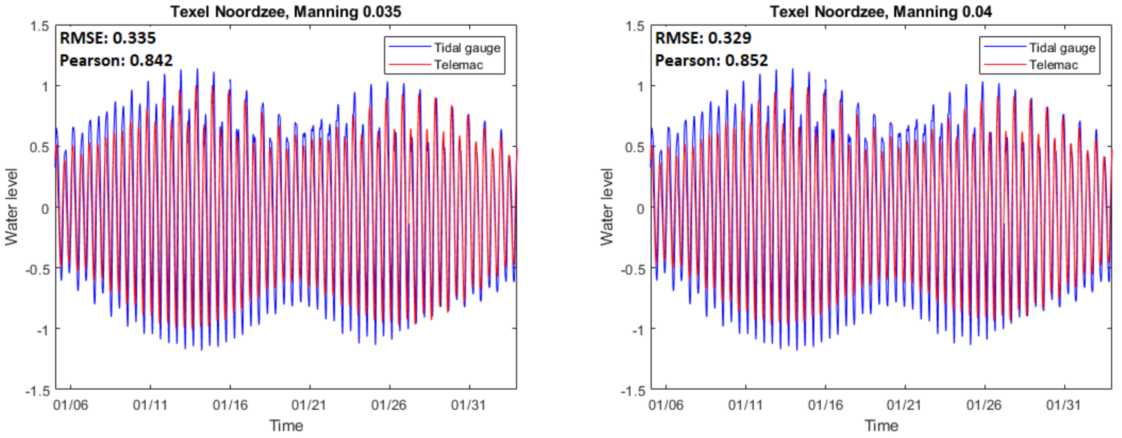

(a) Comparison between tidal gauge data and Delft 3D Manning 0.035

(b) Comparison between tidal gauge data and Delft 3D Manning 0.04

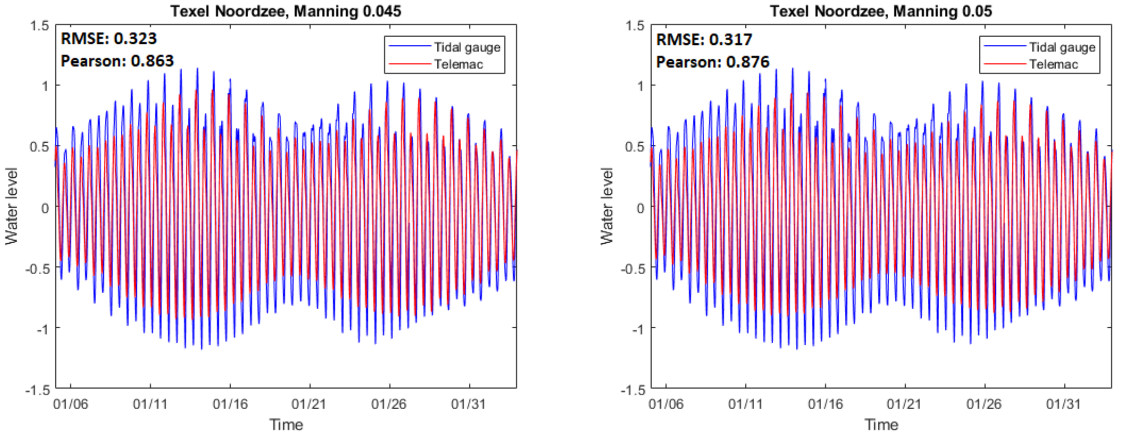

(c) Comparison between tidal gauge data and Delft 3D Manning 0.045

(d) Comparison between tidal gauge data and Delft 3D Manning 0.05

Figure C.22: The comparison between the tidal station Texel Noordzee and the different Delft 3D models, Manning 0.035-0.05

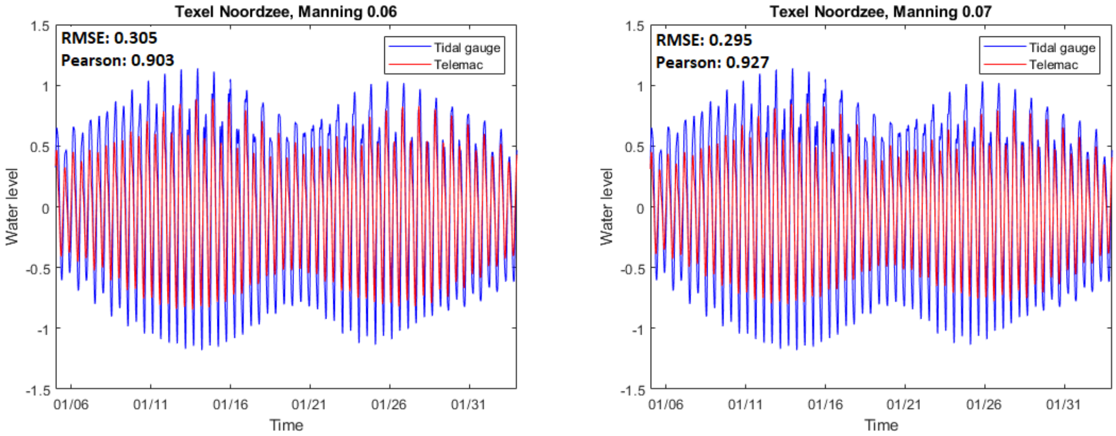

(a) Comparison between tidal gauge data and Delft 3D Manning 0.06 (b) Comparison between tidal gauge data and Delft 3D Manning 0.07

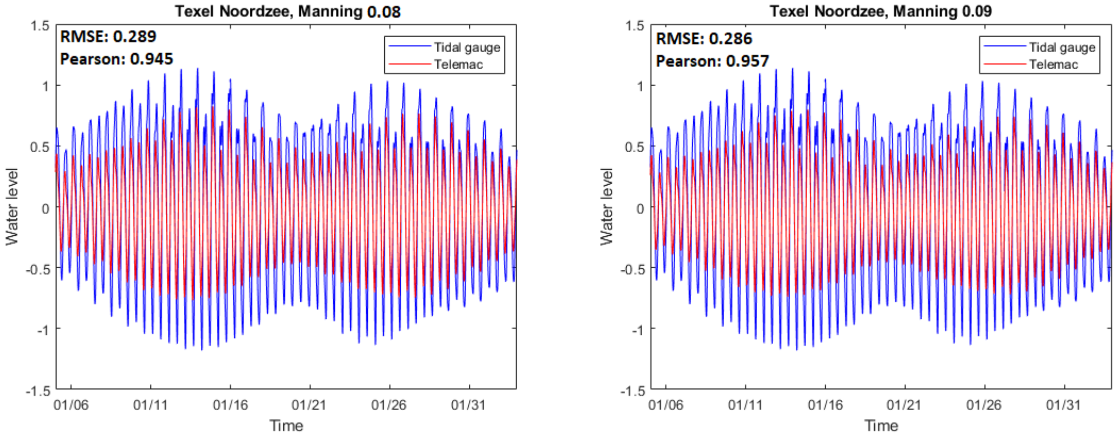

(c) Comparison between tidal gauge data and Delft 3D Manning 0.08 (d) Comparison between tidal gauge data and Delft 3D Manning 0.09

Figure C.23: The comparison between the tidal station Texel Noordzee and the different Delft 3D models, Manning 0.06-0.09

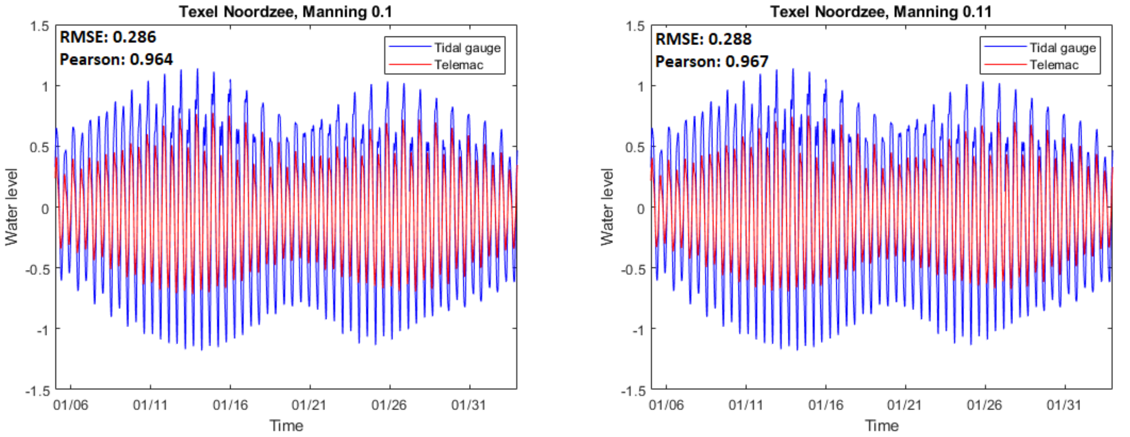

(a) Comparison between tidal gauge data and Delft 3D Manning 0.1

(b) Comparison between tidal gauge data and Delft 3D Manning 0.11

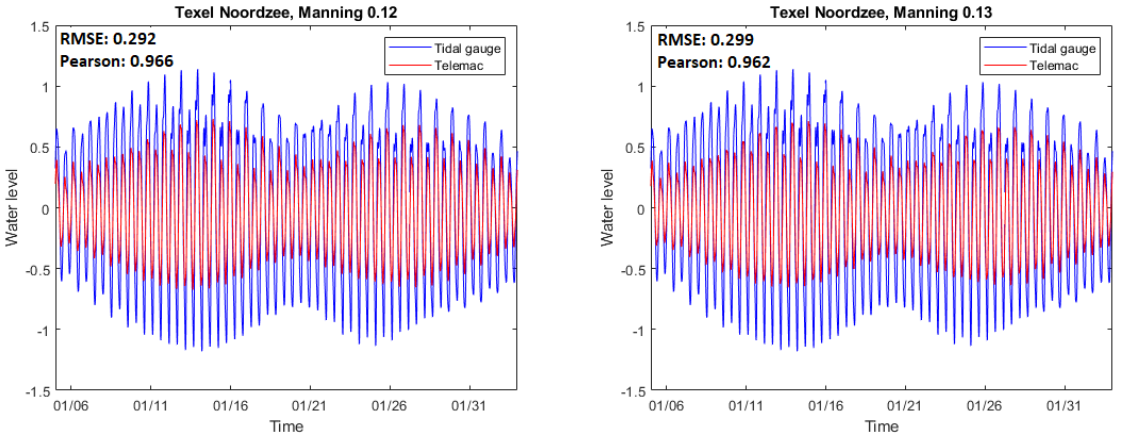

(c) Comparison between tidal gauge data and Delft 3D Manning 0.12

(d) Comparison between tidal gauge data and Delft 3D Manning 0.13

Figure C.24: The comparison between the tidal station Texel Noordzee and the different Delft 3D models, Manning 0.1-0.13

In the following figures the scatter plots can be seen. From the scatter plots it can be concluded were the difference between the 2 data sets are. The red line demonstrates that the 2 data sets have the same value. From this the scatter index can be determined.

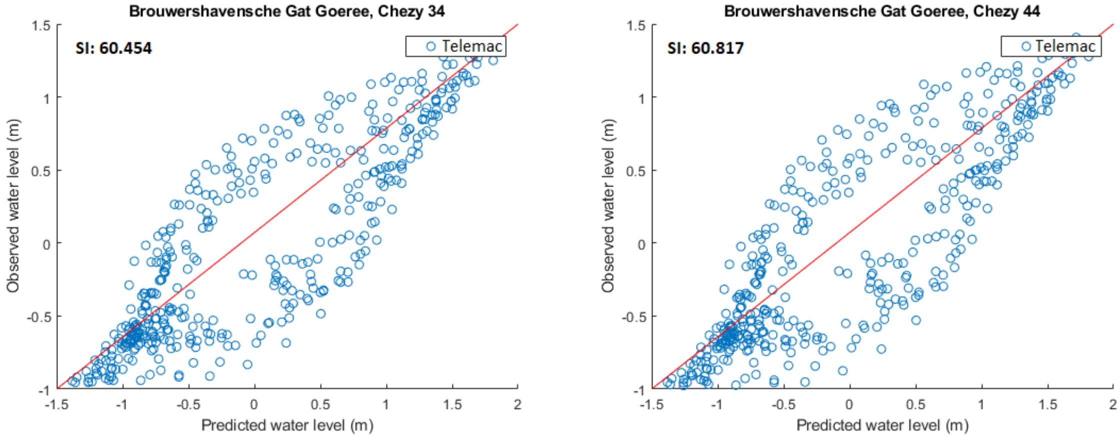

(a) Comparison between tidal gauge data and Delft 3D Chezy 34

(b) Comparison between tidal gauge data and Delft 3D Chezy 44

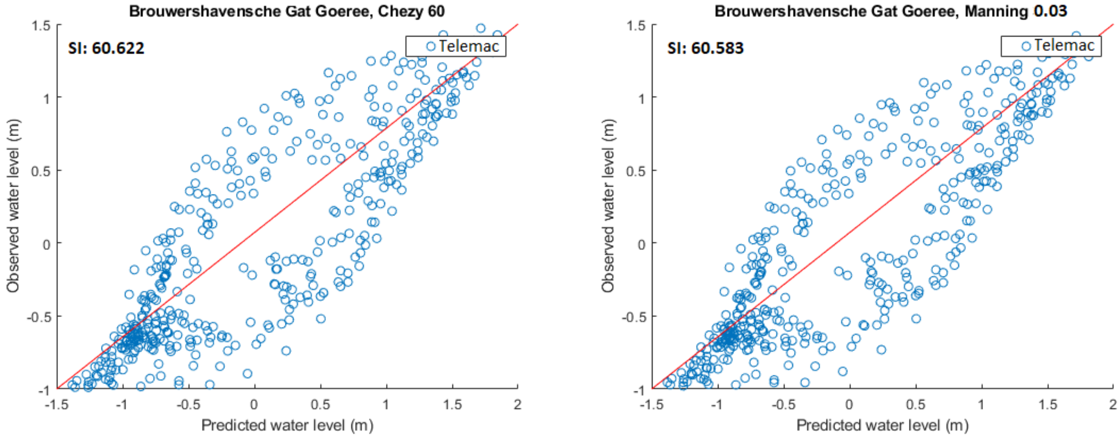

(c) Comparison between tidal gauge data and Delft 3D Chezy 60

(d) Comparison between tidal gauge data and Delft 3D Manning 0.03

Figure C.25: The scatter index between the tidal station Brouwers Havensche Gat and the different Telemac models, Chezy 34-60 and Manning 0.03

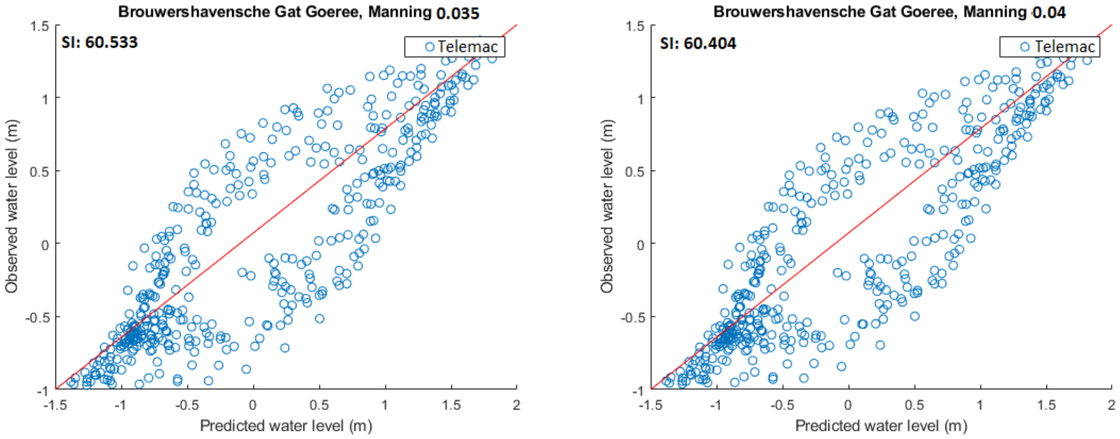

(a) Comparison between tidal gauge data and Delft 3D Manning 0.035

(b) Comparison between tidal gauge data and Delft 3D Manning 0.04

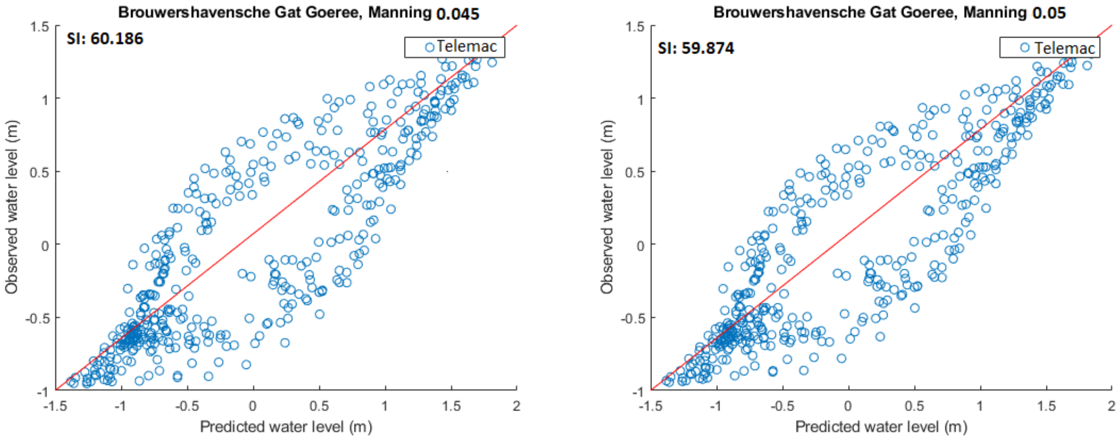

(c) Comparison between tidal gauge data and Delft 3D Manning 0.045

(d) Comparison between tidal gauge data and Delft 3D Manning 0.05

Figure C.26: The scatter index between the tidal station Brouwers Havensche Gat and the different Telemac models, Manning 0.035-0.05

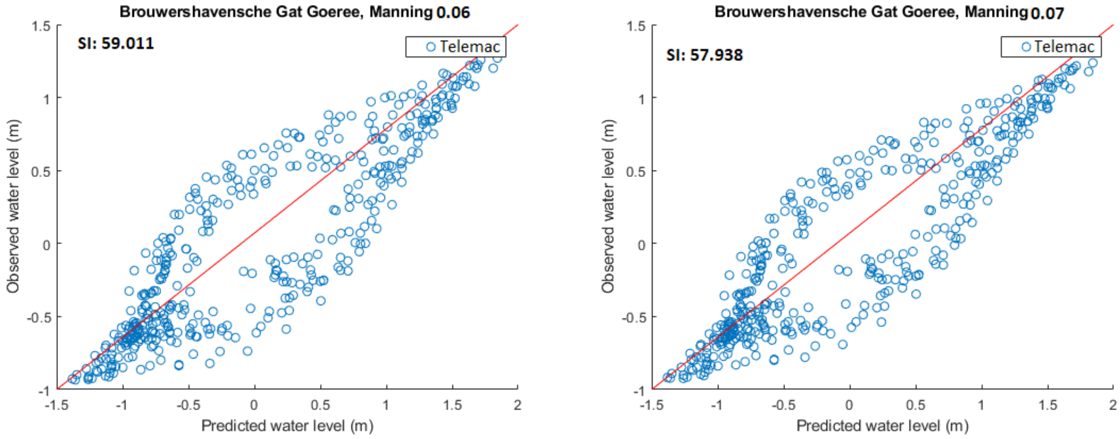

(a) Comparison between tidal gauge data and Delft 3D Manning 0.06

(b) Comparison between tidal gauge data and Delft 3D Manning 0.07

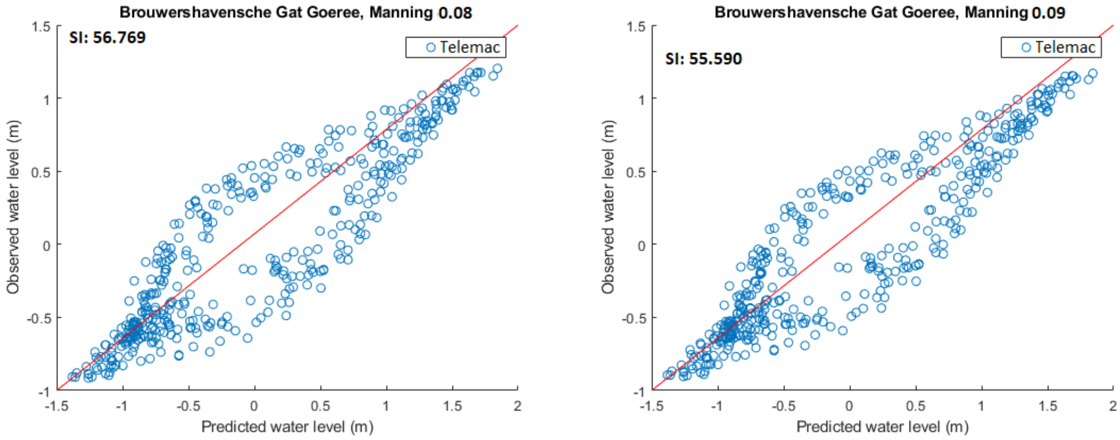

(c) Comparison between tidal gauge data and Delft 3D Manning 0.08

(d) Comparison between tidal gauge data and Delft 3D Manning 0.09

Figure C.27: The scatter index between the tidal station Brouwers Havensche Gat and the different Telemac models, Manning 0.06-0.09

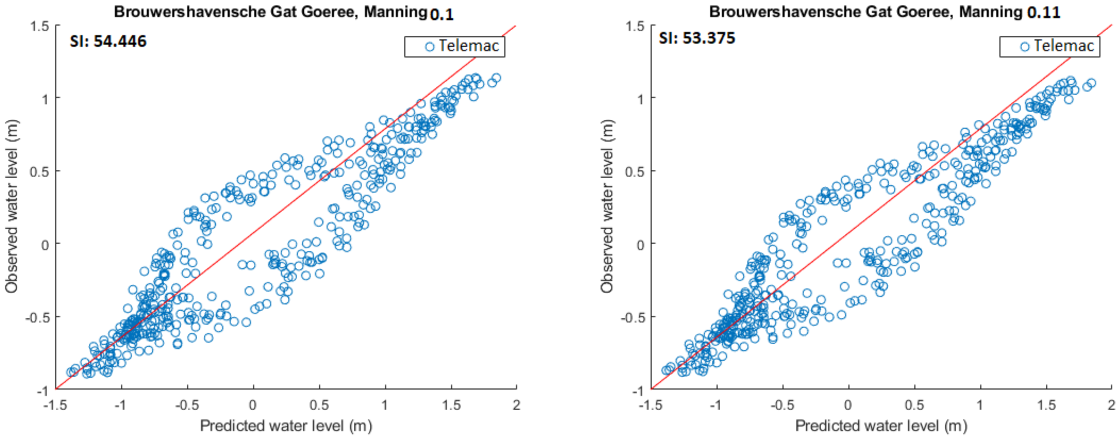

(a) Comparison between tidal gauge data and Delft 3D Manning 0.1

(b) Comparison between tidal gauge data and Delft 3D Manning 0.11

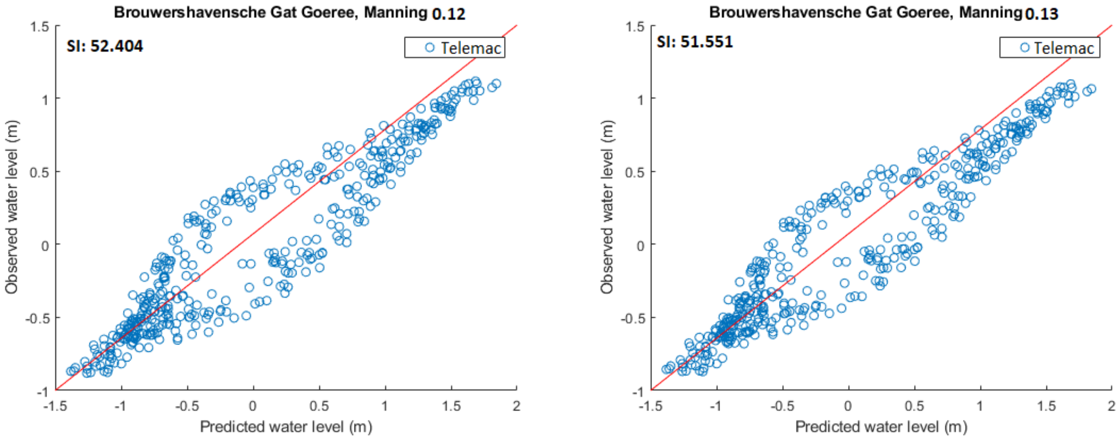

(c) Comparison between tidal gauge data and Delft 3D Manning 0.12

(d) Comparison between tidal gauge data and Delft 3D Manning 0.13

Figure C.28: The scatter index between the tidal station Brouwers Havensche Gat and the different Telemac models, Manning 0.1-0.13

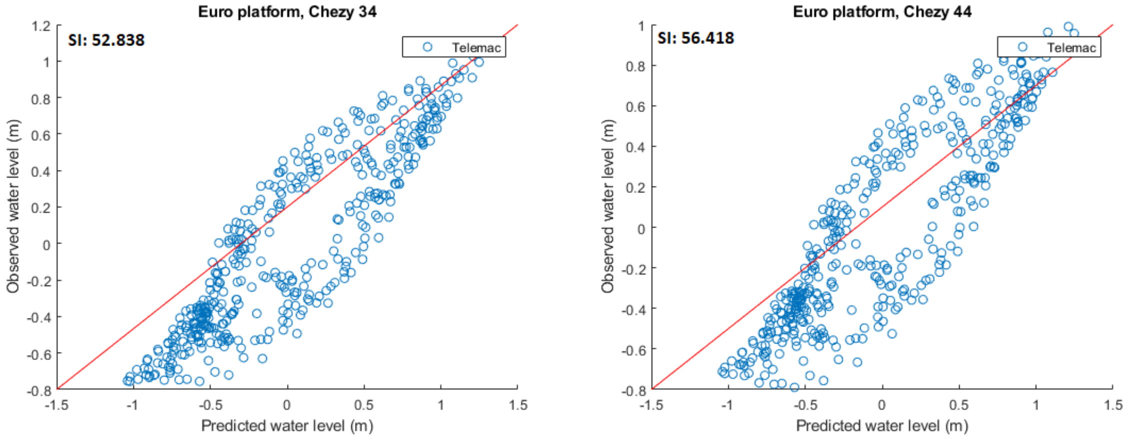

(a) Comparison between tidal gauge data and Delft 3D Chezy 34

(b) Comparison between tidal gauge data and Delft 3D Chezy 44

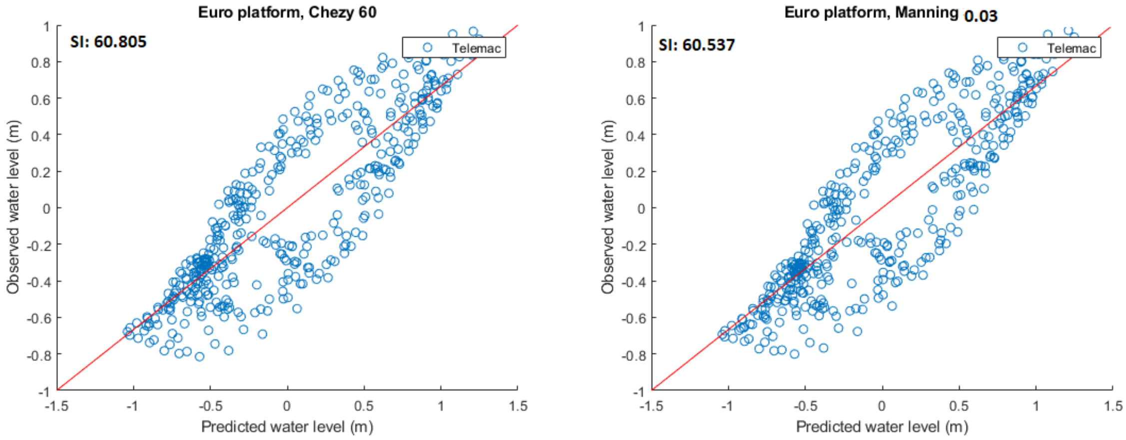

(c) Comparison between tidal gauge data and Delft 3D Chezy 60

(d) Comparison between tidal gauge data and Delft 3D Manning 0.03

Figure C.29: The scatter index between the tidal station Euro platform and the different Telemac models, Chezy 34-60 and Manning 0.03

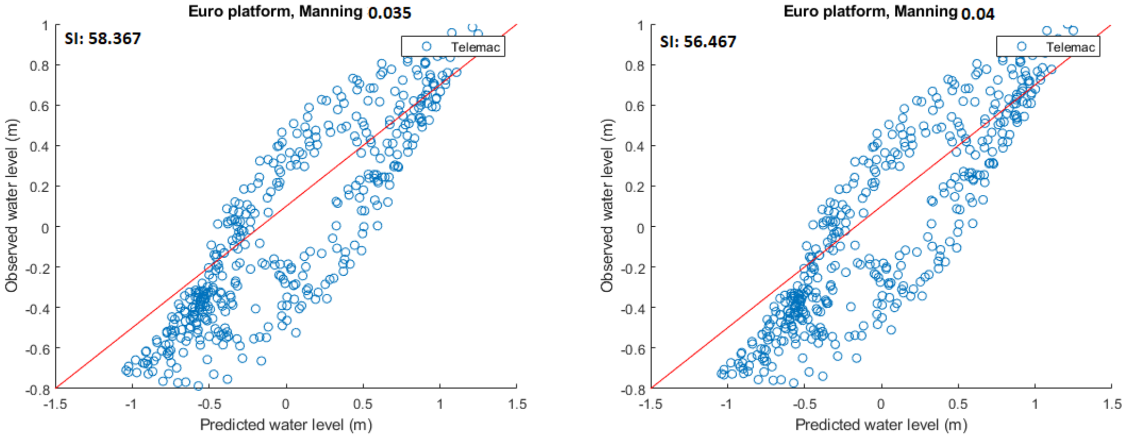

(a) Comparison between tidal gauge data and Delft 3D Manning 0.035

(b) Comparison between tidal gauge data and Delft 3D Manning 0.04

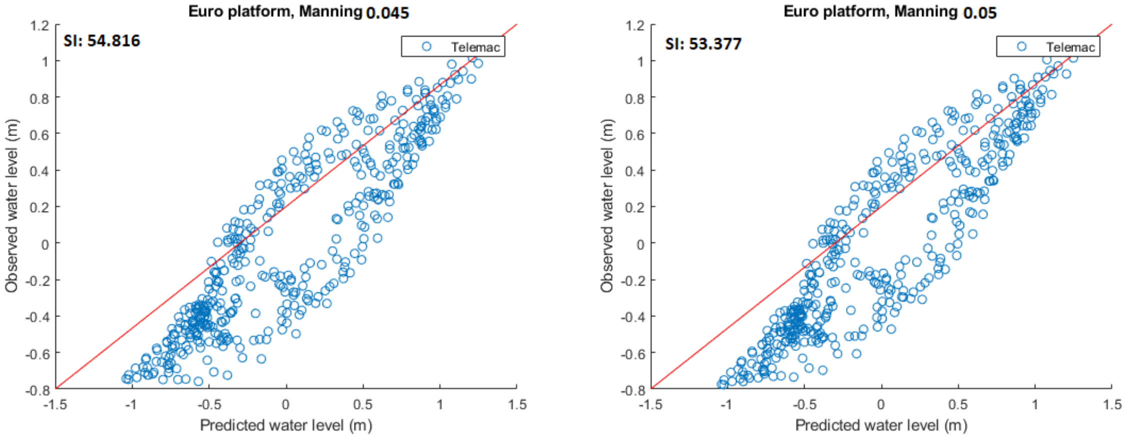

(c) Comparison between tidal gauge data and Delft 3D Manning 0.045

(d) Comparison between tidal gauge data and Delft 3D Manning 0.05

Figure C.30: The scatter index between the tidal station Euro platform and the different Telemac models, Manning 0.035-0.05

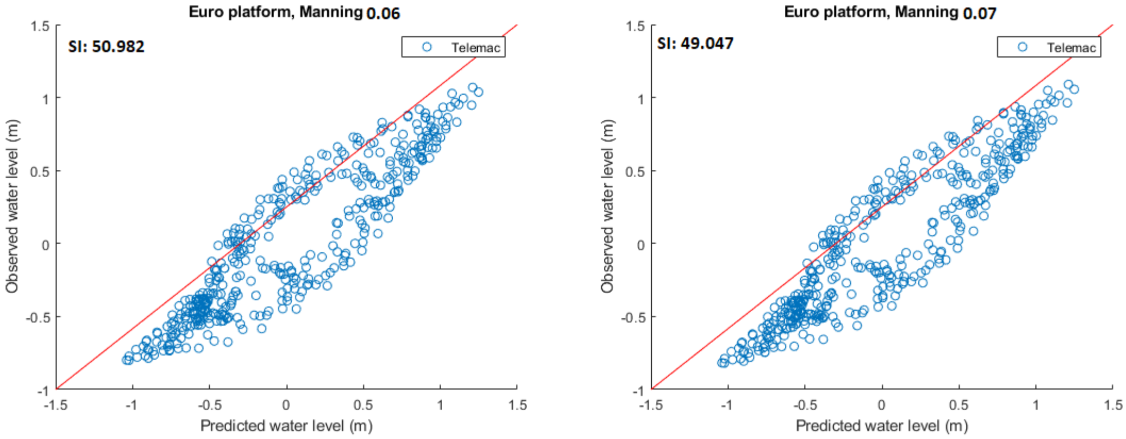

(a) Comparison between tidal gauge data and Delft 3D Manning 0.06

(b) Comparison between tidal gauge data and Delft 3D Manning 0.07

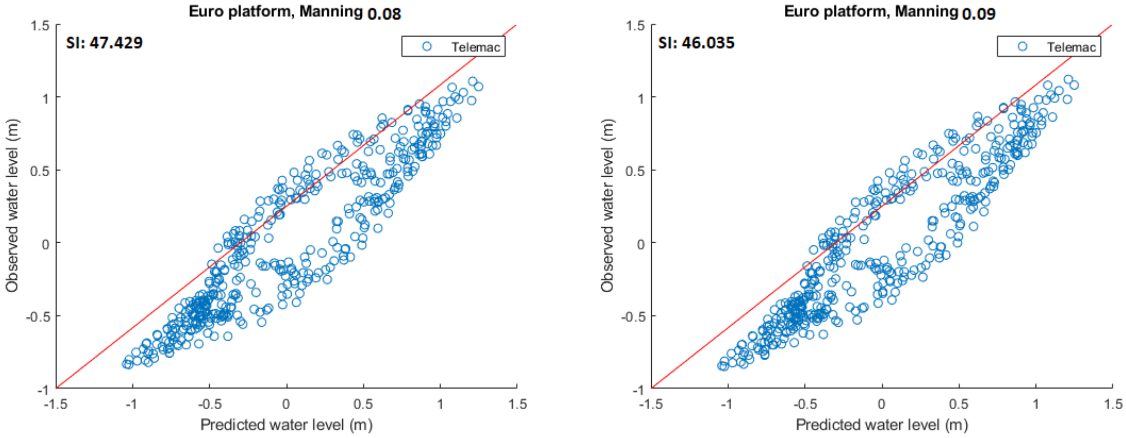

(c) Comparison between tidal gauge data and Delft 3D Manning 0.08

(d) Comparison between tidal gauge data and Delft 3D Manning 0.09

Figure C.31: The scatter index between the tidal station Euro platform and the different Telemac models, Manning 0.06-0.09

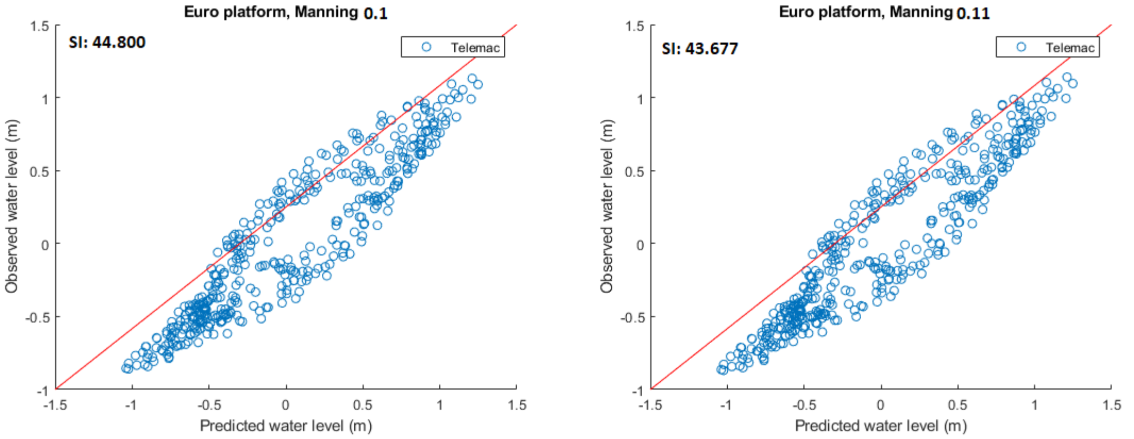

(a) Comparison between tidal gauge data and Delft 3D Manning 0.1

(b) Comparison between tidal gauge data and Delft 3D Manning 0.11

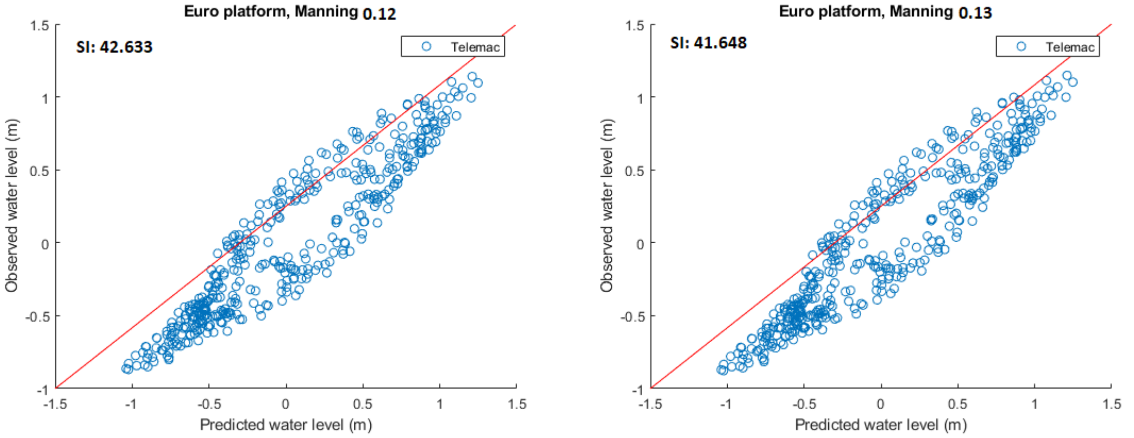

(c) Comparison between tidal gauge data and Delft 3D Manning 0.12

(d) Comparison between tidal gauge data and Delft 3D Manning 0.13

Figure C.32: The scatter index between the tidal station Euro platform and the different Telemac models, Manning 0.1-0.13

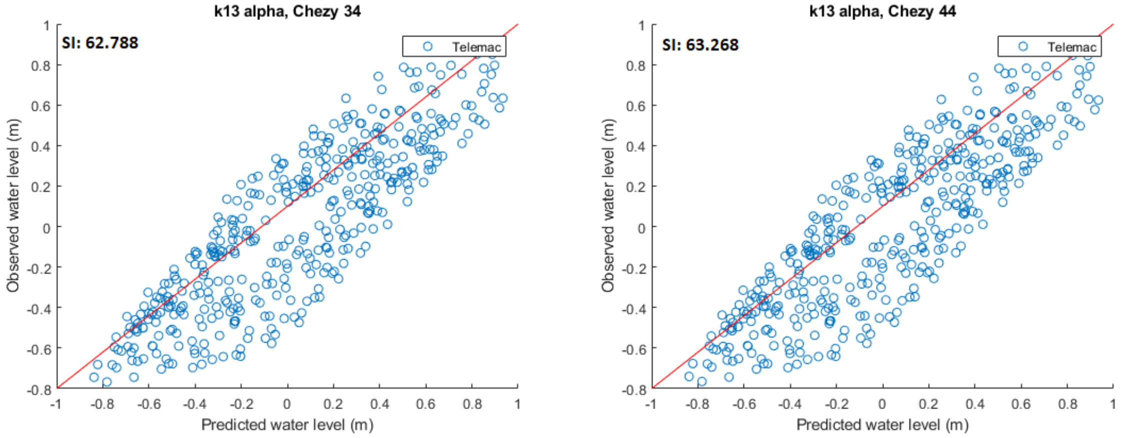

(a) Comparison between tidal gauge data and Delft 3D Chezy 34 (b) Comparison between tidal gauge data and Delft 3D Chezy 44

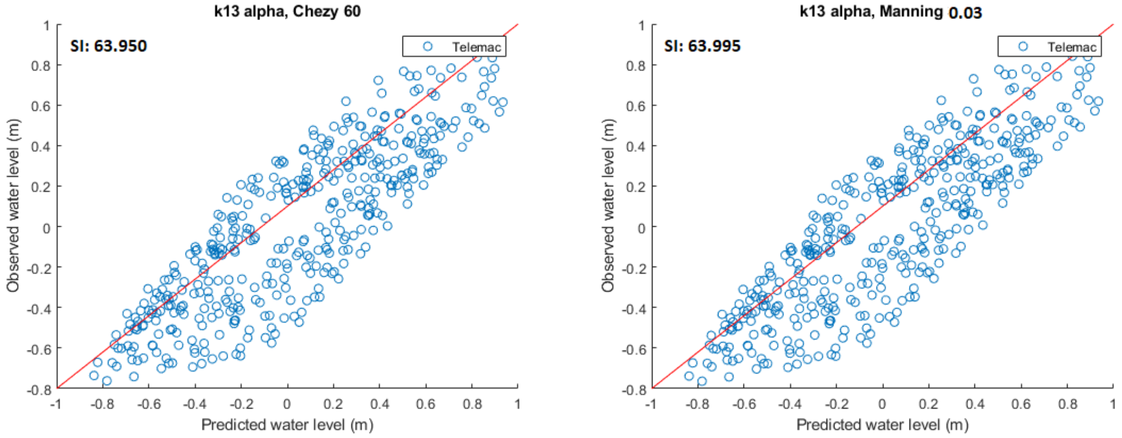

(c) Comparison between tidal gauge data and Delft 3D Chezy 60 (d) Comparison between tidal gauge data and Delft 3D Manning 0.03

Figure C.33: The scatter index between the tidal station K13 alpha and the different Telemac models, Chezy 34-60 and Manning 0.03

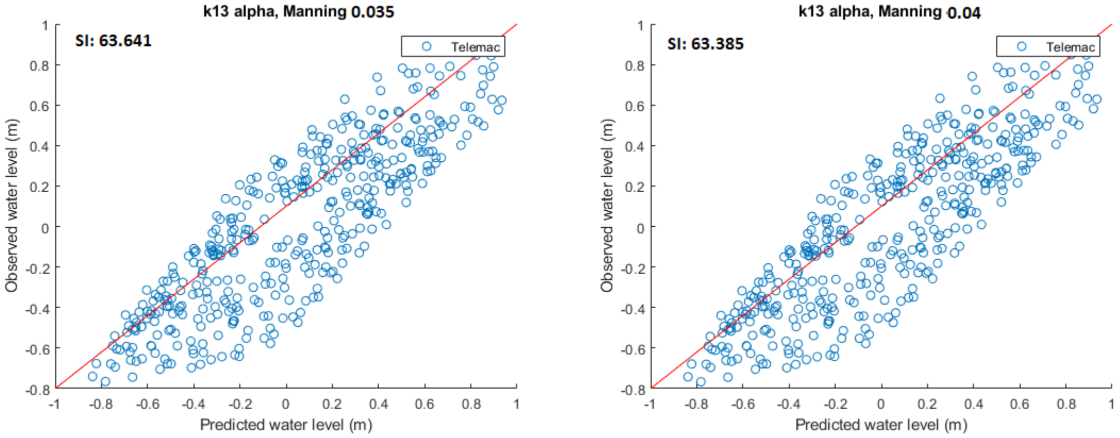

(a) Comparison between tidal gauge data and Delft 3D Manning 0.035 (b) Comparison between tidal gauge data and Delft 3D Manning 0.04

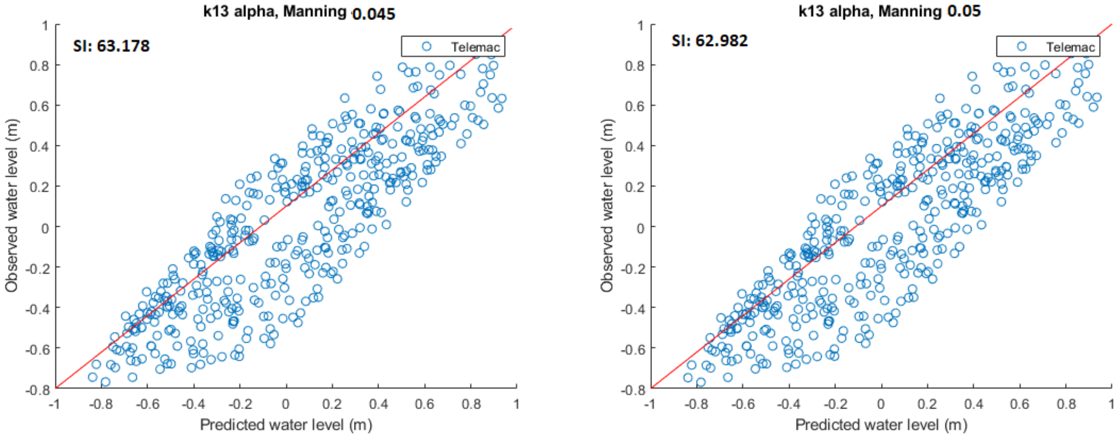

(c) Comparison between tidal gauge data and Delft 3D Manning 0.045 (d) Comparison between tidal gauge data and Delft 3D Manning 0.05

Figure C.34: The scatter index between the tidal station K13 alpha and the different Telemac models, Manning 0.035-0.05

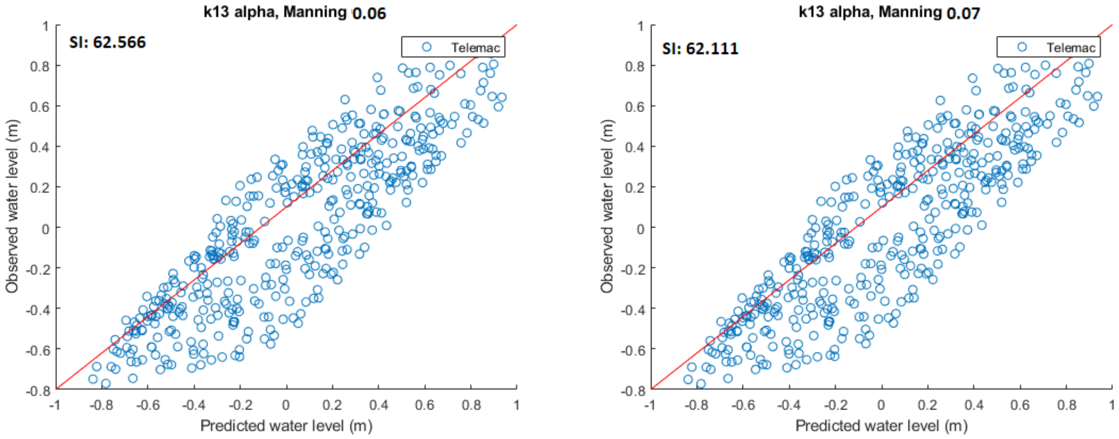

(a) Comparison between tidal gauge data and Delft 3D Manning 0.06 (b) Comparison between tidal gauge data and Delft 3D Manning 0.07

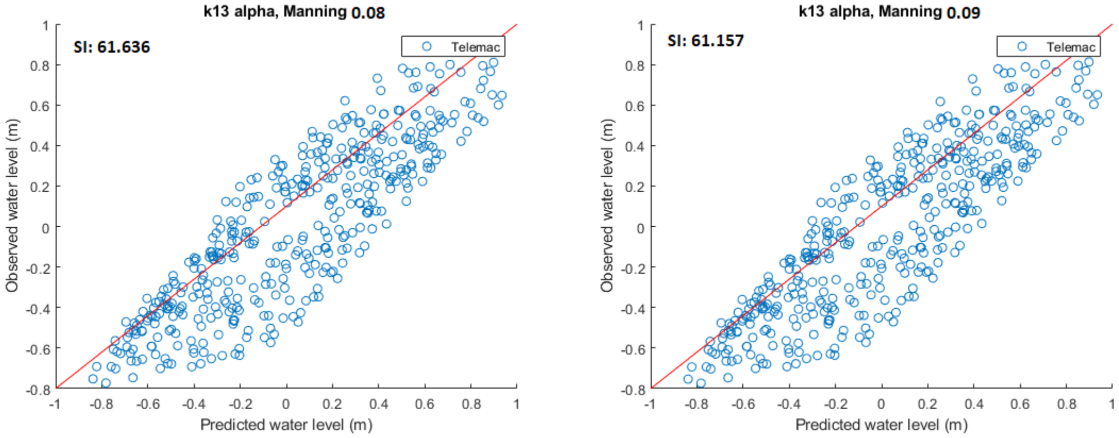

(c) Comparison between tidal gauge data and Delft 3D Manning 0.08 (d) Comparison between tidal gauge data and Delft 3D Manning 0.09

Figure C.35: The scatter index between the tidal station K13 alpha and the different Telemac models, Manning 0.06-0.09

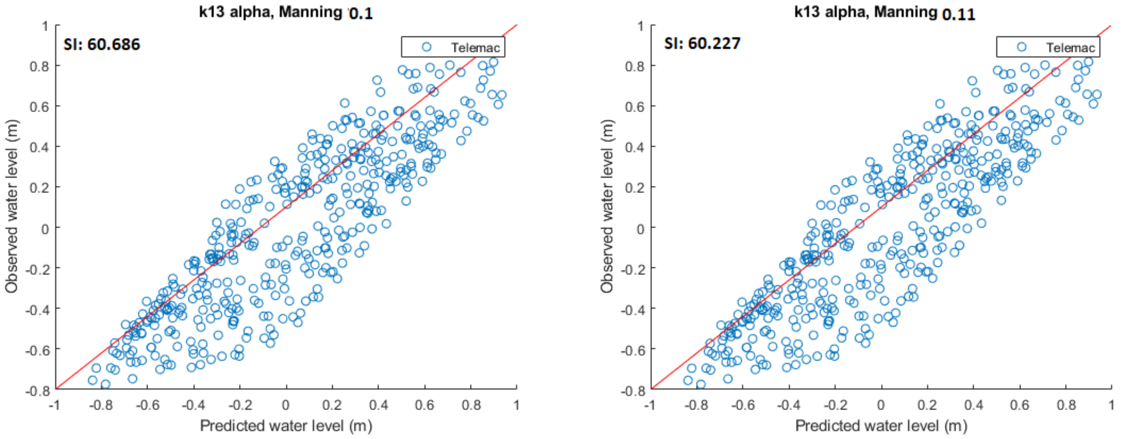

(a) Comparison between tidal gauge data and Delft 3D Manning 0.1

(b) Comparison between tidal gauge data and Delft 3D Manning 0.11

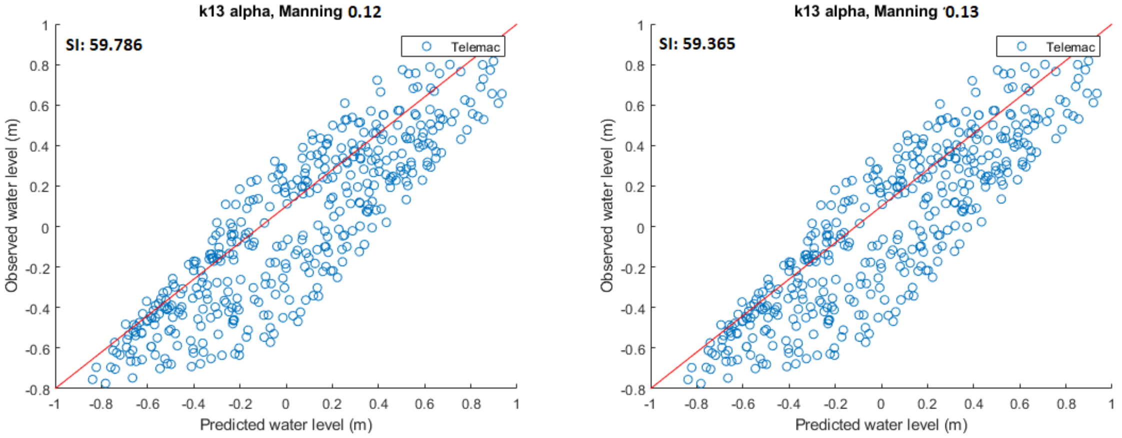

(c) Comparison between tidal gauge data and Delft 3D Manning 0.12

(d) Comparison between tidal gauge data and Delft 3D Manning 0.13

Figure C.36: The scatter index between the tidal station K13 alpha and the different Telemac models, Manning 0.1-0.13

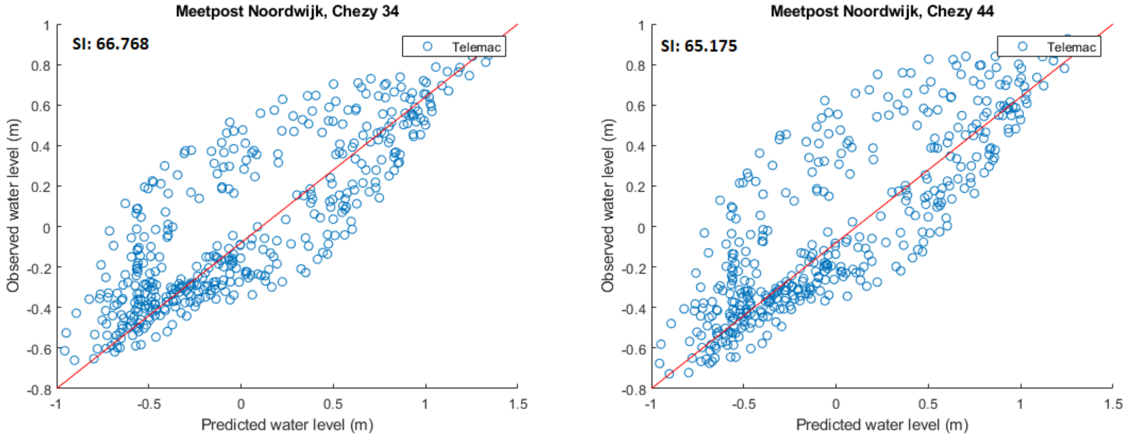

(a) Comparison between tidal gauge data and Delft 3D Chezy 34 (b) Comparison between tidal gauge data and Delft 3D Chezy 44

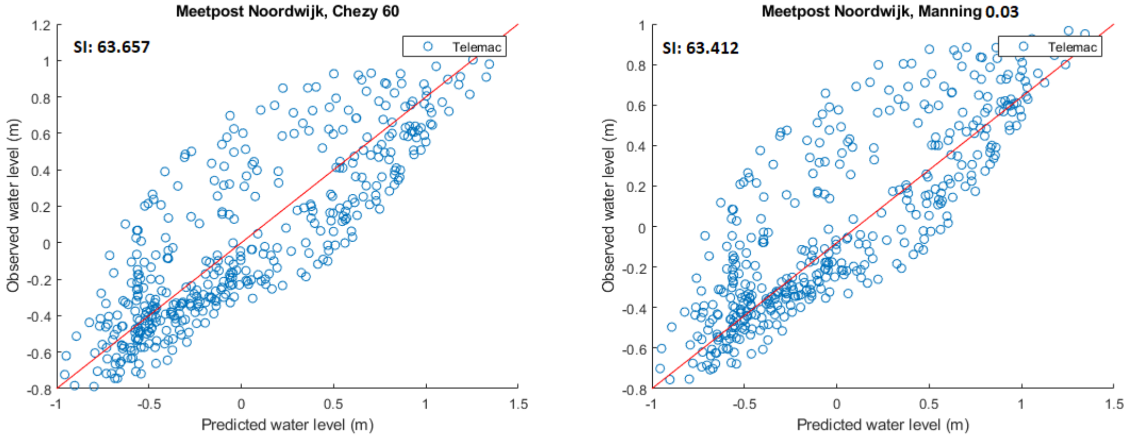

(c) Comparison between tidal gauge data and Delft 3D Chezy 60 (d) Comparison between tidal gauge data and Delft 3D Manning 0.03

Figure C.37: The scatter index between the tidal station Meetpost Noordwijk and the different Telemac models, Chezy 34-60 and Manning 0.03

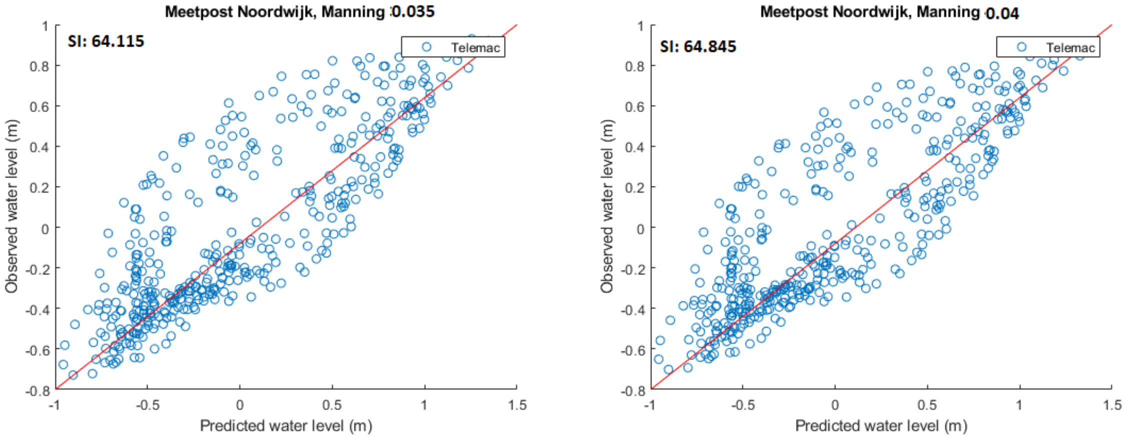

(a) Comparison between tidal gauge data and Delft 3D Manning 0.035 (b) Comparison between tidal gauge data and Delft 3D Manning 0.04

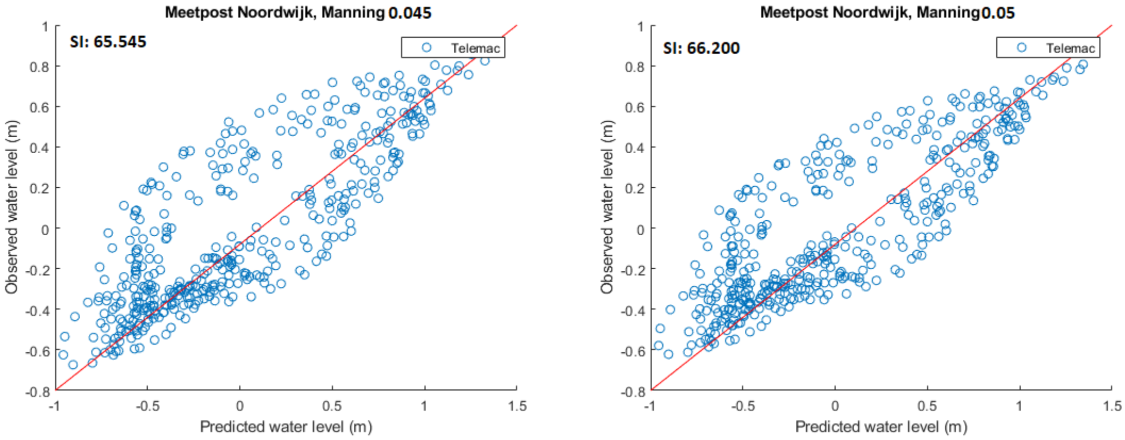

(c) Comparison between tidal gauge data and Delft 3D Manning 0.045 (d) Comparison between tidal gauge data and Delft 3D Manning 0.05

Figure C.38: The scatter index between the tidal station Meetpost Noordwijk and the different Telemac models, Manning 0.035-0.05

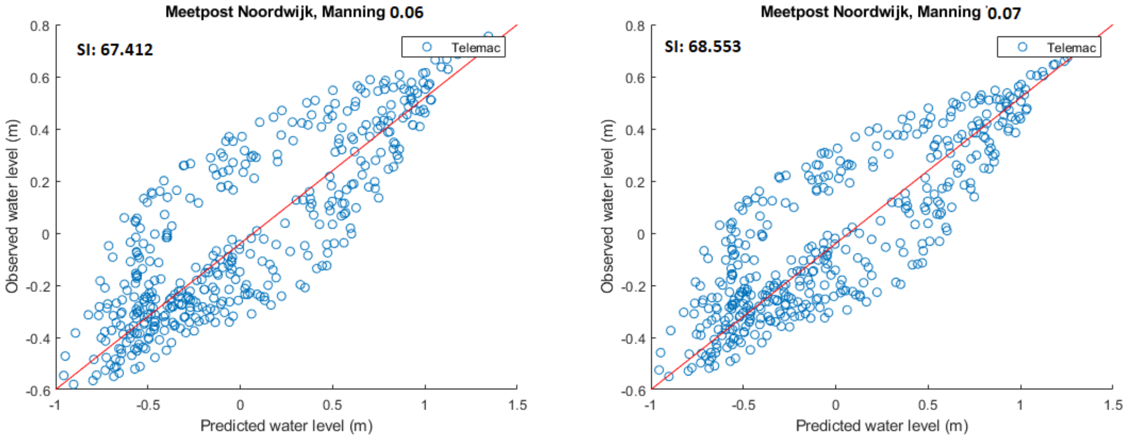

(a) Comparison between tidal gauge data and Delft 3D Manning 0.06

(b) Comparison between tidal gauge data and Delft 3D Manning 0.07

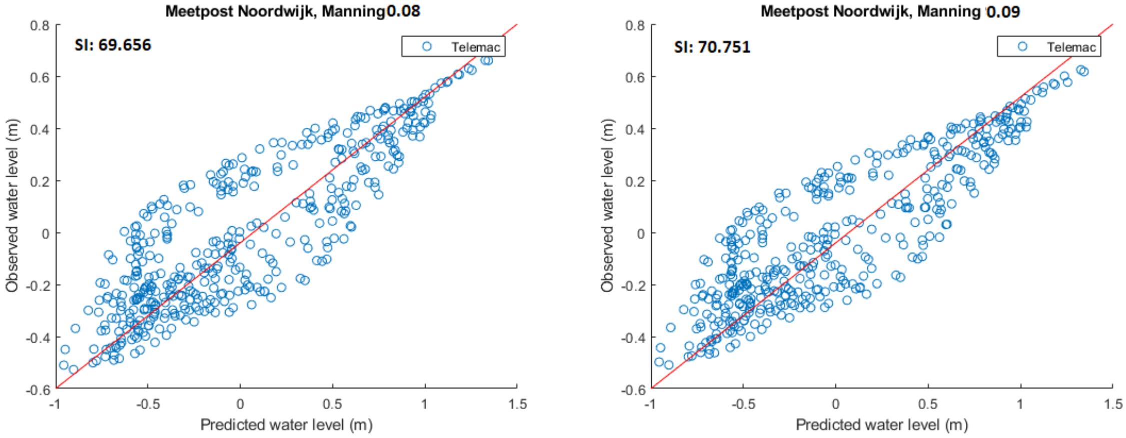

(c) Comparison between tidal gauge data and Delft 3D Manning 0.08

(d) Comparison between tidal gauge data and Delft 3D Manning 0.09

Figure C.39: The scatter index between the tidal station Meetpost Noordwijk and the different Telemac models, Manning 0.06-0.09

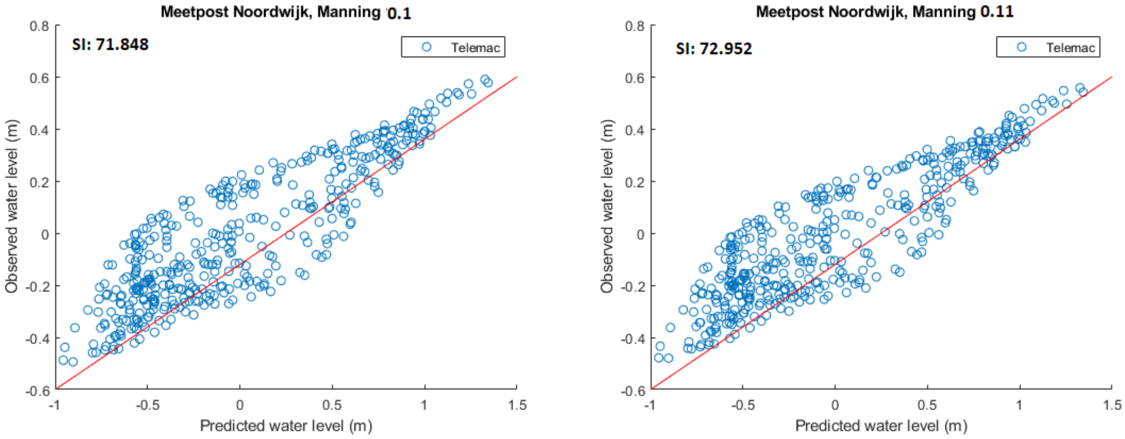

(a) Comparison between tidal gauge data and Delft 3D Manning 0.1

(b) Comparison between tidal gauge data and Delft 3D Manning 0.11

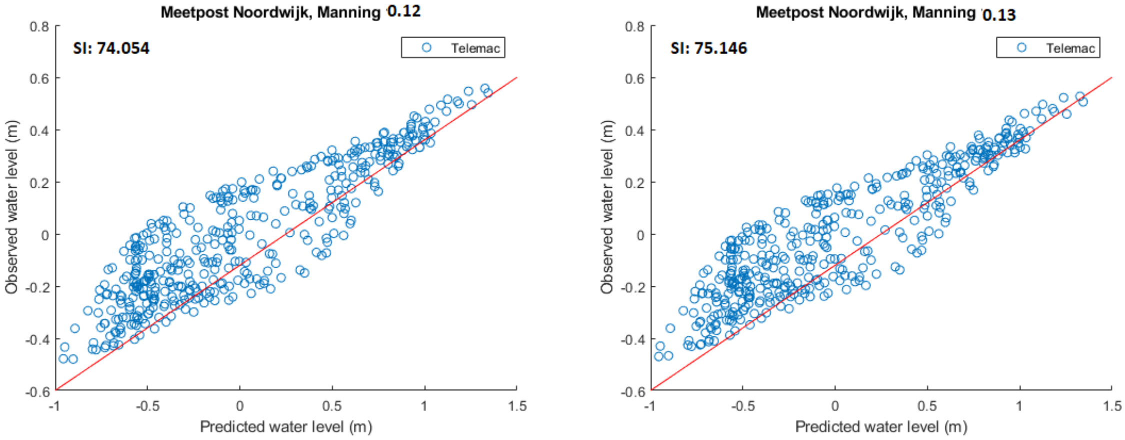

(c) Comparison between tidal gauge data and Delft 3D Manning 0.12

(d) Comparison between tidal gauge data and Delft 3D Manning 0.13

Figure C.40: The scatter index between the tidal station Meetpost Noordwijk and the different Telemac models, Manning 0.1-0.13

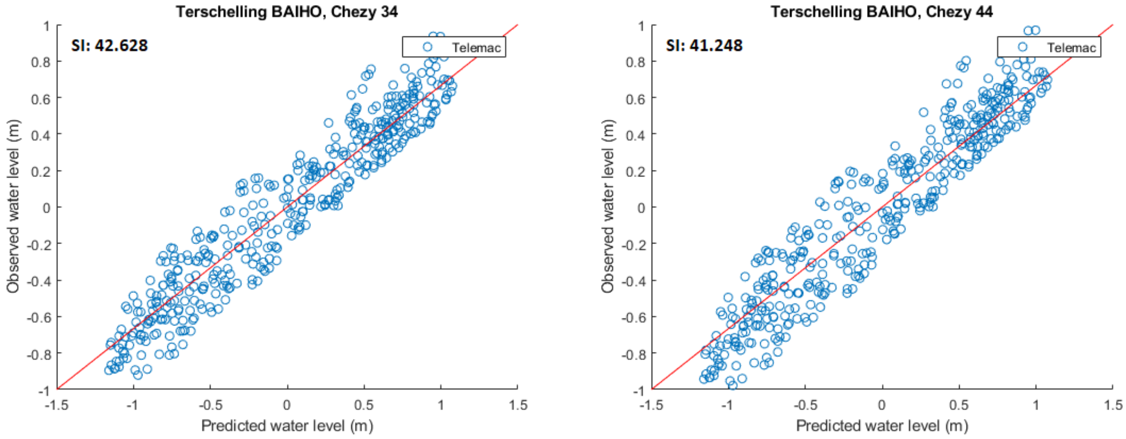

(a) Comparison between tidal gauge data and Delft 3D Chezy 34

(b) Comparison between tidal gauge data and Delft 3D Chezy 44

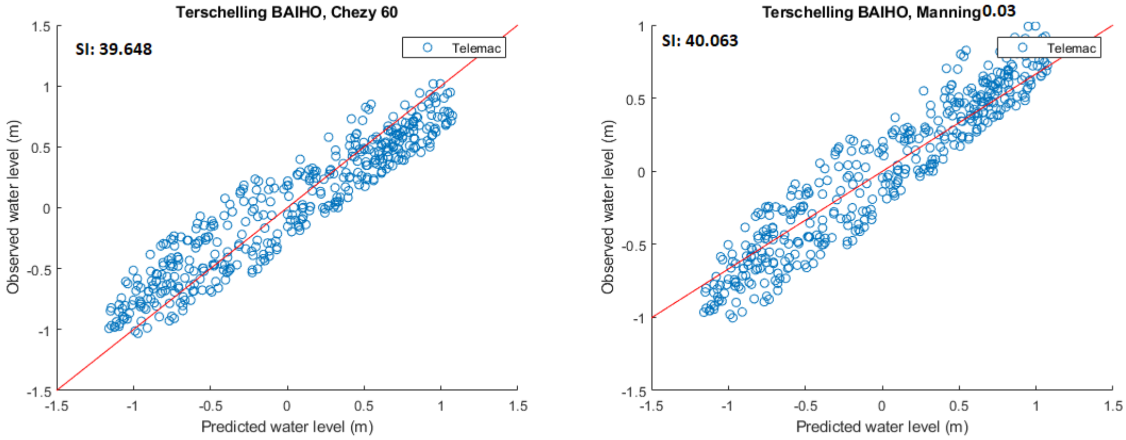

(c) Comparison between tidal gauge data and Delft 3D Chezy 60

(d) Comparison between tidal gauge data and Delft 3D Manning 0.03

Figure C.41: The scatter index between the tidal station Terschellinger BAIHO and the different Telemac models, Chezy 34-60 and Manning 0.03

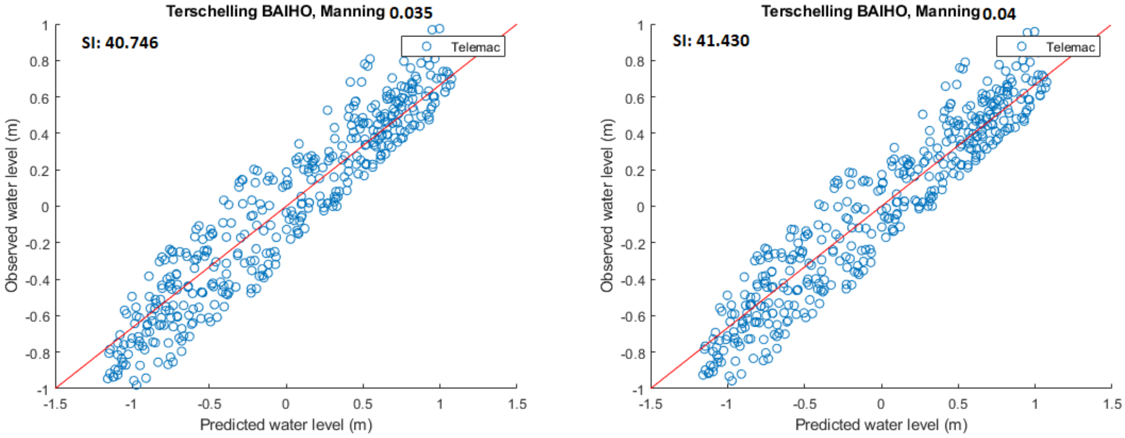

(a) Comparison between tidal gauge data and Delft 3D Manning 0.035

(b) Comparison between tidal gauge data and Delft 3D Manning 0.04

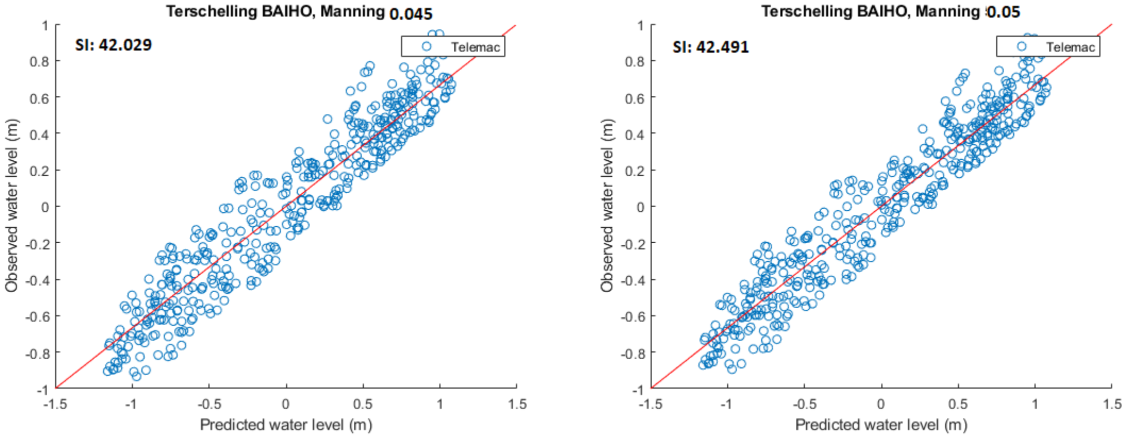

(c) Comparison between tidal gauge data and Delft 3D Manning 0.045

(d) Comparison between tidal gauge data and Delft 3D Manning 0.05

Figure C.42: The scatter index between the tidal station Terschellinger BAIHO and the different Telemac models, Manning 0.035-0.05

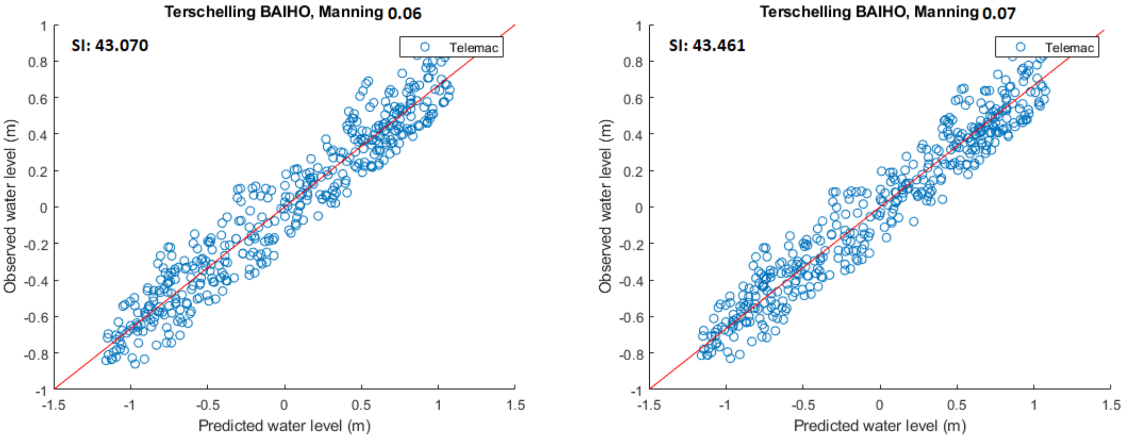

(a) Comparison between tidal gauge data and Delft 3D Manning 0.06

(b) Comparison between tidal gauge data and Delft 3D Manning 0.07

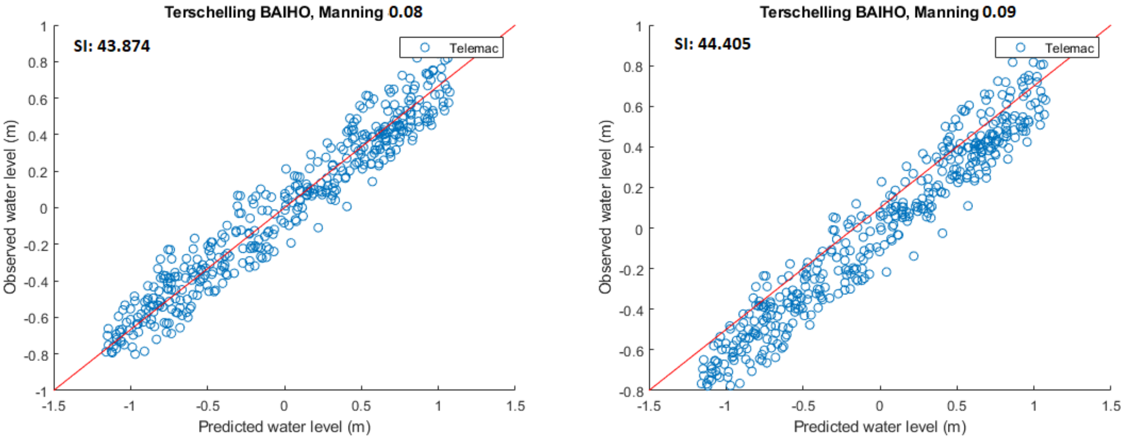

(c) Comparison between tidal gauge data and Delft 3D Manning 0.08

(d) Comparison between tidal gauge data and Delft 3D Manning 0.09

Figure C.43: The scatter index between the tidal station Terschellinger BAIHO and the different Telemac models, Manning 0.06-0.09

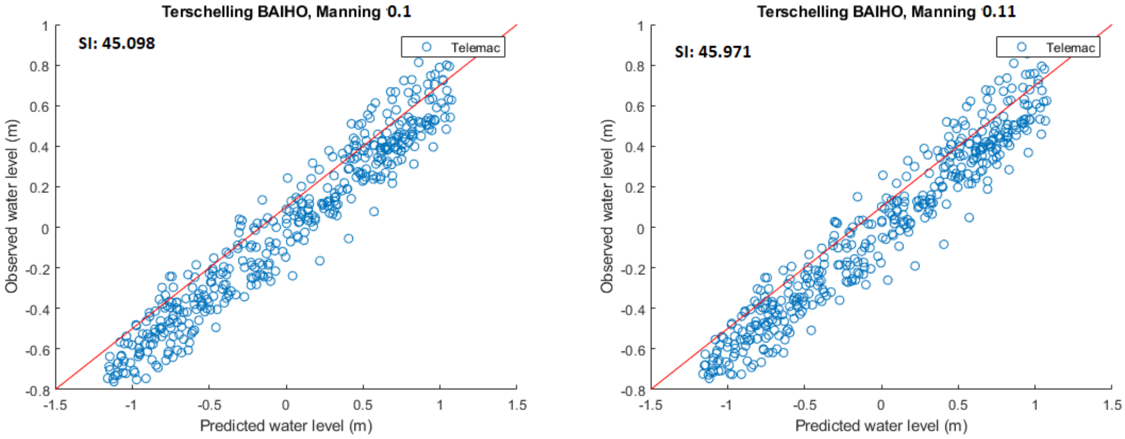

(a) Comparison between tidal gauge data and Delft 3D Manning 0.1

(b) Comparison between tidal gauge data and Delft 3D Manning 0.11

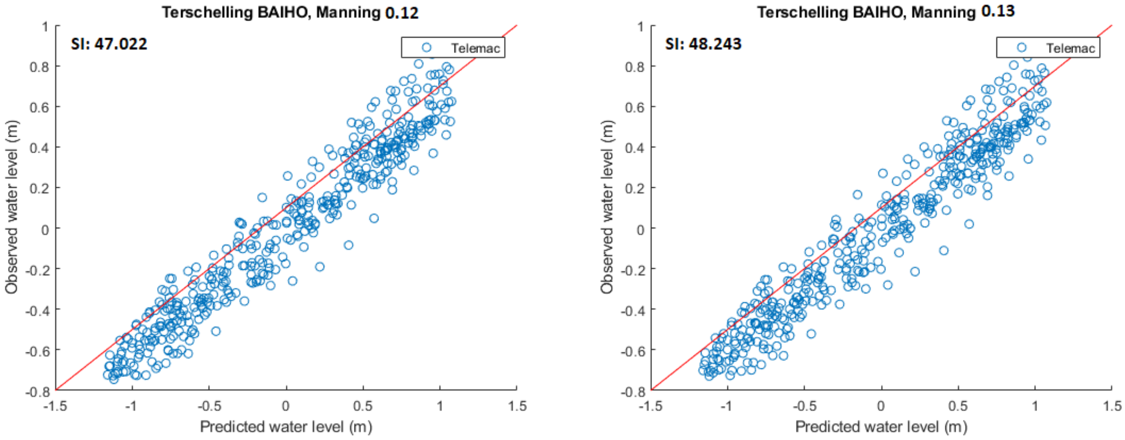

(c) Comparison between tidal gauge data and Delft 3D Manning 0.12

(d) Comparison between tidal gauge data and Delft 3D Manning 0.13

Figure C.44: The scatter index between the tidal station Terschellinger BAIHO and the different Telemac models, Manning 0.1-0.13

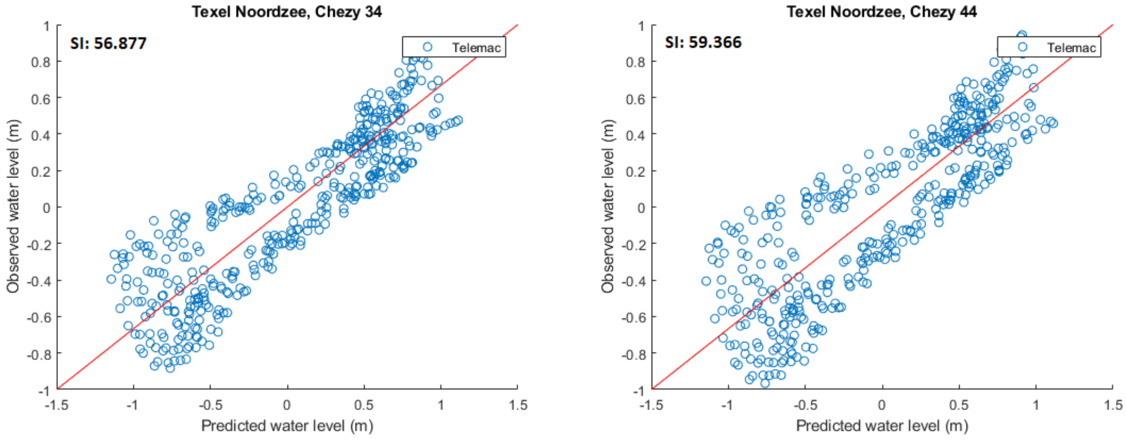

(a) Comparison between tidal gauge data and Delft 3D Chezy 34

(b) Comparison between tidal gauge data and Delft 3D Chezy 44

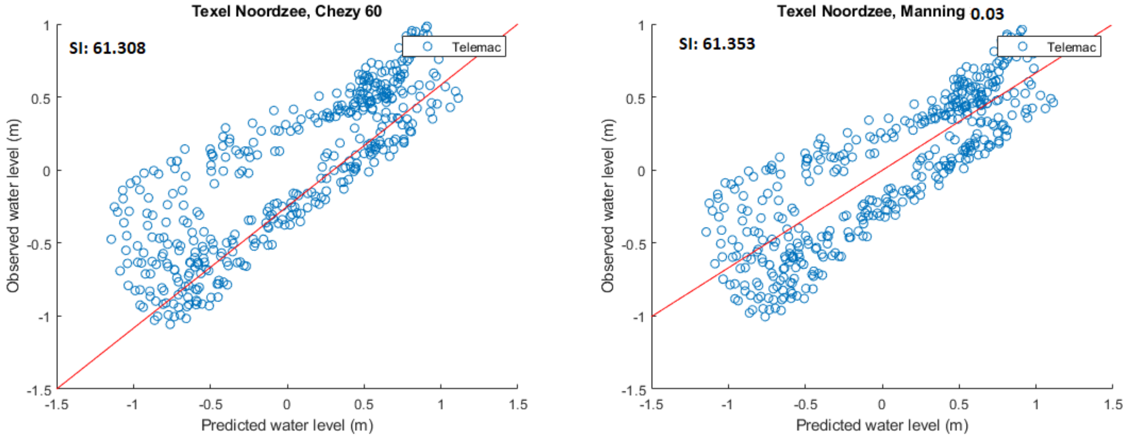

(c) Comparison between tidal gauge data and Delft 3D Chezy 60

(d) Comparison between tidal gauge data and Delft 3D Manning 0.03

Figure C.45: The scatter index between the tidal station Texel Noordzee and the different Telemac models, Chezy 34-60 and Manning 0.03

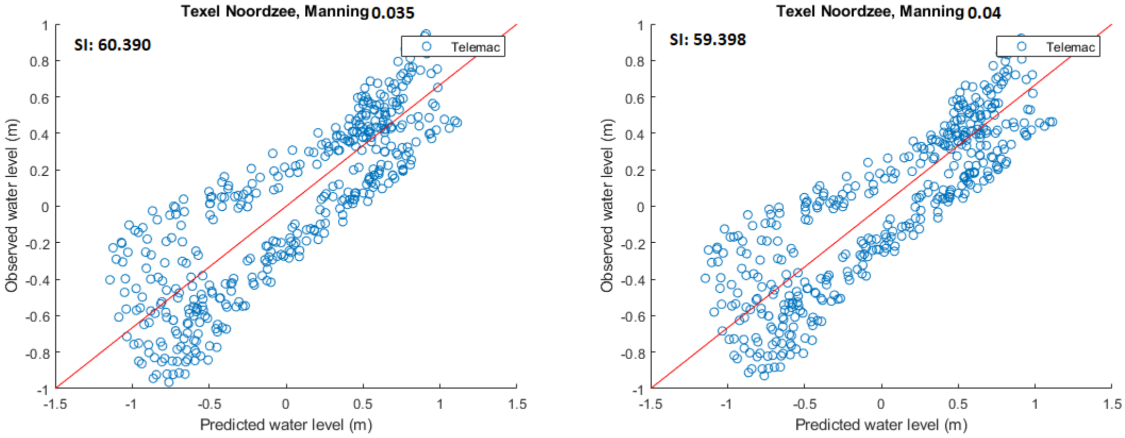

(a) Comparison between tidal gauge data and Delft 3D Manning 0.035 (b) Comparison between tidal gauge data and Delft 3D Manning 0.04

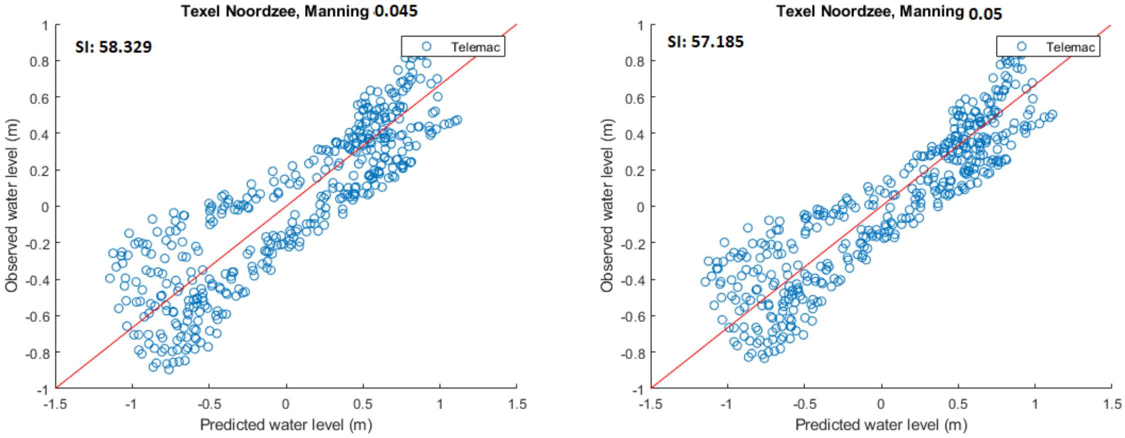

(c) Comparison between tidal gauge data and Delft 3D Manning 0.045 (d) Comparison between tidal gauge data and Delft 3D Manning 0.05

Figure C.46: The scatter index between the tidal station Texel Noordzee and the different Telemac models, Manning 0.035-0.05

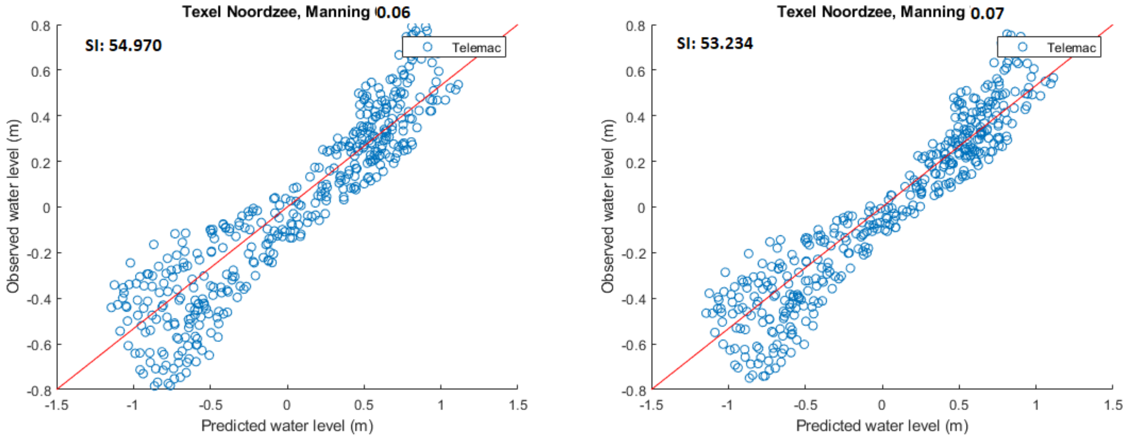

(a) Comparison between tidal gauge data and Delft 3D Manning 0.06

(b) Comparison between tidal gauge data and Delft 3D Manning 0.07

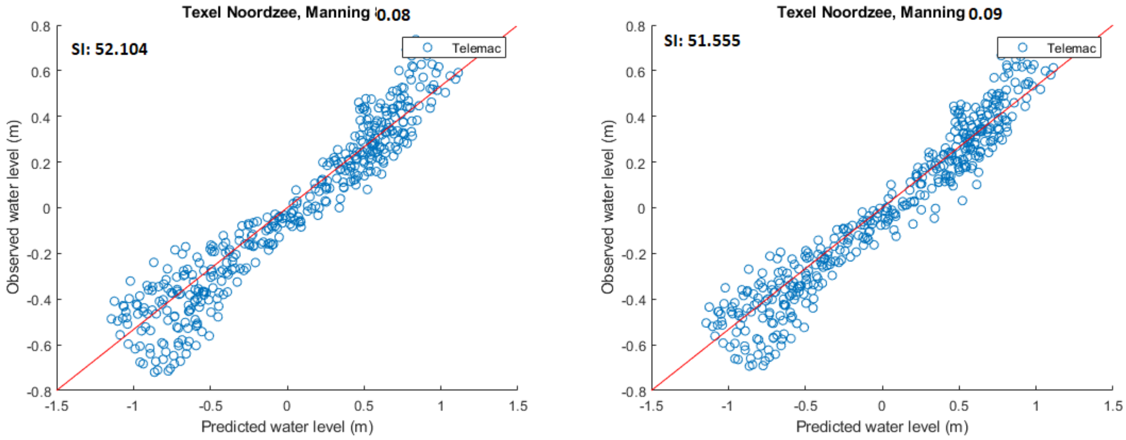

(c) Comparison between tidal gauge data and Delft 3D Manning 0.08

(d) Comparison between tidal gauge data and Delft 3D Manning 0.09

Figure C.47: The scatter index between the tidal station Texel Noordzee and the different Telemac models, Manning 0.06-0.09

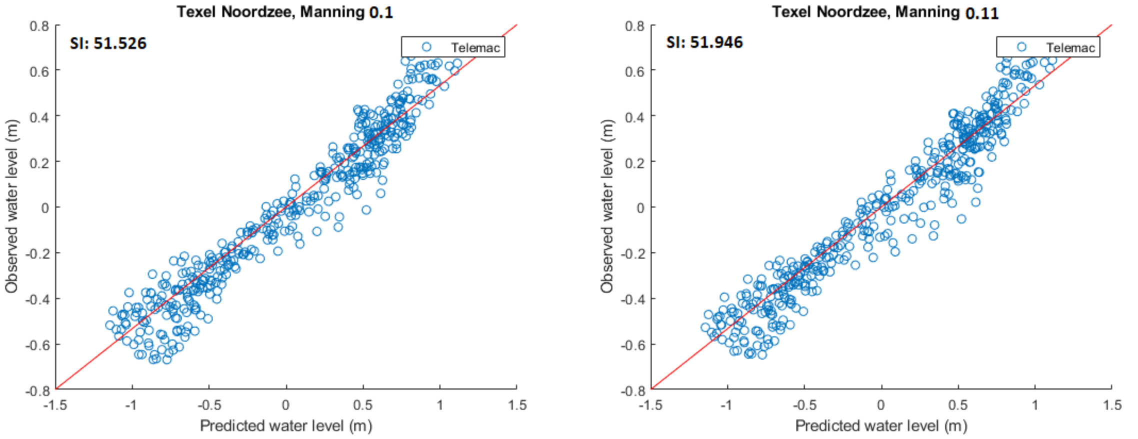

(a) Comparison between tidal gauge data and Delft 3D Manning 0.1

(b) Comparison between tidal gauge data and Delft 3D Manning 0.11

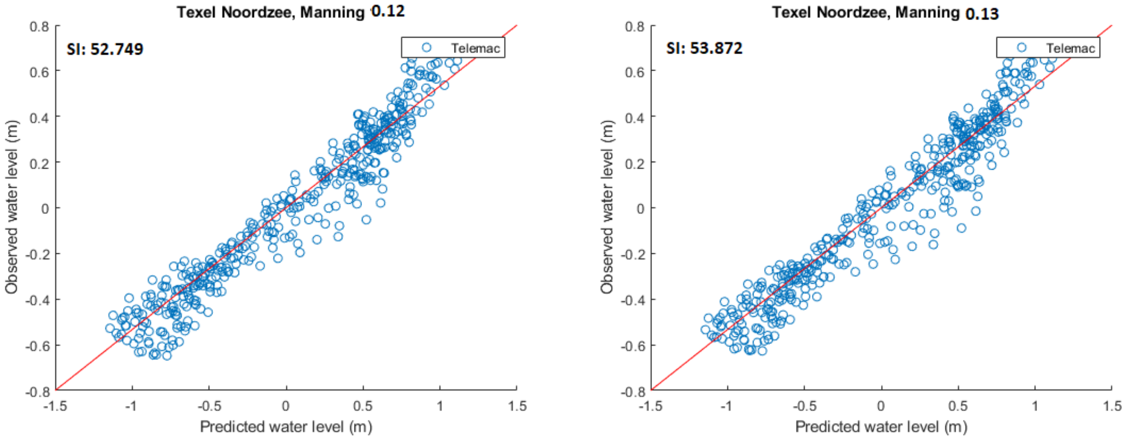

(c) Comparison between tidal gauge data and Delft 3D Manning 0.12

(d) Comparison between tidal gauge data and Delft 3D Manning 0.13

Figure C.48: The scatter index between the tidal station Texel Noordzee and the different Telemac models, Manning 0.1-0.13

D

Delft 3D analysis

In the following tables the analysis of different tidal stations can be seen. Here the RMSE, Pearson coefficient and the scatter index for the different bottom roughness can be calculated.

Table D.1: RMSE, Pearson and Scatter index of the tidal station Brouwers Havensche Gat

Brouwers	Chezy 34	Chezy 44	Chezy 60	Manning 0.03	Manning 0.035	Manning 0.04	Manning 0.045	Manning 0.05	Manning 0.06
RMSE	0.3462	0.3534	0.3616	0.3031	0.3144	0.2945	0.2886	0.2853	0.2877
Pearson	0.9223	0.9148	0.9109	0.9391	0.9331	0.9450	0.9510	0.9571	0.9686
Scatter index	44.6253	45.5454	46.6059	39.0585	40.5166	37.95896	37.1926	36.7685	37.0779

Table D.2: RMSE, Pearson and Scatter index of the tidal station Euro platform

Euro	Chezy 34	Chezy 44	Chezy 60	Manning 0.03	Manning 0.035	Manning 0.04	Manning 0.045	Manning 0.05	Manning 0.06
RMSE	0.2623	0.2538	0.2467	0.2491	0.2607	0.2672	0.2458	0.2529	0.2569
Pearson	0.8937	0.9012	0.907	0.905	0.8951	0.8892	0.9076	0.9019	0.8985
Scatter index	51.495	49.8157	48.4199	48.8902	51.1836	52.4589	48.2458	49.649	50.4337

Table D.3: RMSE, Pearson and Scatter index of the tidal station K13 alpha

K13	Chezy 34	Chezy 44	Chezy 60	Manning 0.03	Manning 0.035	Manning 0.04	Manning 0.045	Manning 0.05	Manning 0.06
RMSE	0.2023	0.2057	0.20839	0.2077	0.2034	0.2004	0.2088	0.2067	0.2049
Pearson	0.8924	0.8879	0.8839	0.8853	0.8910	0.8948	0.8835	0.8872	0.8891
Scatter index	56.1637	57.1092	57.8539	57.6538	56.4798	55.6267	57.9784	57.2939	56.8981

Table D.4: RMSE, Pearson and Scatter index of the tidal station Meetpost Noordwijk

Meetpost Noordwijk	Chezy 34	Chezy 44	Chezy 60	Manning 0.03	Manning 0.035	Manning 0.04	Manning 0.045	Manning 0.05	Manning 0.06
RMSE	0.2979	0.2768	0.2717	0.2696	0.2939	0.3134	0.2686	0.2757	0.2843
Pearson	0.8532	0.8699	0.8834	0.8784	0.8566	0.8465	0.8843	0.8710	0.8635
Scatter index	61.287	56.9419	55.8855	55.4706	60.4709	64.4817	55.2565	56.7131	58.4866

Table D.5: RMSE, Pearson and Scatter index of the tidal station Terschellinger BAIHO

Terschellinger	Chezy 34	Chezy 44	Chezy 60	Manning 0.03	Manning 0.035	Manning 0.04	Manning 0.045	Manning 0.05	Manning 0.06
RMSE	0.1951	0.1983	0.2012	0.1996	0.1956	0.193	0.2009	0.1983	0.197
Pearson	0.9572	0.9551	0.953	0.9541	0.9568	0.9584	0.9532	0.9551	0.956
Scatter index	33.7037	34.2629	34.7621	34.4941	33.797	33.3395	34.712	34.2656	34.0321

Table D.6: RMSE, Pearson and Scatter index of the tidal station Texel Noordzee

Texel	Chezy 34	Chezy 44	Chezy 60	Manning 0.03	Manning 0.035	Manning 0.04	Manning 0.045	Manning 0.05	Manning 0.06
RMSE	0.2834	0.307	0.3262	0.3145	0.2835	0.2659	0.3237	0.3041	0.2936
Pearson	0.8981	0.8698	0.8566	0.863	0.8971	0.9212	0.8576	0.8725	0.8844
Scatter index	51.1172	55.3663	58.8367	56.7118	51.1333	47.9553	58.3713	54.8433	52.9469

In the following table the bottom roughness scores for the different tidal stations can be seen. This is to give a overview of the scores.

Table D.7: Bottom roughness compared to the different tidal stations

		Brouwers	Euro platform	K13	Meetpost	Terschellinger IHO	Texel
Chezy 34	RMSE (m)	0.3462	0.2623	0.2023	0.2979	0.1951	0.2834
	R^2(Pearson)	0.9223	0.8937	0.8924	0.8532	0.95715	0.8981
	SI (%)	44.6253	51.495	56.1637	61.287	33.7037	51.1172
Chezy 44	RMSE (m)	0.3534	0.2538	0.2057	0.2768	0.1983	0.3069
	R^2(Pearson)	0.9148	0.9012	0.8879	0.87	0.9551	0.8698
	SI (%)	45.5454	49.8157	57.1092	56.9419	34.2629	55.3663
Chezy 60	RMSE (m)	0.3616	0.2467	0.2084	0.2717	0.2012	0.3262
	R^2(Pearson)	0.9109	0.907	0.8839	0.8834	0.953	0.8566
	SI (%)	46.606	48.4199	57.8539	55.8855	34.7621	58.83685
Manning 0.03	RMSE (m)	0.3144	0.2458	0.2088	0.2686	0.2009	0.3237
	R^2(Pearson)	0.9331	0.9076	0.8835	0.8843	0.9532	0.8576
	SI (%)	40.5166	48.2458	57.9784	55.2565	34.712	58.3713
Manning 0.035	RMSE (m)	0.3031	0.2491	0.2077	0.2696	0.1996	0.3145
	R^2(Pearson)	0.9391	0.905	0.8853	0.8784	0.9541	0.863
	SI (%)	39.05849	48.8902	57.6538	55.4706	34.4941	56.7118
Manning 0.04	RMSE (m)	0.29452	0.2529	0.2064	0.2757	0.1983	0.3041
	R^2(Pearson)	0.945	0.9019	0.8872	0.871	0.9551	0.8725
	SI (%)	37.959	49.649	57.2939	56.713	34.2656	54.8433
Manning 0.045	RMSE (m)	0.2886	0.2569	0.2049	0.2843	0.197	0.2936
	R^2(Pearson)	0.951	0.8985	0.8891	0.8635	0.956	0.8844
	SI (%)	37.1926	50.4337	56.8981	58.4866	34.0321	52.9469
Manning 0.05	RMSE (m)	0.2853	0.2607	0.2034	0.2939	0.1956	0.2835
	R^2(Pearson)	0.9571	0.8951	0.891	0.8566	0.9568	0.8971
	SI (%)	36.7685	51.1836	56.4798	60.4709	33.797	51.1326
Manning 0.06	RMSE (m)	0.2877	0.2672	0.2004	0.3134	0.193	0.2659
	R^2(Pearson)	0.9686	0.8892	0.8948	0.8465	0.9584	0.9212
	SI (%)	37.0779	52.4589	55.6267	64.4817	33.3395	47.9553

The following figures show the comparison of the different tidal stations with their respective tidal gauge data. In these figures it can be seen if the data is in phase and where the difference occurs.

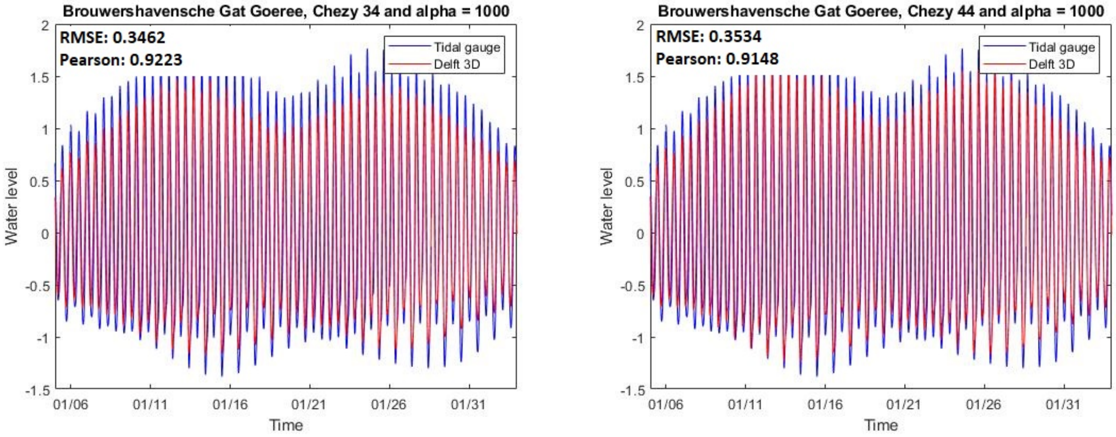

(a) Comparison between tidal gauge data and Delft 3D Chezy 34 (b) Comparison between tidal gauge data and Delft 3D Chezy 44

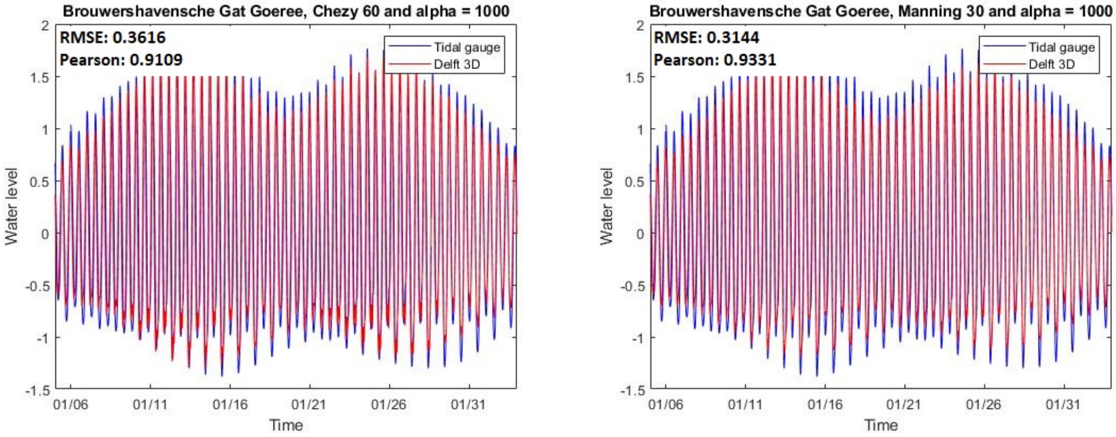

(c) Comparison between tidal gauge data and Delft 3D Chezy 60 (d) Comparison between tidal gauge data and Delft 3D Manning 0.03

Figure D.1: The comparison between the tidal station Brouwers Havensche Gat and the different Delft 3D models, Chezy 34-60 and Manning 0.03

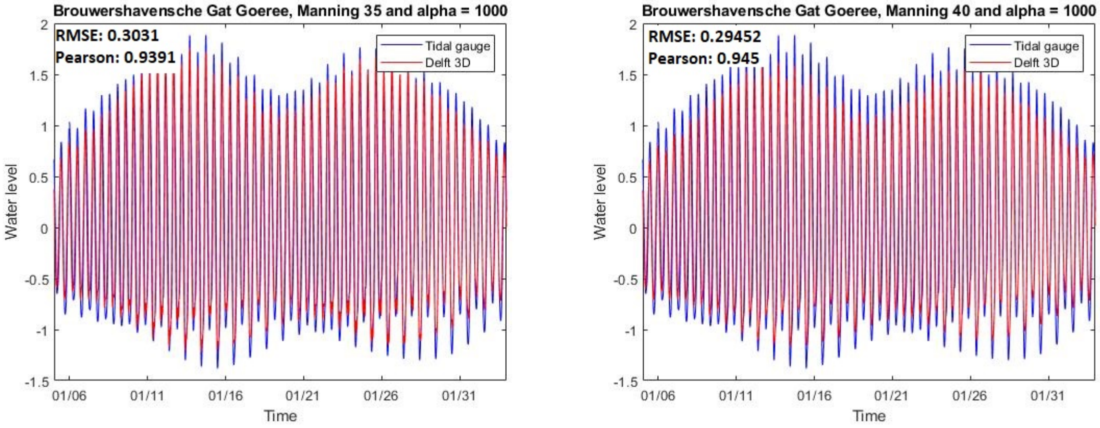

(a) Comparison between tidal gauge data and Delft 3D Manning 0.035

(b) Comparison between tidal gauge data and Delft 3D Manning 0.04

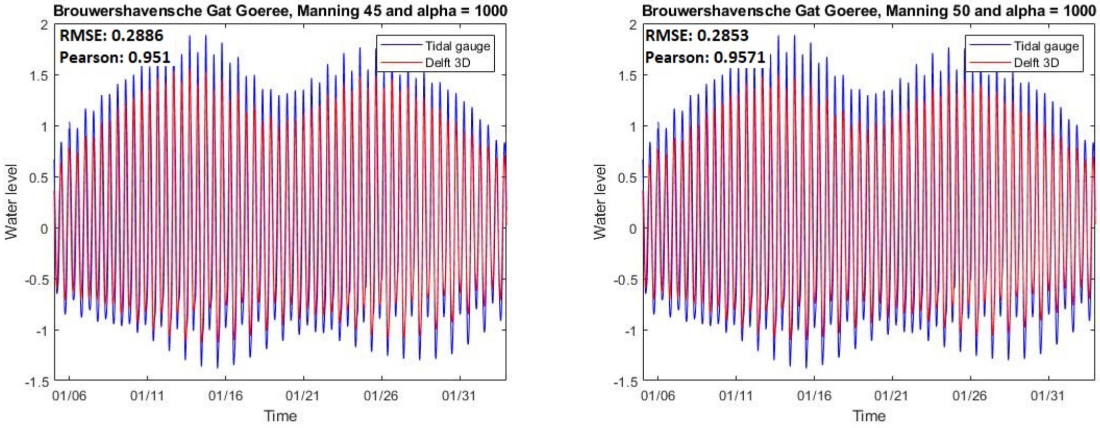

(c) Comparison between tidal gauge data and Delft 3D Manning 0.045

(d) Comparison between tidal gauge data and Delft 3D Manning 0.05

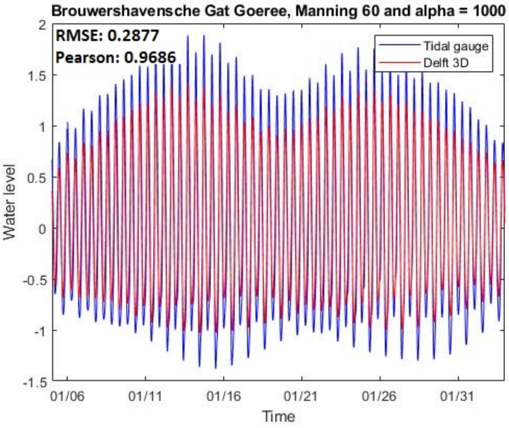

(e) Comparison between tidal gauge data and Delft 3D Manning 0.06

Figure D.2: The comparison between the tidal station Brouwers Havensche Gat and the different Delft 3D models, Manning 0.035-0.06

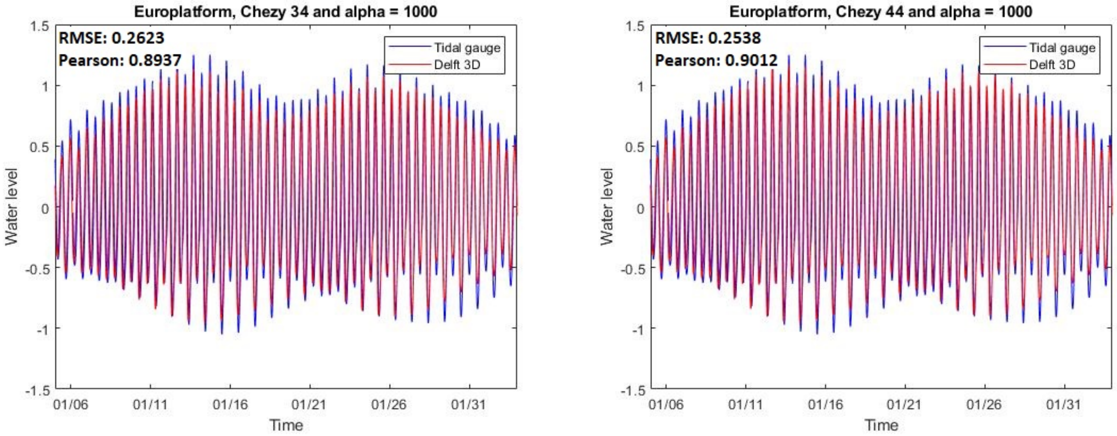

(a) Comparison between tidal gauge data and Delft 3D Chezy 34

(b) Comparison between tidal gauge data and Delft 3D Chezy 44

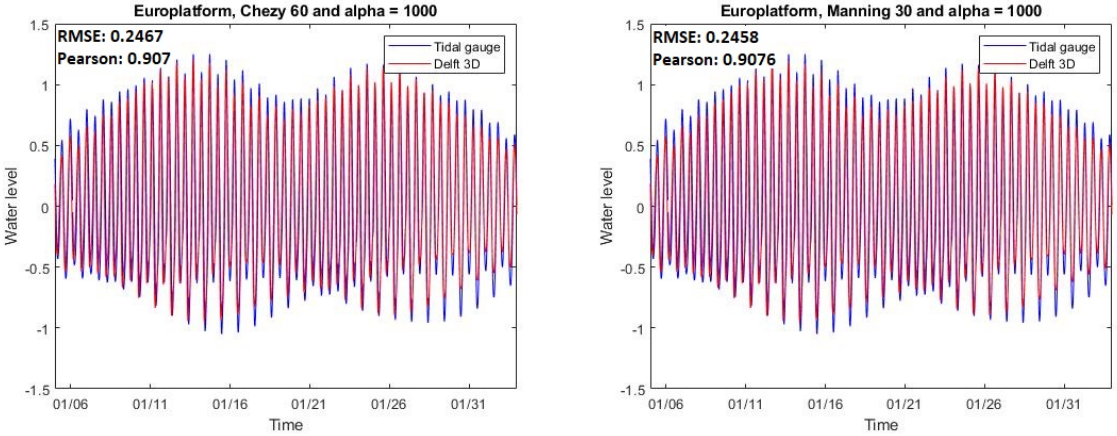

(c) Comparison between tidal gauge data and Delft 3D Chezy 60

(d) Comparison between tidal gauge data and Delft 3D Manning 0.03

Figure D.3: The comparison between the tidal station Euro platform and the different Delft 3D models, Chezy 34-60 and Manning 0.03

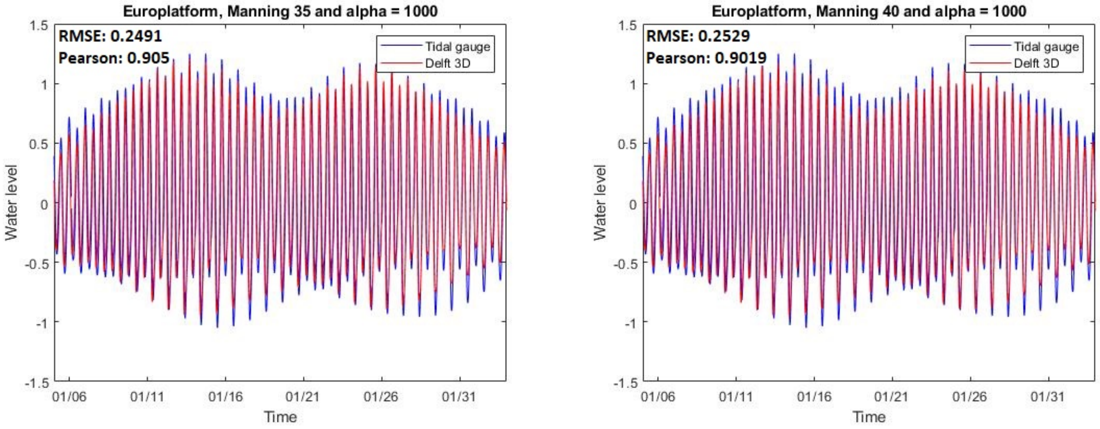

(a) Comparison between tidal gauge data and Delft 3D Manning 0.35

(b) Comparison between tidal gauge data and Delft 3D Manning 0.04

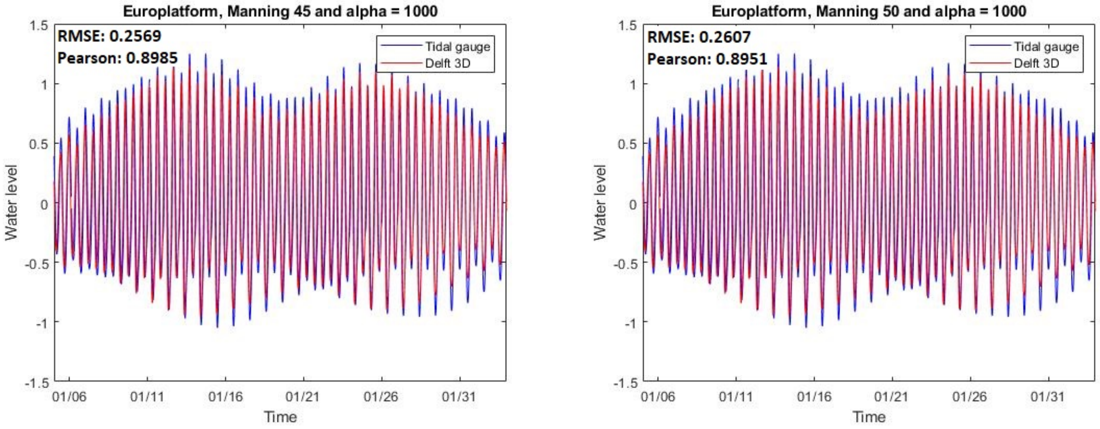

(c) Comparison between tidal gauge data and Delft 3D Manning 0.045

(d) Comparison between tidal gauge data and Delft 3D Manning 0.05

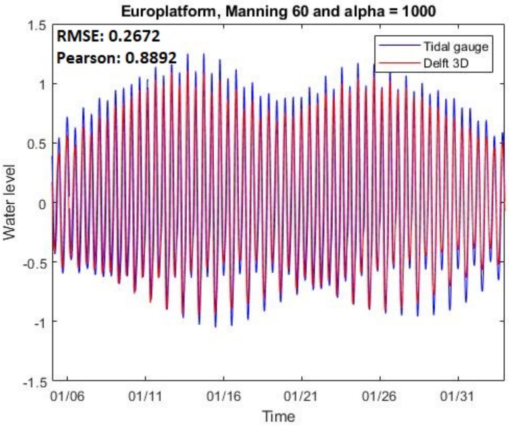

(e) Comparison between tidal gauge data and Delft 3D Manning 0.06

Figure D.4: The comparison between the tidal station Euro platform and the different Delft 3D models, Manning 0.035-0.06

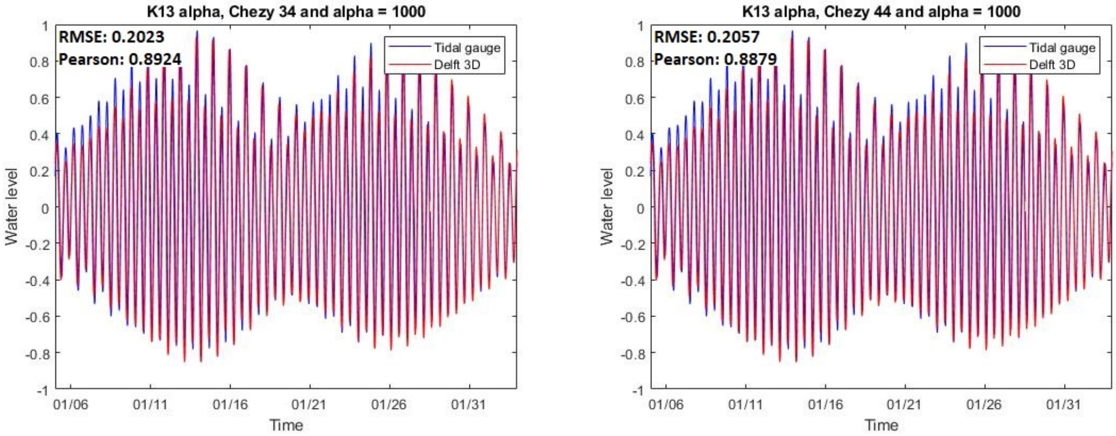

(a) Comparison between tidal gauge data and Delft 3D Chezy 34

(b) Comparison between tidal gauge data and Delft 3D Chezy 44

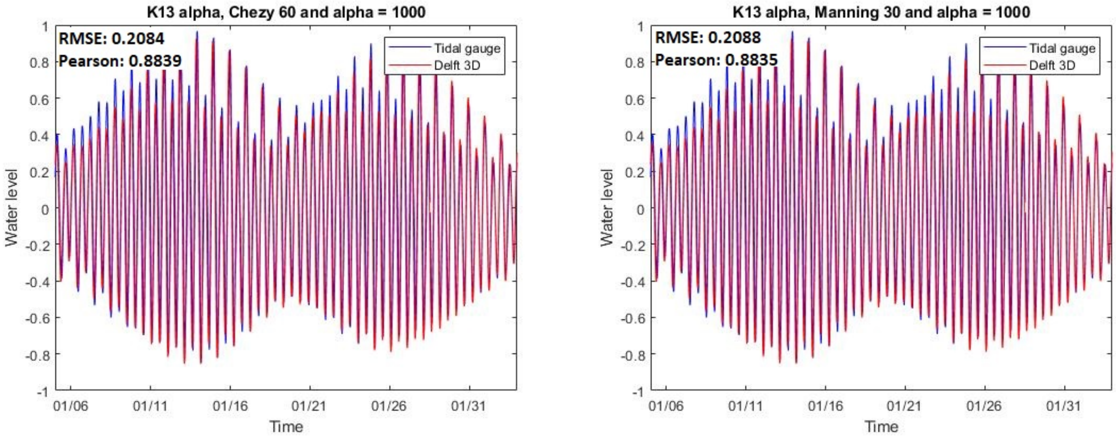

(c) Comparison between tidal gauge data and Delft 3D Chezy 60

(d) Comparison between tidal gauge data and Delft 3D Manning 0.03

Figure D.5: The comparison between the tidal station K13 alpha and the different Delft 3D models, Chezy 34-60 and Manning 0.03

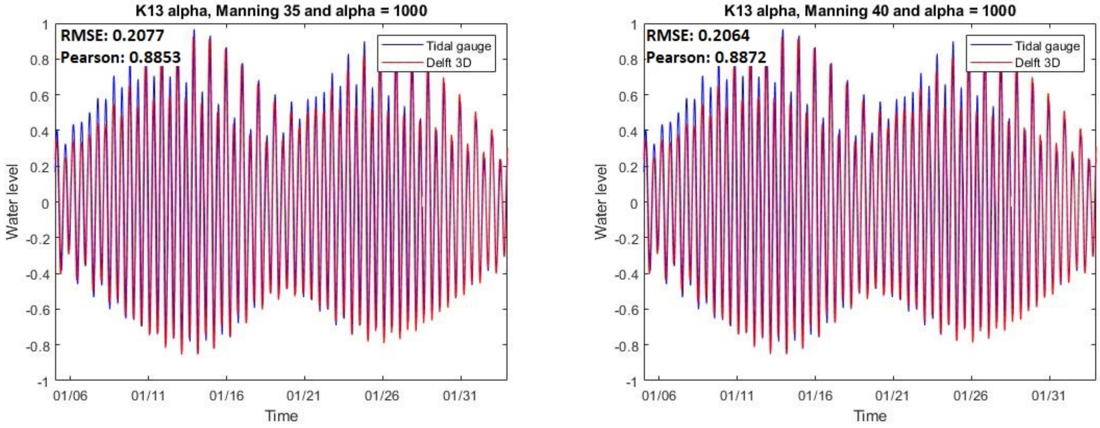

(a) Comparison between tidal gauge data and Delft 3D Manning 0.035 (b) Comparison between tidal gauge data and Delft 3D Manning 0.04

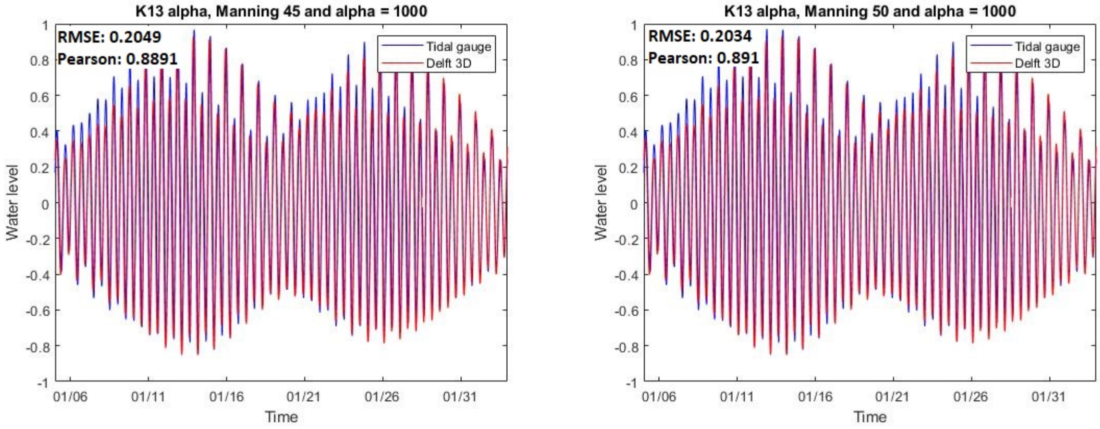

(c) Comparison between tidal gauge data and Delft 3D Manning 0.045 (d) Comparison between tidal gauge data and Delft 3D Manning 0.05

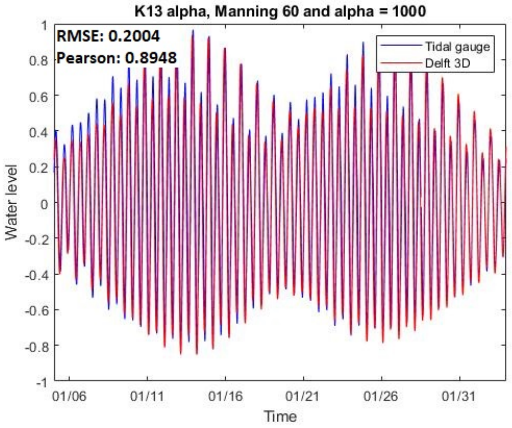

(e) Comparison between tidal gauge data and Delft 3D Manning 0.06

Figure D.6: The comparison between the tidal station K13 alpha and the different Delft 3D models, Manning 0.035-0.06

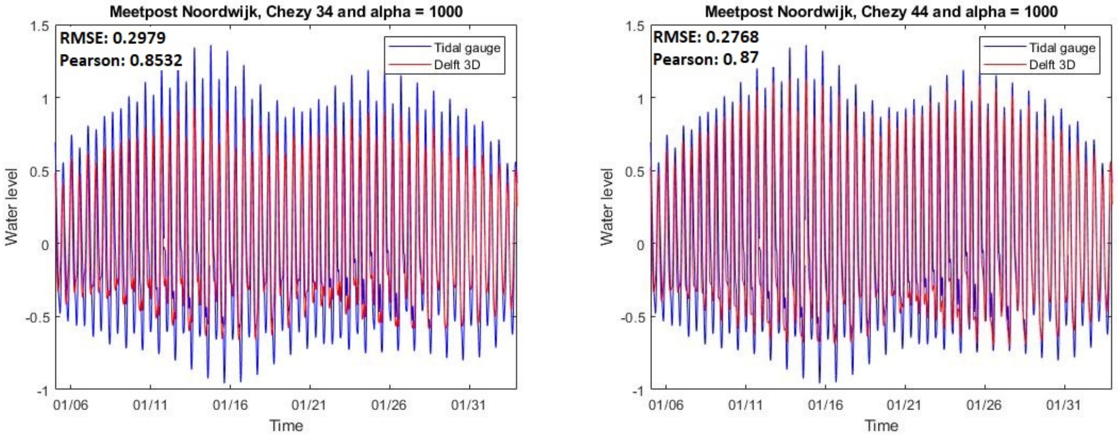

(a) Comparison between tidal gauge data and Delft 3D Chezy 34

(b) Comparison between tidal gauge data and Delft 3D Chezy 44

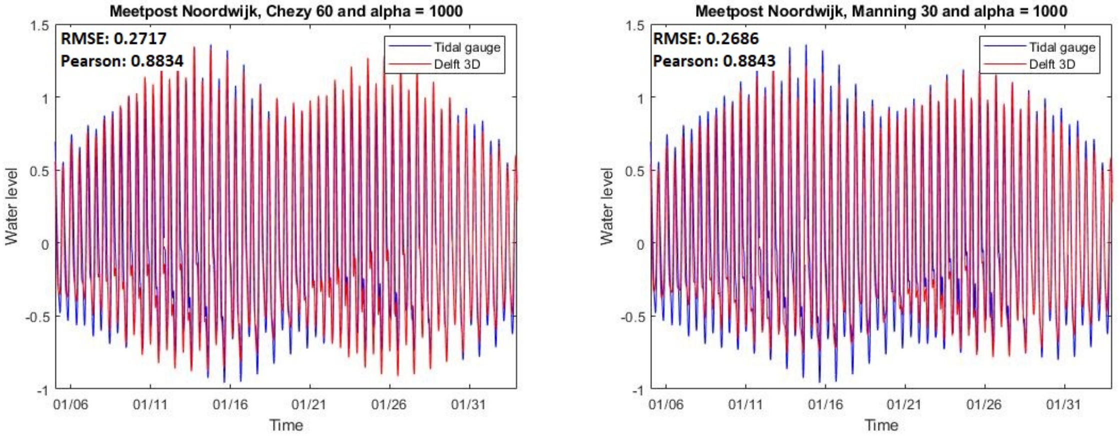

(c) Comparison between tidal gauge data and Delft 3D Chezy 60

(d) Comparison between tidal gauge data and Delft 3D Manning 0.03

Figure D.7: The comparison between the tidal station Meetpost Noordwijk and the different Delft 3D models, Chezy 34-60 and Manning 0.03

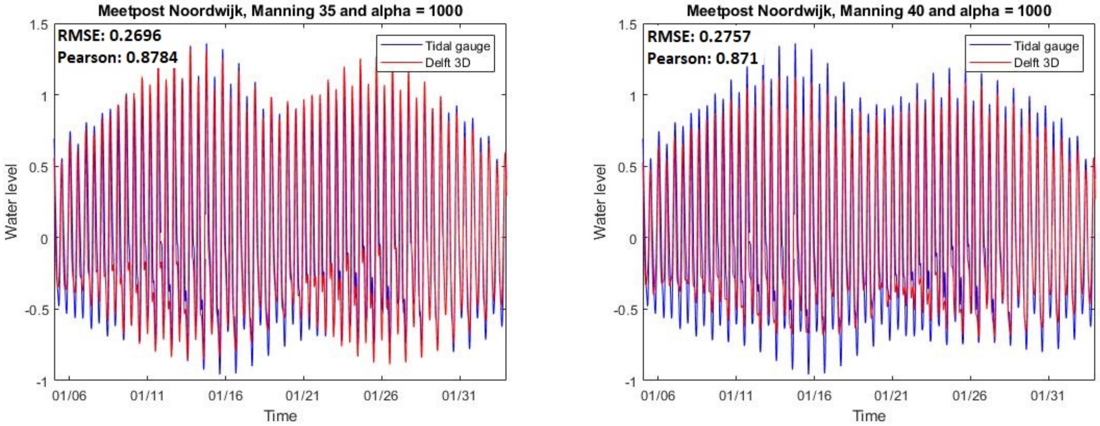

(a) Comparison between tidal gauge data and Delft 3D Manning 0.035

(b) Comparison between tidal gauge data and Delft 3D Manning 0.04

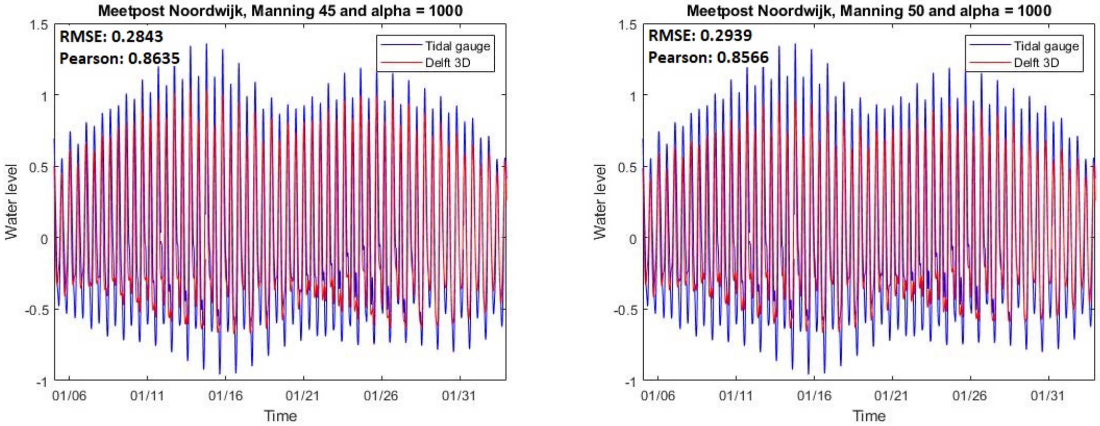

(c) Comparison between tidal gauge data and Delft 3D Manning 0.045

(d) Comparison between tidal gauge data and Delft 3D Manning 0.05

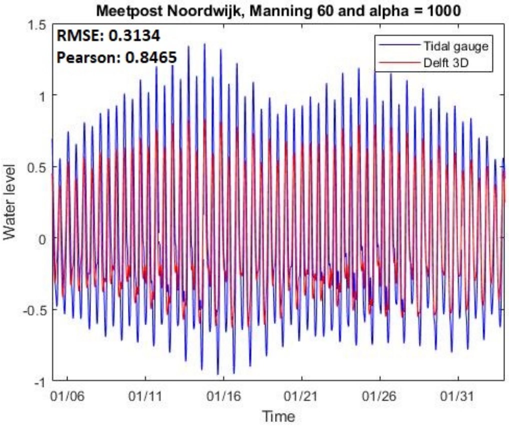

(e) Comparison between tidal gauge data and Delft 3D Manning 0.06

Figure D.8: The comparison between the tidal station Meetpost Noordwijk and the different Delft 3D models, Manning 0.035-0.06

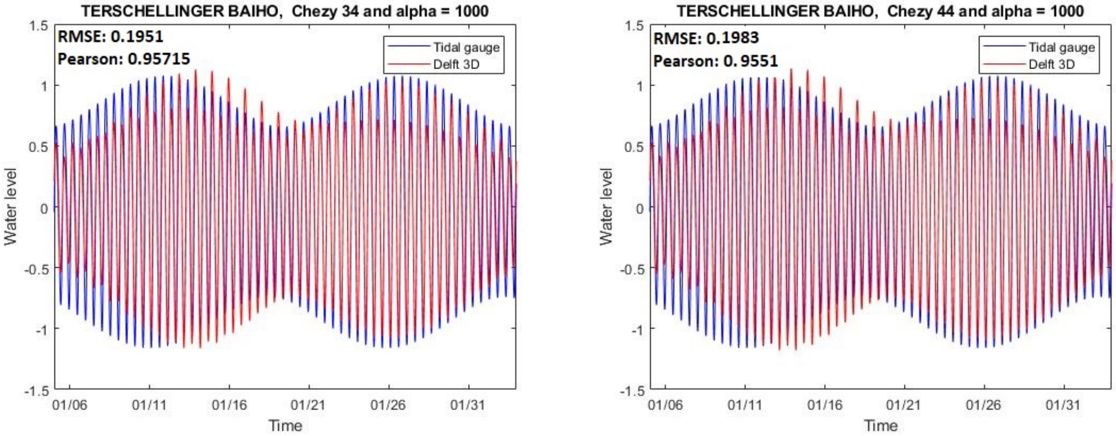

(a) Comparison between tidal gauge data and Delft 3D Chezy 34

(b) Comparison between tidal gauge data and Delft 3D Chezy 44

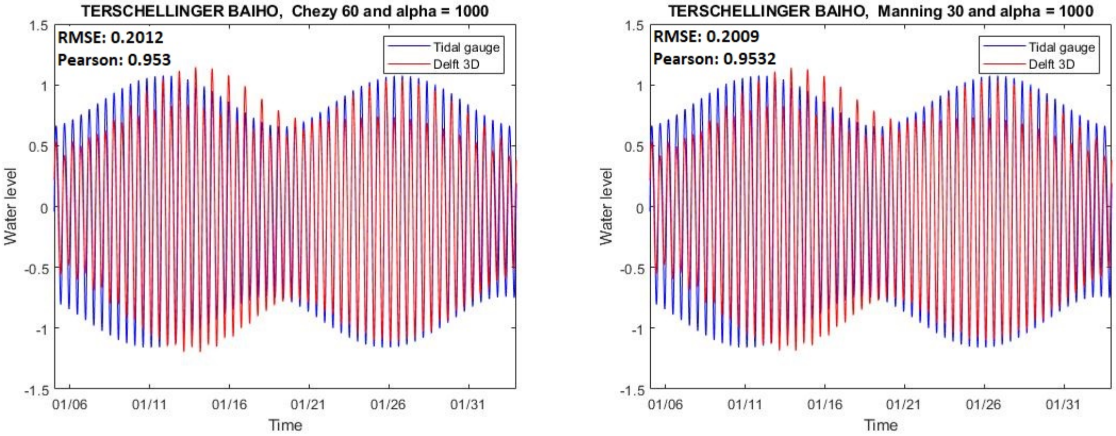

(c) Comparison between tidal gauge data and Delft 3D Chezy 60

(d) Comparison between tidal gauge data and Delft 3D Manning 0.03

Figure D.9: The comparison between the tidal station Terschellinger BAIHO and the different Delft 3D models, Chezy 34-60 and Manning 0.03

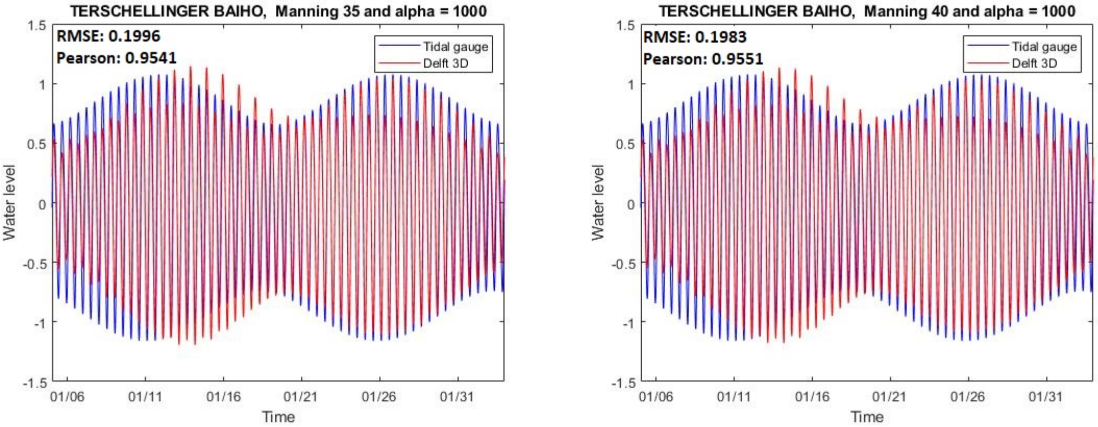

(a) Comparison between tidal gauge data and Delft 3D Manning 0.035 (b) Comparison between tidal gauge data and Delft 3D Manning 0.04

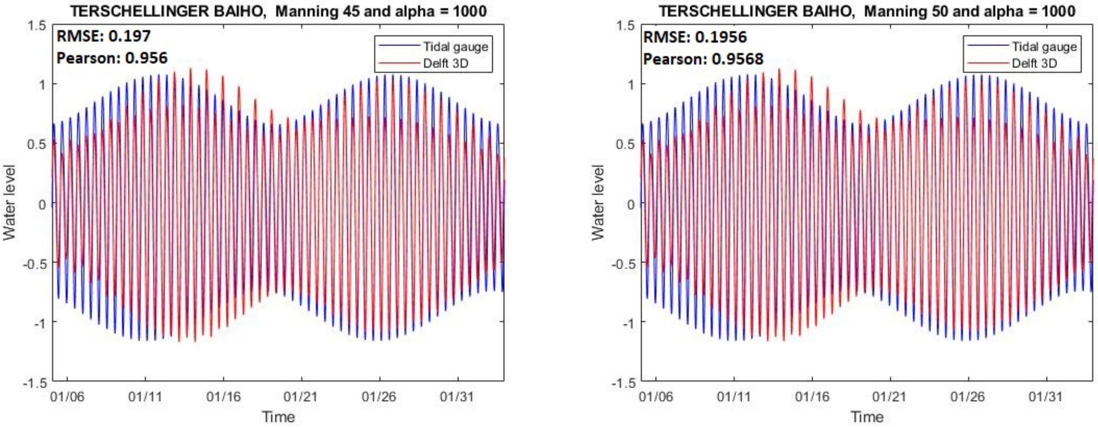

(c) Comparison between tidal gauge data and Delft 3D Manning 0.045 (d) Comparison between tidal gauge data and Delft 3D Manning 0.05

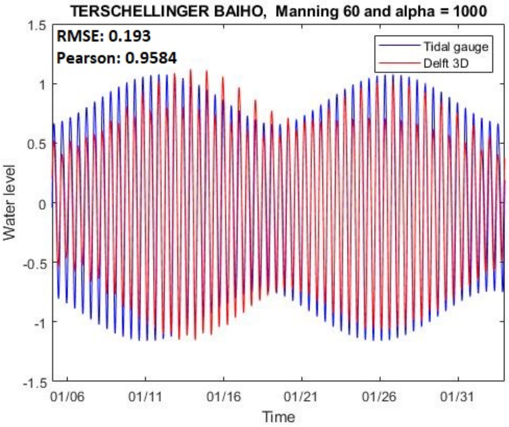

(e) Comparison between tidal gauge data and Delft 3D Manning 0.06

Figure D.10: The comparison between the tidal station Terschellinger BAIHO and the different Delft 3D models, Manning 0.035-0.06

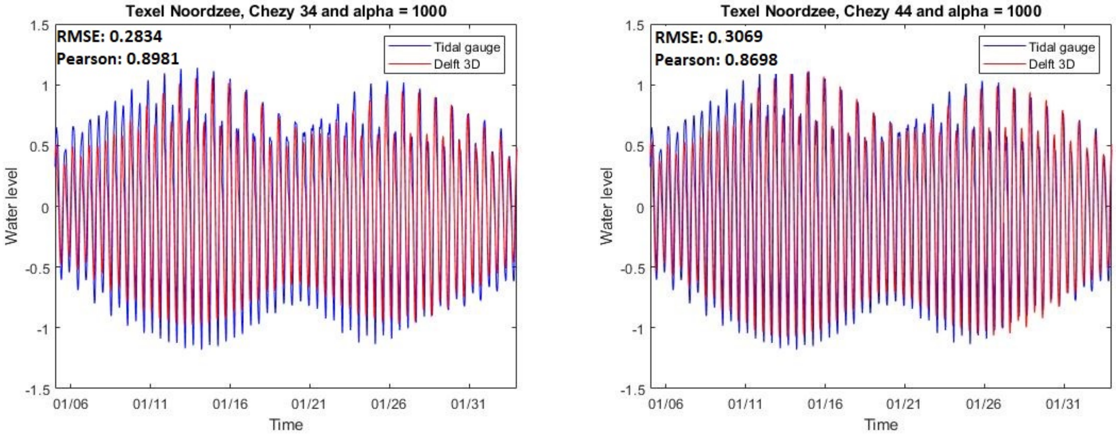

(a) Comparison between tidal gauge data and Delft 3D Chezy 34

(b) Comparison between tidal gauge data and Delft 3D Chezy 44

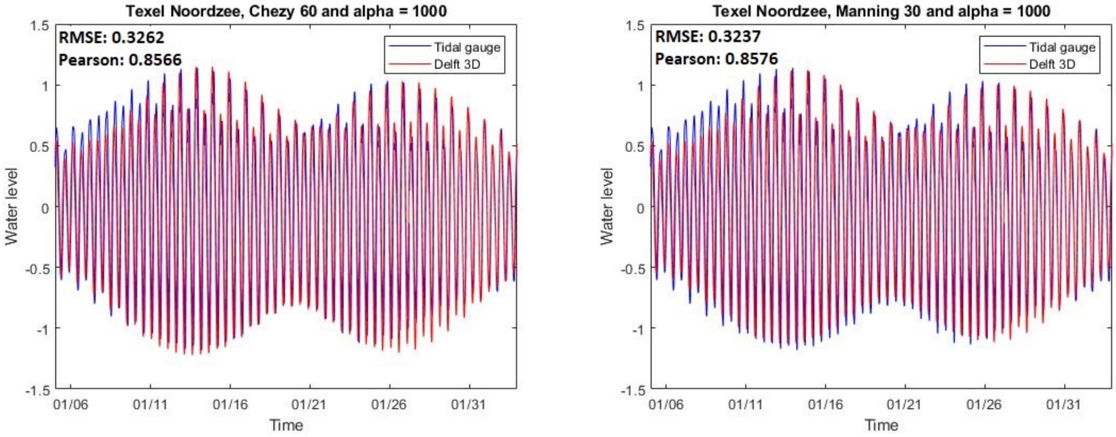

(c) Comparison between tidal gauge data and Delft 3D Chezy 60

(d) Comparison between tidal gauge data and Delft 3D Manning 0.03

Figure D.11: The comparison between the tidal station Texel Noordzee and the different Delft 3D models, Chezy 34-60 and Manning 0.03

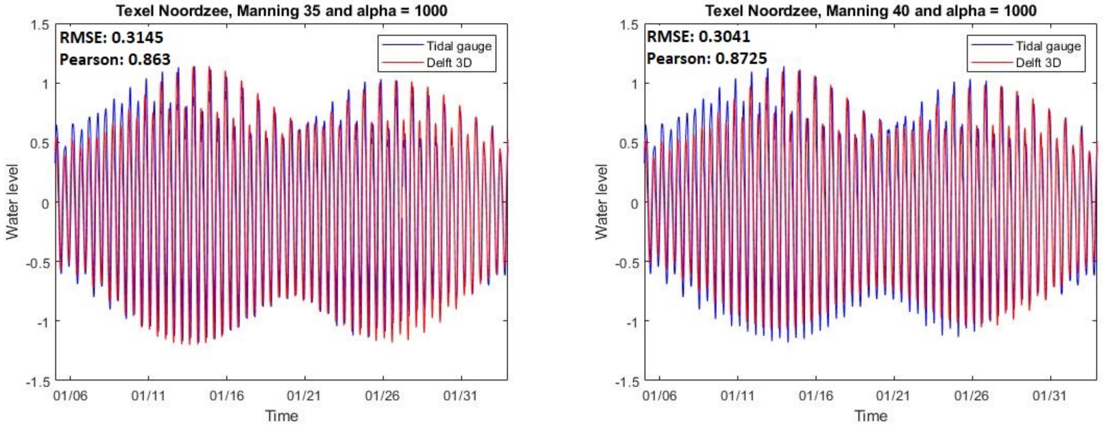

(a) Comparison between tidal gauge data and Delft 3D Manning 0.035

(b) Comparison between tidal gauge data and Delft 3D Manning 0.04

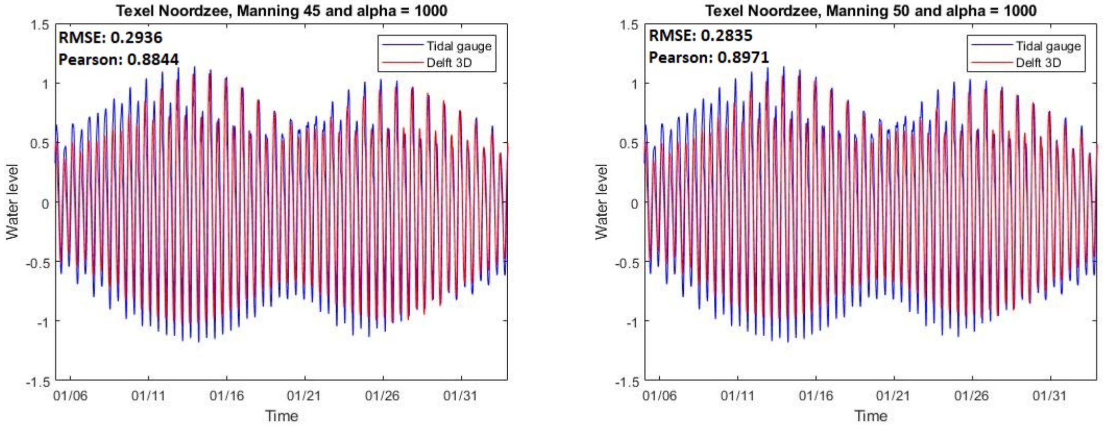

(c) Comparison between tidal gauge data and Delft 3D Manning 0.045

(d) Comparison between tidal gauge data and Delft 3D Manning 0.05

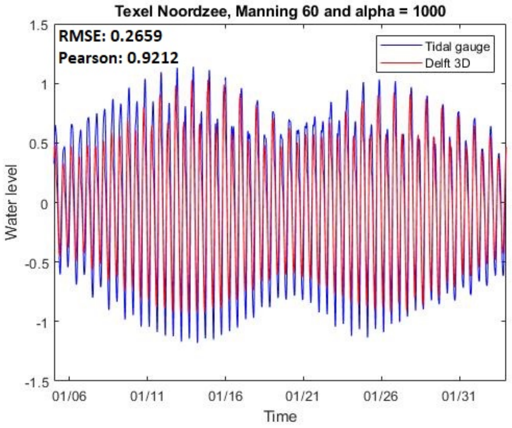

(e) Comparison between tidal gauge data and Delft 3D Manning 0.06

Figure D.12: The comparison between the tidal station Texel Noordzee and the different Delft 3D models, Manning 0.035-0.06

In the following figures the scatter plots can be seen. From the scatter plots it can be concluded were the difference between the 2 data sets are. The red line demonstrates that the 2 data sets have the same value. From this the scatter index can be determined.

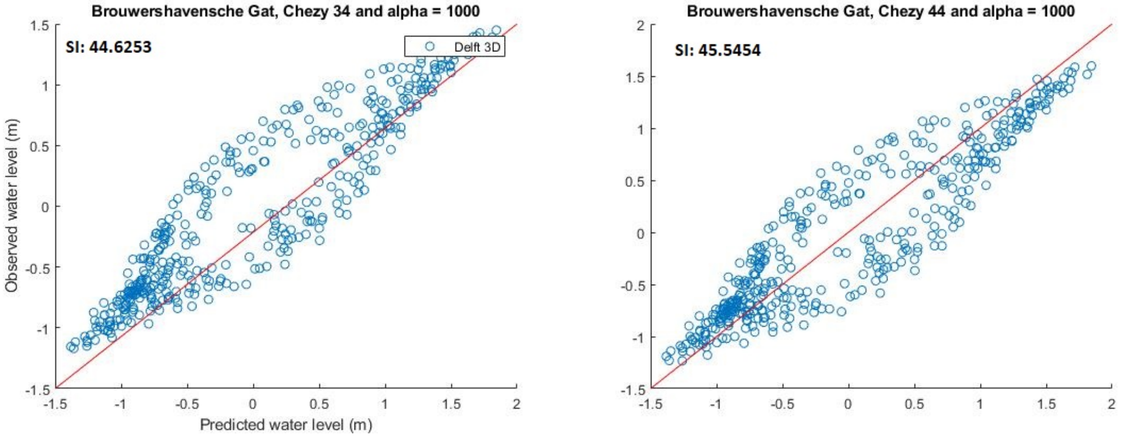

(a) Comparison between tidal gauge data and Delft 3D Chezy 34

(b) Comparison between tidal gauge data and Delft 3D Chezy 44

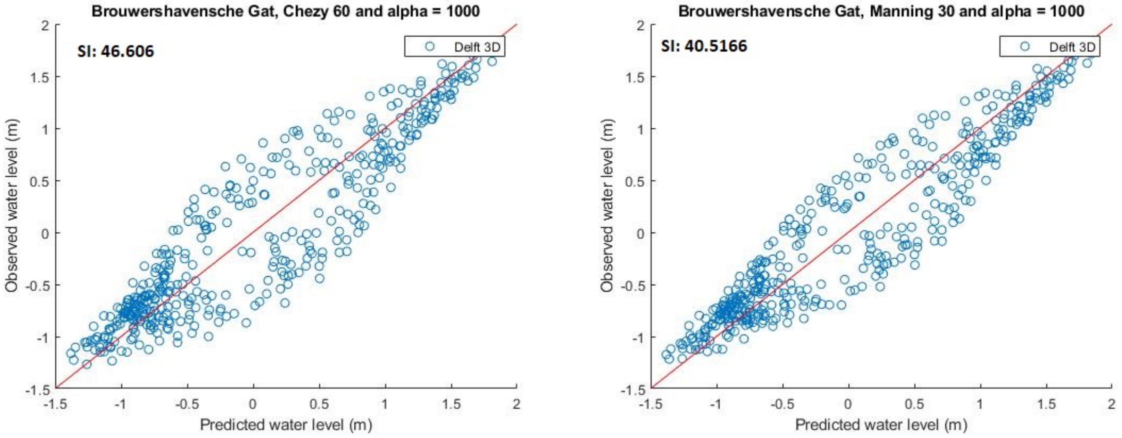

(c) Comparison between tidal gauge data and Delft 3D Chezy 60

(d) Comparison between tidal gauge data and Delft 3D Manning 0.03

Figure D.13: The scatter index between the tidal station Brouwers Havensche Gat and the different Delft 3D models, Chezy 34-60 and Manning 0.03

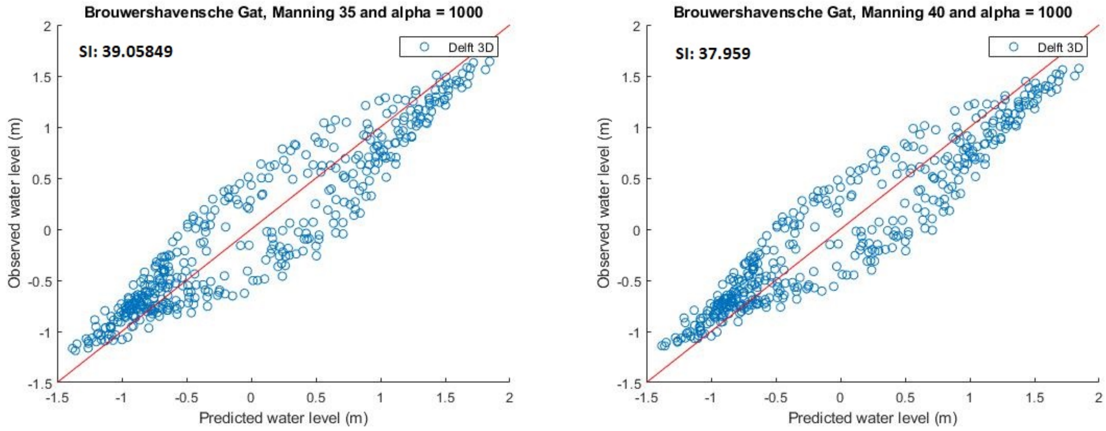

(a) Comparison between tidal gauge data and Delft 3D Manning 0.035

(b) Comparison between tidal gauge data and Delft 3D Manning 0.04

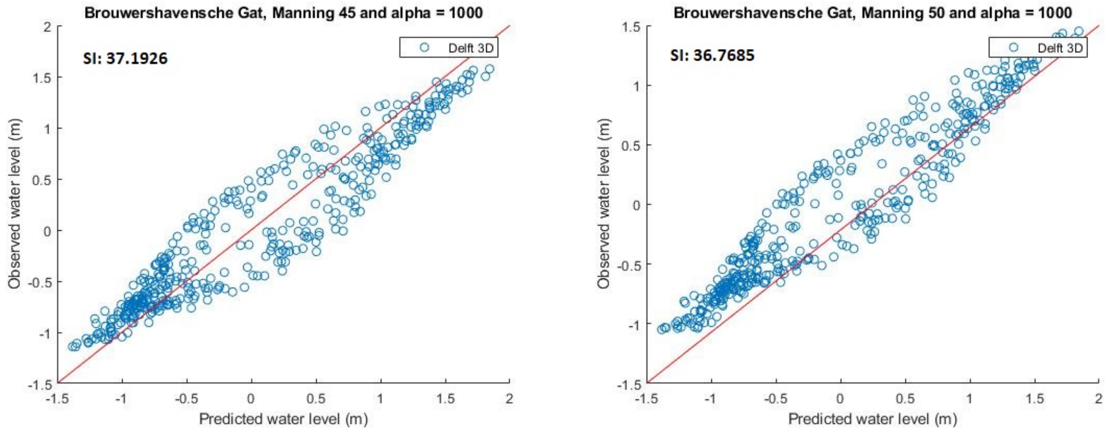

(c) Comparison between tidal gauge data and Delft 3D Manning 0.045

(d) Comparison between tidal gauge data and Delft 3D Manning 0.05

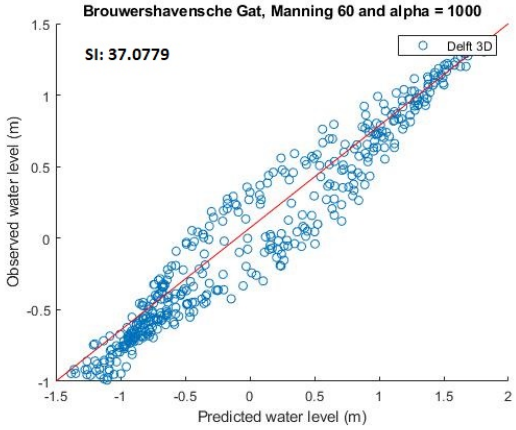

(e) Comparison between tidal gauge data and Delft 3D Manning 0.06

Figure D.14: The scatter index between the tidal station Brouwers Havensche Gat and the different Delft 3D models, Manning 0.035-0.06

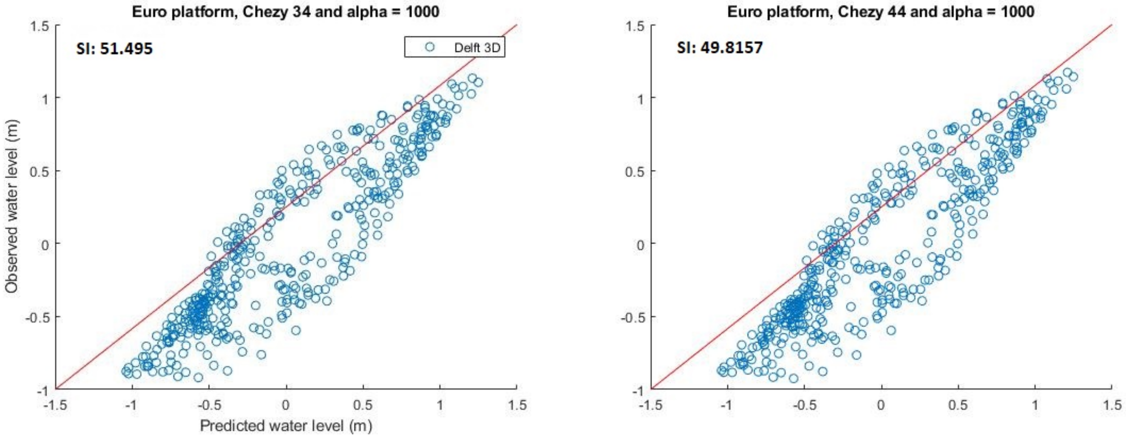

(a) Comparison between tidal gauge data and Delft 3D Chezy 34

(b) Comparison between tidal gauge data and Delft 3D Chezy 44

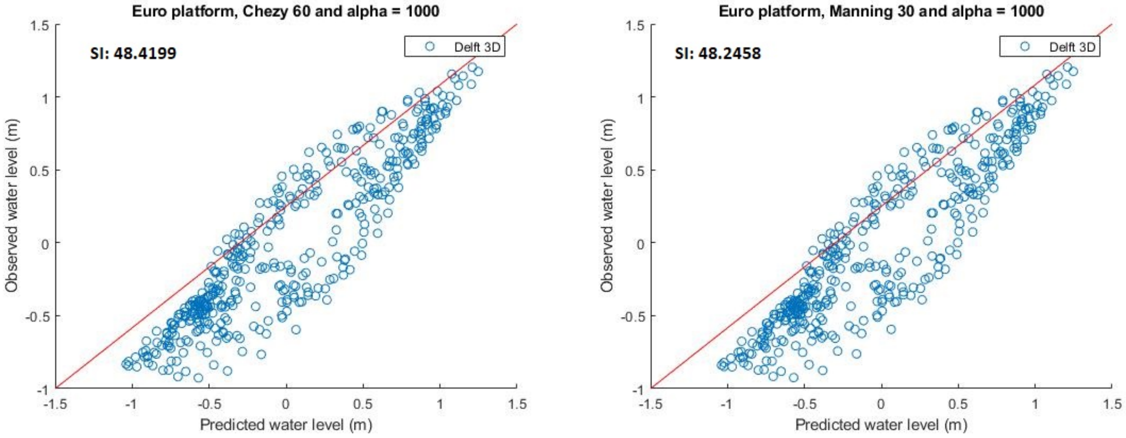

(c) Comparison between tidal gauge data and Delft 3D Chezy 60

(d) Comparison between tidal gauge data and Delft 3D Manning 0.03

Figure D.15: The scatter index between the tidal station Euro platform and the different Delft 3D models, Chezy 34-60 and Manning 0.03

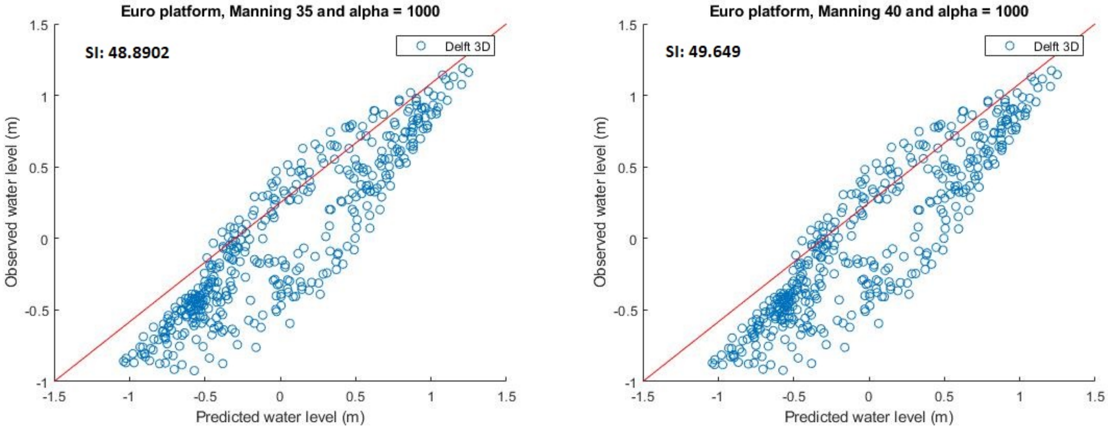

(a) Comparison between tidal gauge data and Delft 3D Manning 0.035

(b) Comparison between tidal gauge data and Delft 3D Manning 0.04

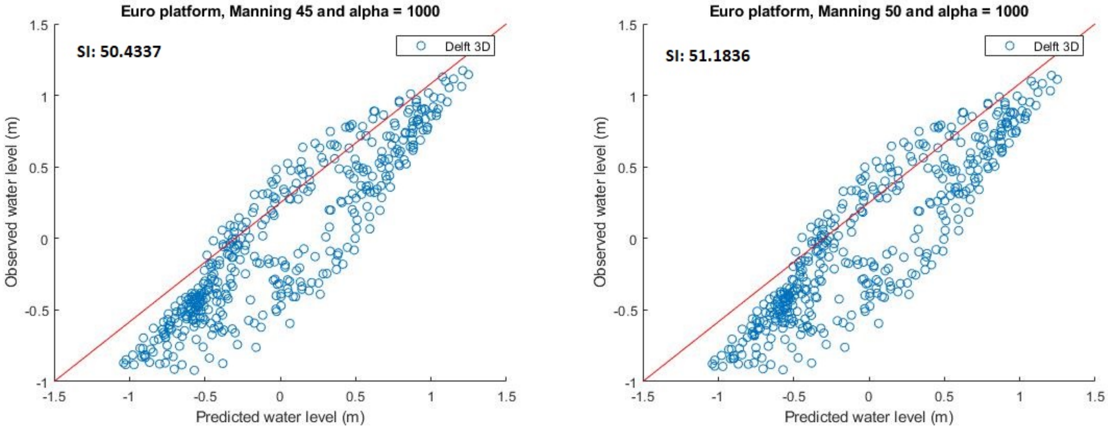

(c) Comparison between tidal gauge data and Delft 3D Manning 0.045

(d) Comparison between tidal gauge data and Delft 3D Manning 0.05

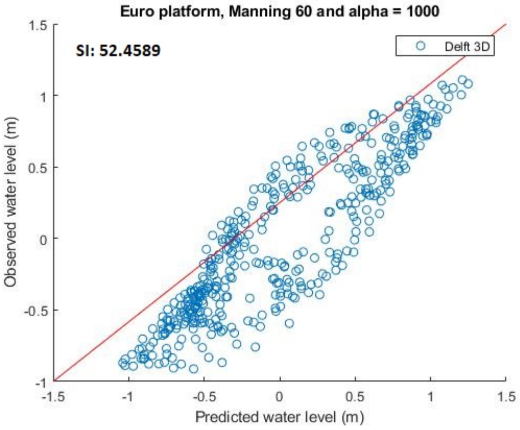

(e) Comparison between tidal gauge data and Delft 3D Manning 0.06

Figure D.16: The scatter index between the tidal station Euro platform and the different Delft 3D models, Manning 0.035-0.06

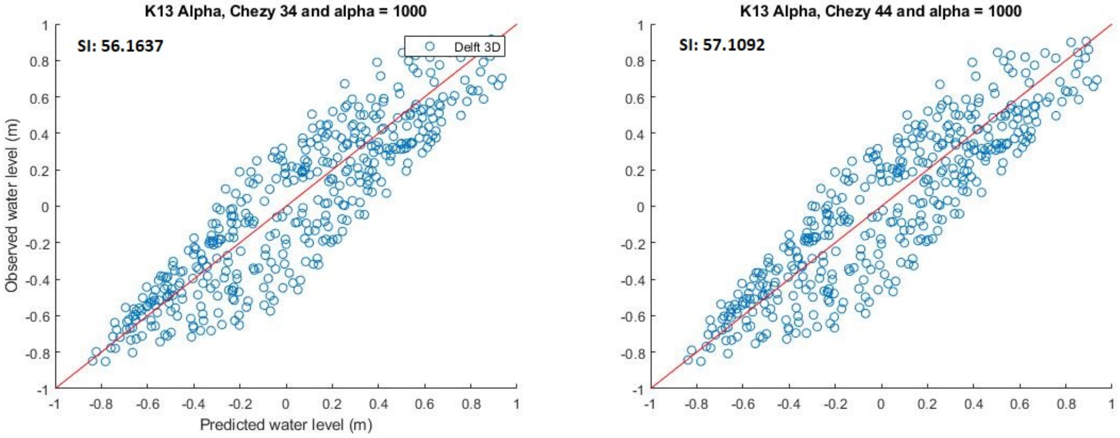

(a) Comparison between tidal gauge data and Delft 3D Chezy 34

(b) Comparison between tidal gauge data and Delft 3D Chezy 44

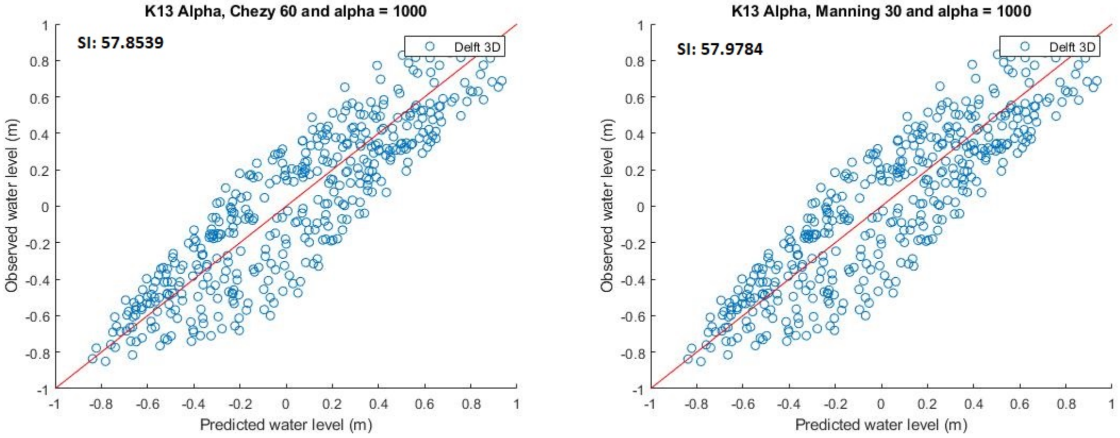

(c) Comparison between tidal gauge data and Delft 3D Chezy 60

(d) Comparison between tidal gauge data and Delft 3D Manning 0.03

Figure D.17: The scatter index between the tidal station K13 alpha and the different Delft 3D models, Chezy 34-60 and Manning 0.03

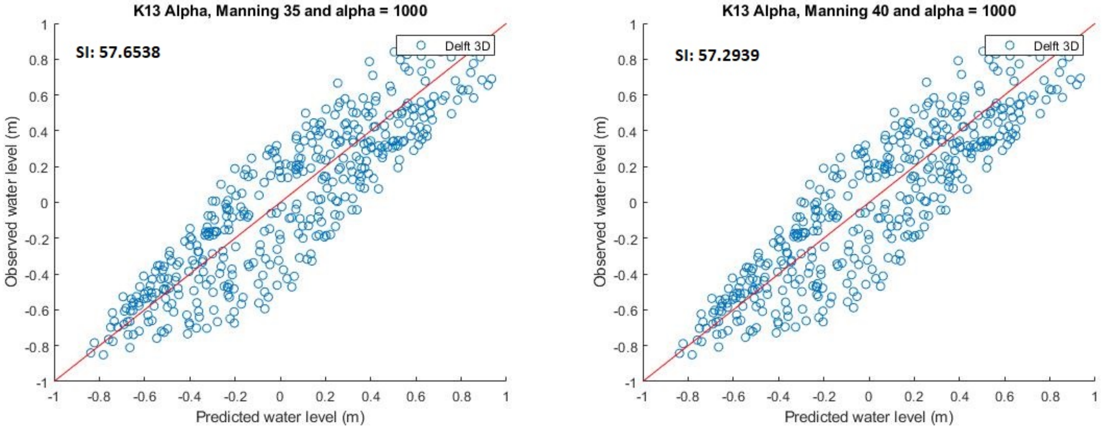

(a) Comparison between tidal gauge data and Delft 3D Manning 0.035 (b) Comparison between tidal gauge data and Delft 3D Manning 0.04

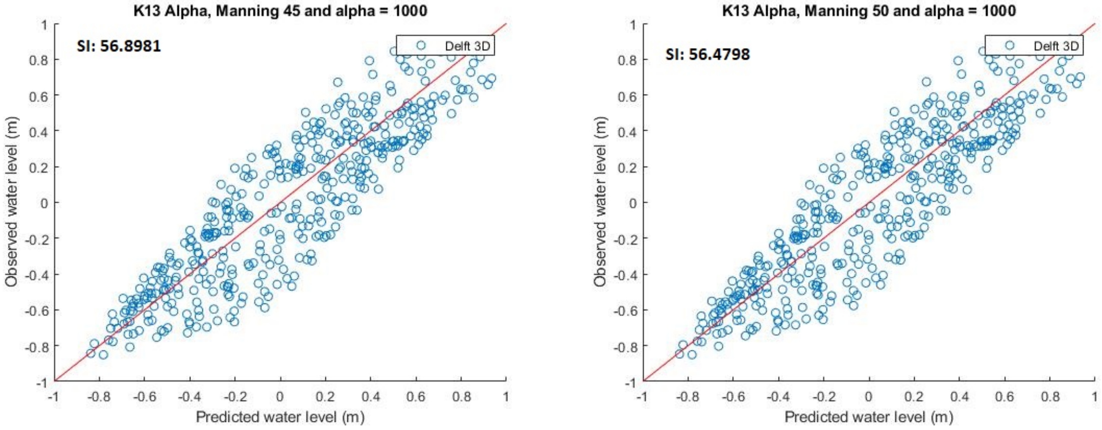

(c) Comparison between tidal gauge data and Delft 3D Manning 0.045 (d) Comparison between tidal gauge data and Delft 3D Manning 0.05

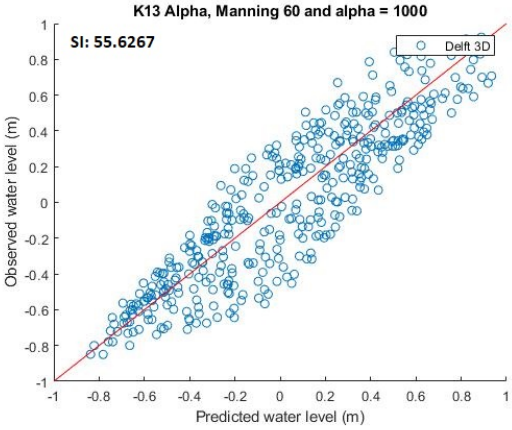

(e) Comparison between tidal gauge data and Delft 3D Manning 0.06

Figure D.18: The scatter index between the tidal station K13 alpha and the different Delft 3D models. Manning 0.035-0.06

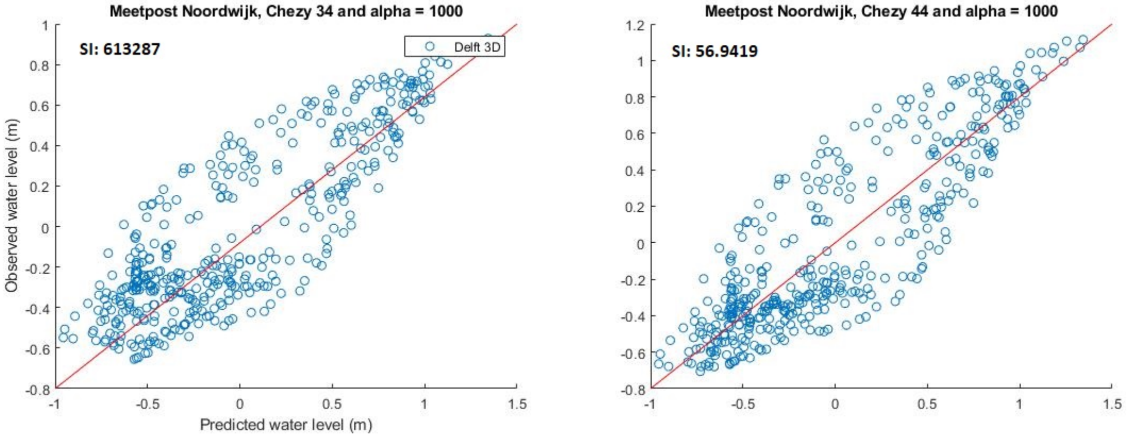

(a) Comparison between tidal gauge data and Delft 3D Chezy 34

(b) Comparison between tidal gauge data and Delft 3D Chezy 44

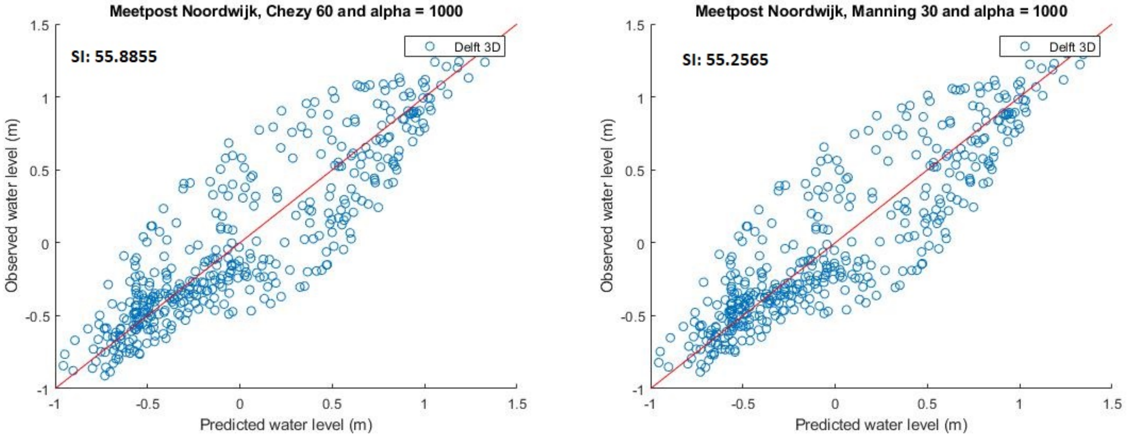

(c) Comparison between tidal gauge data and Delft 3D Chezy 60

(d) Comparison between tidal gauge data and Delft 3D Manning 0.03

Figure D.19: The scatter index between the tidal station Meetpost Noordwijk and the different Delft 3D models, Chezy 34-60 and Manning 0.03

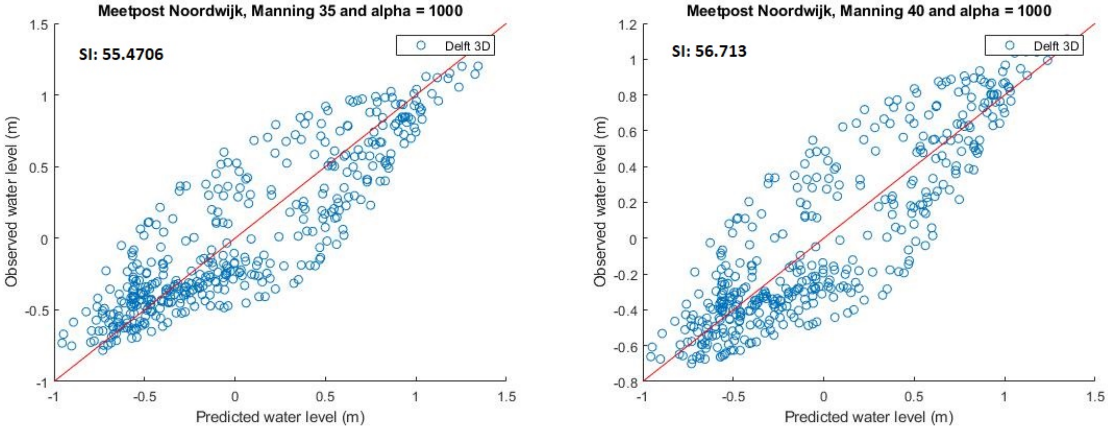

(a) Comparison between tidal gauge data and Delft 3D Manning 0.035

(b) Comparison between tidal gauge data and Delft 3D Manning 0.04

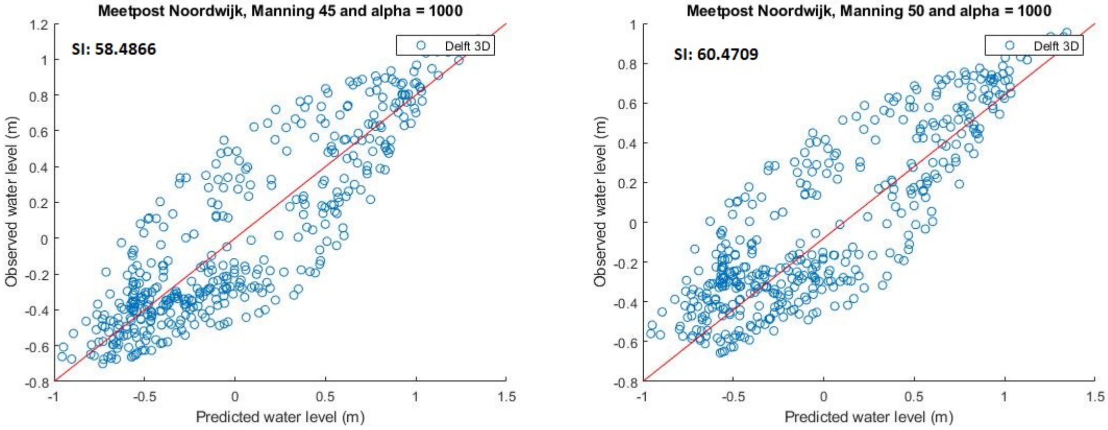

(c) Comparison between tidal gauge data and Delft 3D Manning 0.045

(d) Comparison between tidal gauge data and Delft 3D Manning 0.05

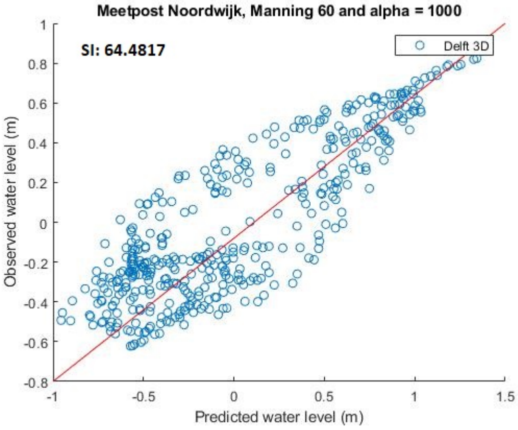

(e) Comparison between tidal gauge data and Delft 3D Manning 0.06

Figure D.20: The scatter index between the tidal station Meetpost Noordwijk and the different Delft 3D models, Manning 0.035-0.06

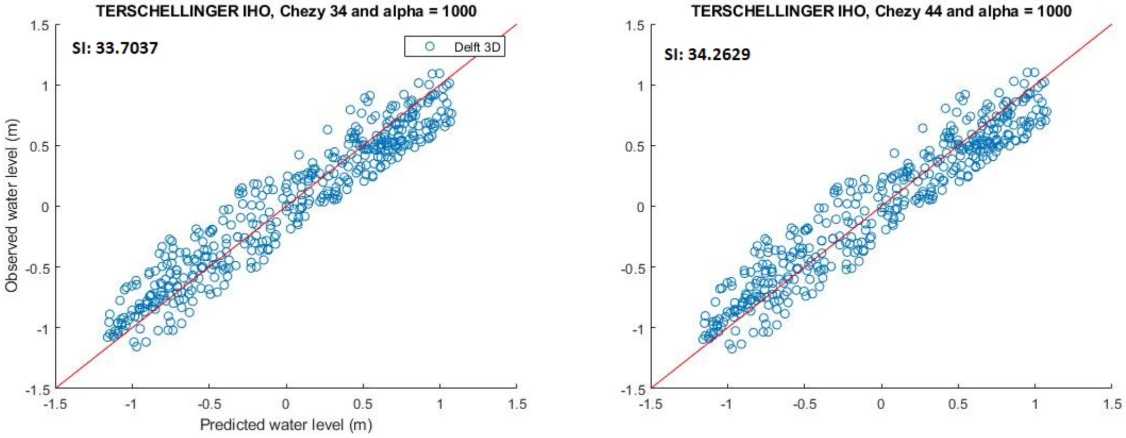

(a) Comparison between tidal gauge data and Delft 3D Chezy 34

(b) Comparison between tidal gauge data and Delft 3D Chezy 44

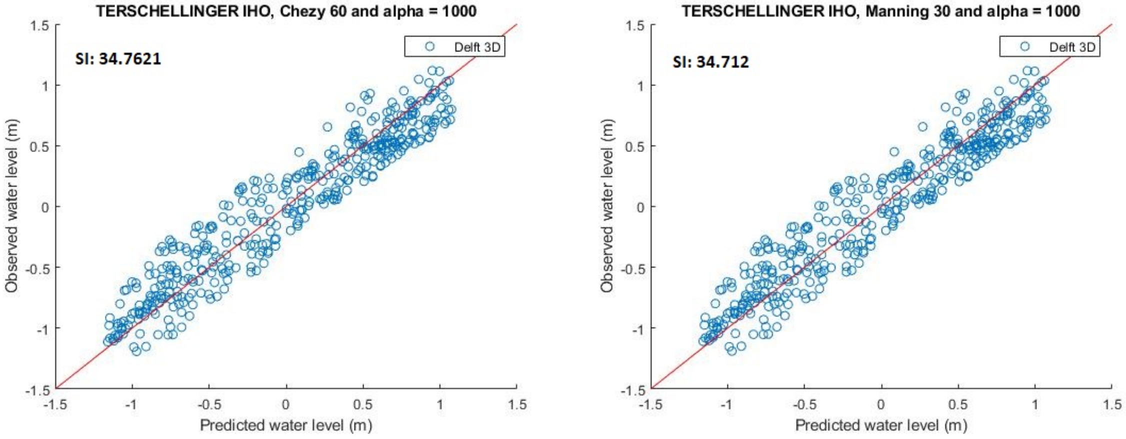

(c) Comparison between tidal gauge data and Delft 3D Chezy 60

(d) Comparison between tidal gauge data and Delft 3D Manning 0.03

Figure D.21: The scatter index between the tidal station Terschellinger BAIHO and the different Delft 3D models, Chezy 34-60 and Manning 0.03

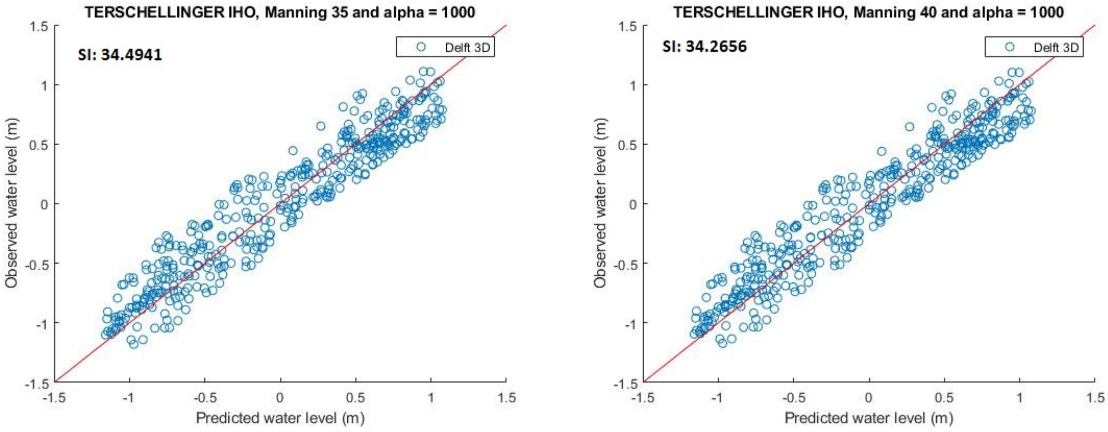

(a) Comparison between tidal gauge data and Delft 3D Manning 0.035 (b) Comparison between tidal gauge data and Delft 3D Manning 0.04

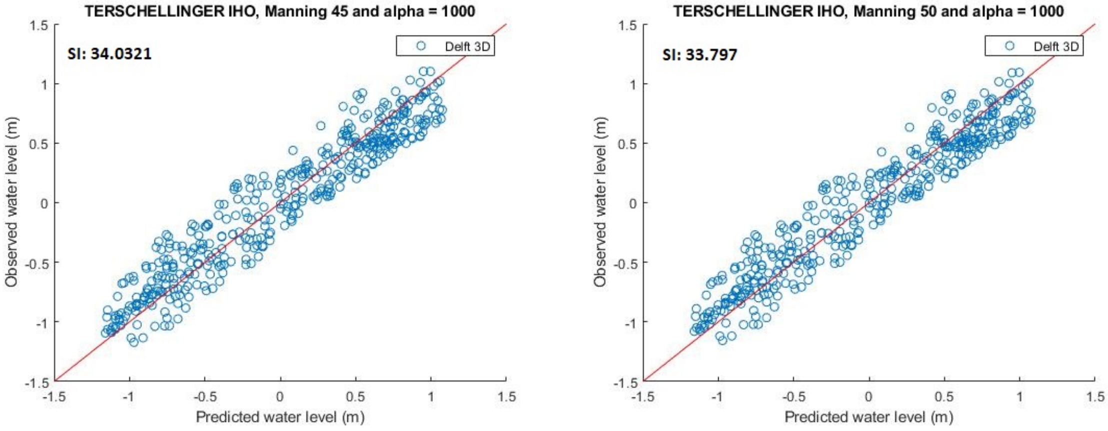

(c) Comparison between tidal gauge data and Delft 3D Manning 0.045 (d) Comparison between tidal gauge data and Delft 3D Manning 0.05

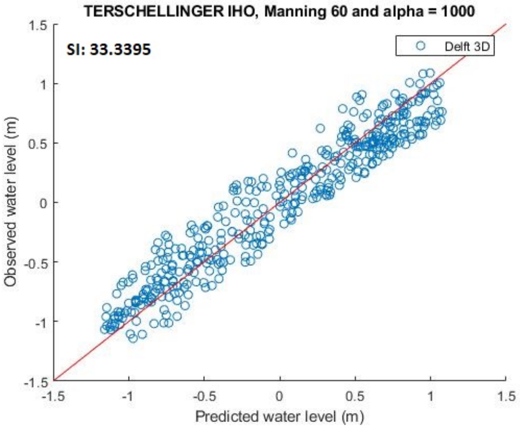

(e) Comparison between tidal gauge data and Delft 3D Manning 0.06

Figure D.22: The scatter index between the tidal station Terschellinger BAIHO and the different Delft 3D models, Manning 0.035-0.06

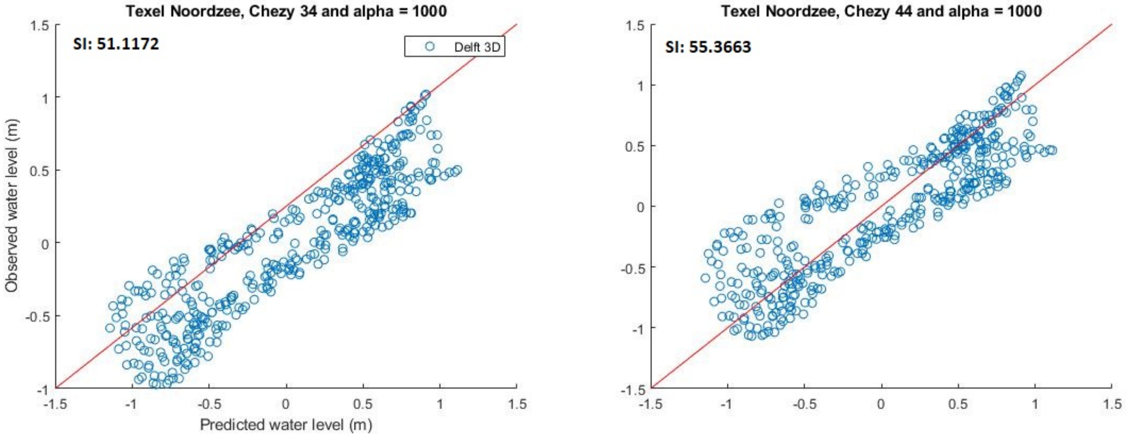

(a) Comparison between tidal gauge data and Delft 3D Chezy 34

(b) Comparison between tidal gauge data and Delft 3D Chezy 44

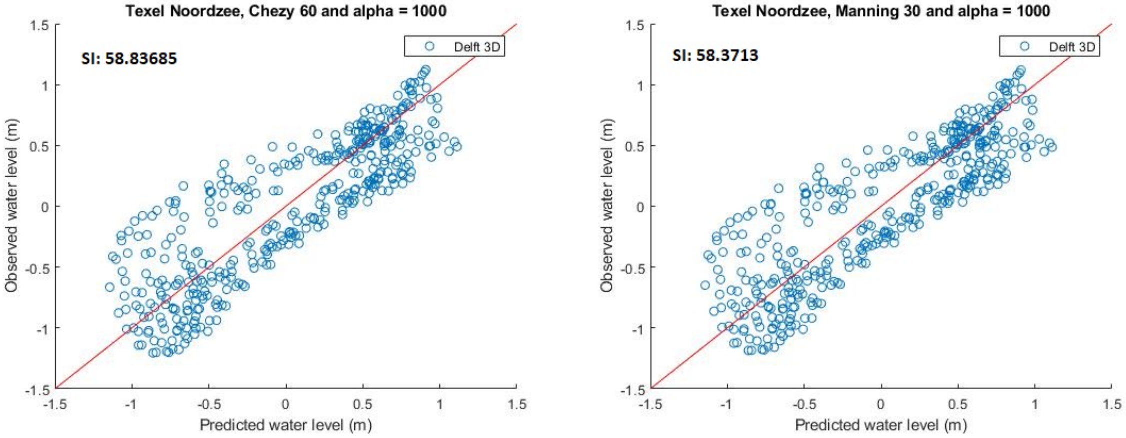

(c) Comparison between tidal gauge data and Delft 3D Chezy 60

(d) Comparison between tidal gauge data and Delft 3D Manning 0.03

Figure D.23: The scatter index between the tidal station Texel Noordzee and the different Delft 3D models, Chezy 34-60 and Manning 0.03

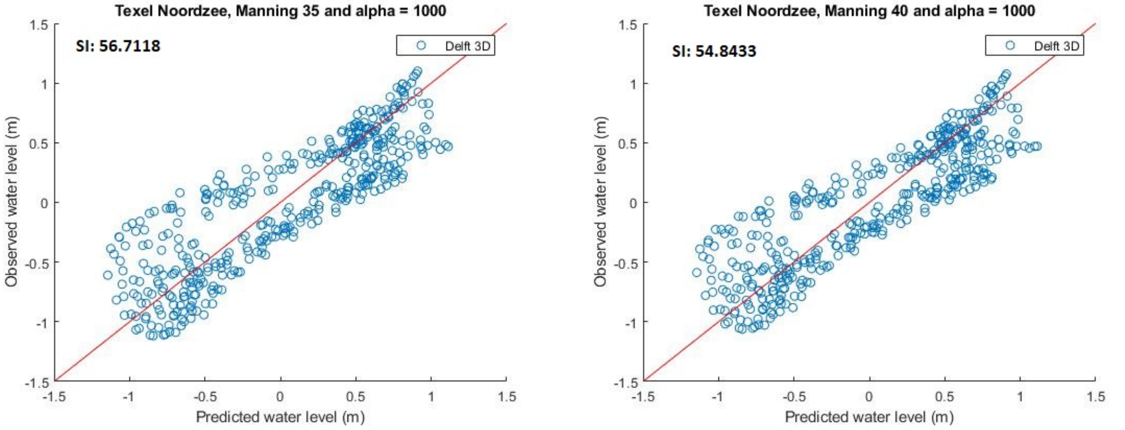

(a) Comparison between tidal gauge data and Delft 3D Manning 0.035 (b) Comparison between tidal gauge data and Delft 3D Manning 0.04

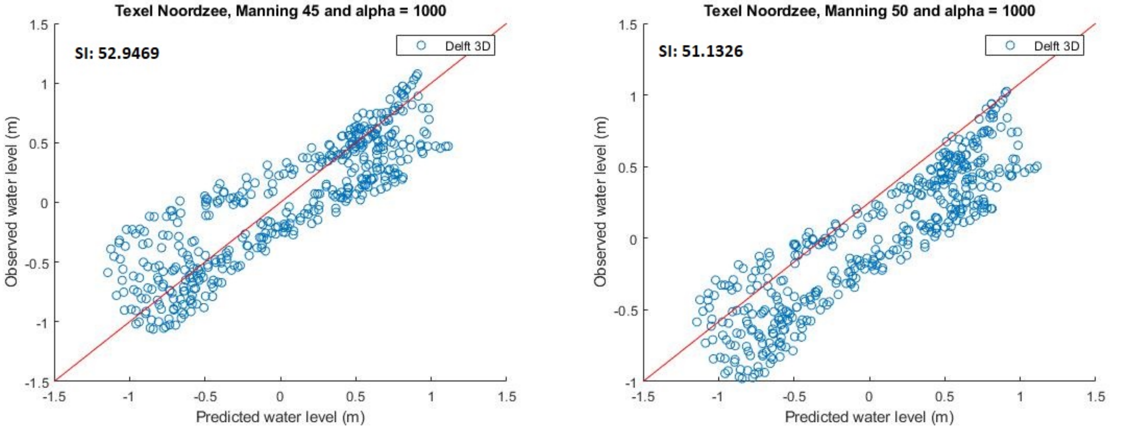

(c) Comparison between tidal gauge data and Delft 3D Manning 0.045 (d) Comparison between tidal gauge data and Delft 3D Manning 0.05

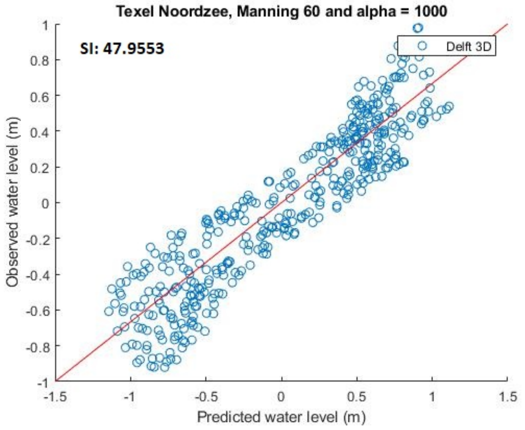

(e) Comparison between tidal gauge data and Delft 3D Manning 0.06

Figure D.24: The scatter index between the tidal station Texel Noordzee and the different Delft 3D models, Manning 0.035-0.06

E

Resource assessment

The highest potential grid point for the different locations.

Table E.1: Westerschelde grid point from Telemac

Total	a	b	c	d	e	f	g	h	i
Max	0.428446	0.445735	0.470351	0.387468	0.476693	0.526938	0.499198	0.503899	0.312455
Average	0.194315	0.2014	0.219886	0.184513	0.223346	0.242055	0.229258	0.231877	0.142684

Table E.2: Westerschelde grid point from Delft 3D

Total	a	b	c	d	e	f	g	h	i	j
Max	0.985875	0.670022	0.961727	0.972214	1.08046	0.656488	0.850905	1.16813	1.23096	1.14779
Average	0.447323	0.175143	0.468501	0.429668	0.516123	0.323525	0.405088	0.533545	0.57427	0.55125

Table E.3: Vlieland grid point from Telemac

Total	a	b	c	d	e
Max	0.381089	0.407566	0.434615	0.434615	0.326216
Average	0.196212	0.209421	0.224625	0.224625	0.167802

Table E.4: Vlieland grid point from Delft 3D

Total	a	b	c	d	e
Max	0.806724	0.663477	0.850181	0.888947	0.5574
Average	0.39129	0.298884	0.386596	0.426828	0.260966

Table E.5: Texel grid point from Telemac

Total	a	b	c	d
Max	0.336892	0.452911	0.401577	0.393411
Average	0.152051	0.207823	0.185896	0.18491

Table E.6: Texel grid point from Delft 3D

Total	a	b	c	d
Max	0.788348	0.793807	0.872071	0.758539
Average	0.423444	0.43064	0.420264	0.390129

Table E.7: Oosterschelde North grid point from Telemac

Total	a	b	c	d
Max	0.458789	0.492345	0.478924	0.433005
Average	0.226351	0.242176	0.223081	0.211271

Table E.8: Oosterschelde North grid point from Delft 3D

Total	a	b	c	d
Max	0.894629	0.778173	0.815418	0.718626
Average	0.424195	0.371578	0.366586	0.301144

Table E.9: Oosterschelde South grid point from Telemac

Total	a	b	c	d
Max	0.375289	0.390878	0.362948	0.372245
Average	0.190105	0.193195	0.177993	0.181093

Table E.10: Oosterschelde South grid point from Delft 3D

Total	a	b	c	d
Max	0.776958	0.854802	1.00201	1.09843
Average	0.346394	0.352676	0.428873	0.505295

The water level elevation over a year determined by Delft 3D can be seen in the following figures.

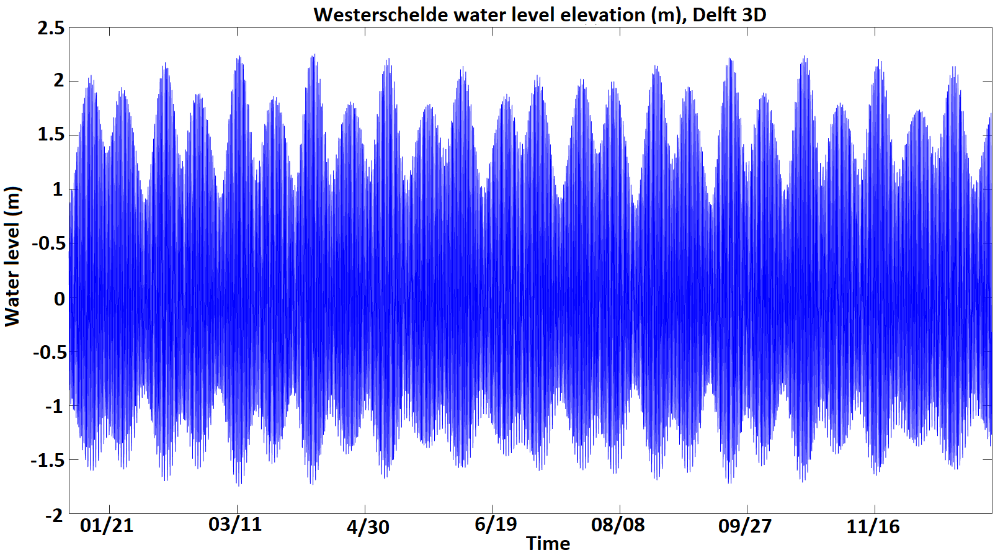

Figure E.1: Westerschelde water level (m)

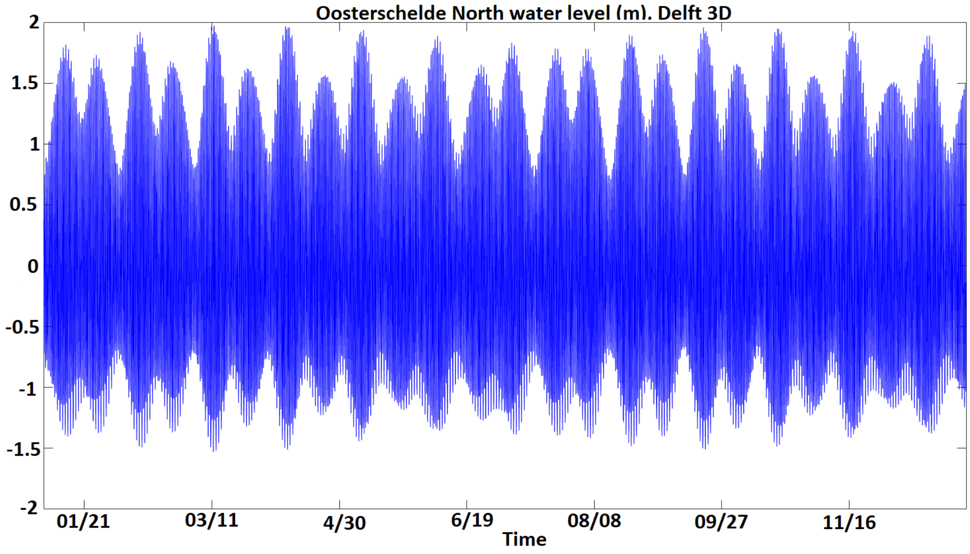

Figure E.2: Oosterschelde North water level (m)

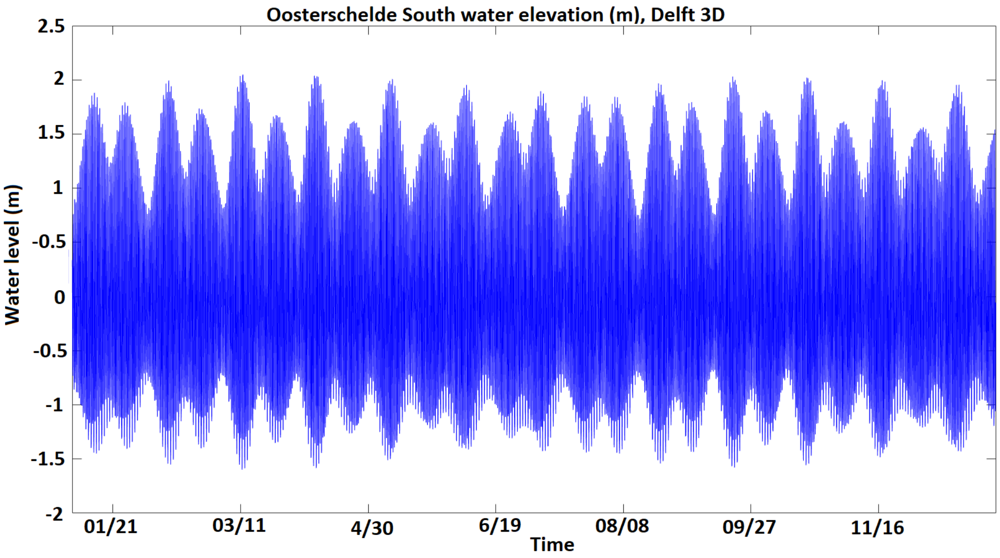

Figure E.3: Oosterschelde South water level (m)

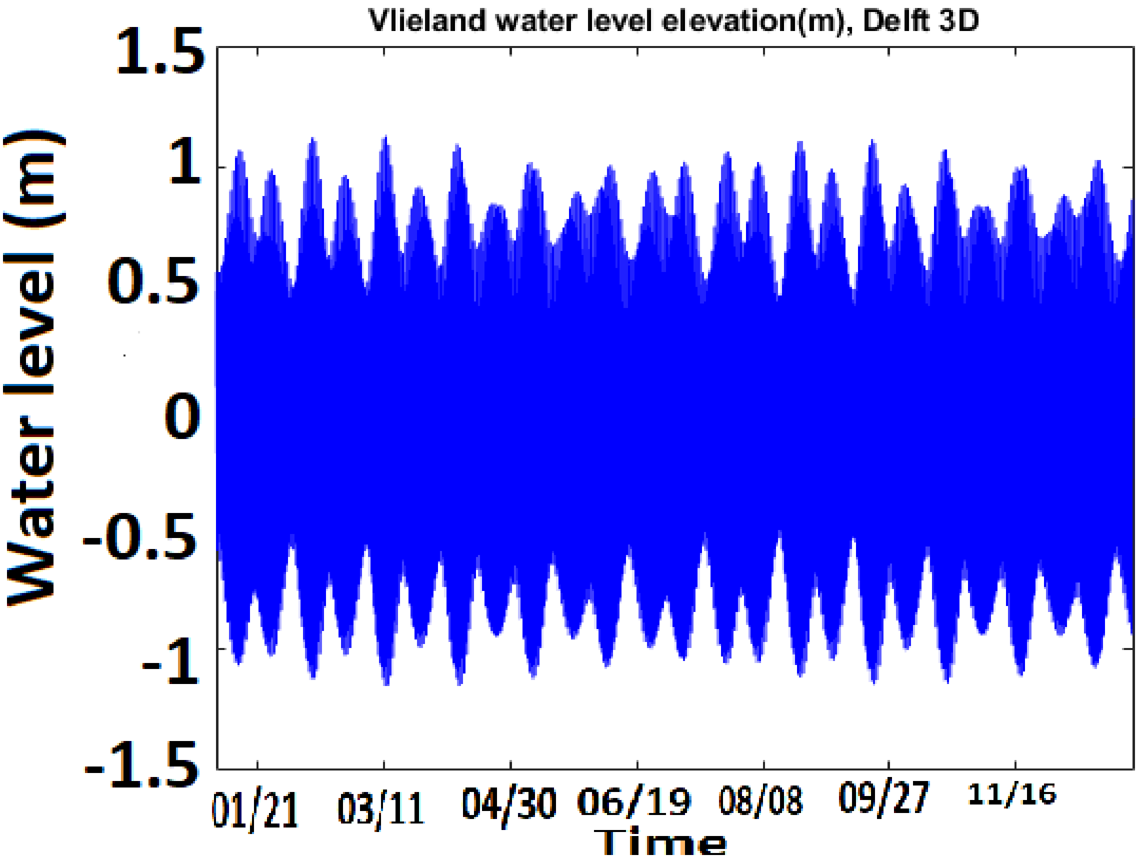

Figure E.4: Vlieland water level (m)

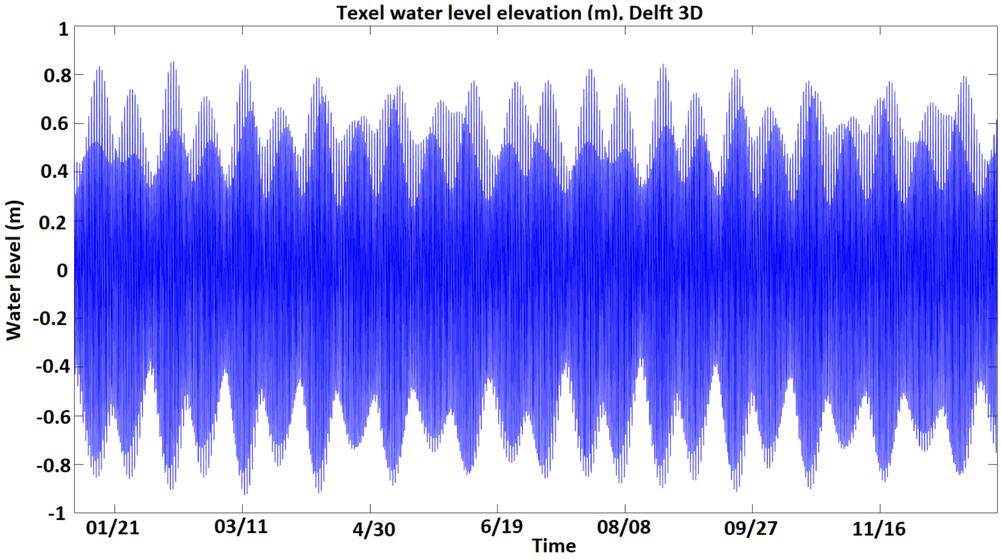

Figure E.5: Texel South water level (m)

The water level elevation over a year determined by Telemac can be seen in the following figures.

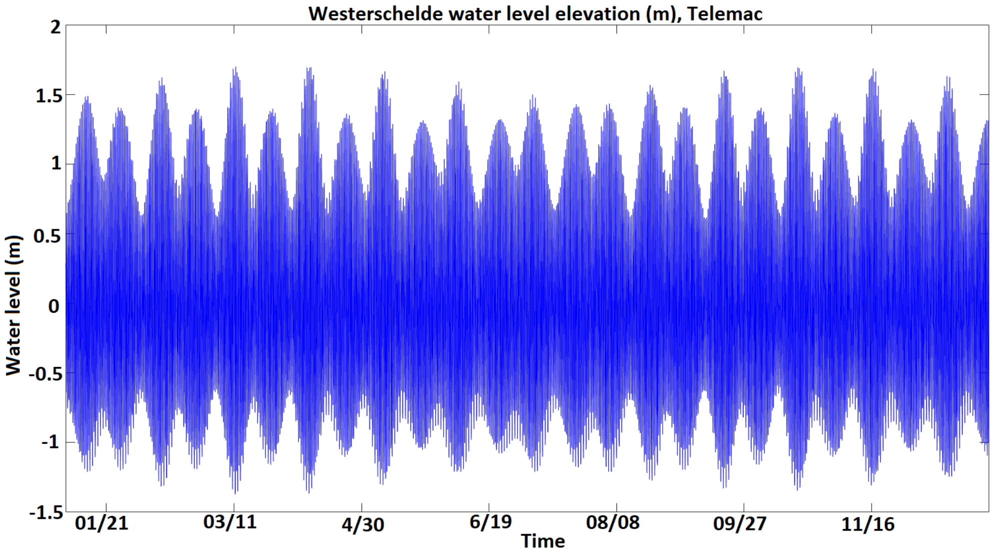

Figure E.6: Westerschelde water level (m)

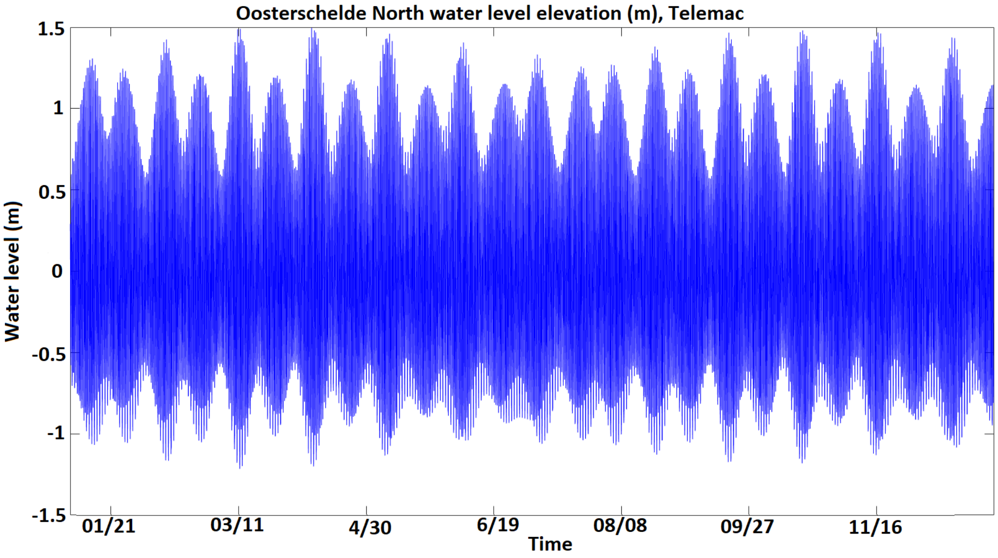

Figure E.7: Oosterschelde North water level (m)

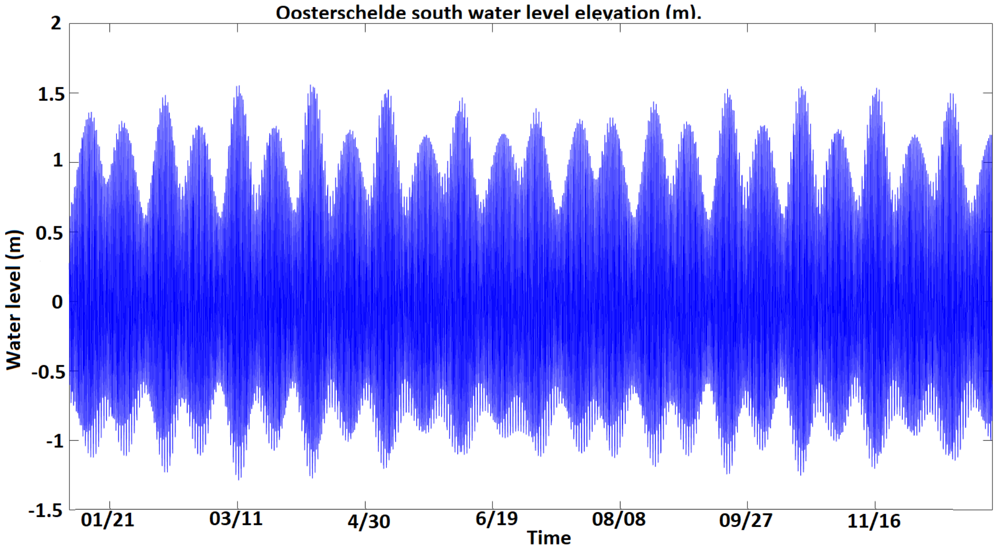

Figure E.8: Oosterschelde South water level (m)

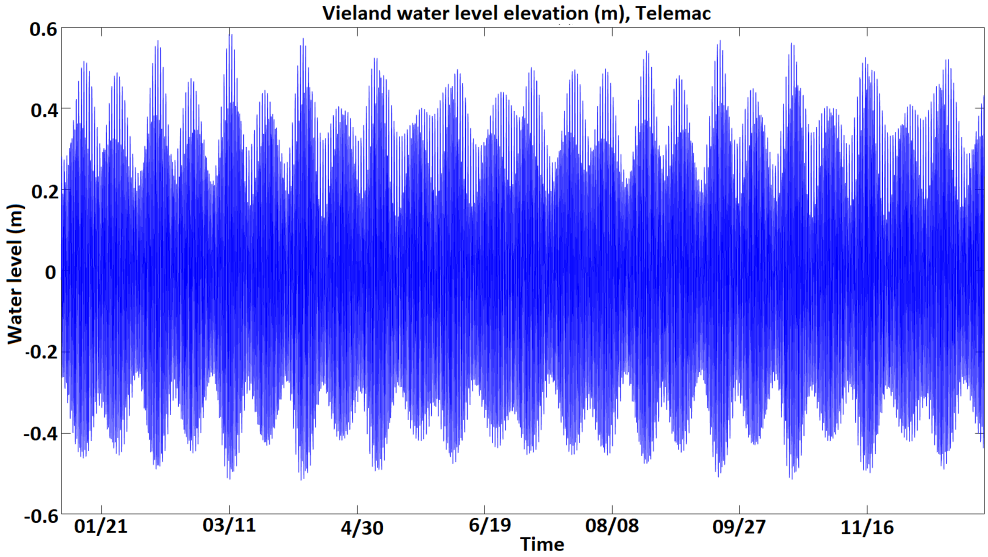

Figure E.9: Vlieland water level (m)

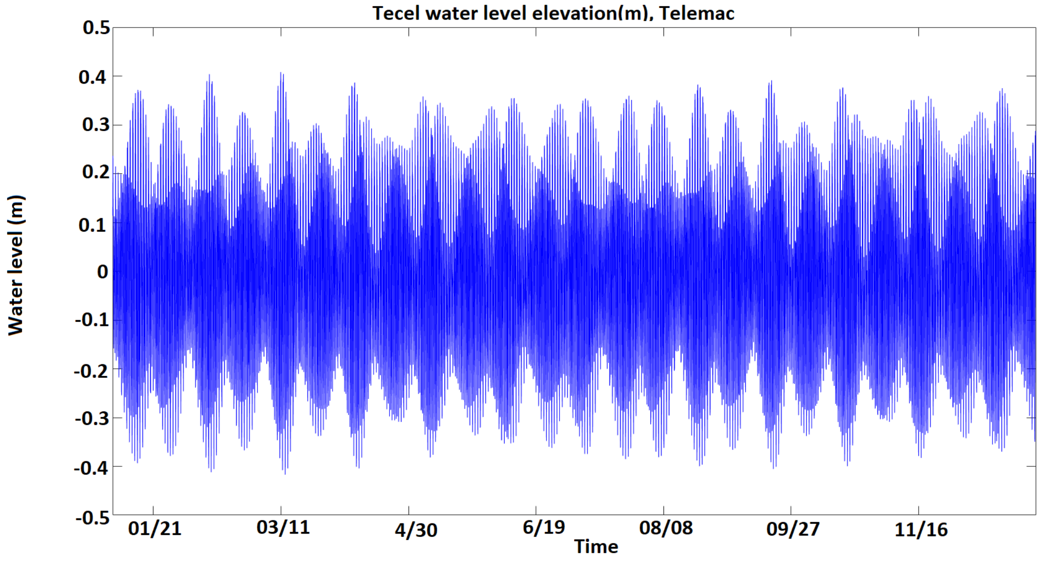

Figure E.10: Texel South water level (m)

Mapping Telemac.

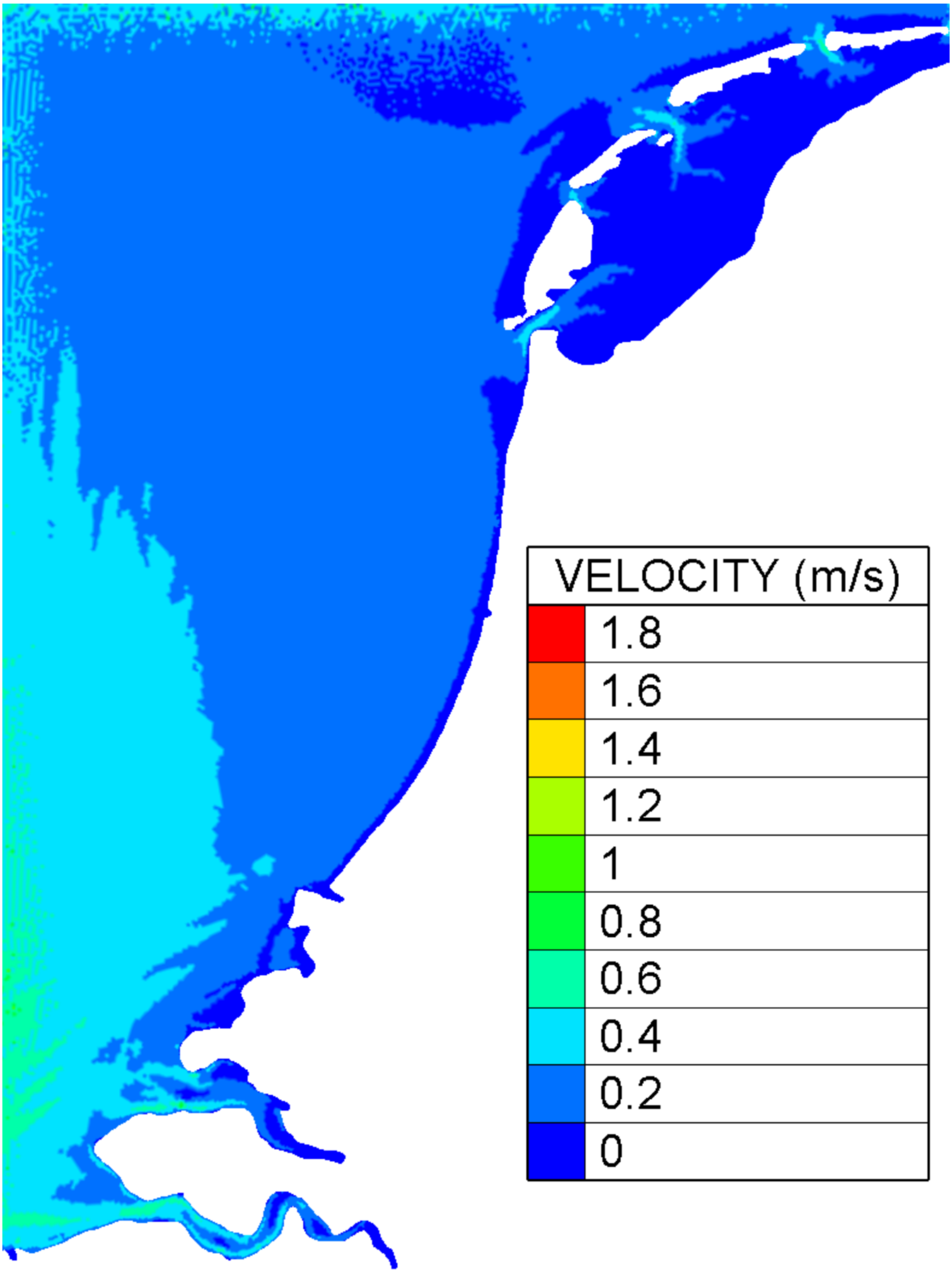

Figure E.11: Max velocity for the winter

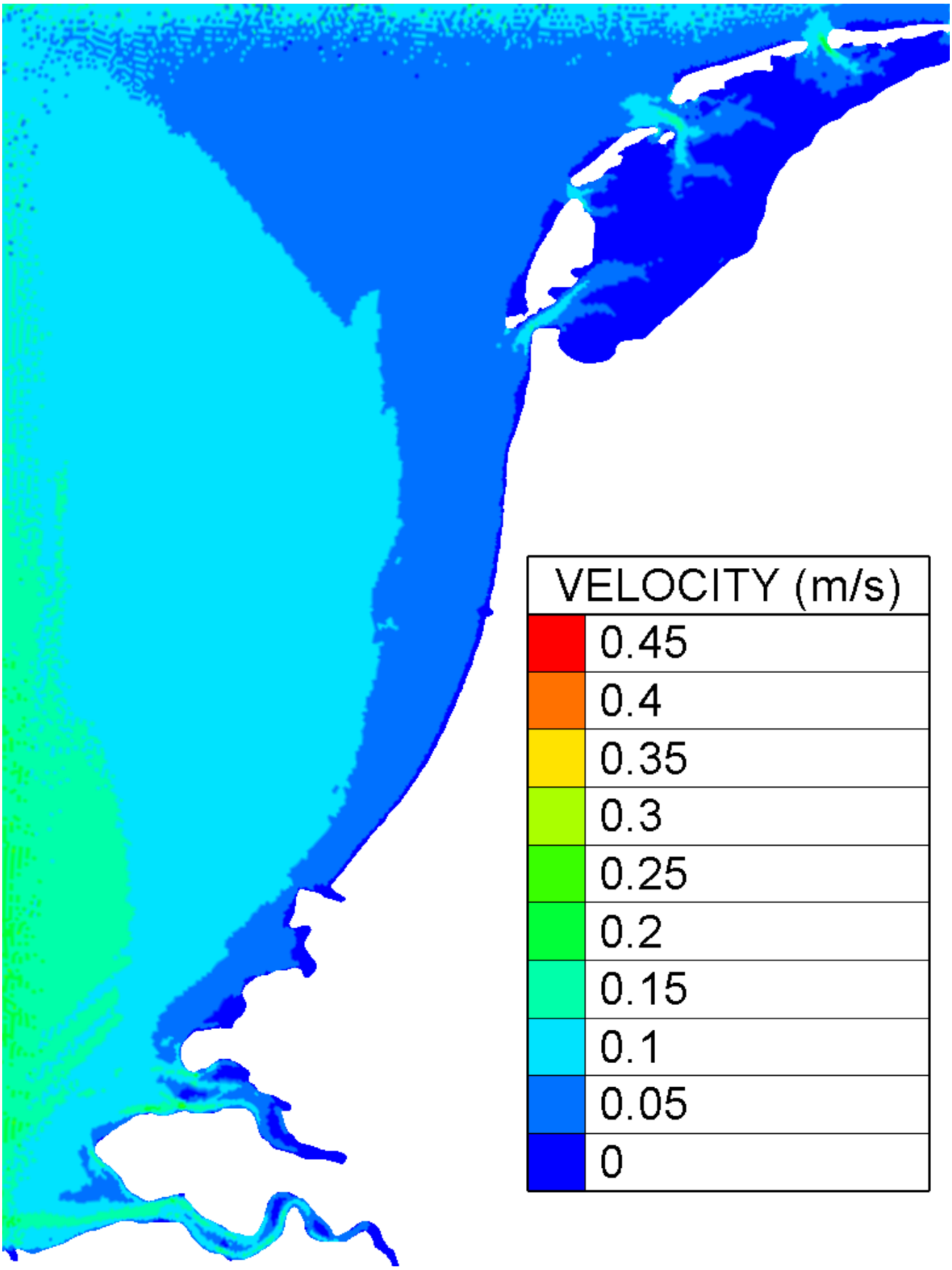

Figure E.12: Mean velocity for the winter

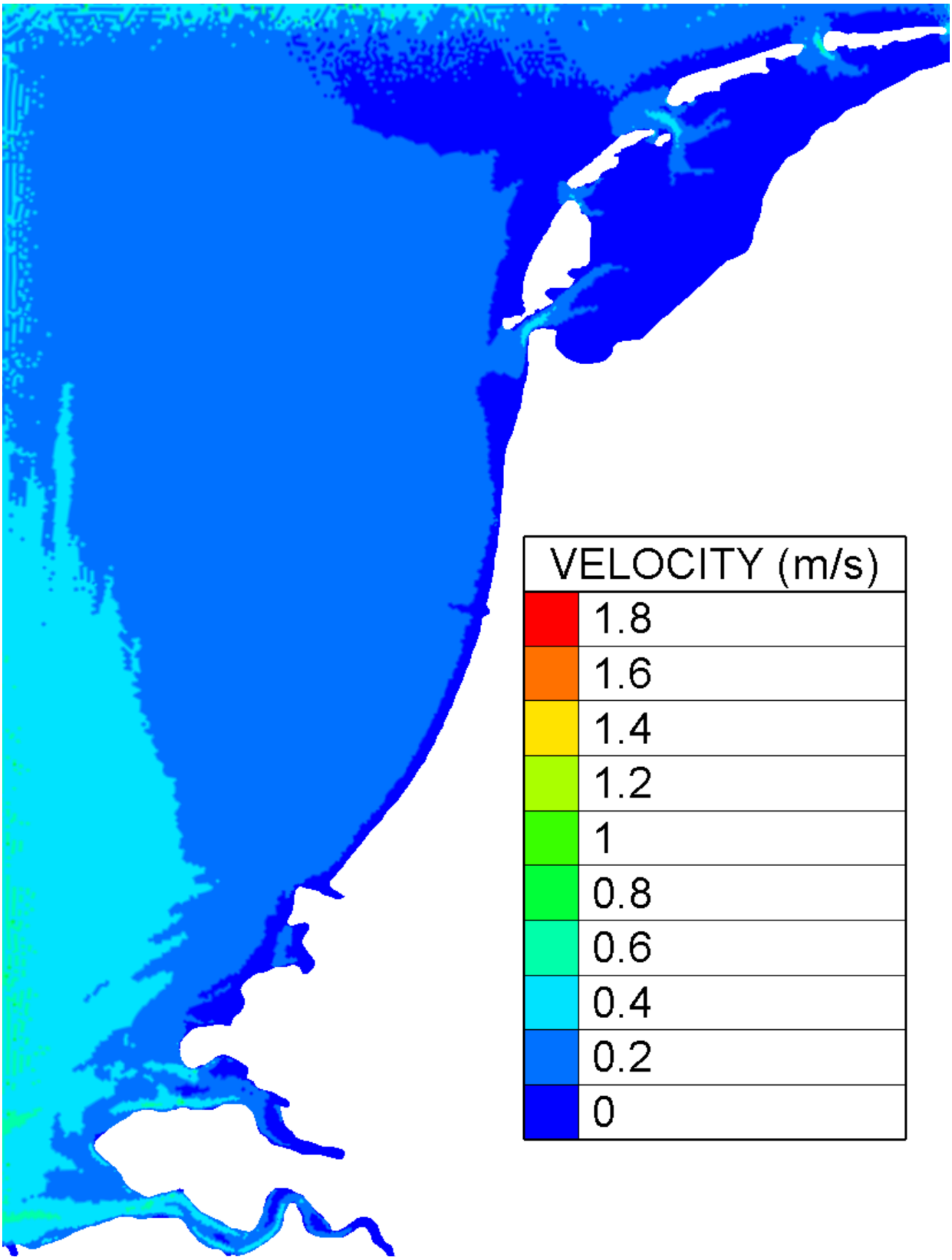

Figure E.13: Max velocity for the spring

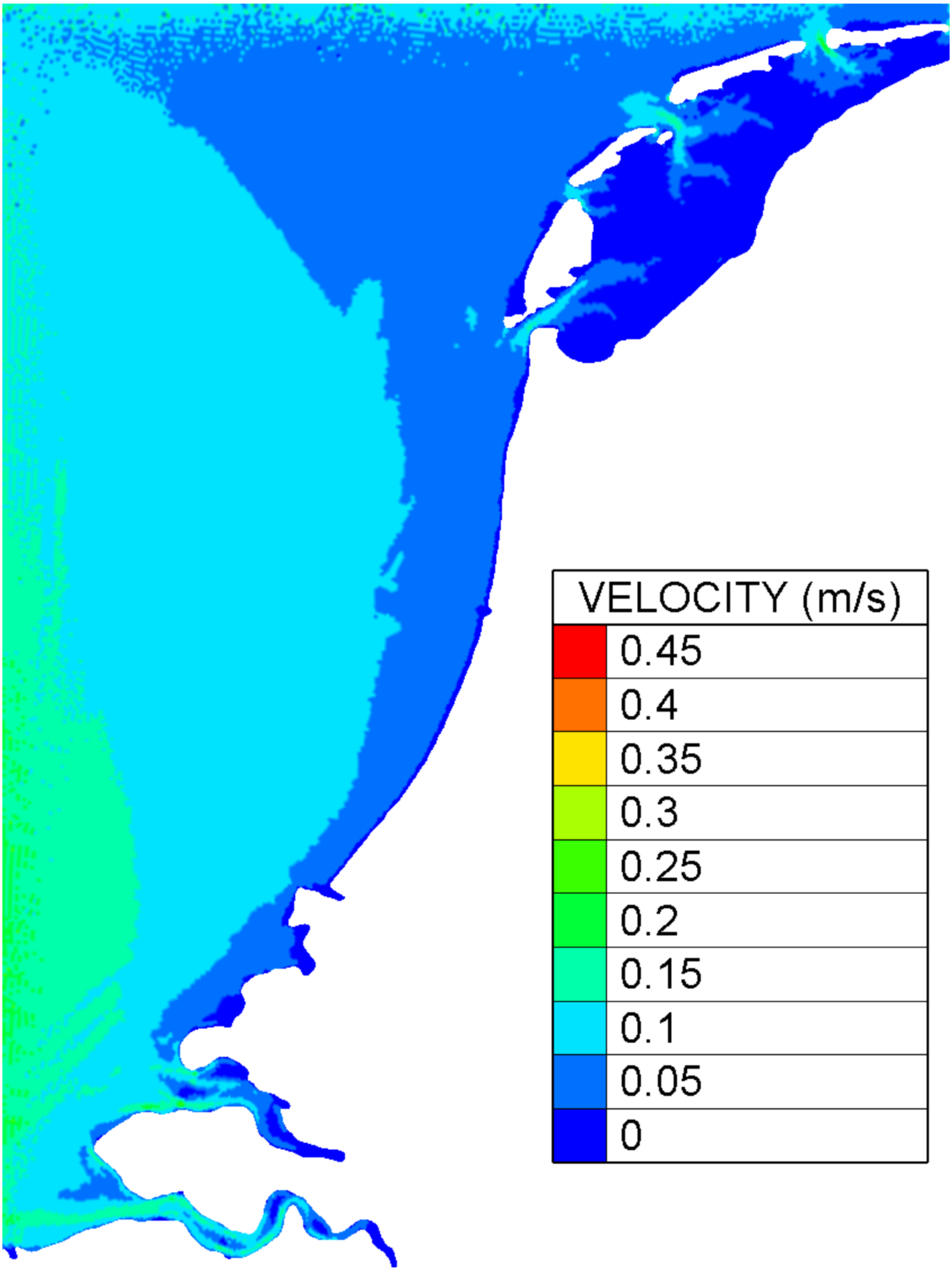

Figure E.14: Mean velocity for the spring

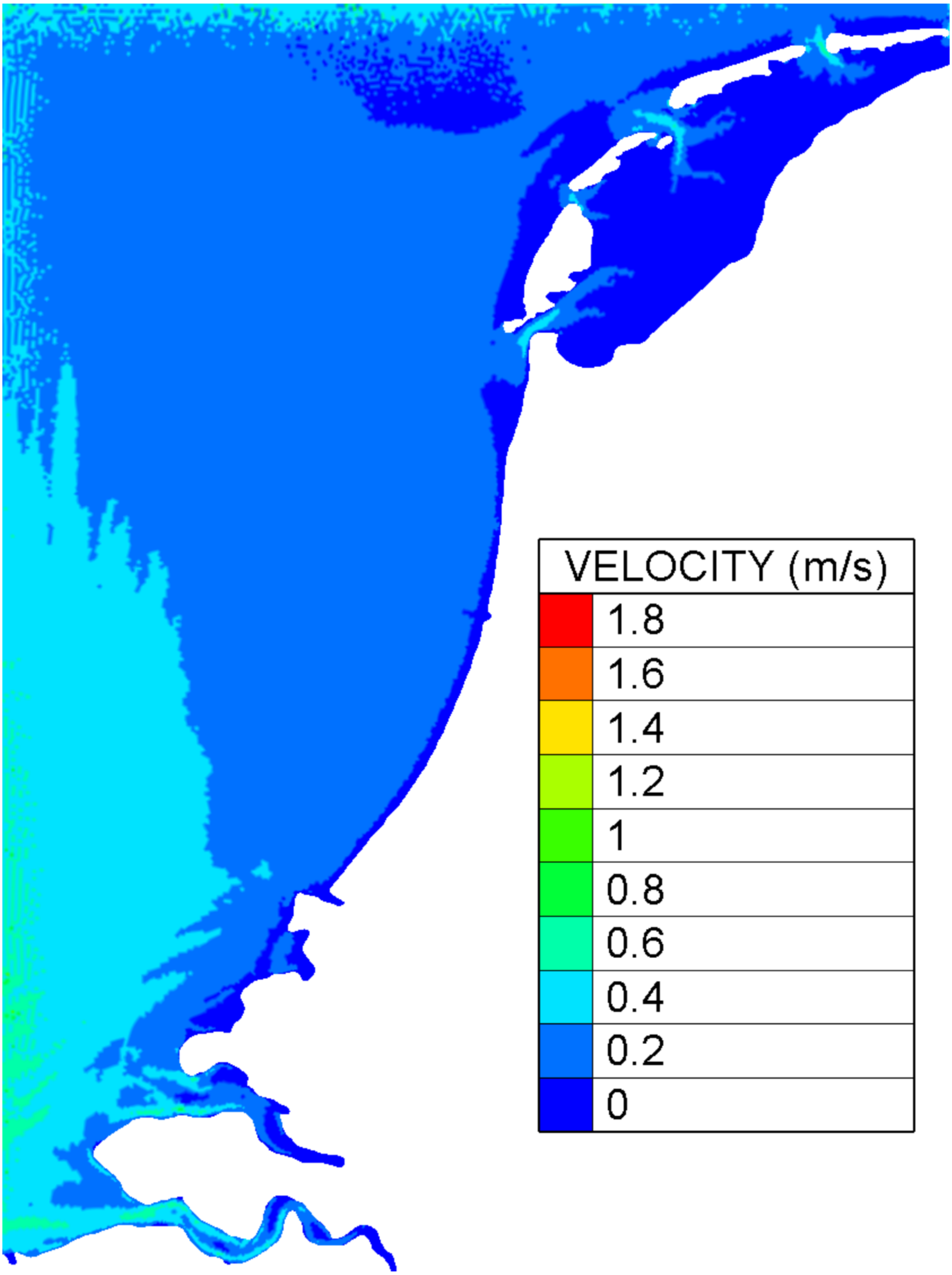

Figure E.15: Max velocity for the summer

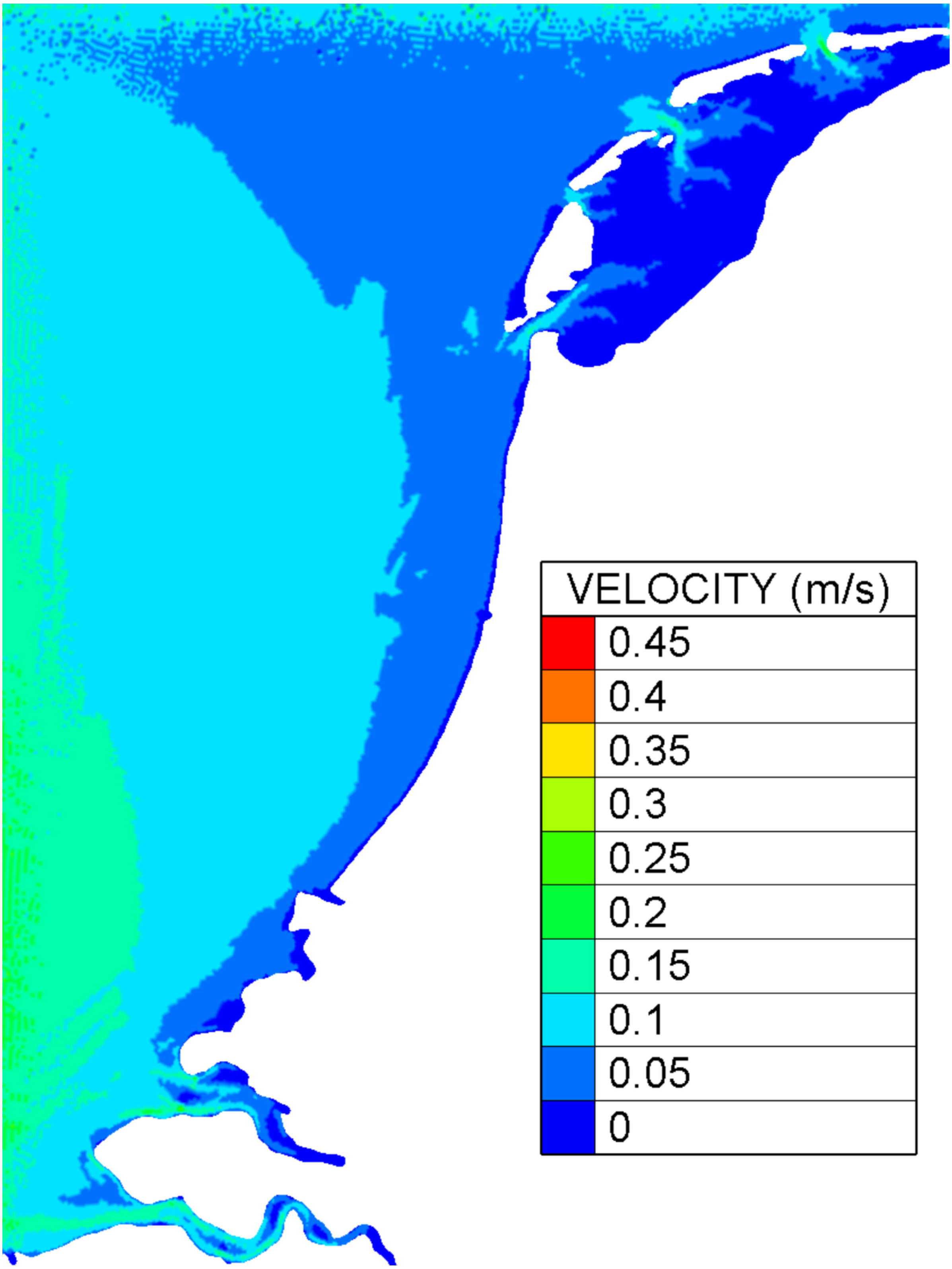

Figure E.16: Mean velocity for the summer

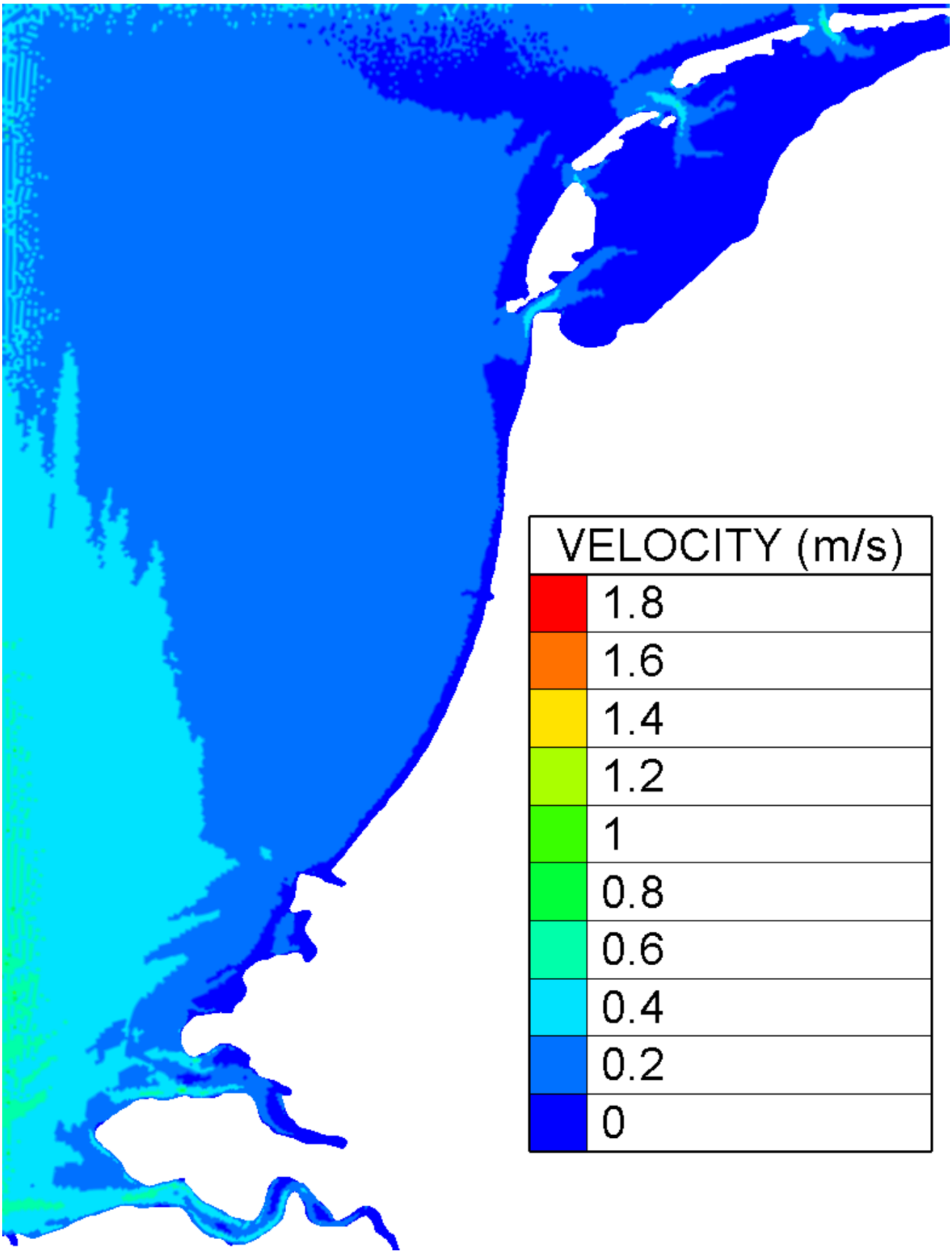

Figure E.17: Max velocity for the autumn

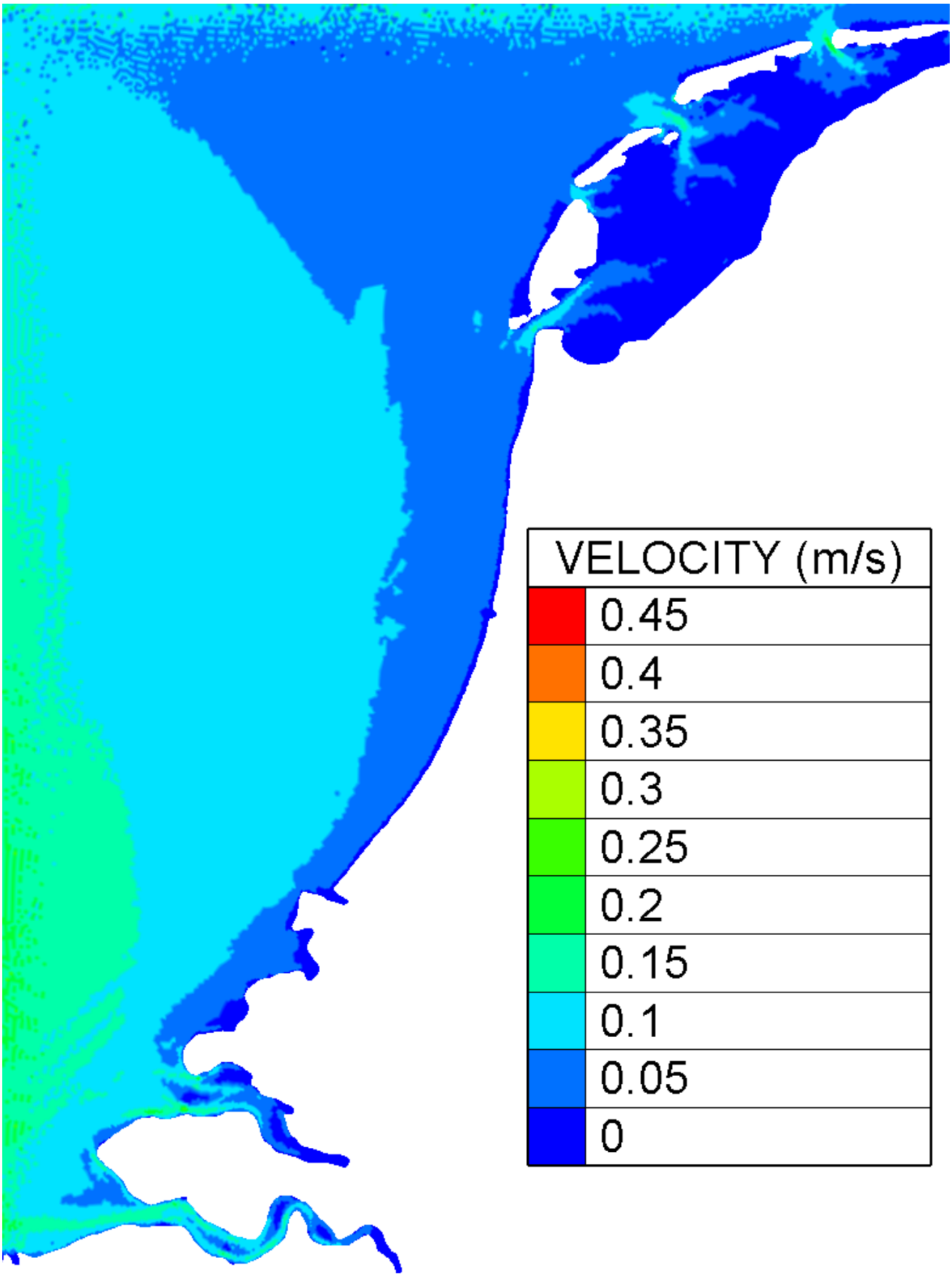

Figure E.18: Mean velocity for the autumn

Mapping Delft 3D.

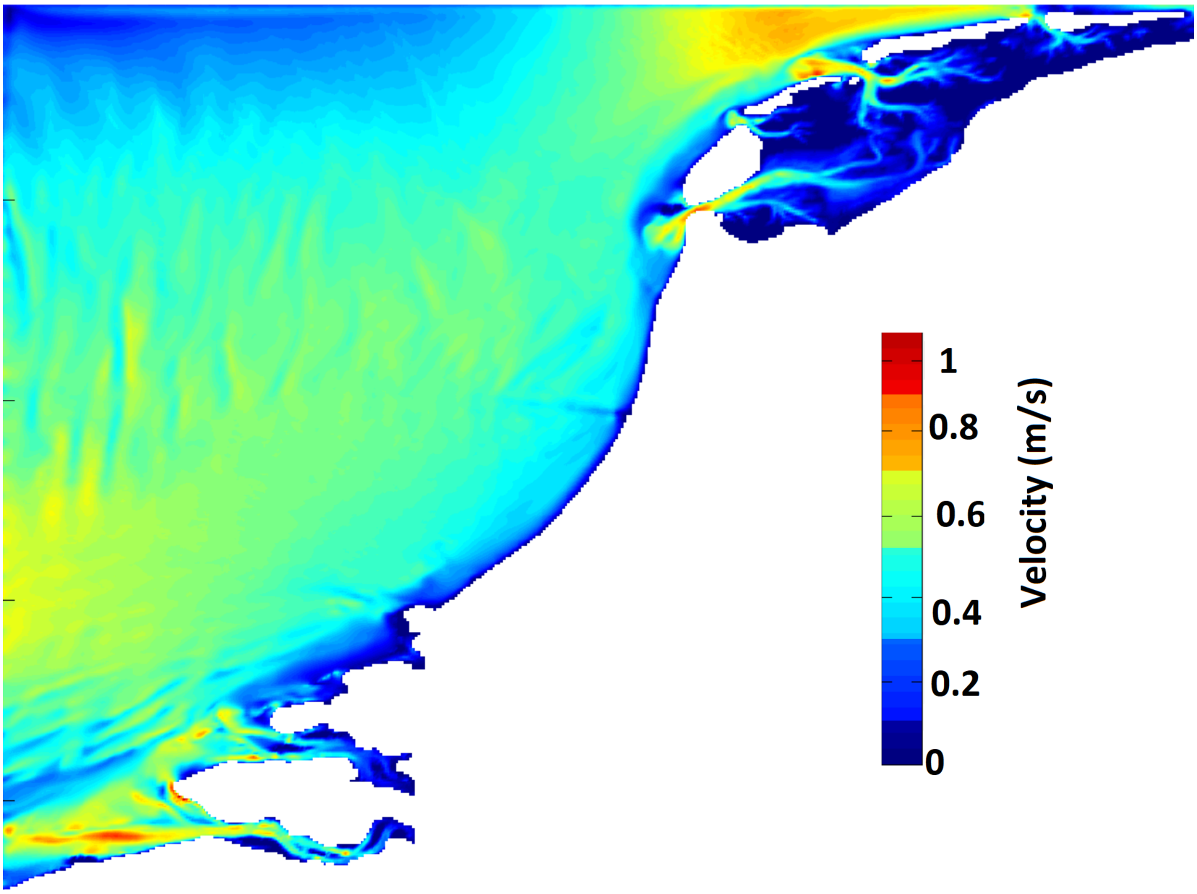

Figure E.19: Max velocity for the winter

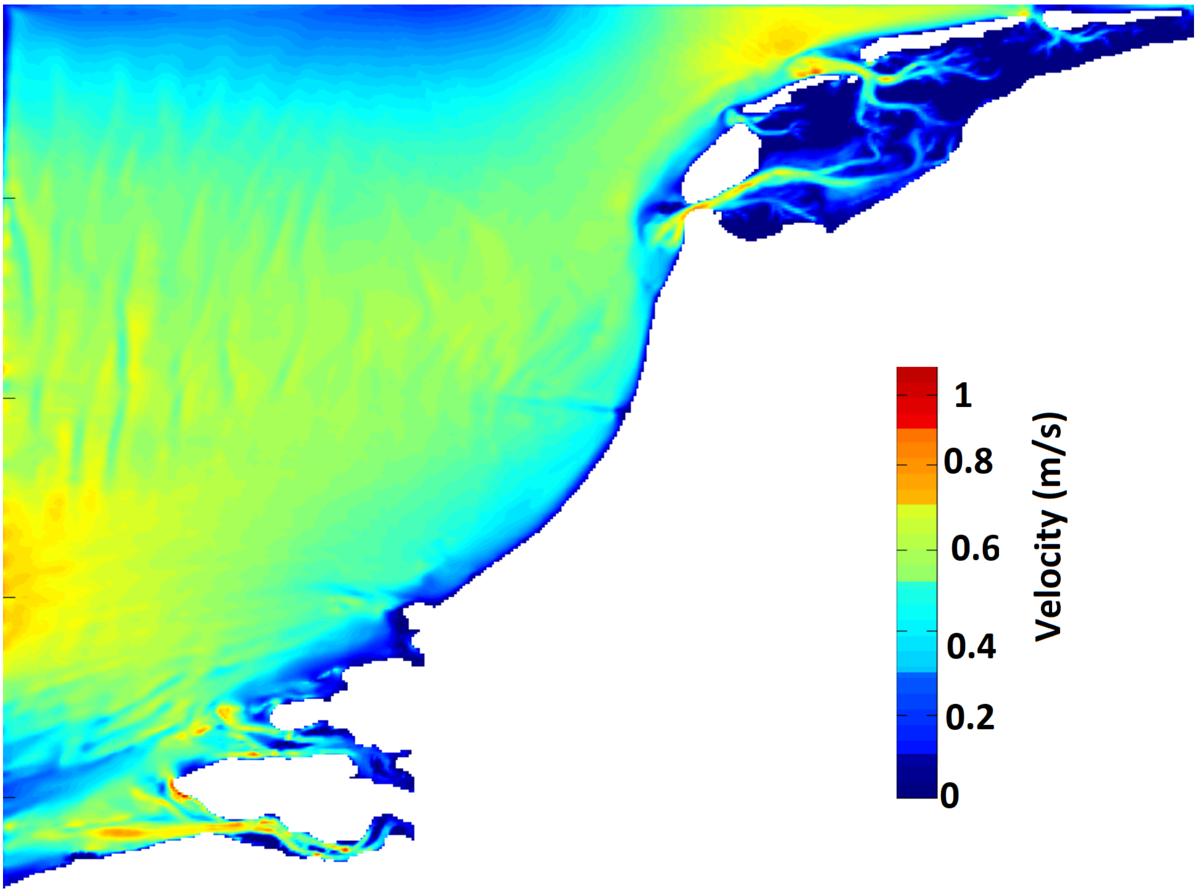

Figure E.20: Mean velocity for the winter

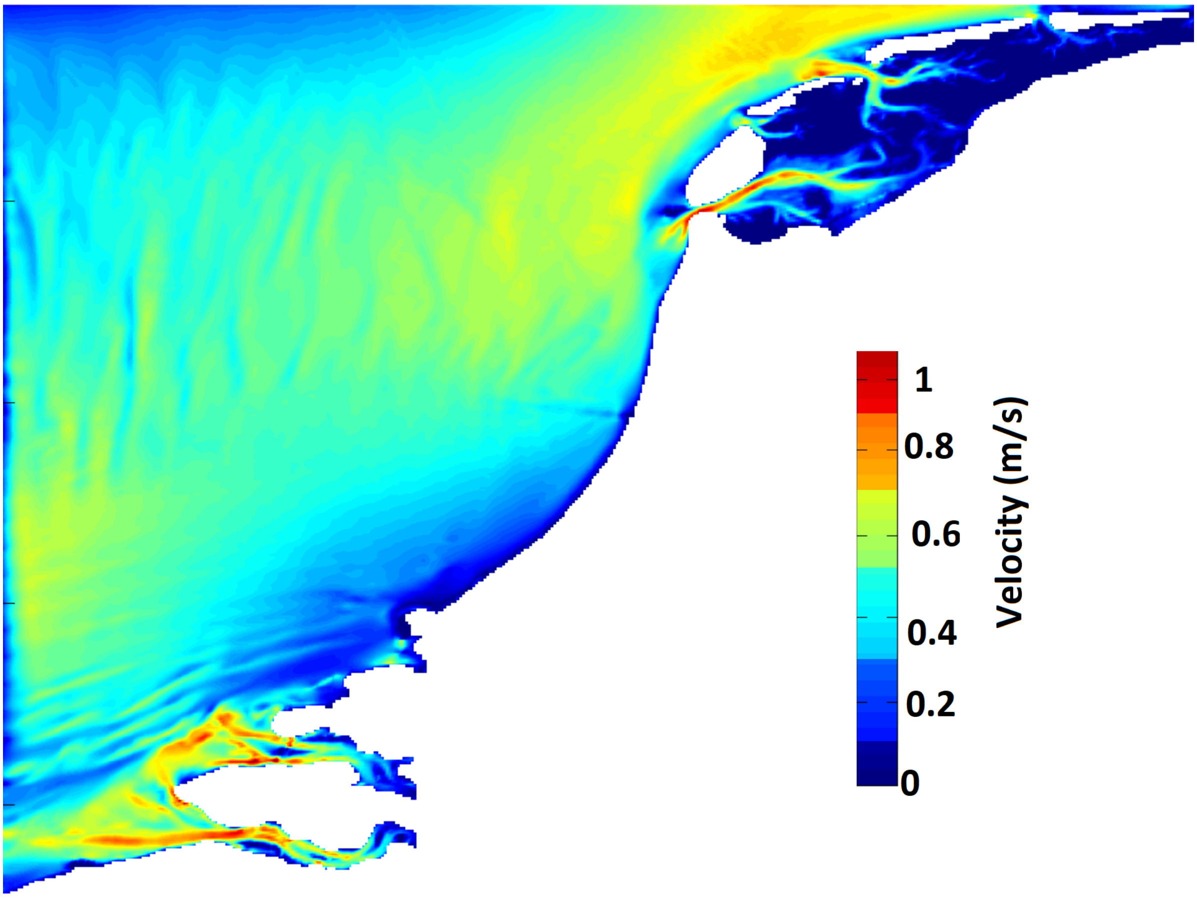

Figure E.21: Max velocity for the spring

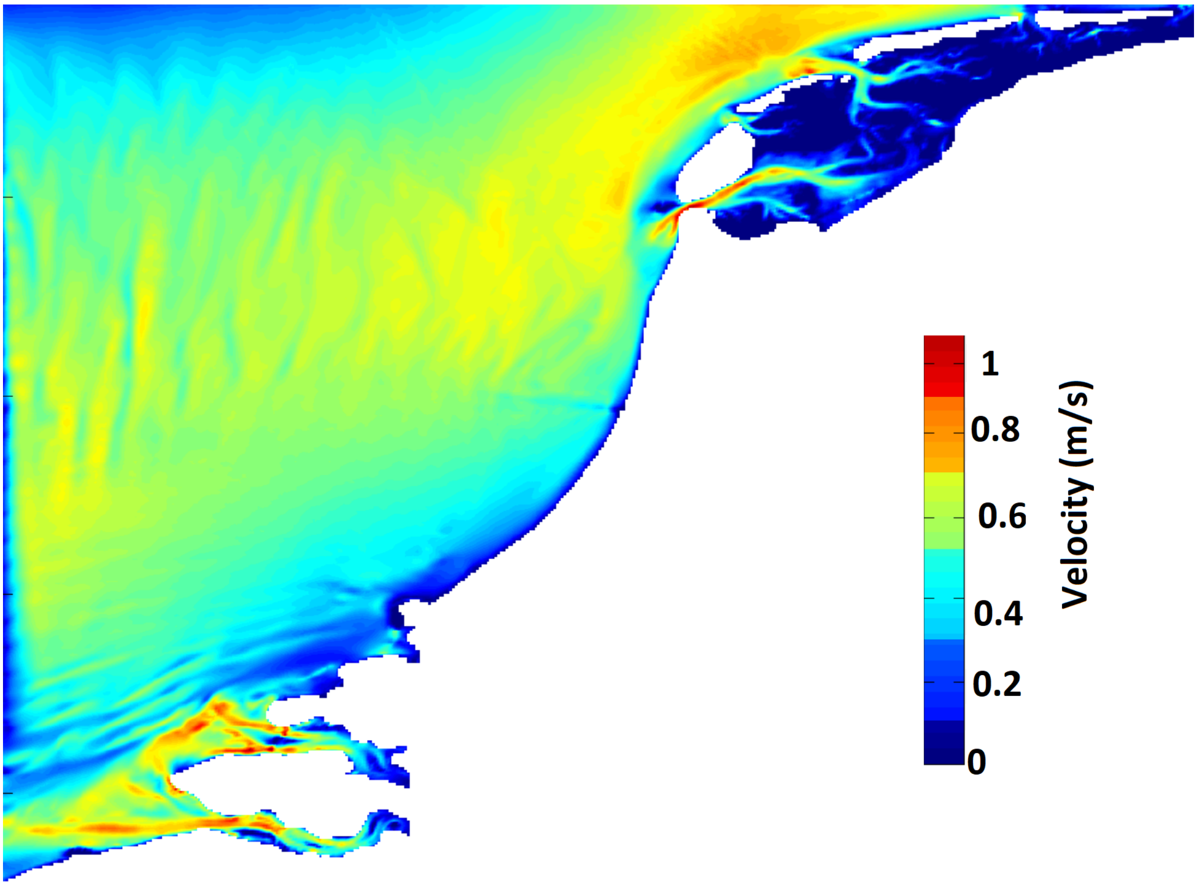

Figure E.22: Mean velocity for the spring

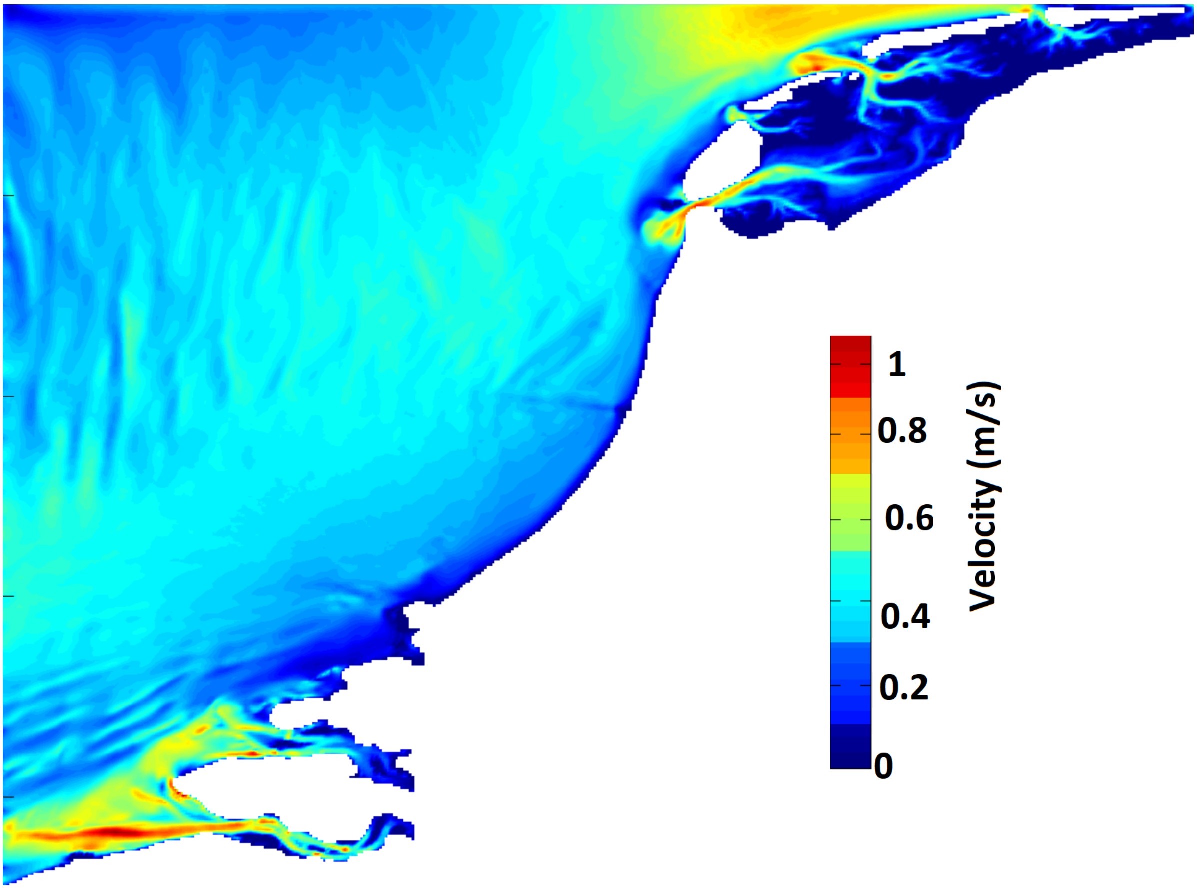

Figure E.23: Max velocity for the summer

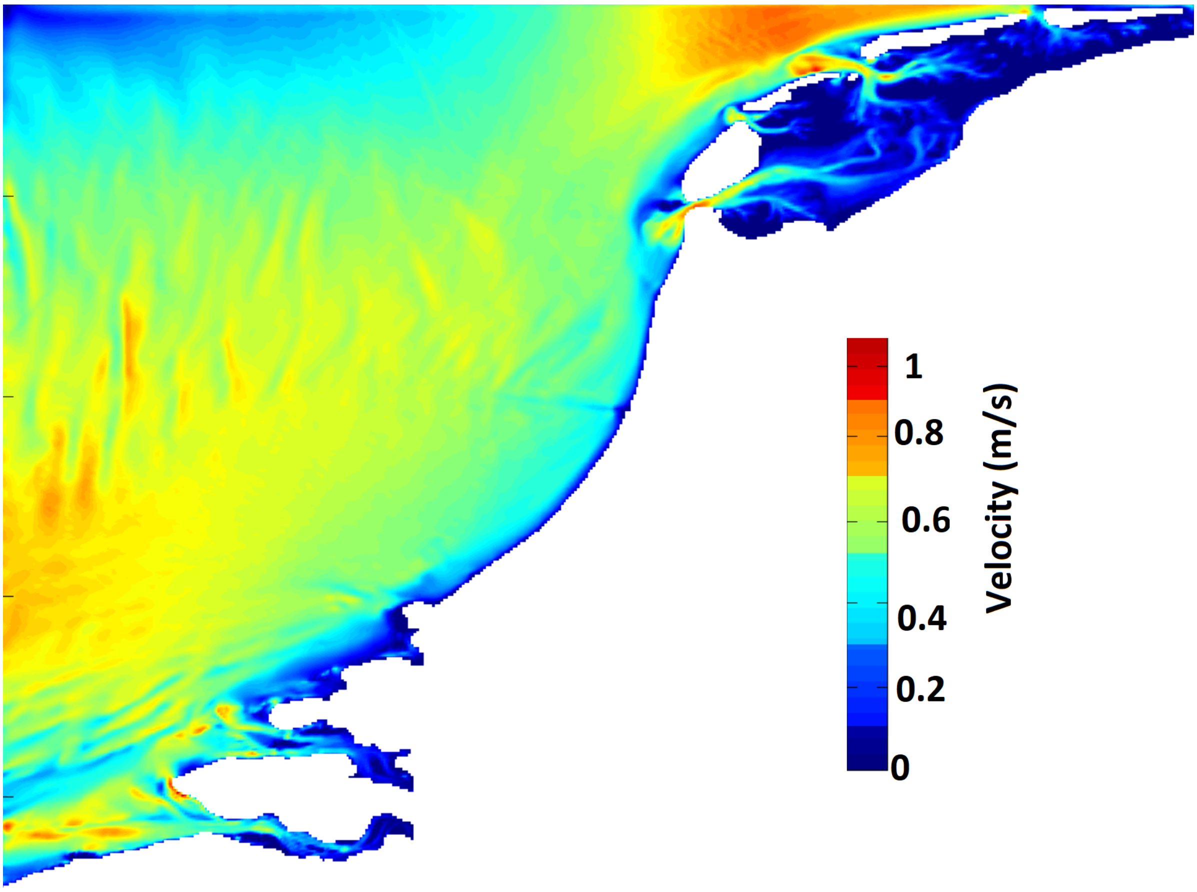

Figure E.24: Mean velocity for the summer

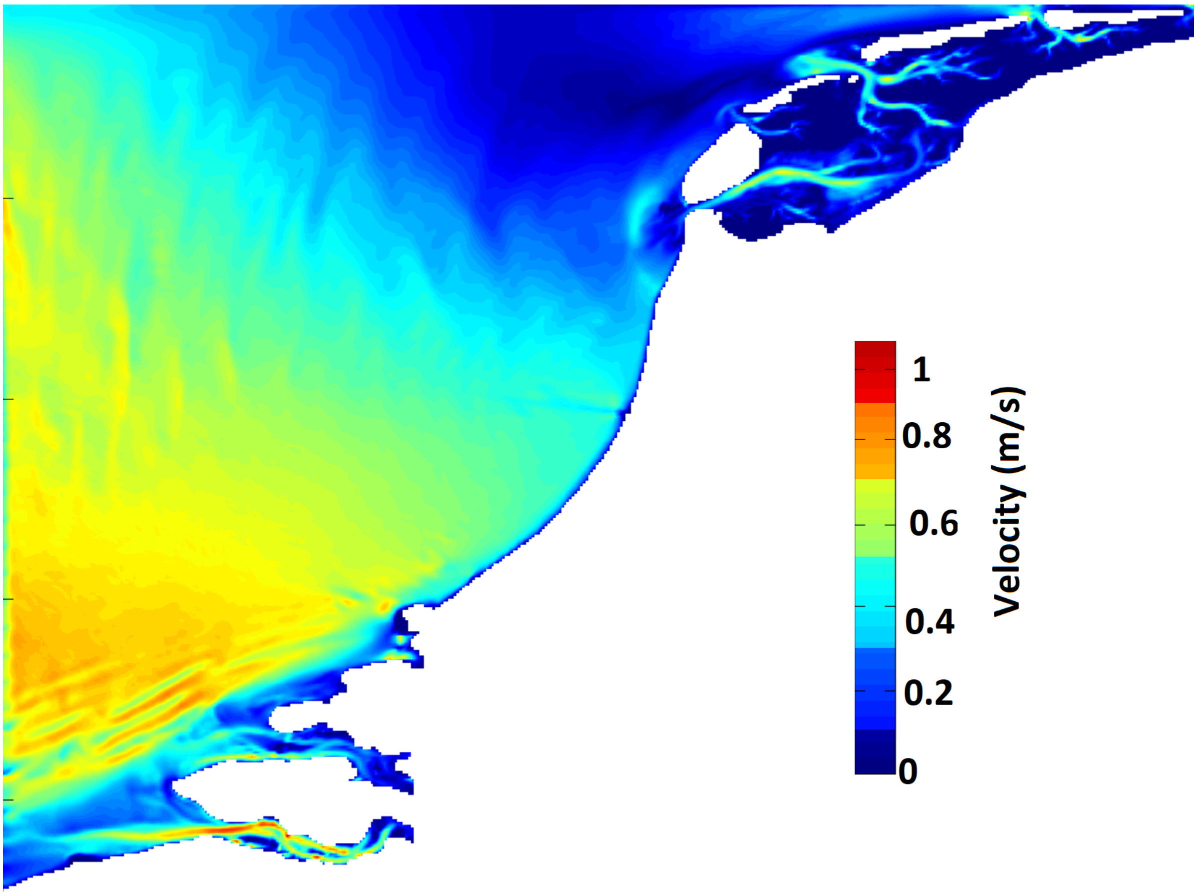

Figure E.25: Max velocity for the autumn

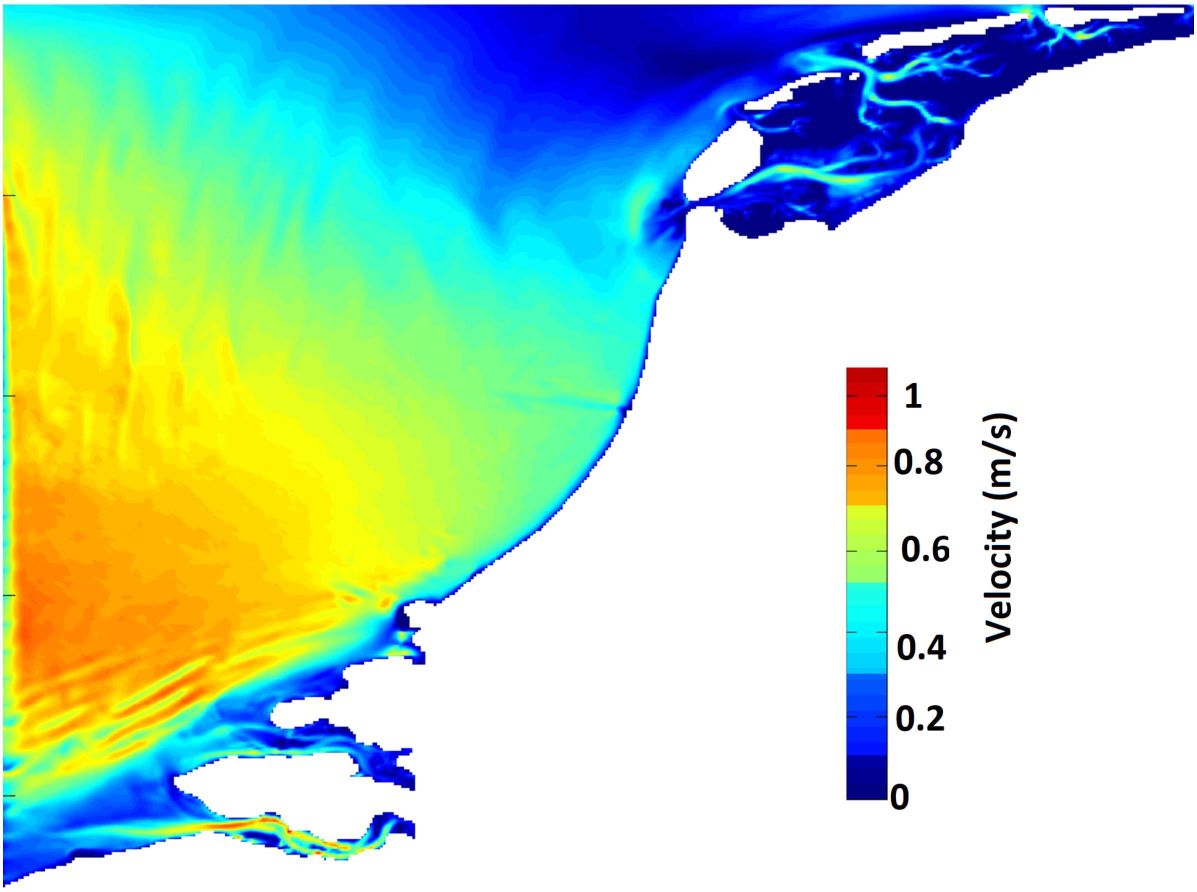

Figure E.26: Mean velocity for the autumn

F
Power

Power curves of the different turbine diameters determine for the resource assessment.

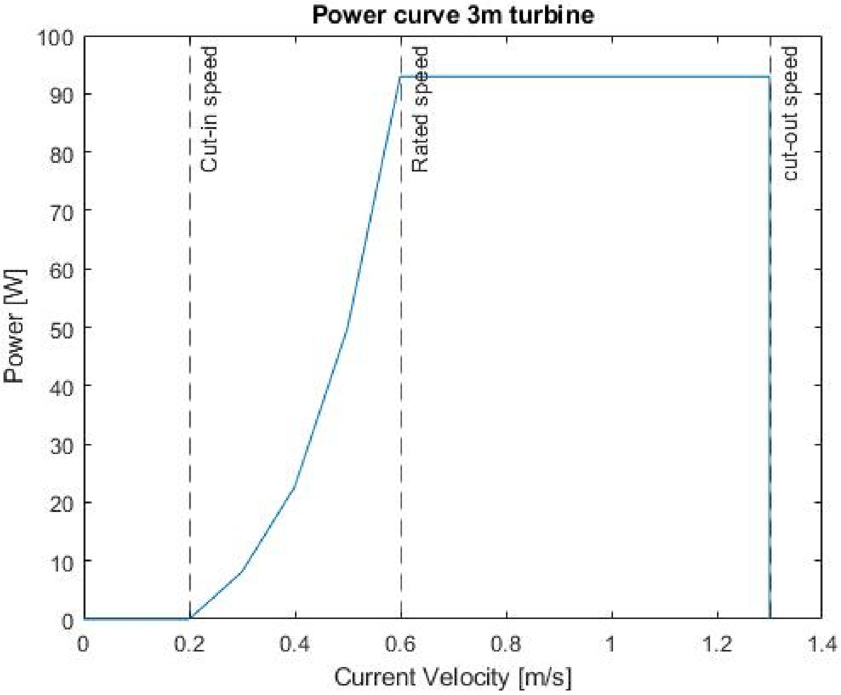

Figure F.1: The power curve of a 3m turbine

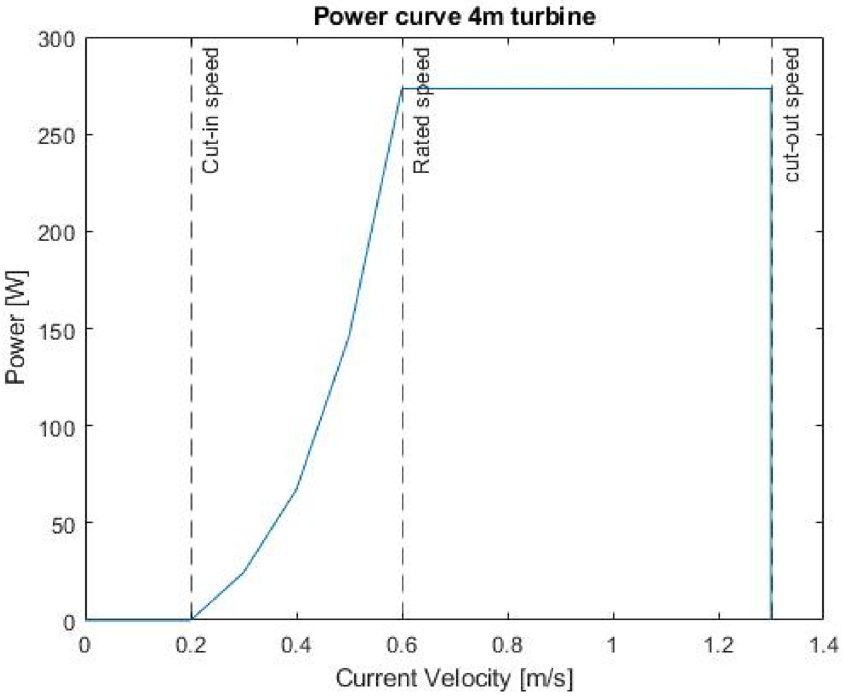

Figure F.2: The power curve of a 4m turbine

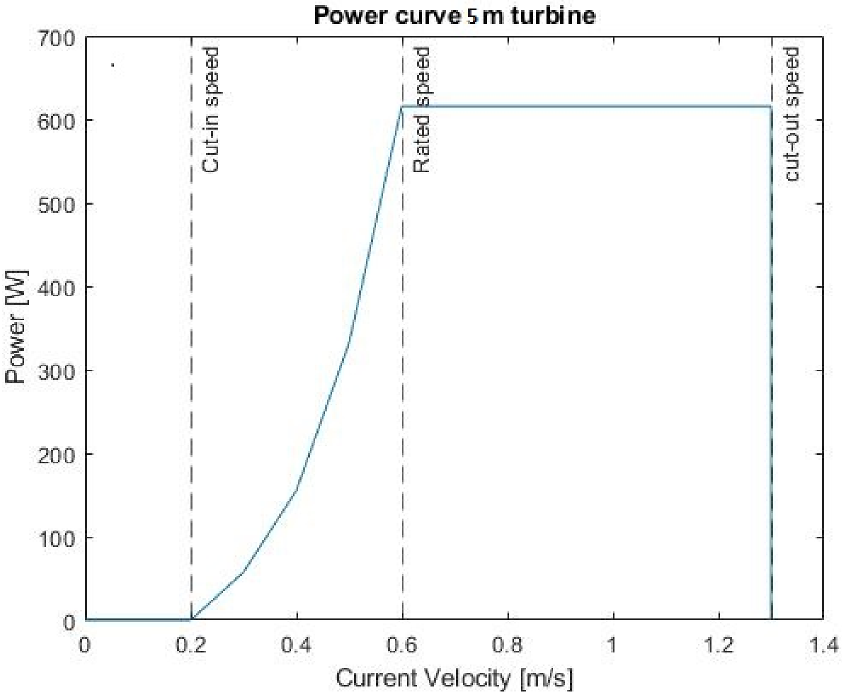

Figure F.3: The power curve of a 5m turbine

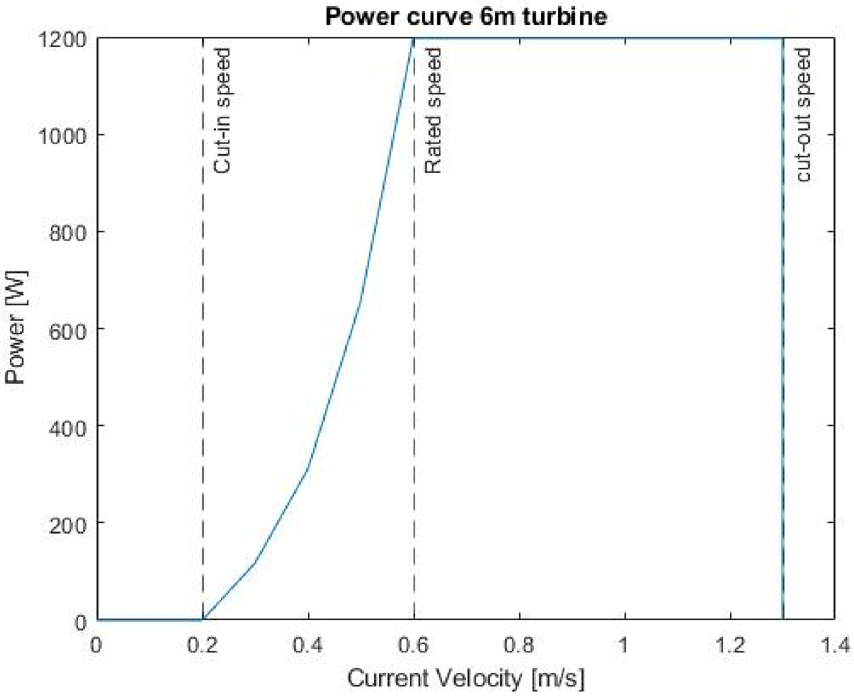

Figure F.4: The power curve of a 6m turbine

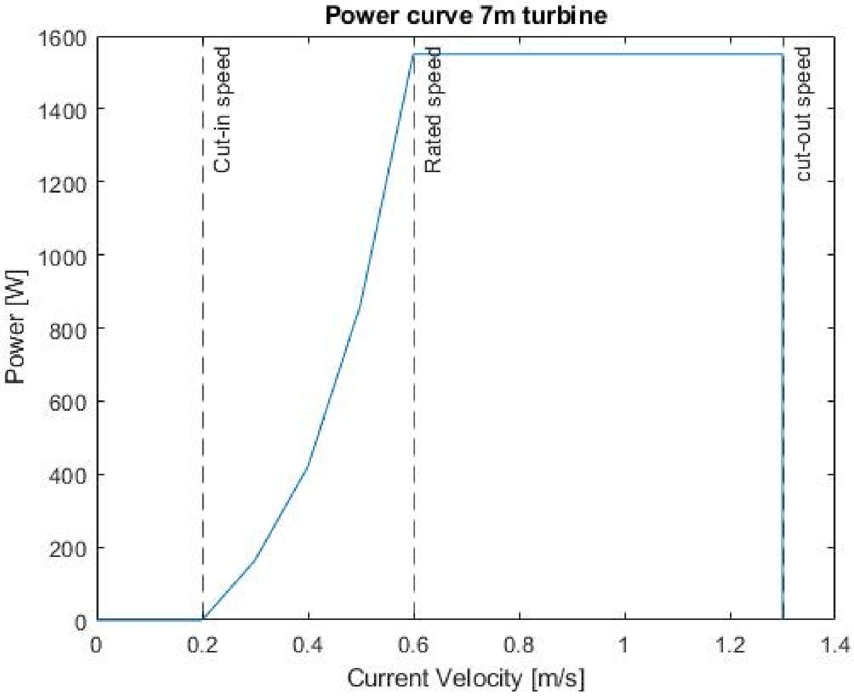

Figure F.5: The power curve of a 7m turbine

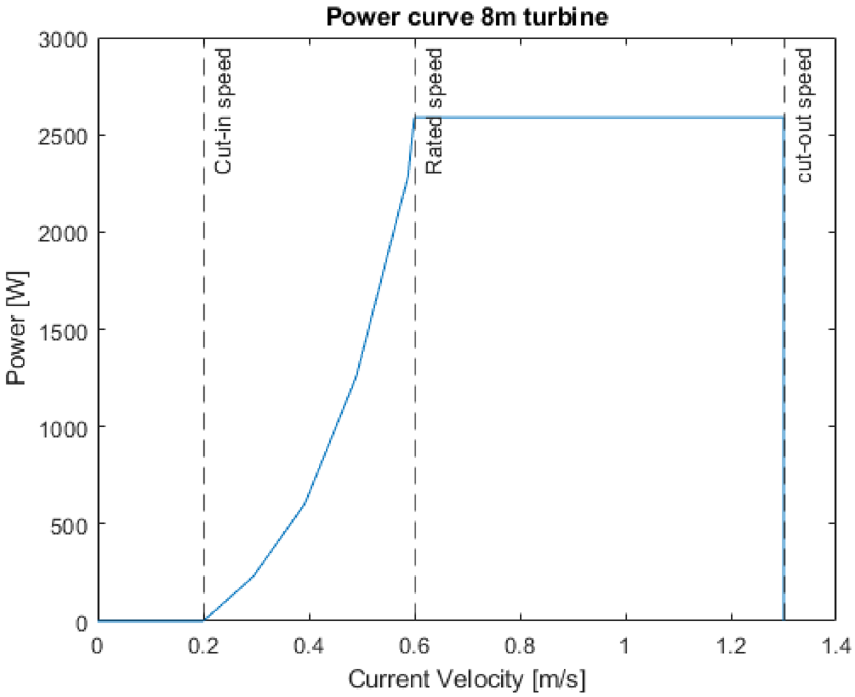

Figure F.6: The power curve of a 8m turbine

G

Site location

Table G.1: AHP model of the different criteria, C1 and C2

Location score	Tidal current(m/s)	Capacity factor(-)	Water depth(m)	Distance from electrical grid (km)	Distance from port (km)
Westerschelde (L1)	8	5	6	10	7
Oosterschelde (L2)	5	5	4	6	3
Oosterschelde (L3)	6	4	10	4	8
Texel (L4)	5	6	8	5	8
Vlieland (L5)	5	6	9	1	1

Table G.2: AHP model of the different criteria, C3 and C4

Location sore	Distance from shipping (m)	Distance from protected areas (km)	Distance from industrial hub (km)	Area size suitable for tidal turbines (km^2)
Westerschelde (L1)	5	6	9	6
Oosterschelde (L2)	9	4	8	6
Oosterschelde (L3)	8	3	7	5
Texel (L4)	6	1	1	10
Vlieland (L5)	7	1	1	6

Table G.3: AHP model of the different locations for the tidal current criteria, tidal current(m/s)

Tidal current(m/s)	L1	L2	L3	L4	L5	priority vector
L1	1.00	3.00	2.00	3.00	3.00	0.39
L2	0.33	1.00	0.50	1.00	1.00	0.12
L3	0.50	2.00	1.00	2.00	2.00	0.23
L4	0.33	1.00	0.50	1.00	1.00	0.12
L5	0.33	1.00	0.50	1.00	1.00	0.12
CR	0.0008					

Table G.4: AHP model of the different locations for the capacity factor criteria, capacity factor(-)

Capacity factor(-)						priority vector
L1	1.00	1.00	2.00	0.50	0.50	0.16
L2	1.00	1.00	2.00	0.50	0.50	0.16
L3	0.50	0.50	1.00	0.33	0.33	0.09
L4	2.00	2.00	3.00	1.00	1.00	0.30
L5	2.00	2.00	3.00	1.00	1.00	0.30
CR	0.002					

Table G.5: AHP model of the different locations for the water depth criteria, water depth(m)

Water depth(m)	L1	L2	L3	L4	L5	priority vector
L1	1.00	2.00	0.25	0.50	0.33	0.09
L2	0.50	1.00	0.17	0.25	0.20	0.05
L3	4.00	6.00	1.00	3.00	2.00	0.42
L4	2.00	4.00	0.33	1.00	0.50	0.17
L5	3.00	5.00	0.50	2.00	1.00	0.27
CR	0.02					

Table G.6: AHP model of the different locations for the distance from electrical grid criteria, distance from electrical grid (km)

Distance from electrical grid (km)	L1	L2	L3	L4	L5	priority vector
L1	1.00	4.00	6.00	5.00	9.00	0.55
L2	0.25	1.00	2.00	2.00	5.00	0.19
L3	0.17	0.50	1.00	0.50	3.00	0.09
L4	0.20	0.50	2.00	1.00	4.00	0.13
L5	0.11	0.20	0.33	0.25	1.00	0.04
CR	0.03					

Table G.7: AHP model of the different locations for the distance from port criteria, distance from port (km)

Distance from port (km)	L1	L2	L3	L4	L5	priority vector
L1	1.00	5.00	0.50	0.50	7.00	0.22
L2	0.20	1.00	0.17	0.17	3.00	0.07
L3	2.00	6.00	1.00	1.00	7.00	0.34
L4	2.00	6.00	1.00	1.00	7.00	0.34
L5	0.14	0.33	0.14	0.14	1.00	0.04
CR	0.02					

Table G.8: AHP model of the different locations for the distance from shipping criteria, distance from shipping (m)

Distance from shipping (m)	L1	L2	L3	L4	L5	priority vector
L1	1.00	0.20	0.25	0.50	0.33	0.06
L2	5.00	1.00	2.00	4.00	3.00	0.42
L3	4.00	0.50	1.00	3.00	2.00	0.26
L4	2.00	0.25	0.33	1.00	0.50	0.10
L5	3.00	0.33	0.50	2.00	1.00	0.16
CR	0.02					

Table G.9: AHP model of the different locations for the distance from protected areas criteria, distance from protected areas (km)

Distance from protected areas (km)	L1	L2	L3	L4	L5	priority vector
L1	1.00	3.00	4.00	6.00	6.00	0.49
L2	0.33	1.00	2.00	4.00	4.00	0.23
L3	0.25	0.50	1.00	3.00	3.00	0.15
L4	0.17	0.25	0.33	1.00	1.00	0.06
L5	0.17	0.25	0.33	1.00	1.00	0.06
CR	0.02					

Table G.10: AHP model of the different locations for the distance from industrial hub criteria, distance from industrial hub (km)

Distance from industrial hub (km)	L1	L2	L3	L4	L5	priority vector
L1	1.00	2.00	3.00	9.00	9.00	0.44
L2	0.50	1.00	2.00	8.00	8.00	0.29
L3	0.33	0.50	1.00	7.00	7.00	0.20
L4	0.11	0.13	0.14	1.00	1.00	0.04
L5	0.11	0.13	0.14	1.00	1.00	0.04
CR	0.03					

Table G.11: AHP model of the different locations for the area size available criteria, area size suitable for tidal turbines (km^2)

Area size suitable for tidal turbines (km^2)	L1	L2	L3	L4	L5	priority vector
L1	1.00	1.00	2.00	0.25	1.00	0.14
L2	1.00	1.00	2.00	0.25	1.00	0.14
L3	0.50	0.50	1.00	0.20	0.50	0.08
L4	4.00	4.00	5.00	1.00	4.00	0.51
L5	1.00	1.00	2.00	0.25	1.00	0.14
CR	0.01					

H

Array

In the following table the power production and thrust of the individual for each diameter and array can be seen.

Table H.1: Power and thrust for a 8 diameter turbine for array 1

Array 1	Row 1		Row 2		Row 3	
	Power	Thrust	Power	Thrust	Power	Thrust
Outer	2103.841	9446.109	1213.65	7600.314	916.9933	6775.8
Middle	2163.409	9530.203	1185.866	7713.631	935.804	7060.252
Bottom	2103.841	9446.109	1213.65	7600.314	916.9933	6775.8

Table H.2: Power and thrust for a 8 diameter turbine for array 2

Array 2	Row 1		Row 2		Row 3	
	Power	Thrust	Power	Thrust	Power	Thrust
Outer	2138.702	9552.908	1545.713	8256.546	1285.947	7585.847
Middle	2070.858	9481.642	1490.666	8061.593	1151.995	7177.92
Bottom	2138.702	9552.908	1545.713	8256.546	1285.947	7585.847

Table H.3: Power and thrust for a 8 diameter turbine for array 3

Array 3	Row 1		Row 2		Row 3	
	Power	Thrust	Power	Thrust	Power	Thrust
Outer	2186.191	9569.142	1675.912	8475.213	1424.143	7839.542
Middle	2054.087	9504.288	1560.232	8202.326	1395.2446	7313.59
Bottom	2186.191	9569.142	1675.912	8475.213	1424.143	7839.542

Table H.4: Power and thrust for a 8 diameter turbine for array 4

Array 4	Row 1		Row 2		Row 3	
	Power	Thrust	Power	Thrust	Power	Thrust
Outer	2085.861	9404.201	1194.742	7387.608	812.3082	6372.01
Middle	2070.61	9263.052	1124.119	6943.555	768.8567	5678.948
Bottom	2085.861	9404.201	1194.742	7387.608	812.3082	6372.01

Table H.5: Power and thrust for a 8 diameter turbine for array 5

Array 5	Row 1		Row 2		Row 3	
	Power	Thrust	Power	Thrust	Power	Thrust
Outer	2221.431	9575.639	1162.445	7731.139	945.4467	7217.359
Middle	2181.106	9536.687	1166.724	7734.058	946.4563	7172.295
Bottom	2221.431	9575.639	1162.445	7731.139	945.4467	7217.359

Table H.6: Power and thrust for a 8 diameter turbine for array 6

Array 6	Row 1		Row 2		Row 3	
	Power	Thrust	Power	Thrust	Power	Thrust
Outer	2231.959	9595.145	1569.486	8368.559	1402.024	7978.331
Middle	2212.626	9601.651	1581.492	8408.095	1401.439	7975.365
Bottom	2231.959	9595.145	1569.486	8368.559	1402.024	7978.331

Table H.7: Power and thrust for a 8 diameter turbine for array 7

Array 7	Row 1		Row 2		Row 3	
	Power	Thrust	Power	Thrust	Power	Thrust
Outer	2186.799	9598.398	2598.45	9827.468	2074.255	9091.282
Middle	2169.543	9539.93	2535.005	9781.438	2136.725	8955.652
Bottom	2221.392	9562.646	2446.718	9906.629	2198.442	9062.81

Table H.8: Power and thrust for a 8 diameter turbine for array 8

Array 8	Row 1		Row 2		Row 3	
	Power	Thrust	Power	Thrust	Power	Thrust
Outer	2189.384	9608.159	2262.823	9333.493	2003.117	9002.849
Middle	2155.649	9569.142	2199.474	9288.636	1872.524	8551.807
Bottom	2210.025	9585.389	2287.982	9660.307	1971.993	8730.833

Table H.9: Power and thrust for a 8 diameter turbine for array 9

Array 9	Row 1		Row 2		Row 3	
	Power	Thrust	Power	Thrust	Power	Thrust
Outer	2190.246	9611.414	2073.67	9040.696	1973.83	8668.89
Middle	2146.281	9582.139	2000.596	9006	1551.966	8277.68
Bottom	2201.104	9598.398	2191.695	9530.203	1811.321	8610.249

Table H.10: Power and thrust for a 8 diameter turbine for array 10

Array 10	Row 1		Row 2		Row 3	
	Power	Thrust	Power	Thrust	Power	Thrust
Outer	2235.513	9614.67	2668.152	10213.02	2110.841	9304.644
Middle	2233.727	9601.651	2647.842	10226.45	2280.438	9536.687
Bottom	2249.315	9595.145	2491.346	10119.28	2292.188	9543.174

Table H.11: Power and thrust for a 8 diameter turbine for array 11

Array 11	Row 1		Row 2		Row 3	
	Power	Thrust	Power	Thrust	Power	Thrust
Outer	2243.394	9617.926	2568.193	9999.384	2210.22	9452.564
Middle	2237.264	9614.67	2542.695	10006.03	2303.717	9520.481
Bottom	2256.275	9601.651	2350.226	10015.99	2335.501	9569.142

Table H.12: Power and thrust for a 8 diameter turbine for array 12

Array 12	Row 1		Row 2		Row 3	
	Power	Thrust	Power	Thrust	Power	Thrust
Outer	2054.395	9423.532	1739.84	7954.621	1476.303	7635.091
Middle	2040.686	9269.445	1699.125	7860.135	1023.287	6311.192
Bottom	2111.761	9400.981	2037.144	8946.228	1225.519	6808.639

Table H.13: Power and thrust for a 8 diameter turbine for array 13

Array 13	Row 1		Row 2		Row 3	
	Power	Thrust	Power	Thrust	Power	Thrust
Outer	2242.507	9614.67	2324.577	9604.905	2206.978	9465.482
Middle	2230.248	9627.698	2292.022	9601.651	2139.184	9247.08
Bottom	2252.048	9611.414	2348.293	9814.306	2199.275	9346.329

Table H.14: Power and thrust for a 7 diameter turbine for array 1

Array 1	Row 1		Row 2		Row 3	
	Power	Thrust	Power	Thrust	Power	Thrust
Outer	1410.226	7642.719	847.6222	6486.884	662.9952	5980.06
Middle	1366.695	7572.716	814.8142	6379.596	642.7436	5759.164
Bottom	1410.226	7642.719	847.6222	6486.884	662.9952	5980.06

Table H.15: Power and thrust for a 7 diameter turbine for array 2

Array 2	Row 1		Row 2		Row 3	
	Power	Thrust	Power	Thrust	Power	Thrust
Outer	1391.677	7663.523	1049.839	6809.211	879.6366	6320.378
Middle	1340.51	7606.381	956.8491	6578.18	791.6171	5998.463
Bottom	1391.677	7663.523	1049.839	6809.211	879.6366	6320.378

Table H.16: Power and thrust for a 7 diameter turbine for array 3

Array 3	Row 1		Row 2		Row 3	
	Power	Thrust	Power	Thrust	Power	Thrust
Outer	1383.281	7679.144	1092.499	6937.358	958.2006	6472.528
Middle	1325.612	7624.539	1040.616	6718.756	822.7322	6090.906
Bottom	1383.281	7679.144	1092.499	6937.358	958.2006	6472.528

Table H.17: Power and thrust for a 7 diameter turbine for array 4

Array 4	Row 1		Row 2		Row 3	
	Power	Thrust	Power	Thrust	Power	Thrust
Outer	1367.396	7544.288	841.8232	6209.796	535.5825	5414.816
Middle	1355.923	7441.366	811.7885	5883.904	351.2214	4956.837
Bottom	1367.396	7544.288	841.8232	6209.796	535.5825	5414.816

Table H.18: Power and thrust for a 7 diameter turbine for array 5

Array 5	Row 1		Row 2		Row 3	
	Power	Thrust	Power	Thrust	Power	Thrust
Outer	1476.172	7697.389	799.3068	6482.097	649.4277	6142.051
Middle	1455.915	7684.354	798.1106	6510.848	603.5887	6104.833
Bottom	1476.172	7697.389	799.3068	6482.097	649.4277	6142.051

Table H.19: Power and thrust for a 7 diameter turbine for array 6

Array 6	Row 1		Row 2		Row 3	
	Power	Thrust	Power	Thrust	Power	Thrust
Outer	1461.497	7710.434	1068.726	6920.038	955.488	6628.907
Middle	1438.919	7702.606	1075.746	6942.311	957.9227	6614.394
Bottom	1461.497	7710.434	1068.726	6920.038	955.488	6628.907

Table H.20: Power and thrust for a 7 diameter turbine for array 7

Array 7	Row 1		Row 2		Row 3	
	Power	Thrust	Power	Thrust	Power	Thrust
Outer	1425.925	7702.606	1692.185	7757.489	1360.217	7313.707
Middle	1409.686	7647.917	1642.886	7723.49	1403.96	7161.975
Bottom	1451.537	7671.331	1579.278	7857.296	1447.574	7250.292

Table H.21: Power and thrust for a 7 diameter turbine for array 8

Array 8	Row 1		Row 2		Row 3	
	Power	Thrust	Power	Thrust	Power	Thrust
Outer	1425.923	7710.434	1465.884	7431.113	1305.073	7245.231
Middle	1397.09	7673.935	1417.21	7397.838	1212.532	6873.135
Bottom	1439.4	7689.567	1469.735	7689.567	1284.443	7014.322

Table H.22: Power and thrust for a 7 diameter turbine for array 9

Array 9	Row 1		Row 2		Row 3	
	Power	Thrust	Power	Thrust	Power	Thrust
Outer	1423.734	7715.655	1338.442	7252.823	1275.398	7219.951
Middle	1388.706	7689.567	1287.704	7227.53	1105.723	6735.823
Bottom	1434.605	7705.215	1418.715	7614.16	1193.516	6902.739

Table H.23: Power and thrust for a 7 diameter turbine for array 10

Array 10	Row 1		Row 2		Row 3	
	Power	Thrust	Power	Thrust	Power	Thrust
Outer	1235.345	7723.49	1738.634	8069.503	1394.304	7497.886
Middle	1458.78	7705.215	1718.075	8072.173	1505.532	7627.135
Bottom	1472.555	7702.606	1618.523	8021.51	1506.222	7616.754

Table H.24: Power and thrust for a 7 diameter turbine for array 11

Array 11	Row 1		Row 2		Row 3	
	Power	Thrust	Power	Thrust	Power	Thrust
Outer	1468.057	7726.103	1664.378	7907.439	1444.91	7567.543
Middle	1459.966	7718.267	1647.82	7907.439	1497.798	7572.716
Bottom	1475.835	7710.434	1585.364	7939.191	1517.702	7601.197

Table H.25: Power and thrust for a 7 diameter turbine for array 12

Array 12	Row 1		Row 2		Row 3	
	Power	Thrust	Power	Thrust	Power	Thrust
Outer	1344.507	7559.787	1167.761	6494.069	1002.815	6308.567
Middle	1347.499	7446.495	1138.396	6420.022	771.0372	5351.568
Bottom	1379.706	7533.964	1345.629	7202.281	832.8056	5693.931

Table H.26: Power and thrust for a 7 diameter turbine for array 13

Array 13	Row 1		Row 2		Row 3	
	Power	Thrust	Power	Thrust	Power	Thrust
Outer	1511.126	7720.878	1542.963	7627.135	1465.283	7541.706
Middle	1497.628	7723.49	1519.437	7621.944	1408.864	7339.151
Bottom	1517.139	7713.044	1560.448	7802.061	1450.739	7415.746

Table H.27: Power and thrust for a 6 diameter turbine for array 1

Array 1	Row 1		Row 2		Row 3	
	Power	Thrust	Power	Thrust	Power	Thrust
Outer	851.9479	5725.049	538.4292	5035.314	432.594	4710.572
Middle	825.0841	5676.527	555.684	4968.05	425.2067	4544.458
Bottom	851.9479	5725.049	538.4292	5035.314	432.594	4710.572

Table H.28: Power and thrust for a 6 diameter turbine for array 2

Array 2	Row 1		Row 2		Row 3	
	Power	Thrust	Power	Thrust	Power	Thrust
Outer	836.9505	5742.567	659.2803	5224.945	555.1241	4899.439
Middle	804.2292	5701.733	639.3157	5106.704	498.8674	4666.568
Bottom	836.9505	5742.567	659.2803	5224.945	555.1241	4899.439

Table H.29: Power and thrust for a 6 diameter turbine for array 3

Array 3	Row 1		Row 2		Row 3	
	Power	Thrust	Power	Thrust	Power	Thrust
Outer	827.0871	5750.361	692.2996	5292.05	593.0636	4978.927
Middle	792.2997	5715.328	643.2997	5136.137	510.9173	4717.631
Bottom	827.0871	5750.361	692.2996	5292.05	593.0636	4978.927

Table H.30: Power and thrust for a 6 diameter turbine for array 4

Array 4	Row 1		Row 2		Row 3	
	Power	Thrust	Power	Thrust	Power	Thrust
Outer	865.5336	5630.141	604.7276	4705.28	342.1328	3885.748
Middle	844.1169	5572.426	473.8544	4596.593	356.5814	4064.007
Bottom	865.5336	5630.141	604.7276	4705.28	342.1328	3885.748

Table H.31: Power and thrust for a 6 diameter turbine for array 5

Array 5	Row 1		Row 2		Row 3	
	Power	Thrust	Power	Thrust	Power	Thrust
Outer	894.5529	5769.87	515.0738	5070.031	424.182	4847.399
Middle	877.1039	5754.26	513.6926	5082.852	433.5387	4859.935
Bottom	894.5529	5769.87	515.0738	5070.031	424.182	4847.399

Table H.32: Power and thrust for a 6 diameter turbine for array 6

Array 6	Row 1		Row 2		Row 3	
	Power	Thrust	Power	Thrust	Power	Thrust
Outer	879.6634	5777.683	670.9204	5320.137	602.3543	5123.25
Middle	864.7329	5769.87	675.9812	5327.64	441.6417	5099.359
Bottom	879.6634	5777.683	670.9204	5320.137	602.3543	5123.25

Table H.33: Power and thrust for a 6 diameter turbine for array 7

Array 7	Row 1		Row 2		Row 3	
	Power	Thrust	Power	Thrust	Power	Thrust
Outer	856.1832	5767.918	1013.972	5730.885	504.3912	5126.93
Middle	847.1264	5728.939	985.1875	5715.328	853.29	5363.348
Bottom	879.149	5750.361	942.8598	5832.522	881.0358	5431.334

Table H.34: Power and thrust for a 6 diameter turbine for array 8

Array 8	Row 1		Row 2		Row 3	
	Power	Thrust	Power	Thrust	Power	Thrust
Outer	854.6942	5775.73	879.1831	5545.594	797.2733	5452.192
Middle	838.1907	5750.361	843.2124	5520.737	726.5804	5178.596
Bottom	867.8671	5764.014	877.8763	5734.778	773.2656	5278.969

Table H.35: Power and thrust for a 6 diameter turbine for array 9

Array 9	Row 1		Row 2		Row 3	
	Power	Thrust	Power	Thrust	Power	Thrust
Outer	854.2604	5781.592	802.7324	5454.091	765.6849	5433.228
Middle	828.3099	5758.161	769.0255	5429.439	660.9604	5097.523
Bottom	861.2594	5773.776	847.9215	5692.032	716.6635	5211.947

Table H.36: Power and thrust for a 6 diameter turbine for array 10

Array 10	Row 1		Row 2		Row 3	
	Power	Thrust	Power	Thrust	Power	Thrust
Outer	879.9332	5787.457	1052.3	5962.81	851.3639	5639.789
Middle	878.6848	5771.823	1033.398	5958.84	922.6915	5697.851
Bottom	890.8515	5771.823	969.3685	5942.977	923.8655	5690.092

Table H.37: Power and thrust for a 6 diameter turbine for array 11

Array 11	Row 1		Row 2		Row 3	
	Power	Thrust	Power	Thrust	Power	Thrust
Outer	881.9489	5791.369	1000.02	5852.17	868.1255	5661.044
Middle	877.5936	5781.592	982.4893	5848.238	902.3546	5633.999
Bottom	890.8273	5779.638	947.3185	5887.62	913.0937	5651.378

Table H.38: Power and thrust for a 6 diameter turbine for array 12

Array 12	Row 1		Row 2		Row 3	
	Power	Thrust	Power	Thrust	Power	Thrust
Outer	817.0373	5668.783	724.7669	4962.616	630.7086	4865.313
Middle	829.2211	5593.554	710.9727	4912.042	457.7602	4239.567
Bottom	844.2809	5653.31	811.2308	5404.844	525.2706	4458.227

Table H.39: Power and thrust for a 6 diameter turbine for array 13

Array 13	Row 1		Row 2		Row 3	
	Power	Thrust	Power	Thrust	Power	Thrust
Outer	882.6024	5795.282	894.731	5686.215	850.678	5643.651
Middle	871.3301	5793.325	876.6741	5680.401	815.0321	5490.22
Bottom	887.0618	5789.413	902.2397	5807.029	838.6972	5539.853

Table H.40: Power and thrust for a 4 diameter turbine for array 1

Array 1	Row 1		Row 2		Row 3	
	Power	Thrust	Power	Thrust	Power	Thrust
Outer	214.9805	2731.357	153.74	2553.675	125.4843	2449.057
Middle	209.697	2711.935	164.33	2518.856	126.4664	2376.78
Bottom	214.9805	2731.357	153.74	2553.675	125.4843	2449.057

Table H.41: Power and thrust for a 4 diameter turbine for array 2

Array 2	Row 1		Row 2		Row 3	
	Power	Thrust	Power	Thrust	Power	Thrust
Outer	228.2269	2739.702	175.9562	2594.148	151.1529	2489.58
Middle	200.9074	2723.025	173.1118	2543.83	136.1032	2401.91
Bottom	228.2269	2739.702	175.9562	2594.148	151.1529	2489.58

Table H.42: Power and thrust for a 4 diameter turbine for array 3

Array 3	Row 1		Row 2		Row 3	
	Power	Thrust	Power	Thrust	Power	Thrust
Outer	204.8842	2745.273	180.5359	2607.71	151.1529	2489.58
Middle	196.137	2729.505	166.2665	2547.408	135.4897	2414.96
Bottom	204.8842	2745.273	180.5359	2607.71	151.1529	2489.58

Table H.43: Power and thrust for a 4 diameter turbine for array 4

Array 4	Row 1		Row 2		Row 3	
	Power	Thrust	Power	Thrust	Power	Thrust
Outer	218.0462	2706.399	162.7387	2485.159	118.0489	2333.762
Middle	226.1683	2683.391	164.7599	2407.126	104.217	2216.237
Bottom	218.0462	2706.399	162.7387	2485.159	118.0489	2333.762

Table H.44: Power and thrust for a 4 diameter turbine for array 5

Array 5	Row 1		Row 2		Row 3	
	Power	Thrust	Power	Thrust	Power	Thrust
Outer	223.4437	2752.709	144.5741	2584.226	120.9629	2516.187
Middle	216.5647	2741.558	145.8997	2581.523	127.8329	2507.302
Bottom	223.4437	2752.709	144.5741	2584.226	120.9629	2516.187

Table H.45: Power and thrust for a 4 diameter turbine for array 6

Array 6	Row 1		Row 2		Row 3	
	Power	Thrust	Power	Thrust	Power	Thrust
Outer	217.123	2757.361	179.35	2642.225	162.5435	2577.921
Middle	211.1947	2748.989	181.7677	2634.94	164.5455	2553.675
Bottom	217.123	2757.361	179.35	2642.225	162.5435	2577.921

Table H.46: Power and thrust for a 4 diameter turbine for array 7

Array 7	Row 1		Row 2		Row 3	
	Power	Thrust	Power	Thrust	Power	Thrust
Outer	211.2694	2749.919	252.1257	2696.263	206.6088	2655.912
Middle	209.0336	2731.357	242.2004	2687.985	214.247	2579.721
Bottom	219.5345	2741.558	229.0391	2748.989	221.9465	2612.239

Table H.47: Power and thrust for a 4 diameter turbine for array 8

Array 8	Row 1		Row 2		Row 3	
	Power	Thrust	Power	Thrust	Power	Thrust
Outer	270.5701	2733.211	269.8764	2595.955	245.2517	2579.721
Middle	263.3875	2713.782	256.1472	2583.324	217.1696	2437.665
Bottom	276.7268	2725.801	273.3406	2694.423	235.5343	2489.58

Table H.48: Power and thrust for a 4 diameter turbine for array 9

Array 9	Row 1		Row 2		Row 3	
	Power	Thrust	Power	Thrust	Power	Thrust
Outer	269.5595	2736.919	248.0005	2574.322	238.5692	2572.523
Middle	259.4289	2720.25	235.6124	2562.642	199.6132	2419.318
Bottom	273.2609	2732.284	265.2416	2682.473	220.3982	2471.92

Table H.49: Power and thrust for a 4 diameter turbine for array 10

Array 10	Row 1		Row 2		Row 3	
	Power	Thrust	Power	Thrust	Power	Thrust
Outer	217.5835	2762.95	264.7179	2779.748	216.3943	2712.858
Middle	216.5863	2750.849	257.8452	2776.011	238.2573	2706.399
Bottom	221.3708	2754.569	237.942	2790.976	239.3144	2710.089

Table H.50: Power and thrust for a 4 diameter turbine for array 11

Array 11	Row 1		Row 2		Row 3	
	Power	Thrust	Power	Thrust	Power	Thrust
Outer	248.8242	2712.858	172.9371	2667.802	145.7958	2200.408
Middle	210.1468	2745.273	203.4847	2796.598	281.0535	2839.89
Bottom	210.8645	2773.209	218.9051	2825.737	232.0867	2809.739

Table H.51: Power and thrust for a 4 diameter turbine for array 12

Array 12	Row 1		Row 2		Row 3	
	Power	Thrust	Power	Thrust	Power	Thrust
Outer	211.0217	2710.089	193.0233	2480.742	171.028	2456.959
Middle	223.384	2684.31	194.1569	2462.234	130.0016	2264.907
Bottom	221.5291	2704.555	216.4014	2620.4	141.0826	2329.482

Table H.52: Power and thrust for a 4 diameter turbine for array 13

Array 13	Row 1		Row 2		Row 3	
	Power	Thrust	Power	Thrust	Power	Thrust
Outer	217.292	2768.543	217.8126	2703.633	207.1834	2699.026
Middle	212.3158	2762.95	210.1204	2699.026	195.0786	2628.574
Bottom	218.4879	2764.814	218.3106	2753.639	204.8719	2652.258

Table H.53: Power and thrust for a 3 diameter turbine for array 1

Array 1	Row 1		Row 2		Row 3	
	Power	Thrust	Power	Thrust	Power	Thrust
Outer	77.90252	1604.785	60.13489	1537.042	48.41532	1492.167
Middle	78.36483	1596.102	65.006	1517.955	48.9393	1456.746
Bottom	77.90252	1604.785	60.13489	1537.042	48.41532	1492.167

Table H.54: Power and thrust for a 3 diameter turbine for array 2

Array 2	Row 1		Row 2		Row 3	
	Power	Thrust	Power	Thrust	Power	Thrust
Outer	75.42742	1609.68	65.98842	1550.367	56.72202	1505.823
Middle	74.15649	1602.069	65.35465	1525.893	50.96058	1466.081
Bottom	75.42742	1609.68	65.98842	1550.367	56.72202	1505.823

Table H.55: Power and thrust for a 3 diameter turbine for array 3

Array 3	Row 1		Row 2		Row 3	
	Power	Thrust	Power	Thrust	Power	Thrust
Outer	73.76124	1612.947	66.17499	1554.643	57.79446	1511.092
Middle	77.02707	1605.329	61.52527	1528.014	49.90078	1472.32
Bottom	73.76124	1612.947	66.17499	1554.643	57.79446	1511.092

Table H.56: Power and thrust for a 3 diameter turbine for array 4

Array 4	Row 1		Row 2		Row 3	
	Power	Thrust	Power	Thrust	Power	Thrust
Outer	82.26439	1593.935	63.9994	1504.77	46.76609	1442.284
Middle	87.85932	1583.661	65.84675	1470.759	41.47086	1392.744
Bottom	82.26439	1593.935	63.9994	1504.77	46.76609	1442.284

Table H.57: Power and thrust for a 3 diameter turbine for array 5

Array 5	Row 1		Row 2		Row 3	
	Power	Thrust	Power	Thrust	Power	Thrust
Outer	79.8344	1616.218	55.02557	1555.178	46.88571	1526.953
Middle	77.72147	1610.224	56.66731	1550.901	49.6933	1517.426
Bottom	79.8344	1616.218	55.02557	1555.178	46.88571	1526.953

Table H.58: Power and thrust for a 3 diameter turbine for array 6

Array 6	Row 1		Row 2		Row 3	
	Power	Thrust	Power	Thrust	Power	Thrust
Outer	162.8025	1619.492	66.16657	1575.035	60.09552	1547.163
Middle	75.66339	1614.582	68.12228	1568.581	61.2181	1531.197
Bottom	162.8025	1619.492	66.16657	1575.035	60.09552	1547.163

Table H.59: Power and thrust for a 3 diameter turbine for array 7

Array 7	Row 1		Row 2		Row 3	
	Power	Thrust	Power	Thrust	Power	Thrust
Outer	75.20753	1614.582	90.40809	1582.581	74.0474	1571.806
Middle	76.12318	1605.329	86.2139	1577.728	76.39796	1531.728
Bottom	79.07823	1610.224	80.8545	1609.68	79.43188	1548.765

Table H.60: Power and thrust for a 3 diameter turbine for array 8

Array 8	Row 1		Row 2		Row 3	
	Power	Thrust	Power	Thrust	Power	Thrust
Outer	74.88098	1617.309	76.48137	1567.507	69.75585	1565.359
Middle	73.60786	1609.68	72.75057	1563.213	62.71066	1514.785
Bottom	77.02899	1614.582	75.51287	1602.069	68.31524	1533.852

Table H.61: Power and thrust for a 3 diameter turbine for array 9

Array 9	Row 1		Row 2		Row 3	
	Power	Thrust	Power	Thrust	Power	Thrust
Outer	73.58436	1618.946	71.01018	1563.749	67.88321	1563.213
Middle	70.7988	1612.947	67.2728	1559.461	57.81509	1511.619
Bottom	75.33798	1617.309	73.57552	1599.355	64.23447	1530.135

Table H.62: Power and thrust for a 3 diameter turbine for array 10

Array 10	Row 1		Row 2		Row 3	
	Power	Thrust	Power	Thrust	Power	Thrust
Outer	77.40363	1622.222	95.2201	1618.946	78.52917	1599.355
Middle	77.51042	1615.127	91.9836	1616.763	86.82307	1588.523
Bottom	78.98211	1617.309	84.63091	1629.881	87.06734	1592.852

Table H.63: Power and thrust for a 3 diameter turbine for array 11

Array 11	Row 1		Row 2		Row 3	
	Power	Thrust	Power	Thrust	Power	Thrust
Outer	76.99975	1623.315	86.3784	1604.242	76.09636	1595.56
Middle	75.82091	1617.854	84.06409	1602.612	78.01776	1571.806
Bottom	76.2523	1620.037	80.5944	1622.222	80.25268	1580.963

Table H.64: Power and thrust for a 3 diameter turbine for array 12

Array 12	Row 1		Row 2		Row 3	
	Power	Thrust	Power	Thrust	Power	Thrust
Outer	78.75716	1595.018	72.12586	1497.412	64.48724	1486.931
Middle	87.01651	1584.201	74.61929	1489.025	50.98758	1409.5
Bottom	83.97882	1592.852	80.98168	1553.573	51.93353	1435.081

Table H.65: Power and thrust for a 3 diameter turbine for array 13

Array 13	Row 1		Row 2		Row 3	
	Power	Thrust	Power	Thrust	Power	Thrust
Outer	76.6214	1624.955	76.33157	1591.228	73.19162	1591.228
Middle	75.08862	1621.676	73.56402	1589.605	68.03908	1556.783
Bottom	77.45722	1623.315	76.62726	1615.672	72.1474	1569,118

The average wake effect for a tidal cycle for array configuration 110 for a 6 and 8 diameter turbine.

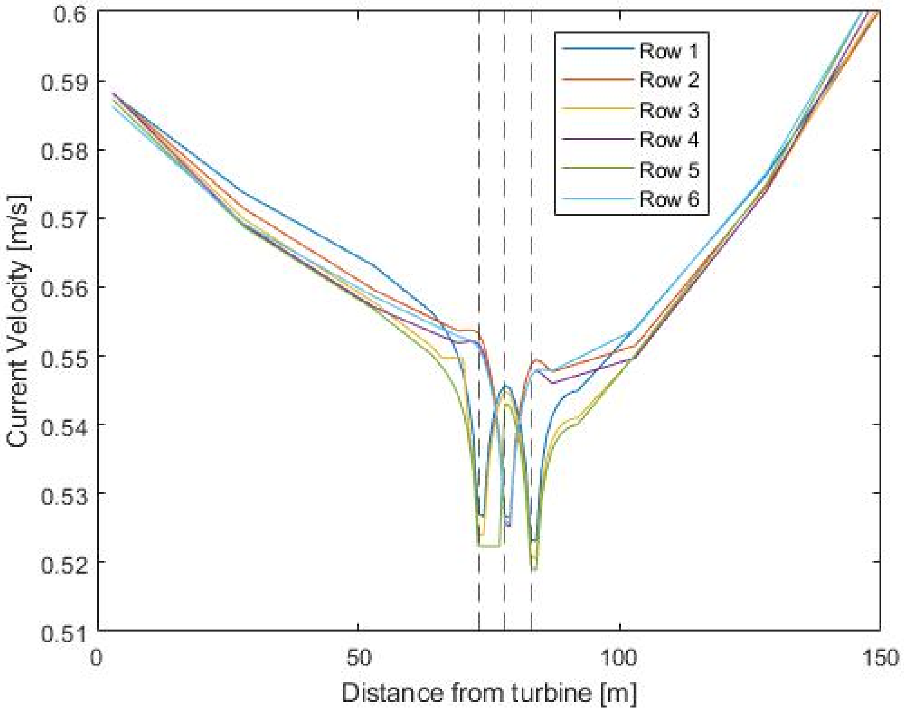

Figure H.1: The average wake effect for a tidal cycle for a 6 m turbine (velocity is in magnitude)

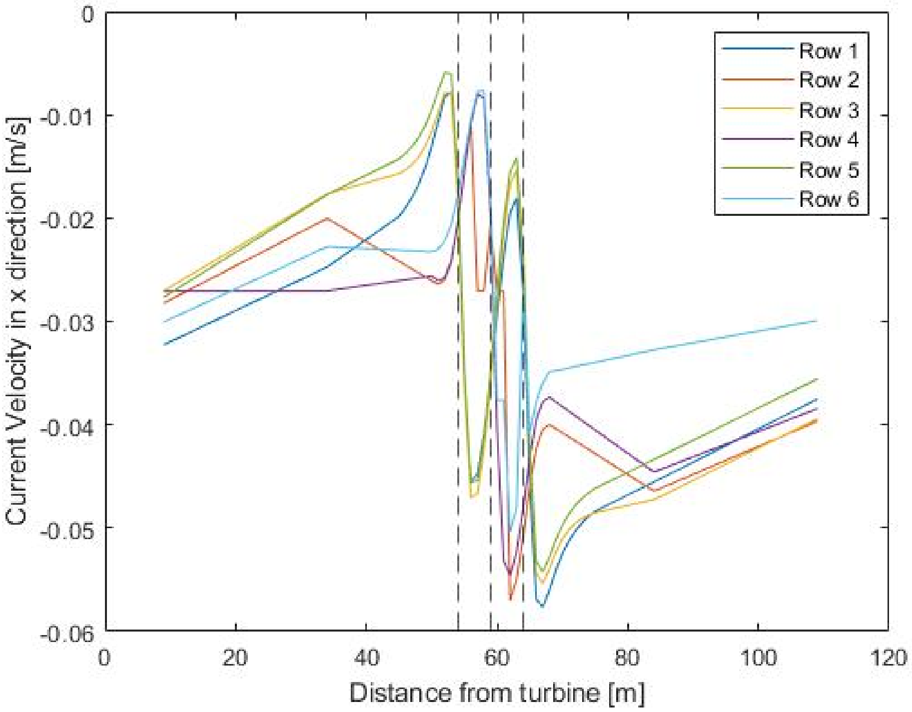

Figure H.2: The average wake effect for a tidal cycle for a 8 m turbine (velocity is x direction)

Bibliography

[1] M. L.S. Abundo, A. C. Nerves, M R. C.O. Ang, E. C. Paringit, L. P.C. Bernardo, and C. L. Villanoy. “Energy potential metric for rapid macro-level resource assessment of tidal in-stream energy in the Philippines”. In: *Date accessed: 31/03/2022.* Date accessed: 31/03/2022, 2011. ISBN: 9781424487820. DOI: 10.1109/EEEIC.2011.5874712. URL: https://www.researchgate.net/publication/224241697_Energy_potential_metric_for_rapid_macro-level_resource_assessment_of_tidal_in-stream_energy_in_the_Philippines.

[2] U. Ahmed, D. D. Apsley, I. Afgan, T. Stallard, and P. K. Stansby. “Fluctuating loads on a tidal turbine due to velocity shear and turbulence: Comparison of CFD with field data”. In: *Date accessed: 25/01/2022* 112 (Nov. 2017), pp. 235–246. ISSN: 0960-1481. DOI: 10.1016/J.RENENE.2017.05.048. URL: https://www.sciencedirect.com/science/article/pii/S0960148117304330.

[3] M.A. Almoghayer and D.K. Woolf. “An assessment of efficient tidal stream energy extraction using 3D numerical modelling techniques OceanFlux Greenhouse Gases View project Orkney: Grid connection and new futures scenario for Renewable development View project”. In: *Date accessed: 26/01/2022* (2019). URL: https://www.researchgate.net/publication/335620057.

[4] A. Angeloudis, S.C. Kramer, N. Hawkins, and M. D. Piggott. “On the potential of linked-basin tidal power plants: An operational and coastal modelling assessment”. In: *Date accessed: 17/11/2021* 155 (Aug. 2020), pp. 876–888. ISSN: 0960-1481. DOI: 10.1016/J.RENENE.2020.03.167. URL: https://www.sciencedirect.com/science/article/pii/S0960148120305000.

[5] Atlantis Resources. “AR1500 TIDAL TURBINE”. In: *Date accessed: 10/03/2022* (2022). URL: https://simecatlantis.com/wp-content/uploads/2016/08/AR1500-Brochure-Final-1.pdf.

[6] V Bagoãius, E.K. Zavadskas, and Z Turskis. “SEQUENCE DETERMINING OF CONSTRUCTION OF THE OFFSHORE WIND FARM CONSTRUCTION APPLYING PERMUTATION METHOD”. In: *Date accessed: 23/01/2022* (2014). DOI: 10.15240/tul/001/2014-3-005. URL: https://www.researchgate.net/publication/274905173_Sequence_determining_of_construction_of_the_offshore_wind_farm_construction_applying_permutation_method.

[7] S. Barbarelli, B. Nastasi, E. Rusu, and R. Bergillos. “Tides and Tidal Currents—Guidelines for Site and Energy Resource Assessment”. In: *Date accessed: 26/01/2022* 14.19 (Sept. 2021), p. 6123. ISSN: 19961073. DOI: 10.3390/EN14196123. URL: https://www.mdpi.com/1996-1073/14/19/6123/htm%20https://www.mdpi.com/1996-1073/14/19/6123.

[8] S. Baston, R. Harris, D. Kevin Woolf, J. Side, R. E. Harris, D. K. Woolf, R. A. Hiley, and J. C. Side. “Sensitivity Analysis of the Turbulence Closure Models in the Assessment of Tidal Energy Resource in Orkney”. In: *Date accessed: 16/08/2022* (2013). DOI: 10.13140/2.1.3033.3762. URL: https://www.researchgate.net/publication/270880690.

[9] S. Baston, S. M. Waldman, and J. Side. “Modelling energy extraction in tidal flows”. In: *Date accessed: 31/03/2022* (Oct. 2015). DOI: 10.13140/RG.2.1.4620.2481. URL: https://www.researchgate.net/publication/283008185.

[10] A. F. Blumberg and M. S. Bruno. “The Urban Ocean (The Interaction of Cities with Water) || Water Level Changes”. In: *Date accessed: 18/08/2022* (2018), pp. 52–71. DOI: 10.1017/9781108123839.007. URL: https://www.researchgate.net/publication/328222270_The_Urban_Ocean_The_Interaction_of_Cities_with_Water.

[11] A. Boretti. “State-of-the-art of MW-level capacity oceanic current turbines”. In: *Date accessed: 31/03/2022* 9.1 (Jan. 2020), pp. 361–369. ISSN: 21928029. DOI: 10.1515/NLENG-2020-0022/MACHINEREADABLECITATION/RIS. URL: https://www.degruyter.com/document/doi/10.1515/nleng-2020-0022/html?lang=en.

[12] T. Burton, D. Sharpe, N. Jenkins, and E. Bossanyi. *Wind Energy Handbook.* Vol. 2. Date accessed: 24/01/2022, 2001. Chap. 2, pp. 11–39. ISBN: 0471489972. URL: https://books.google.com/books/about/Wind_Energy_Handbook.html?id=4UYm893y-34C.

[13] *Catalogue Shom - Shom.* URL: `https://services.data.shom.fr/geonetwork/srv/dut/catalog.search#/metadata/MNT_ATL100m_HOMONIM_WGS84.xml`.

[14] A. Chaouachi, C. F. Covrig, and M. Ardelean. "Multi-criteria selection of offshore wind farms: Case study for the Baltic States". In: *Date accessed: 23/01/2022* 103 (Apr. 2017), pp. 179–192. ISSN: 0301-4215. DOI: `10.1016/J.ENPOL.2017.01.018`. URL: `https://www.sciencedirect.com/science/article/pii/S0301421517300186`.

[15] ChemicalParks EU. *Integrated chemical parks, sites and clusters in The Netherlands.* 2022. URL: `https://chemicalparks.eu/in/the-netherlands`.

[16] M S Chowdhury, K.S. Rahman, V. Selvanathan, Narissara N., M. Suklueng, A. Mostafaeipour, A. Habib, M. Akhtaruzzaman, N. Amin, and K. Techato. "Current trends and prospects of tidal energy technology". In: *Date accessed: 25/01/2022* 23 (Oct. 2020), pp. 8179–8194. DOI: `10.1007/s10668-020-01013-4`. URL: `https://doi.org/10.1007/s10668-020-01013-4`.

[17] Clarkson Research. *Average Draft by Containership Capacity | The Geography of Transport Systems.* 2022. URL: `https://transportgeography.org/contents/chapter5/maritime-transportation/draft-containership-capacity/`.

[18] CNES / LEGOS. / CLS. *FES2014 tide model - CLS Datastore: Ocean and water.* 2022. URL: `https://datastore.cls.fr/catalogues/fes2014-tide-model/`.

[19] D. S. Coles, L. S. Blunden, and A. S. Bahaj. "Assessment of the energy extraction potential at tidal sites around the Channel Islands". In: *Date accessed: 25/01/2022* 124 (Apr. 2017), pp. 171–186. ISSN: 0360-5442. DOI: `10.1016/J.ENERGY.2017.02.023`. URL: `https://www.sciencedirect.com/science/article/pii/S0360544217301974#:~:text=Estimates%20for%20upper%20bound%20energy,Big%20Roussel%20(0.24%20GW)..`

[20] Zafer Defne, K. A. Haas, and M. F. Hermann. "GIS based multi-criteria assessment of tidal stream power potential: A case study for Georgia, USA". In: *Date accessed: 25/05/2022* 15.5 (2011), pp. 2310–2321. ISSN: 13640321. DOI: `10.1016/J.RSER.2011.02.005`. URL: `https://www.sciencedirect.com/science/article/pii/S1364032111000475`.

[21] Deltaress. *Home - Delft3D - oss.deltares.nl.* 2011. URL: `https://oss.deltares.nl/web/delft3d`.

[22] E. Denny. "The economics of tidal energy". In: *Date accessed: 23/01/2022* 37.5 (May 2009), pp. 1914–1924. ISSN: 0301-4215. DOI: `10.1016/J.ENPOL.2009.01.009`. URL: `https://www.sciencedirect.com/science/article/pii/S0301421509000408`.

[23] INC. DEVINE TARBELL & ASSOCIATES. *INSTREAM TIDAL POWER IN NORTH AMERICA ENVIRONMENTAL AND PERMITTING ISSUES.* Tech. rep. Date accessed: 25/05/2022, 2006. URL: `https://tethys.pnnl.gov/publications/instream-tidal-power-north-america-environmental-permitting-issues`.

[24] DHI technologies. *MIKE 21.* 2022. URL: `https://www.mikepoweredbydhi.com/products/mike-21-3`.

[25] H. Díaz and C. Guedes Soares. "A novel multi-criteria decision-making model to evaluate floating wind farm locations". In: *Date accessed: 23/01/2022* 185 (Feb. 2022), pp. 431–454. ISSN: 0960-1481. DOI: `10.1016/J.RENENE.2021.12.014`. URL: `https://linkinghub.elsevier.com/retrieve/pii/S0960148121017341`.

[26] S. Draper and T. Nishino. "Centred and staggered arrangements of tidal turbines". In: *Date accessed: 26/01/2022* 739 (2014), pp. 72–93. ISSN: 0022-1120. DOI: `10.1017/JFM.2013.593`. URL: `https://www.cambridge.org/core/journals/journal-of-fluid-mechanics/article/abs/centred-and-staggered-arrangements-of-tidal-turbines/23C65EF84C8299775161BD972BB18147`.

[27] G. D. Egbert, A. F. Bennett, and M. G.G. Foreman. "TOPEX/POSEIDON tides estimated using a global inverse model". In: *Date accessed: 31/03/2022* 99.C12 (1994). ISSN: 01480227. DOI: `10.1029/94jc01894`. URL: `https://www.researchgate.net/publication/24157720_TOPEXPoseidon_tides_estimated_using_a_global_inverse_model_J_of_Geoph_Res_99C1224821-24852`.

[28] G.D. Egbert and L. Erofeeva. "Efficient Inverse Modeling of Barotropic Ocean Tides". In: *Journal of Atmospheric and Oceanic Technology* 19.2 (2002), pp. 183–204. URL: `https://www.tpxo.net/tpxo-products-and-registration`.

[29] G.D. Egbert, S.Y. Erofeeva, and R.D. Ray. “Assimilation of altimetry data for nonlinear shallow-water tides: Quarter-diurnal tides of the Northwest European Shelf”. In: *Date accessed: 25/01/2022* 30.6 (Apr. 2010), pp. 668–679. ISSN: 0278-4343. DOI: `10.1016/J.CSR.2009.10.011`. URL: `https://www.sciencedirect.com/science/article/pii/S0278434309003094`.

[30] ELECTRICITE DE FRANCE. *open TELEMAC-MASCARET*. 2022. URL: `https://opentelemac.org/`.

[31] European Commission. *Data Portals Overview | European Marine Observation and Data Network (EMODnet)*. 2022. URL: `https://emodnet.ec.europa.eu/en/portals`.

[32] Exchange rates. *British Pound (GBP) to Euro (EUR) exchange rate history*. 2022. URL: `https://www.exchangerates.org.uk/GBP-EUR-exchange-rate-history.html`.

[33] E. Fakhri, J. Thiébot, H. Gualous, M. Machmoum, and S. Bourguet. “Overall tidal farm optimal design–Application to the Alderney Race and the Fromveur Strait (France)”. In: *Date accessed: 17/02/2022* 106 (Jan. 2021), p. 102444. ISSN: 0141-1187. DOI: `10.1016/J.APOR.2020.102444`. URL: `https://www.researchgate.net/publication/347170474_Overall_tidal_farm_optimal_design-Application_to_the_Alderney_Race_and_the_Fromveur_Strait_France`.

[34] N. Filianie Aziz, S. Sorooshian, and F. Mahmud. “MCDM-AHP METHOD IN DECISION MAKINGS”. In: *Date accessed: 23/01/2022* 11.11 (2016). ISSN: 1819-6608. URL: `www.arpnjournals.com`.

[35] S. W. Funke, P. E. Farrell, and M. D. Piggott. “Tidal turbine array optimisation using the adjoint approach”. In: *Date accessed: 26/01/2022* 63 (Mar. 2014), pp. 658–673. ISSN: 0960-1481. DOI: `10.1016/J.RENENE.2013.09.031`. URL: `https://www.sciencedirect.com/science/article/pii/S0960148113004989+`.

[36] L Gavériaux, G Laverrière, T Wang, N Maslov, and C Claramunt. “GIS-based multi-criteria analysis for offshore wind turbine deployment in Hong Kong”. In: *Date accessed: 23/05/2022* (2019). ISSN: 1947-5691. DOI: `10.1080/19475683.2019.1618393`. URL: `https://www.tandfonline.com/action/journalInformation?journalCode=tagi20`.

[37] GGS. *EMODnet Bathymetry Viewing and Download service*. Jan. 2021. URL: `https://portal.emodnet-bathymetry.eu/`.

[38] I. C. Gil-García, A. Ramos-Escudero, M. S. García-Cascales, H. Dagher, and A. Molina-García. “Fuzzy GIS-based MCDM solution for the optimal offshore wind site selection: The Gulf of Maine case”. In: *Date accessed: 23/01/2022* 183 (Jan. 2022), pp. 130–147. ISSN: 0960-1481. DOI: `10.1016/J.RENENE.2021.10.058`. URL: `https://www.sciencedirect.com/science/article/pii/S0960148121015172`.

[39] Z Goss, S Warder, A Angeloudis, S C Kramer, A Avdis, and M D Piggott. “Tidal modelling with Thetis: preliminary English Channel benchmarking”. In: *Date accessed: 17/11/2021* (2019). URL: `http://thetisproject.org/2https://www.firedrakeproject.org/3viathehttp://pyadjoint.readthedocs.io/library4http://opentidalfarm.readthedocs.io/5https://github.com/meshadaptation/pragmatic`.

[40] Z L Goss, D S Coles, and M D Piggott. “Economic analysis of tidal stream turbine arrays: a review”. In: *Date accessed: 18/08/2022* (2021). URL: `https://arxiv.org/abs/2105.04718`.

[41] Z L Goss, D S Coles, and M D Piggott. “Identifying economically viable tidal sites within the Alderney Race through optimization of levelized cost of energy”. In: *Date accessed: 26/01/2022* (June 2020). DOI: `10.1098/rsta.2019.0500`. URL: `https://royalsocietypublishing.org/doi/10.1098/rsta.2019.0500`.

[42] Z. L. Goss, D. S. Coles, S. C. Kramer, and M. D. Piggott. “Efficient economic optimisation of large-scale tidal stream arrays”. In: *Date accessed: 18/08/2022* 295 (Aug. 2021). ISSN: 03062619. DOI: `10.1016/J.APENERGY.2021.116975`. URL: `https://www.sciencedirect.com/science/article/pii/S0306261921004475`.

[43] M. Grabbe, E. Lalander, S. Lundin, and M. Leijon. “A review of the tidal current energy resource in Norway”. In: *Date accessed: 26/01/2022* 13.8 (Oct. 2009), pp. 1898–1909. ISSN: 1364-0321. DOI: `10.1016/J.RSER.2009.01.026`. URL: `https://www.sciencedirect.com/science/article/pii/S136403210900032X`.

[44] D. Ham and P. Kelly. *The Firedrake project*. 2022. URL: `https://www.firedrakeproject.org/`.

[45] T J Hammons. “Tidal Power in the UK and Worldwide to Reduce Greenhouse Gas Emissions”. In: *Date accessed: 23/01/2022* 3.2 (2011). URL: `www.intechopen.com`.

[46] T.J. HAMMONS. “Tidal Power ”. In: *Date accessed: 19/01/2022* 81.3 (Mar. 1993), pp. 419–433. URL: `https://ieeexplore.ieee.org/document/241486`.

[47] F. Harcourt, A. Angeloudis, and M.D. Piggott. “Utilising the flexible generation potential of tidal range power plants to optimise economic value | Elsevier Enhanced Reader”. In: *Date accessed: 17/11/2021* (Jan. 2019), pp. 873–884. URL: `https://www.sciencedirect.com/science/article/abs/pii/S0306261918319093`.

[48] M. E. Harrison, W. M.J. Batten, L. E. Myers, and A. S. Bahaj. “Comparison between CFD simulations and experiments for predicting the far wake of horizontal axis tidal turbines”. In: *Date accessed: 24/01/2022* 4.6 (Nov. 2010), pp. 613–627. ISSN: 17521416. DOI: `10.1049/IET-RPG.2009.0193/CITE/REFWORKS`. URL: `https://www.researchgate.net/publication/224189174_Comparison_between_CFD_simulations_and_experiments_for_predicting_the_far_wake_of_horizontal_axis_tidal_turbines`.

[49] D. Haverson, J. Bacon, and H. Smith. “Modelling the far field impacts of a tidal energy development at Ramsey Sound”. In: *Date accessed: 24/01/2022* (2014), pp. 119–124. URL: `https://henry.baw.de/handle/20.500.11970/104261`.

[50] T. Höfer, Y. Sunak, H. Siddique, and R. Madlener. “Wind farm siting using a spatial Analytic Hierarchy Process approach: A case study of the Städteregion Aachen”. In: *Date accessed: 25/05/2022* 163 (Feb. 2016), pp. 222–243. ISSN: 03062619. DOI: `10.1016/J.APENERGY.2015.10.138`. URL: `https://www.sciencedirect.com/science/article/pii/S030626191501380X`.

[51] Institute for Maritime and Inland Waterways. *Fudaa*. Oct. 2014. URL: `https://sourceforge.net/projects/fudaa/files/prepro/`.

[52] International Hydrographic Organization(IHO). *GEBCO*. 2022. URL: `https://download.gebco.net/`.

[53] A. Joly, C. Pham, M. Andreewsky, S. Saviot, and L. Fillot. “Using the DRAGFO subroutine to model Tidal Energy Converters in Telemac-2D”. In: *Date accessed: 17/08/2022* (Oct. 2015). URL: `https://hal.archives-ouvertes.fr/hal-01702806%20https://hal.archives-ouvertes.fr/hal-01702806/document`.

[54] S.C. Kramer and M.D. Piggott. “A correction to the enhanced bottom drag parameterisation of tidal turbines | Elsevier Enhanced Reader”. In: *Date accessed: 17/11/2021* (Feb. 2016), pp. 387–396. URL: `https://www.sciencedirect.com/science/article/pii/S0960148116301239`.

[55] M. Lewis, R. O’Hara Murray, S. Fredriksson, J. Maskell, A. de Fockert, S. P. Neill, and P. E. Robins. “A standardised tidal-stream power curve, optimised for the global resource”. In: *Date accessed: 31/03/2022* 170 (June 2021), pp. 1308–1323. ISSN: 18790682. DOI: `10.1016/j.renene.2021.02.032`. URL: `https://www.sciencedirect.com/science/article/pii/S0960148121001993`.

[56] O. A. Lo Brutto, V. T. Nguyen, S. S. Guillou, J. Thiébot, and H. Gualous. “Tidal farm analysis using an analytical model for the flow velocity prediction in the wake of a tidal turbine with small diameter to depth ratio”. In: *Date accessed: 17/02/2022* 99 (Dec. 2016), pp. 347–359. ISSN: 0960-1481. DOI: `10.1016/J.RENENE.2016.07.020`. URL: `https://www.sciencedirect.com/science/article/pii/S0960148116306164`.

[57] O. A. Lo Brutto, J. Thiébot, S. S. Guillou, and H. Gualous. “A semi-analytic method to optimize tidal farm layouts – Application to the Alderney Race (Raz Blanchard), France”. In: *Date accessed: 17/02/2022* 183 (Dec. 2016), pp. 1168–1180. ISSN: 0306-2619. DOI: `10.1016/J.APENERGY.2016.09.059`. URL: `https://www.sciencedirect.com/science/article/pii/S0306261916313617`.

[58] L. Mackie, D. Coles, M. Piggott, and A. Angeloudis. “The Potential for Tidal Range Energy Systems to Provide Continuous Power: A UK Case Study”. In: *Date accessed: 17/11/2021* (Oct. 2020), pp. 1–23. URL: `https://www.mdpi.com/2077-1312/8/10/780`.

[59] A. D. Mekonnen and P. V. Gorsevski. “A web-based participatory GIS (PGIS) for offshore wind farm suitability within Lake Erie, Ohio”. In: *Date accessed: 25/05/2022* 41 (2015), pp. 162–177. ISSN: 13640321. DOI: `10.1016/J.RSER.2014.08.030`. URL: `https://www.sciencedirect.com/science/article/pii/S1364032114007060`.

[60] F.R. Menter. "Review of the shear-stress transport turbulence model experience from an industrial perspective". In: *Date accessed: 24/01/2022* (May 2009), pp. 305–316. URL: `https://www.tandfonline.com/doi/abs/10.1080/10618560902773387`.

[61] Michel J., Dunagan H., Boring C., Healy E., Evans W., Dean J.M., McGillis A., and Hain J. *Worldwide Synthesis and Analysis of Existing Information Regarding Environmental Effects of Alternative Energy Uses on the Outer Continental Shelf.* Tech. rep. Date accessed: 25/05/2022, June 2007. URL: `https://tethys.pnnl.gov/sites/default/files/publications/Worldwide_Synthesis_and_Analysis_of_MHK.pdf`.

[62] P. Milan, M. Wächter, S. Barth, and J. Peinke. "CHAPTER 18 Power curves for wind turbines". In: *Date accessed: 31/03/2022* (2010). DOI: `10.2495/978-1-84564-/205-1`. URL: `www.witpress.com,`.

[63] Ministerie van Infrastructuur en Waterstaat, Natuur en Voedselveiligheid Ministerie van Landbouw, Ministerie van Economische Zaken en Klimaat, and Ministerie van Binnenlandse Zaken en Koninkrijksrelaties. *Programma Noordzee 2022-2027 - Noordzeeloket.* 2022. URL: `https://www.noordzeeloket.nl/beleid/programma-noordzee-2022-2027/`.

[64] B. Muhtar and M. M. A. Albayati. "Determination Of Chezys And Mannings Coefficient For Different Aggregate Bed Using Different Notches In Hydraulic Bench". In: *Date accessed: 16/08/2022* 5.03 (2016). ISSN: 2277-8616. URL: `www.ijstr.org`.

[65] J. Murphy, K. Lynch, L. Serri, D. Airdoldi, and M. Lopes. "Site Selection Analysis For Offshore Combined Resource Projects in Europe". In: *Date accessed: 25/05/2022* (2011). URL: `http://orecca.rse-web.it/doc_info/Site_Selection_Analysis_Report.pdf`.

[66] L. E. Myers and A. S. Bahaj. "Experimental analysis of the flow field around horizontal axis tidal turbines by use of scale mesh disk rotor simulators". In: *Date accessed: 24/01/2022* 37.2-3 (Feb. 2010), pp. 218–227. ISSN: 0029-8018. DOI: `10.1016/J.OCEANENG.2009.11.004`. URL: `https://www.sciencedirect.com/science/article/pii/S0029801809002613`.

[67] National Research Council Canada. *Blue Kenue™: software tool for hydraulic modellers.* 2022. URL: `https://nrc.canada.ca/en/research-development/products-services/software-applications/blue-kenuetm-software-tool-hydraulic-modellers`.

[68] S.P. Neill, A. Angeloudis, P. E. Robins, I. Walkington, S.L. Ward, I. Masters, M.J. Lewis, M. Piano, A. Avdis, M. D. Piggott, G. Aggidis, P. Evans, T.A.A. Adcock, A. Židonis, R. Ahmadian, and R. Falconer. "Tidal range energy resource and optimization – Past perspectives and future challenges". In: *Date accessed: 17/11/2021* 127 (Nov. 2018), pp. 763–778. ISSN: 0960-1481. DOI: `10.1016/J.RENENE.2018.05.007`. URL: `https://www.researchgate.net/publication/324910310_Tidal_range_energy_resource_and_optimization_-_past_perspectives_and_future_challenges`.

[69] Simon P. Neill and M. Reza Hashemi. "Offshore Wind". In: *Fundamentals of Ocean Renewable Energy.* Elsevier, 2018, pp. 83–106. DOI: `10.1016/b978-0-12-810448-4.00004-5`. URL: `https://www.elsevier.com/books/fundamentals-of-ocean-renewable-energy/neill/978-0-12-810448-4`.

[70] Q. D. Nguyen and C. Lei. "Hydrodynamic characteristics of a confined circular cylinder in cross-flows". In: *Date accessed: 03/08/2022* 221 (Feb. 2021), p. 108567. ISSN: 0029-8018. DOI: `10.1016/J.OCEANENG.2021.108567`. URL: `https://www.sciencedirect.com/science/article/pii/S0029801821000020`.

[71] V. Nguyen. "An arbitrary Lagrangian–Eulerian discontinuous Galerkin method for simulations of flows over variable geometries | Elsevier Enhanced Reader". In: *Date accessed: 21/10/2021* (2021). URL: `https://www.sciencedirect.com/science/article/abs/pii/S0889974609001315`.

[72] V. Nguyên, A. S. Cruz, S. Guillou, M. S. Elsouk, J. Thiebot, J. T. Effects, V. T. Nguyen, A. Santa Cruz, S. S. Guillou, M. N. Shiekh Elsouk, and Jérôme Thiébot. "Effects of the Current Direction on the Energy Production of a Tidal Farm: The Case of Raz Blanchard (France)". In: *Date accessed: 17/02/2022* 12.13 (2019). DOI: `10.3390/en12132478{\"{i}}`. URL: `www.mdpi.com/journal/energies`.

[73] Nova Innovation. *Products - Nova Innovation.* 2022. URL: `https://www.novainnovation.com/products/`.

[74] M. O'Connor and B. Holmes. *Equitable Testing and Evaluation of Marine Energy Extraction Device, Protocols for wave and tidal resource assessments in terms of Performance, Cost and Environmental Impact*. Tech. rep. COMMISSION OF THE EUROPEAN COMMUNITIES: EquiMAr, Dec. 2010. URL: https://tethys.pnnl.gov/sites/default/files/publications/EquiMar_D4.3.pdf.

[75] P. Ouro, L. Ramírez, and M. Harrold. "Analysis of array spacing on tidal stream turbine farm performance using Large-Eddy Simulation". In: *Journal of Fluids and Structures* 91 (Nov. 2019), p. 102732. ISSN: 0889-9746. DOI: 10.1016/J.JFLUIDSTRUCTS.2019.102732. URL: https://www.sciencedirect.com/science/article/pii/S0889974619301161.

[76] S. Pennock, A. Garcia-Teruel, D.R. Noble, O. Roberts, A. de Andres, C. Cochrane, and H. Jeffrey. "Deriving Current Cost Requirements from Future Targets: Case Studies for Emerging Offshore Renewable Energy Technologies". In: *Date accessed: 28/08/2022* 15 (Feb. 20222). DOI: https://doi.org/10.3390/en15051732. URL: https://www.mdpi.com/1996-1073/15/5/1732/pdf.

[77] A. Perez Ortiz, J. Pescatore, and I. Bryden. "A Systematic Approach to Undertake Tidal Energy Resource Assessment with Telemac-2D". In: (2013). URL: https://www.researchgate.net/publication/257416284.

[78] A. Perez-Ortiz, A.G.L. Borthwick, J. McNaughton, and A. Avdis. "Characterization of the tidal resource in Rathlin Sound | Elsevier Enhanced Reader". In: *Date accessed: 17/11/2021* (2017), pp. 229–243. URL: https://www.sciencedirect.com/science/article/pii/S0960148117303336.

[79] A. Pérez-Ortiz, A.G.L. Borthwick, J. McNaughton, H.C.M. Smith, and Q. Xiao. "Resource characterization of sites in the vicinity of an island near a landmass". In: *Date accessed: 25/01/2022* 103 (Apr. 2017), pp. 265–276. ISSN: 0960-1481. DOI: 10.1016/J.RENENE.2016.10.086. URL: https://www.sciencedirect.com/science/article/pii/S0960148116309740.

[80] C. Pham and V.A Martin. "Tidal current turbine demonstration farm in Paimpol-Bréhat (Brittany): tidal characterisation and energy yield evaluation with Telemac". In: *Date accessed: 26/01/2022* (2007). URL: http://www.homepages.ed.ac.uk/shs/Wave%20Energy/EWTEC%202009/EWTEC%202009%20(D)/papers/163.pdf.

[81] M. Piano, S. Ward, P. Robins, S. Neill, M. Lewis, A. Davies, B. Powell, W. Owen, and R. Hashemi. "Characterizing the tidal energy resource of the West Anglesey Demonstration Zone (UK), using TELEMAC-2D and field observations". In: *Date accessed: 26/01/2022* (Oct. 2015), pp. 195–203. URL: https://hdl.handle.net/20.500.11970/104333.

[82] Pricewise. *kWh-prijs 2022 | Alles over de prijs per kilowattuur | Pricewise*. 2022. URL: https://www.pricewise.nl/energieprijzen/kwh-prijs/.

[83] Princeton University. *ThePrincetonOceanModel*. 1996. URL: http://www.ccpo.odu.edu/POMWEB/.

[84] A. Rahman, V. Venugopal, and J. Thiebot. "On the Accuracy of Three-Dimensional Actuator Disc Approach in Modelling a Large-Scale Tidal Turbine in a Simple Channel". In: *Date accessed: 17/11/2021* 11.8 (Aug. 2018), p. 2151. ISSN: 19961073. DOI: 10.3390/EN11082151. URL: https://www.mdpi.com/1996-1073/11/8/2151.

[85] S. Ramos, H. Díaz, C. Guedes Soares, and G Lavidas. "Identifying compatible locations for wave energy exploration with different wave energy devices in Madeira Islands". In: *Date accessed: 26/08/2022* (2021), pp. 111–122. DOI: 10.1201/9781003134572-15. URL: https://www.researchgate.net/publication/344668115_Identifying_compatible_locations_for_wave_energy_exploration_with_different_wave_energy_devices_in_Madeira_Islands.

[86] V. Ramos, R. Carballo, and John V. Ringwood. "Application of the actuator disc theory of Delft3D-FLOW to model far-field hydrodynamic impacts of tidal turbines". In: *Date accessed: 26/01/2022* 139 (Aug. 2019), pp. 1320–1335. ISSN: 0960-1481. DOI: 10.1016/J.RENENE.2019.02.094. URL: https://www.sciencedirect.com/science/article/pii/S0960148119302484.

[87] V. Ramos and J.V. Ringwood. "Implementation and evaluation of the International Electrotechnical Commission specification for tidal stream energy resource assessment: A case study". In: *Ramos* 127 (Aug. 2016), pp. 65–79. DOI: 10.1016/j.enconman.2016.08.078. URL: http://dx.doi.org/10.1016/j.enconman.2016.08.078.

[88] Rijkswaterstaat. *Waterbeheer (Expert) - Rijkswaterstaat Waterinfo.* 2022. URL: `https://waterinfo.rws.nl/#!/kaart/Waterbeheer/`.

[89] F. O. Rourke, F. Boyle, and A. Reynolds. “Tidal energy update 2009”. In: *Date accessed: 23/01/2022* 87.2 (Feb. 2010), pp. 398–409. ISSN: 0306-2619. DOI: `10.1016/J.APENERGY.2009.08.014`. URL: `https://www.sciencedirect.com/science/article/pii/S030626190900347X`.

[90] T. L. Saaty and L. T. Tran. “On the invalidity of fuzzifying numerical judgments in the Analytic Hierarchy Process”. In: *Date accessed: 23/01/2022* 46.7-8 (Oct. 2007), pp. 962–975. ISSN: 0895-7177. DOI: `10.1016/J.MCM.2007.03.022`. URL: `https://www.sciencedirect.com/science/article/pii/S0895717707000787`.

[91] T.L. Saaty. “Decision making with the analytic hierarchy process”. In: *Date accessed: 23/01/2022* 1 (Mar. 2008). ISSN: 1753-6219. DOI: `10.1504/IJBEM.2016.073386`. URL: `https://www.sid.ir/en/Journal/ViewPaper.aspx?ID=88399`.

[92] S. Sánchez, J. López-Gutiérrez, V. Negro, and M. D. Esteban. “Foundations in Offshore Wind Farms: Evolution, Characteristics and Range of Use. Analysis of Main Dimensional Parameters in Monopile Foundations”. In: *Date accessed: 21/10/2021* 7.12 (Dec. 2019), p. 441. DOI: `10.3390/JMSE7120441`. URL: `https://www.mdpi.com/2077-1312/7/12/441/htm%20https://www.mdpi.com/2077-1312/7/12/441`.

[93] S. Schmitz. *The Actuator Disk Model.* 2020. URL: `https://www.e-education.psu.edu/aersp583/node/470`.

[94] E. Segura, R. Morales, and J. A. Somolinos. “Cost assessment methodology and economic viability of tidal energy projects”. In: *Date accessed: 24/08/2022* 10.11 (Nov. 2017). ISSN: 19961073. DOI: `10.3390/en10111806`. URL: `https://www.mdpi.com/1996-1073/10/11/1806`.

[95] M. Shives and C. Crawford. “Adapted two-equation turbulence closures for actuator disk RANS simulations of wind & tidal turbine wakes”. In: *Date accessed: 24/01/2022* 92 (July 2016), pp. 273–292. ISSN: 0960-1481. DOI: `10.1016/J.RENENE.2016.02.026`. URL: `https://www.sciencedirect.com/science/article/pii/S0960148116301276`.

[96] M. Shives and C. Crawford. “Tuned actuator disk approach for predicting tidal turbine performance with wake interaction”. In: *Date accessed: 24/01/2022* 17 (Apr. 2017), pp. 1–20. ISSN: 2214-1669. DOI: `10.1016/J.IJOME.2016.11.001`. URL: `https://www.sciencedirect.com/science/article/pii/S2214166916300686`.

[97] G. Smart and M. Noonan. *TIDAL STREAM AND WAVE ENERGY COST REDUCTION AND INDUSTRIAL BENEFIT.* Tech. rep. Date accessed:09/09/2022, Apr. 2018. URL: `https://www.marineenergywales.co.uk/wp-content/uploads/2018/05/ORE-Catapult-Tidal-Stream-and-Wave-Energy-Cost-Reduction-and-Ind-Benefit-FINAL-v03.02.pdf`.

[98] Solar Feeds. *Energy Sources of the Future - SF Magazine.* Jan. 2014. URL: `https://www.solarfeeds.com/mag/energy-sources-future/`.

[99] M. J. Suárez-López, R. Espina-Valdés, V. M. F. Pacheco, A. N. Manso, E. Blanco-Marigorta, and E. Álvarez-Álvarez. “A Review of Software Tools to Study the Energetic Potential of Tidal Currents”. In: *Date accessed: 15/08/2022* 12.9 (May 2019), p. 1673. ISSN: 1996-1073. DOI: `10.3390/EN12091673`. URL: `https://www.mdpi.com/1996-1073/12/9/1673/htm%20https://www.mdpi.com/1996-1073/12/9/1673`.

[100] Tenet. *Our high-voltage grid - TenneT.* 2022. URL: `https://www.tennet.eu/our-grid/our-high-voltage-grid/our-high-voltage-grid/`.

[101] J. Thiébot, N. Guillou, S. Guillou, A. Good, and M. Lewis. “Wake field study of tidal turbines under realistic flow conditions”. In: *Date accessed: 02/08/2022* 151 (May 2020), pp. 1196–1208. ISSN: 0960-1481. DOI: `10.1016/J.RENENE.2019.11.129`. URL: `https://www.sciencedirect.com/science/article/abs/pii/S0960148119318233`.

[102] J. Thiébot, N. Guillou, S. Guillou, A. Good, and M. Lewix. “Wake field study of tidal turbines under realistic flow conditions | Elsevier Enhanced Reader”. In: *Date accessed: 17/11/2021* (Oct. 2019), pp. 1196–1208. URL: `https://www.sciencedirect.com/science/article/abs/pii/S0960148119318233`.

[103] J. Thiébot, S Guillou, and V.T. Nguyen. “Modelling the effect of large arrays of tidal turbines with depth-averaged Actuator Disks”. In: *Date accessed: 24/01/2022* 126 (Nov. 2016), pp. 265–275. ISSN: 0029-8018. DOI: `10.1016/J.OCEANENG.2016.09.021`. URL: `https://www.sciencedirect.com/science/article/pii/S0029801816303985`.

[104] N. E. Turner and A. Owen. “The development of a tidal turbine for deployment in areas with slow moving tidal flows”. In: *Date accessed: 25/05/2022* (2007). DOI: `10.1109/OCEANSE.2007.4302428`. URL: `https://ieeexplore.ieee.org/document/4302428`.

[105] D. G. Vagiona and M. Kamilakis. “Sustainable Site Selection for Offshore Wind Farms in the South Aegean-Greece”. In: *Date accessed: 23/01/2022* (2018). DOI: `10.3390/su10030749`. URL: `www.mdpi.com/journal/sustainability`.

[106] D.G. VAGIONA and N.M. KARANIKOLAS. “A multicriteria approach to evaluate offshore wind farms siting in Greece”. In: *Date accessed: 23/01/2022* 14.2 (Mar. 2012), pp. 235–243. URL: `https://www.researchgate.net/publication/237051895_A_multicriteria_approach_to_evaluate_offshore_wind_farms_siting_in_Greece`.

[107] R. Vennell, S.W. Funke, S. Draper, C. Stevens, and T. Divett. “Designing large arrays of tidal turbines: A synthesis and review”. In: *Date accessed: 26/01/2022* 41 (Jan. 2015), pp. 454–472. ISSN: 1364-0321. DOI: `10.1016/J.RSER.2014.08.022`. URL: `https://www.sciencedirect.com/science/article/pii/S1364032114006984`.

[108] S. Waldman, S. Bastón, R. Nemalidinne, A. Chatzirodou, V. Venugopal, and J. Side. “Implementation of tidal turbines in MIKE 3 and Delft3D models of Pentland Firth & Orkney Waters”. In: *Date accessed: 26/01/2022* 147 (Oct. 2017), pp. 21–36. ISSN: 0964-5691. DOI: `10.1016/J.OCECOAMAN.2017.04.015`. URL: `https://www.sciencedirect.com/science/article/pii/S0964569117304192`.

[109] Y. Wang, Q. Liang, G. Kesserwani, and J. W. Hall. “A positivity-preserving zero-inertia model for flood simulation”. In: *Date accessed: 15/08/2022* 46.1 (July 2011), pp. 505–511. ISSN: 0045-7930. DOI: `10.1016/J.COMPFLUID.2011.01.026`. URL: `https://www.sciencedirect.com/science/article/pii/S0045793011000338`.

[110] E. W. Weisstein. *Cylinder Drag – from Eric Weisstein's World of Physics*. 2017. URL: `https://scienceworld.wolfram.com/physics/CylinderDrag.html`.

[111] P. L. Woodworth. “A survey of recent changes in the main components of the ocean tide”. In: *Date accessed: 19/01/2022* (June 2010), pp. 1680–1691. DOI: `10.1016/j.csr.2010.07.002`. URL: `www.elsevier.com/locate/csr`.

[112] B. Wu, T. L. Yip, L. Xie, and Y. Wang. “A fuzzy-MADM based approach for site selection of offshore wind farm in busy waterways in China”. In: *Date accessed: 25/05/2022* 168 (Nov. 2018), pp. 121–132. ISSN: 00298018. DOI: `10.1016/J.OCEANENG.2018.08.065`. URL: `https://www.sciencedirect.com/science/article/pii/S0029801818304736`.

[113] Y. Wu, C. Xu, and H. Xu. “Optimal Site Selection of Tidal Power Plants Using a Novel Method: A Case in China”. In: *Date accessed: 23/01/2022* 9.10 (Oct. 2016), p. 832. ISSN: 19961073. DOI: `10.3390/EN9100832`. URL: `https://www.mdpi.com/1996-1073/9/10/832/htm%20https://www.mdpi.com/1996-1073/9/10/832`.

[114] D. Zhang, X. Liu, M. Tan, P. Qian, and Y. Si. “Flow field impact assessment of a tidal farm in the Putuo-Hulu Channel”. In: *Date accessed: 26/01/2022* 208 (July 2020), p. 107359. ISSN: 0029-8018. DOI: `10.1016/J.OCEANENG.2020.107359`. URL: `https://www.sciencedirect.com/science/article/pii/S0029801820303905`.